Title
Mechanistic Effects of Porosity on Structural Composite Materials

Author
Siver, Andrew

Publication Date
2014

Peer reviewed|Thesis/dissertation

University of California
Los Angeles

Mechanistic Effects of Porosity on Structural Composite Materials

A thesis submitted in partial satisfaction
of the requirements for the degree
Master of Science in Mechanical Engineering

by

Andrew Siver

2014

Abstract of the Thesis

Mechanistic Effects of Porosity on Structural Composite Materials

by

Andrew Siver

Master of Science in Mechanical Engineering

University of California, Los Angeles, 2014

Professor Ajit K. Mal, Chair

As fiber reinforced composites continue to gain popularity as primary structures in aerospace, automotive, and powersports industries, quality control becomes an extremely important aspect of materials and mechanical engineering. The ability to recognize and control manufacturing induced defects can greatly reduce the likelihood of unexpected catastrophic failure. Porosity is the result of trapped volatiles or air bubbles during the layup process and can significantly compromise the strength of fiber reinforced composites. A comprehensive study was performed on an AS4C-UF3352 TCR carbon fiber-epoxy prepreg system to determine the effect of porosity on flexural, shear, low-velocity impact, and damage residual strength properties. Autoclave cure pressure was controlled to induce varying levels of porosity to construct six laminates with porosity concentrations between 0-40%. Porosity concentrations were measured using several destructive and nondestructive techniques including resin burnoff, sectioning and optical analysis, and X-ray computed tomography (CT) scanning. Ultrasonic transmission, thermography, and CT scanning provided nondestructive imaging to evaluate impact damage. A bilinear relationship accurately characterizes the change in mechanical properties with increasing porosity. Strength properties are relatively unaffected when porosity concentrations are below approximately 2.25% and decrease linearly by up to 40% in high porosity specimens.

The thesis of Andrew Siver is approved.

Timothy Briggs

Stanley B. Dong

William S. Klug

Ajit K. Mal, Committee Chair

University of California, Los Angeles

2014

Table of Contents

Acknowledgments

The author would like to acknowledge the invaluable assistance of Dr. Timothy Briggs and Sandia National Laboratories for providing the resources, facilities, and funding to complete this research; Professor Ajit Mal of UCLA for his excellent guidance and support; and the author's family and friends for their encouragement and support throughout his graduate research.

Sandia National Laboratories is a multi-program laboratory managed and operated by Sandia Corporation, a wholly owned subsidiary of Lockheed Martin Corporation, for the U.S. Department of Energy's National Nuclear Security Administration under contract DE-AC04-94AL85000.

1 Introduction

This study focused on the affect of porosity on mechanical strength properties of structural composite materials. An overview of composite terminology, types of composites and their applications, construction, and induced defects is presented in the following sections.

1.1 Definition of Composite Materials

In its most basic form, a composite material is one consisting of two or more constituents working together to produce material properties different than the properties of those elements on their own. To exclude alloys and any materials containing impurities, all constituents must be discernible at 1μm to be classified as a composite. Most composites consist of a bulk material, known as the matrix, and a reinforcement or stiffening material commonly in a fibrous form. The fibers are used as primary load carriers while the matrix is used to transfer loads between fibers. Common materials such as concrete, plywood, and fiberglass are all classified as composite materials and are shown in Figure 1.

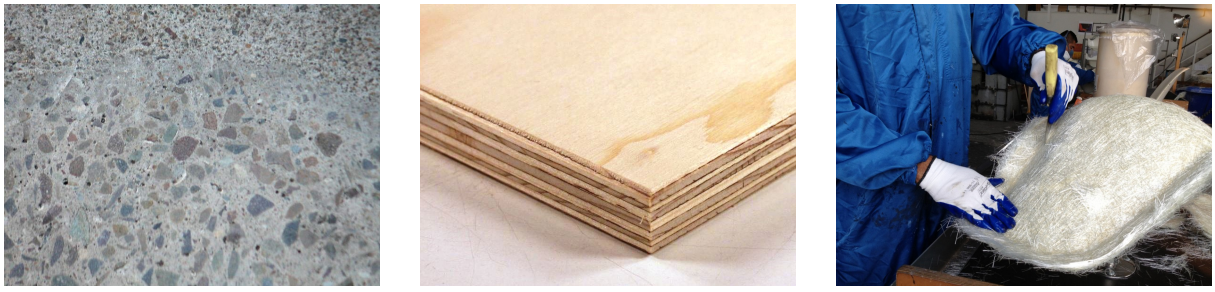

Figure 1: Concrete (left), plywood (center), and fiberglass (right) are all classified as composites.

Concrete consists of a course granular material (aggregate), embedded in a matrix material (cement) and has been widely used as a building material used in the construction of buildings, bridges, and dams. Plywood consists of thin sheets of wood veneer glued together in alternating orientations. Fiberglass is constructed of glass fibers as primary load carriers bound together in an epoxy matrix often cured in a mold or tool. Fiberglass is an example

of a well known composite material and can be found in a number of varying applications ranging from fishing boats to car entertainment systems. Composites consisting of long fibrous reinforcement and epoxy matrix will be investigated deeply in this study.

The measured strength of a material is always significantly less than the theoretical strength of the material. This discrepancy is often attributed to imperfections found within the material, reducing the actual strength of the material. Materials consisting of small cross sections are desired as an attempt to reduce the imperfections within a material. Fibers, because of their small cross-sectional dimensions, are not directly usable in engineering applications. Therefore, they are embedded in matrix materials to form fibrous composites. Fibrous composites have become an extremely important class of composite materials because they are capable of achieving very high strengths [1].

Individual continuous fibers are bundled together to form a tow, designated by a number followed by "K," indicating how many fibers are in each tow. For example, a 3K tow consists of 3,000 individual fibers bundled together and is shown in Figure 2, taken with an optical microscope at 200x magnification.

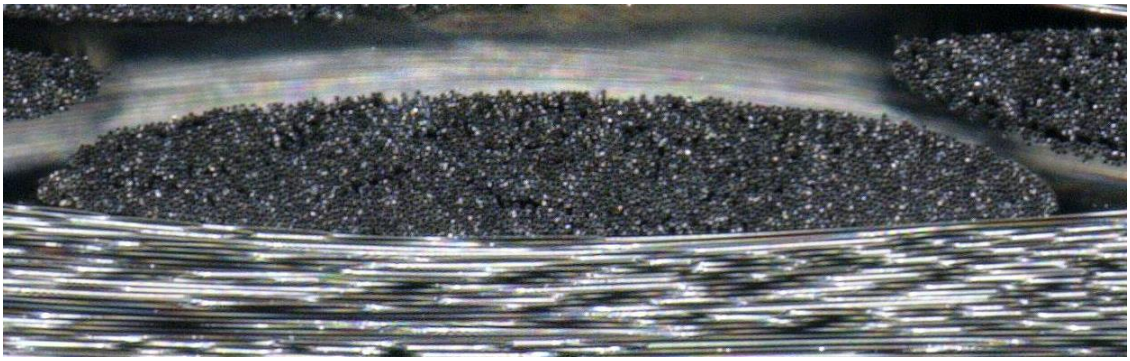

Figure 2: Thousands of individual fibers are bundled together to form a tow. The tow shown here consists of 3,000 fibers.

Fibrous composites are extremely strong in the fiber's longitudinal direction, however provide

little support in transverse directions. Strength in the transverse direction can be added by placing fibers oriented in the perpendicular direction. For applications where more than one fiber orientation is required, a fabric combining 0° and 90° fiber orientations is useful. Woven fabrics are produced by interlacing of warp, 0°, and weft, 90°, fibers in a regular pattern or weave style. The fabric's integrity is maintained by the mechanical interlocking of the fibers [2]. The most common weave styles are plain, twill, and satin, shown in Figure 3.

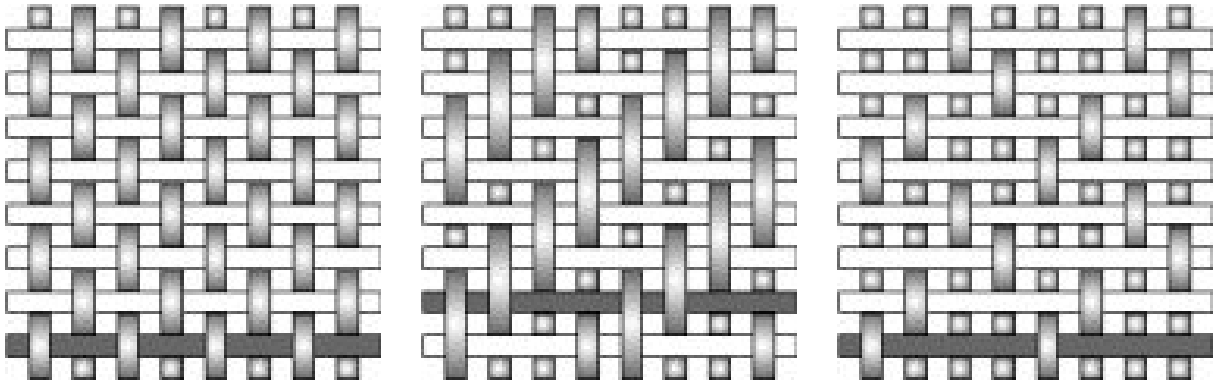

Figure 3: Plain weave (left), twill weave (center) and satin weave (right) are common weave patterns used in structural composite applications.

In a plain weave, each warp tow passes alternately over and under each weft tow. The weave is symmetric, balanced, and stable against shearing. However, the high level of crimp makes it difficult to drape and conform to complex geometry.

A twill weave is very similar to a plain weave, however each warp tow passes alternately over and under two or more weft tows. Twill weaves possess superior wet-out, drapability, and mechanical properties due to a reduction in crimp without a significant reduction in shearing stability.

Satin weaves are modified twill weaves with fewer intersections of warp and weft. The "harness" number used to define the weave is the total number of tows crossed and passed under before the pattern repeats. The weave shown on the right in Figure 3 is a 4-harness satin

weave since each warp tow goes over 3 weft tows before going under the next weft tow. Satin weaves possess excellent wet-out, drapability, and material properties due to the very low crimp of each tow. However, satin weaves are unstable, prone to in plane shearing, and are asymmetric [2]. Care must be taken when assembling laminates of multiple plies of satin weaves to ensure that residual stresses or curvature are not present due to asymmetry. This study features laminates constructed of an 8-harness satin weave.

Combinations of varying materials to make up the fibers and matrix can be combined to construct a composite material tailored to the specific application. Common materials used as the fibers are listed below:

- E-glass, S-glass
- Carbon
- Aramid (Kevlar, Nomex, Technora)

Glass fibers are maunfactured by blending sand, kaolin, limestone, and colemanite at high temperatures to form liquid glass. The liquid is passed through bushings and cooled to produce fiber filaments, drawn together and coated to provide filament cohesion and to protect from abrasion. E-glass is the most common form of reinforcing fiber used in composites due to its low cost, high tensile and compressive strength, and good electrical properties. S-glass has higher tensile strength and modulus, greater wet-out, and interlaminar shear strength properties.

Carbon fiber is produced by bonding carbon atoms together in crystals aligned parallel to the long axis of the fibers, done by spinning and stretching precursor through a spinnerette [3]. This alignment gives the fibers an extremely high strength-to-volume ratio. Carbon fibers are widely used in the aerospace, military, and civil engineering industries due to their high stiffness, tensile strength, chemical resistance, temperature tolerance, low weight and ther-

mal expansion [4].

Aramid fibers (commonly known by the trademarked name Kevlar developed by DuPont), are manufactured by extruding an acidic solution of an organic precursor through a spinnerette to orient the molecules in the direction of the longitudinal axis, similar to the manufacturing process of carbon fibers. Kevlar fibers have the lowest specific gravity and highest tensile strength-to-weight ratio among current reinforcing fibers,and are very resistant to impact damage making them very popular in the aerospace, military, and civil engineering industries [4]. Kevlar is commonly used in applications where impact or resistance is a major concern. However, Kevlar reinforced composites are not widely used due to very high cost and difficulty in manufacturing.

Common materials used as the matrix are listed below:

- Polymer
- Metal
- Ceramic

Polymer matrix materials are very common due several advantages such as their low cost, easy processability, good chemical resistance, and low specific gravity. However, polymers have relativity low strength, low modulus, and low operating temperatures [1]. Polymer matrices include epoxy, phenolic, and polyester.

Metalic matrices are commonly found when high operating temperatures are required, however, metallic matrices are difficult to manufacture due to their high melting point. Other factors that can limit the use of metallic matrix is their reactivity with fibers and corrosion. In addition to high operating temperature, they possess high modulus and strength, impact

toughness and resilience.

Ceramic matrices are used in very high temperature environments where polymers and metallics cannot survive. Ceramic matrices trade strength and modulus for ductility; they possess extremely high strength properties but are very brittle and expensive to manufacture. The composites used in this study consist of carbon fibers embedded in an epoxy matrix.

1.2 Applications of Fiber Composites

Two outstanding features of oriented-fiber composites are their high strength-weight ratio and controlled anisotropy [1]. Strength and density properties of commonly used structural materials are presented in Table 1. All numbers were compiled by the authors of [1].

Table 1: Properties of conventional structural materials and cross-ply fiber composites

Material	E (GPa)	σ_u (GPa)	ρ (g/cm^3)	E/ρ	σ/ρ
Mild Steel	210	0.6	7.8	26.92	0.08
Aluminum 2024-T4	73	0.41	2.7	27.04	0.15
Aluminum 6061-T6	69	0.26	2.7	25.56	0.10
E-glass-epoxy	21.5	0.57	1.97	10.91	0.29
Carbon fiber-epoxy	83	0.38	1.54	53.90	0.25
Kevlar 49-epoxy	40	0.65	1.4	28.57	0.46

From the right column of Table 1, it is clear that fiber-reinforced composites possess much greater strength-weight properties than steel and aluminum alloys. However, the major advantage of fiber-reinforced composites is the ability to control the strength in specific directions. Unidirectional fibers are anisotropic by nature; the material properties in the longitudinal directions are significantly greater than those in the transverse directions. Laminates are designed and constructed from unidirectional composites to obtain desired directional properties to match requirements of specific applications. The ability to customize compos-

ites to the specific application significantly reduces weight since material can be added or removed throughout the structure. Complex geometry is easily constructed from composites, reducing the complexity and number of parts of assemblies.

The reduction of raw materials and manufacturing costs have given composites an increasing role in structural applications. Composites are a popular material for applications where high strength and minimum weight is required, such as the transportation and power sport industries. Applications range from airplanes and automobiles to skis and mountain bikes.

Polymers are a widely used matrix material for fiber composites. Thermosetting plastics (such as epoxy) have cross-linked structures that irreversibly cures. Prior to cure, thermoset plastics are liquid or malleable, designed to be molded into their final form. Cure is usually induced by heat, commonly applied in an oven or autoclave ramping up to approximately 200°F. To ensure compaction and reduce porosity, pressure is often applied during cure. This is achieved by curing the laminate in an autoclave. Thermocouples are often used to measure the temperature of the laminate, ambient autoclave air, and tool surface. This allows for greater control of heating and cooling during the cure process. Cures for large laminates often utilize many thermocouples throughout the length and thickness of the part to ensure even heating. Rheology analysis can be performed on the resin to determine the viscosity and modulus as a function of time and temperature. Rheological curves are used to determine the optimal temperature to apply autoclave pressure, often slightly prior to the resin's minimum viscosity. Applied pressure as the resin approaches its minimum viscosity allows the resin to flow with little resistance, ensuring complete compaction and reducing porosity.

1.3 Manufacturing Induced Defects: Porosity

Porosity can be a significant source for concern if viscous resins are used in a laminate. Composite parts, constructed under seemingly identical conditions, can often exhibit significantly varying quality levels and mechanical properties [5]. Porosity is induced by voids becoming trapped between plies during the laminate construction process. Voids can include air or solvents such as release or residual chemicals used to clean the tool surface. Refrigeration is often used to increase shelf life of prepreg composites, making them susceptible to moisture accumulation when removed from the freezer. During the layup process, air, moisture, or other volatiles can become trapped.

During autoclave cure, ambient temperature is increased to a level where cross-linking within the matrix transforms a liquid polymer into a rigid, solid material. While elevated temperatures are required to cure the matrix, elevated temperature increases the vapor pressure within each void. Void growth will occur if the internal vapor pressure is greater than the hydrostatic pressure of the resin. Alternatively, void supression will occur if the hydrostatic pressure within the resin is greater than the vapor pressure of each void. A diagram detailing void growth or suppression is shown in Figure 4.

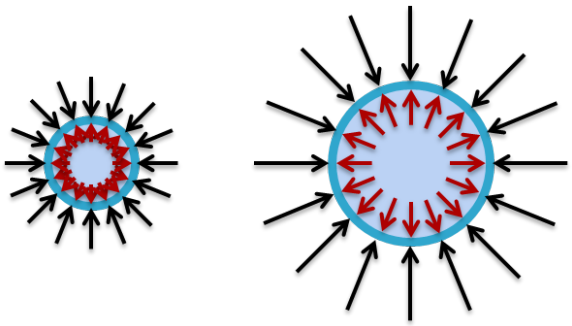

Figure 4: Voids are suppressed into solution (left) if the hydrostatic pressure (black arrows) is greater than the vapor pressure (red arrows). Alternatively, void growth occurs when vapor pressure is greater than hydrostatic pressure.

Vapor pressure increases exponentially as temperature increases. The internal battle between increasing hydrostatic resin pressure and increasing vapor pressure determines whether or not voids are present in the cured laminate. If voids are not removed or suppressed into solution, they can remain trapped and create permanent voids in the laminate. These voids create discontinuities in the matrix, creating a nonuniform flow field and reduced load transfer capabilities.

The resin hydrostatic pressure seen at each pore differs from the autoclave pressure due to the compliance of composite constituents. In a simplified model, the fiber bed and matrix act as springs and reduce the hydrostatic pressure at voids in plies deep into the laminate, shown in Figure 5.

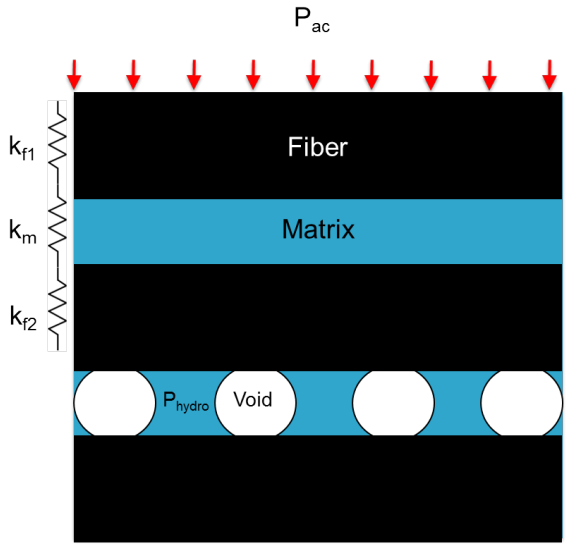

Figure 5: The fiber bed and matrix in plies above pores act as springs and reduce the hydrostatic pressure seen by each pore.

Hydrostatic pressure as a function of autoclave is dependent on several factors, such as fiber type, weave, thickness, resin, and temperature. If voids are unable to migrate out of the matrix, autoclave pressure is used to suppress voids into solution. However, increasing autoclave pressure above a threshold can result in severe resin bleed out, increasing the fiber to

resin ratio and creating a resin lean composite. Resin lean laminates do not contain enough matrix to properly distribute loads between fibers and greatly reduce the load carrying capabilities.

A typical cure cycle used to manufacture composite parts for defense applications is shown in Figure 6.

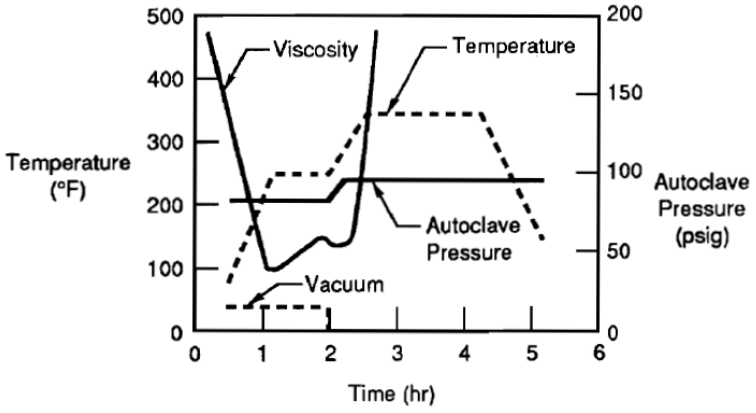

Figure 6: Temperature and autoclave pressure are adjusted as a function of time to properly cure composite parts.

The cure cycle shown in Figure 6 consists of two temperature ramps and isothermal holds, autoclave pressure ramp and hold, and vacuum start up. The first ramp and isothermal hold is intended decrease the viscosity of the resin, allowing it to flow. While the resin is approaching its minimum viscosity, volatiles are able to escape since the resistance to migration out of the resin has been reduced. The imposed viscosity curve shows the significant drop in resin viscosity as the prepreg resin begins to flow [5]. The second ramp and hold is used to polymerize the resin. During this stage, the viscosity rises dramatically as the resin begins to gel and crosslinking occurs. Prior to the second ramp, vacuum bag pressure is vented and autoclave pressure is increased. At this point during the cure, voliatiles remaining in the resin are unlikely to migrate out due to the increasing viscosity. Autoclave pressure is applied to attempt to suppress any remaining volatiles into solution, reducing the size and

affect porosity has on the cured laminate. Vacuum pressure is vented prior to the second ramp to decrease the risk out outgassing.

To summarize, voids are induced into laminates during the layup by trapping air as plies are laid up. Autoclave cure schedules are designed to include temperature and pressure ramps and holds to allow volatiles to escape. As the resin approaches its minimum viscosity, autoclave pressure is increased to suppress any remaining volatiles into solution. The cured laminate can be inspected to determine porosity. The void formation and growth process is complex and is not fully understood. However, a number of basic principles are well understood and have been investiaged in several research studies [6], [7], [8], [9].

2 Literature Review

Several studies have been performed to investigate the affects of porosity on mechanical properties of structural composite materials. Together, these studies were used as guidelines and provided insight throughout the study.

2.1 Inducing Porosity

Voids are one of the most common types of manufacturing process induced defects in composite materials that have detrimental effect on the material properties [9]. Inducing porosity posed a unique challenge—creating imperfect composite materials is not a common practice. Curing of thermoset resin composites requires the application of heat and pressure. Heat is used to facilitate and control the chemical reactions. Pressure is applied to squeeze out excess resin, to consolidate plies, and to minimize void content. Thus, to ensure proper cure, the magnitudes and duration of the heat and pressure (referred to as cure cycle) must be chosen carefully [7]. Several authors control autoclave cure pressure as an attempt to induce and control porosity concentration [5–8, 10–20]. Autoclave pressures ranged from 0-1 MPa (0-145 psi) producing laminates with porosity concentrations between 0-10%.

Without proper layup materials, increasing the autoclave pressure may lead to inhomogenities throughout the laminate. As indicated by [7], enough bleeder must be present to fully absorb excess resin during cure. If autoclave pressures are too high and too much resin is forced from the laminate, uneven curing could occur, creating resin rich and resin lean areas. This phenomenon is shown in Figure 7.

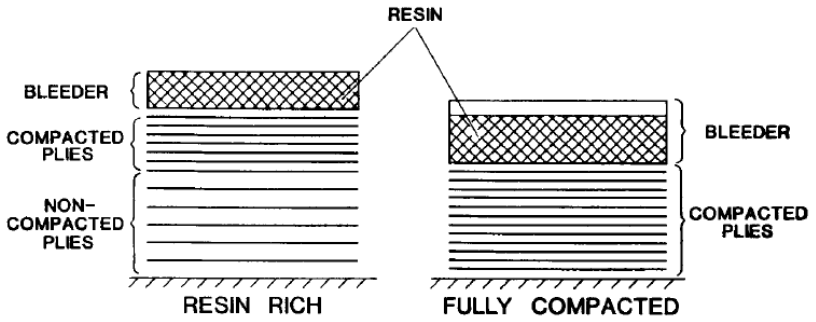

Figure 7: The quality of a composite is highly dependent on layup materials such as bleeder thickness.

If the bleeder is too thin (left), the bleeder becomes saturated before compaction is complete and resin rich layers are present. Bleeder of proper thickness (right) ensures all excess resin is absorbed throughout cure. Chemical properties such as viscosity and glass transition temperature, vary for each resin system and can be used as customization for a specific application. Thus, a rehological study should be performed to determine the appropriate resin system for optimal performance.

Alternative methods, such as spraying the laminate with water during the layup procedure, were suggested to induce porosity [6, 7]. Since composites are susceptible to moisture and humidity, it may be difficult to determine whether the observed change of mechanical properties were a result of porosity or hygrometric affects.

It is possible to obtain 90% of the performance at 60% of the cost, the last 10% of performance being 40% of the cost. The engineer can cut production costs by knowing the acceptable void level for the particular application. Loosening the quality control standards translates to a lower cost end product [8]. The acceptable level of porosity greatly depends on the application of the structure and customer. Some manufacturers limit the acceptable porosity concentration for primary structural components in dynamic aerospace structures at 1%. Others allow between 2-5% [21].

2.2 Effect on Mechanical Properties

Composite materials are highly strain-rate dependent. Thus, a literature review on both quasi-static and dynamic loading was performed to capture differences in strain-rate.

2.2.1 Quasi-Static Loading

With the increasing popularity of fiber reinforced composites in the aerospace and automotive industry, the effect of porosity on mechanical strength properties of fiber composite materials has been a popular topic of study. Several authors in the literature present the unaffected affect of porosity on tensile properties [7, 13–16, 21]. Longitudinal tensile properties of CFRP unidirectional laminates do not appear to be influenced by voids. Most other mechanical properties such as longitudinal compressive modulus and strength, transverse tensile modulus and strength, and bending and shear properties are influenced by voids [17, 18]. All mechanical properties decrease, but porosity has a different influence of each property. In a study to characterize voids by ultrasonic inspection, the authors of [19] measured for a 1% increase in porosity, interlaminar shear strength decreases by 9%, tensile strength by 6%, and the tensile modulus by 2%. As a comparison, the authors of a similar study measured a 9.7% interlaminar shear strength reduction, 10.3% flexural strength reduction, and a 5.3% flexural modulus reduction for each percent porosity [22]. While many authors agreed in regards to which properties were greatly affected by porosity, few were able to reproduce similar results. All studies reported a reduction in strength properties, however the relative magnitude was wildly inconsistent.

The following properties were found to be greatly affected by porosity:

- Interlaminar Shear Strength
- Flexural Modulus
- Flexural Strength

- Impact Energy
- Delamination Area

This list of affected mechanical properties is not surprising considering they are all largely affected by the state of the matrix. Since porosity greatly affects the integrity of the matrix, it is expected to severely impact properties carried by the matrix.

Compression after impact testing is used to determine residual strength properties after an out-of-plane impact event. Delaminations produced by low-velocity impact events greatly reduce the composite's ability to withstand and transfer compressive loads. Under uniaxial compression, delamations can result in three types of buckling, shown in Figure 111.

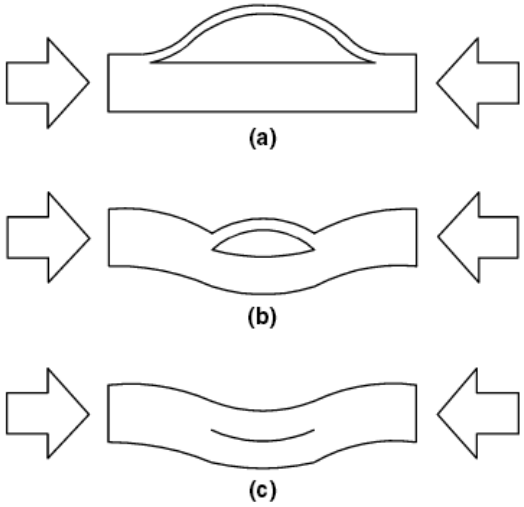

Figure 8: Local buckling (top), mixed-mode buckling (center), and global buckling (bottom) can occur in delamainted composite materials loaded in uniaxial compression.

A delaminated ply can be modeled as a buckling problem with fixed-fixed boundary conditions. To isolate the compressive properties of the delaminated ply, a custom fixture must be used to prevent mixed-mode and global buckling. Compression after impact testing has become increasingly popular and has been the subject of numerous technical papers [23]. Common compression after impact failure modes are shown in Figure 9 [24].

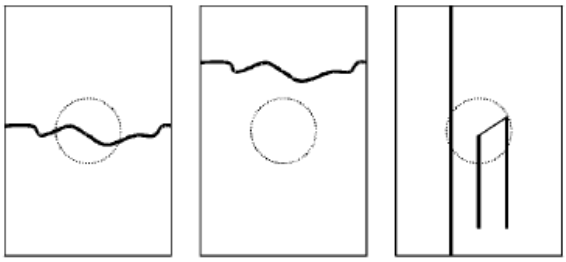

Figure 9: Transverse failure through the impacted area (left), transverse global compressive failure, and longitudinal/shear failure (right) are common failure modes of damaged composites loaded in uniaxial compression.

The authors of [23] calculated compressive strength and modulus of composite panels impacted at various impact velocities. As expected, residual compressive strength decreased as impact energy increased. Few resources were found which investigated impact and compression after impact results of samples with increasing porosity concentrations.

2.2.2 Dynamic Loading

During the lifetime of a structure, impacts by foreign objects can be expected to occur during manufacturing, service, and maintenance operations [25]. Out-of-plane impact loads are one of the most common ways by which damage is introduced within a composite structure during usage. Low-velocity impacts of this nature occur frequently during the service and maintenance of aircraft (e.g. impacts due to dropped tools) and produce visually undetectable localized damage [23]. This internal damage can cause a severe loss in strength, and if gone unnoticed can lead to catastrophic failures. For conditions of low velocity impact loading, the size and shape of the target determines its energy-absorbing capability and therefore its impact response [26].

Flat and hemispherical tup geometries are commonly used to determine the affects of impact events on fiber reinforced composites. Flat and hemispherical impact tups can be found in

Figure 10.

Figure 10: Flat (left) and hemispherical (right) tup geometries were used to mimic real world impact scenarios.

Flat tups are similar to an impact caused by a blunt object, such as a hammer or wrench on a structure. Hemispherical tups are analogous to impacts caused by round objects, such as rocks. Since the size and type of damage is dependent on the size and shape of the target, a comprehensive study would include both geometries.

Unlike quasi-static events such as flexure or compression loading in a load frame, impact events test the mechanical integrity of the structure at a much higher strain rate. The strength of fiber reinforced composites are heavily dependent on strain rate and differ from quasi-static loading. Stress-strain relationships for quasistatic and high strain rate loading can be found in Figure 11.

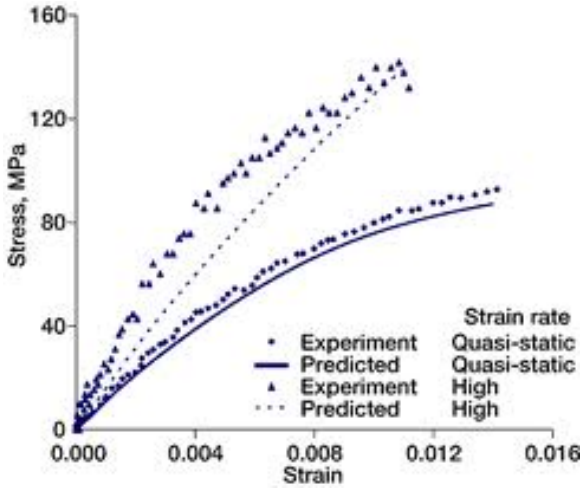

Figure 11: Composites are highly dependent on strain rate. Higher strain rates induce greater stress for a given strain when compared to quasistatic loading.

Damage area and residual strength is highly dependent on the impact energy. The impact energy guarenteed to produce delamination within the sample is calculated using Eq. (1).

$$E_{delam} = C_E h \tag{1}$$

where E_{delam} is the required energy for delamination, C_E is the ratio of delamination energy to specimen thickness equal to 6.672 J/mm found in ASTM D7136, and h is the sample thickness. The authors of a study investigating residual compressive strength of impacted composite panels determined an impact energy equal to 24 J to be sufficient to produce visible impact damage [23].

When a solid is subjected to any kind of loading, static or dynamic, it can absorb energy by two basic mechanisms: material deformation and creation of new surfaces. If the loading supplies a sufficient amount of energy, a crack may initiate and propagate, creating new surfaces [1]. The energy requried per unit area of the composite for fracture of fibers in tension is given by the following expression [27],

$$u = \frac{V_f \sigma_{fu}^2 l}{6E_f} \tag{2}$$

where V_f is the fiber volume fraction, σ_{fu} is the ultimate strength of the fibers, E_f is the fiber modulus, and l is the fiber length. Fiber volume fraction, ultimate fiber strength, and fiber modulus are all manufacturer supplied quantities, making the energy required per unit area an easily calculated value.

Although fibers are responsible for imparting high strength to the composite, the fracture of fibers accounts for a small percentage of the total energy absorbed. Instead, fiber debonding, fiber pullout, and matrix deformation contribute larger percentages of total energy absorbed [28]. Impact events can create several types of damage within the composite. Examples of each type of damage can be found in Figure 12 [29].

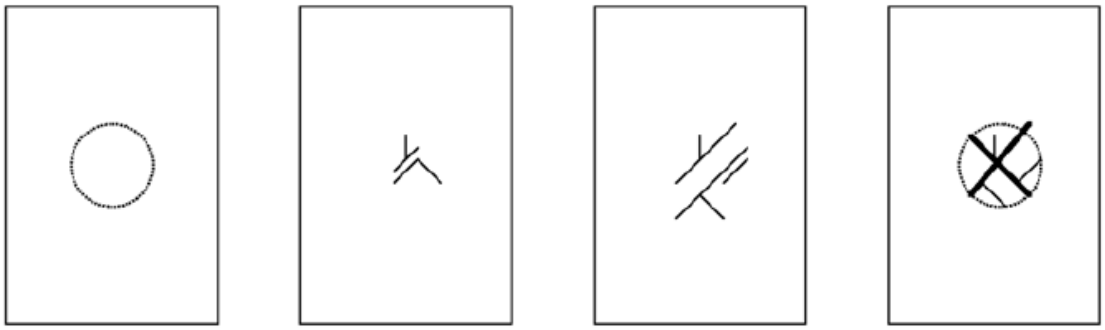

Figure 12: Types of external visible damage include a dent/depression, splits or cracks, delaminations, and puncture (left to right).

The damage modes of an impacted composite plate can be classified as fiber breakage, delamination, and matrix cracking. In low-velocity impact, delamination accompanied by matrix cracking has been found to be the major damage mode. The delamination at the interface of two adjacent laminae is caused by a mismatch in their stiffnesses as a result of their different orientations [1]. It has been observed that the delamination area depends on the impacting energy. Figure 13 shows four crossply laminates impacted with increasing velocities. As the impacting energy increases, the interface delamination area increases [30].

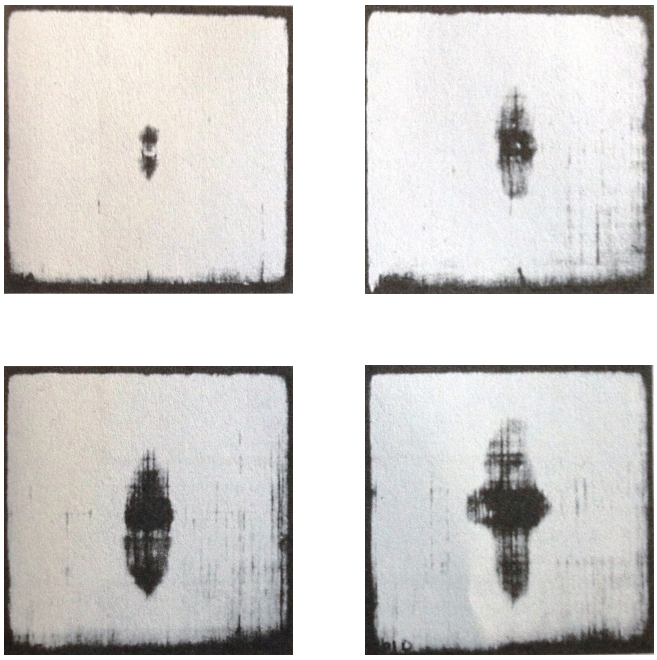

Figure 13: Delamination area increased with increasing impact velocity.

2.3 Damage Evaluation Techinques

2.3.1 Ultrasonic Imaging

The images above were generated using ultrasonic imaging. A high frequency sound wave in periodic short bursts of a few cycles is transmitted into the material being examined. The wave is reflected by discontinuities in the material such as voids, delaminations, and cracks as well as the back wall of the material. If the wave encounters discontinuities, the reflected wave may not return to the transducer, shown as a loss in signal amplitude. Ultrasonics have become an increasingly popular method of evaluating the integrity of composite materials due to the simplicity and reliability of their readings. Safe operation of composite structures requires careful monitoring of the initiation and growth of such defects before they grow to a critical size resulting in possible catastrophic failure of the structure. Ultrasonic methods offer a nondestructive and reliable method for defect monitoring in advanced structures [31]. Dozens of successful studies have been conducted using ultrasonic scanning as a

nondestructive method for the evaluation and detection of barely-visible impact damage in fiber-reinforced composite materials [12, 31–35].

2.3.2 Thermographic Imaging

Thermography is another nondestructive technique to inspect the integrity of a composite material. The thermal conductivity of a material at a flaw location is different from that at a location without a flaw, and heat is generated at flaws under cyclic loading [1]. Flaws are detected by recording thermal patterns with an infrared camera on the surface when a material is heated by an external source. Delaminations and interlaminar cracks have been studied and detected by several authors in the literature [36–38]. In comparison with ultrasonic inspection, thermographic inspection provides poor resolution [39]. However, it is a relatively fast and non-contact inspection technique that has a wide coverage area. It can be used to detect delaminations, impact damage, water ingression into a honeycomb, inclusions, and density variations [40].

2.3.3 X-ray Computed Tomography

Intensity of a monochromatic beam of X-rays as it propagates through any matter decreases because of absorption [1]. The relationship between the intensity, I, and the distance traveled, x, is given by,

$$I = I_0 e^{-\mu x} \tag{3}$$

where I_0 is the initial intensity of the beam, and μ is the linear absorption coefficient, dependent on the beam wavelength and material. In the X-radiography technique, an X-ray beam is passed through the material, and the emerging beam exposes a photographic film. The exposure patterns on the film provide information about the material. The highly exposed areas are indicative of material with smaller absorption coefficients; allowing voids

and delaminations easily distinguishable [1]. The material is scanned at various incident angles, producing a 3-dimensional reconstruction throughout the thickness of the material. Although it requires very complex and expensive equipment, X-ray computed tomography can produce models of very high resolution. For this reason, X-ray computed tomography as an inspection technique is rarely used for large structures which need to be evaluated for routine in-service inspections.

3 Experimental Work

The materials, equipment, and cure schedule used in the study are outlined in the following sections.

3.1 Materials

All experimental work was conducted on a carbon fiber reinforced polymer (CFRP) material. Its numerous advantageous qualities has led to the adoption of its primary use in automotive, aerospace, and defense applications. All specimens were constructed of [0/90] prepreg consisting of an 8 harness-satin weave and an UF3352 TCR epoxy resin matrix. Unlike a plain weave, an 8 harness-satin weave is resistant to crimping and possesses excellent drapebility properties, allowing it to easily conform to tight corners and complex shapes. A diagram comparing a plain weave to an 8 harness-satin weave lamina can be found in Figure 14.

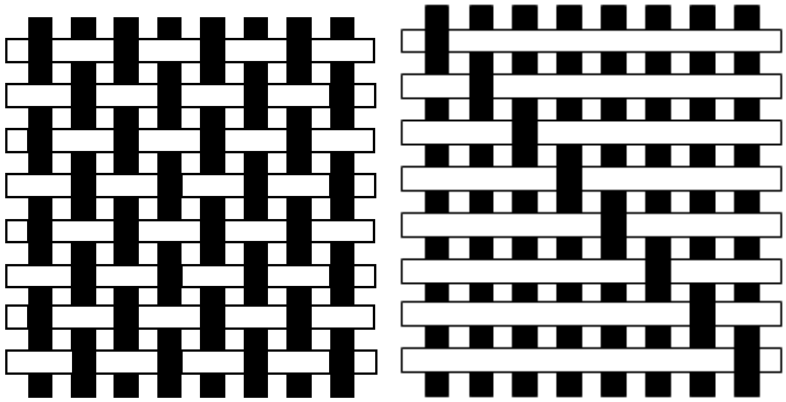

Figure 14: The plain weave (left)and 8-harness satin weave (right)

Unlike a plain weave, fibers in the warp direction of an 8 harness satin weave run over 7 weft tows and under one. This pattern alternates, giving the weave a diagonal appearance. Due to the nature of the weave, a single ply is asymmetric and will warp when cured. When an axial external load is applied (thermal or mechanical), the extension-bending coupling causes the laminate to bend or warp. Forcing the laminate to remain flat so it possesses no curvature during cure induces residual stresses, reducing the load carrying capabilities

of the composite. To eliminate the extension-bending coupling without introducing residual stresses, a symmetric laminate was constructed. Extension-bending coupling is dependent on the geometric properties of each ply and the distance from the mid surface of the laminate. This effect is eliminated by placing the same angled plies the same distance from the mid surface in the opposite direction. To remain consistent, all test specimens were constructed from the same stack sequence.

The 8-harness satin weave was pre-impregnated with UF3352 TCR™ Resin system. The UF3352 resin system is a thermosetting epoxy matrix resin system typically used in sporting goods, commercial products, pressure vessels, rocket motor cases, and aerospace structural components.

3.2 Specimen Dimensions

A balanced and symmetric layup were chosen to eliminate extension-shear, and extension-bending coupling arising from the asymmetry of the weave. Specimen dimensions were determined by the respective ASTM standard. Required dimensions for each test standard are given in Table 2.

Table 2: Required Specimen Dimensions

Test	ASTM Standard	Final Dimensions (mm)	Plies
4-Point Bend	ASTM D790	$120 \times 25 \times 6.11$	16
Short Beam Shear	ASTM D2344	$40 \times 12 \times 6.11$	16
Low-Velocity Impact	ASTM D7136	$150 \times 100 \times 4.60$	12
Compression After Impact	ASTM D7137	$150 \times 100 \times 4.60$	12

The specimen thicknesses were chosen to minimize the total number of autoclave cures. With only two required specimen thicknesses, two laminates were constructed for each porosity

concentration. The size of each laminate was chosen to ensure all 10 specimens could be cut from one panel. Panel dimensions and cutouts for the 16 ply laminate are given in Figure 15.

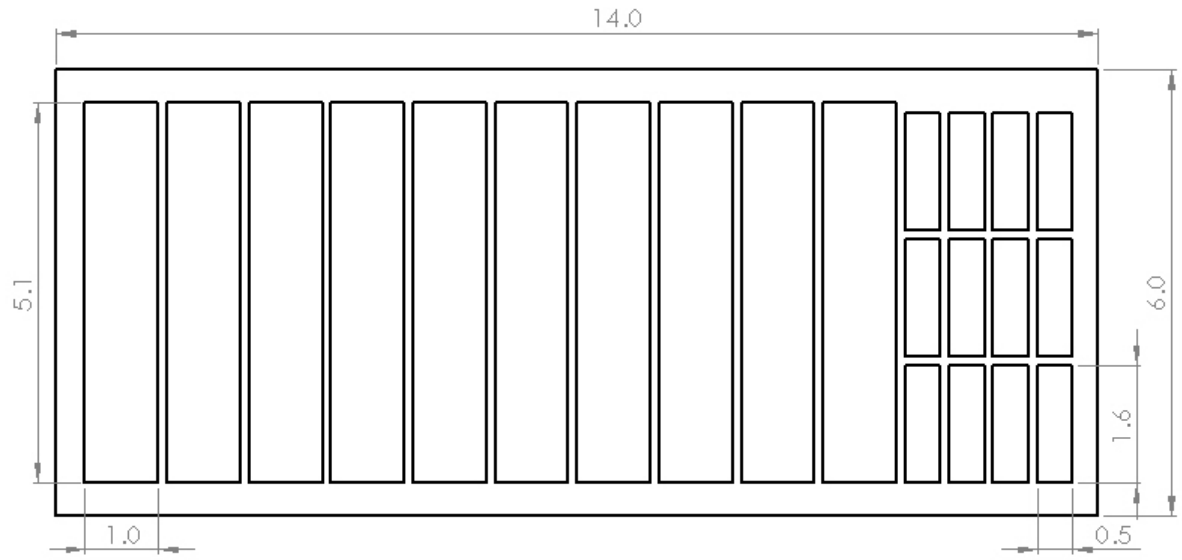

Figure 15: Four point bend and short beam shear specimens were cut from the same laminate.

Panel dimensions and cutouts for the 12 ply laminate are given in Figure 16.

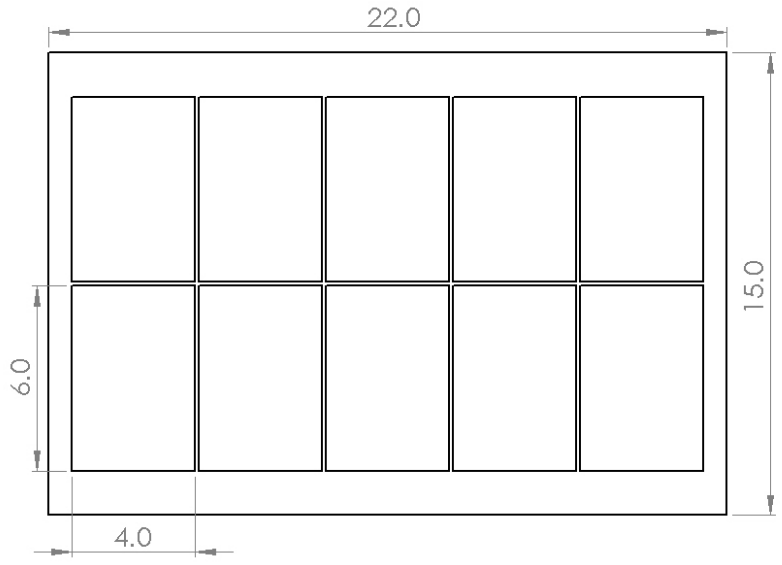

Figure 16: Impact and compression after impact specimens were cut from the same laminate.

Cutting all specimens from the same laminate and minimizing the number of autoclave cures helped reduce the variability seen among test samples.

3.3 Specimen Prep and Consolidation

With the specimen and laminate dimensions determined, the panels were constructed and autoclave cured. Six laminates of each thickness were constructed, one for each porosity condition and one extra. Using a CNC ply cutter, 96 plies were cut for the laminate shown in Figure 15 and 72 plies were cut for the laminate shown in Figure 16. The CNC ply cutter greatly reduced cutting and layup time and minimized waste. The CNC ply cutter can be seen cutting the plies for the 16 ply laminate in Figure 17.

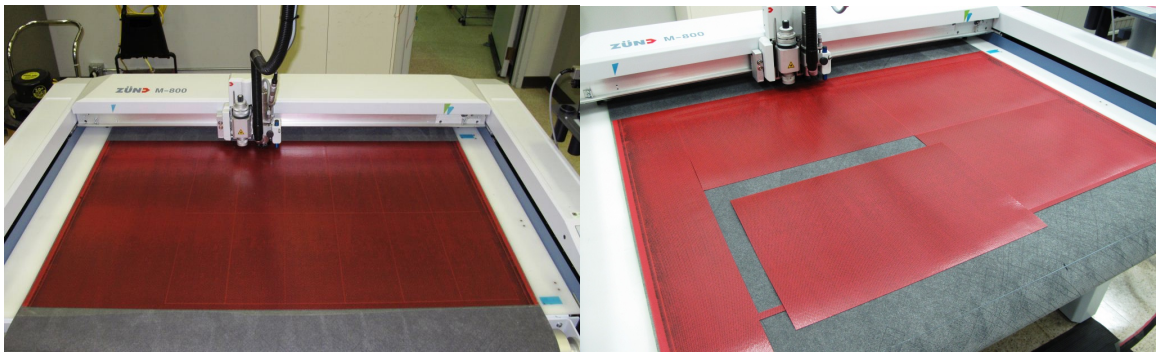

Figure 17: A CNC ply cutter saved time and reduced waste.

With the plies cut, the laminates were constructed according to the specified stack sequence. The stack sequence for each laminate is given in Table 3.

Table 3: Laminate Stack Sequence

Laminate	Laminate Code	Plies
Flexure, Short Beam Shear	$[(90/0)_{8c}]_s$	16
Impact, Compression After Impact	$[(0/90)_{6c}]_s$	12

The orientation of the outer plies were chosen to ensure the warp direction was in the

lengthwise direction of the test specimens. With the laminates laid up, they were bagged and autoclave cured. The bagging schedule used is shown in Figure 18.

Figure 18: The bag schedule consisted of several components, all serving different purposes.

In order from back to front, the bag schedule is as follows:

1. Aluminum tool (silver)
2. Silicone caul plate (orange)
3. Non-perforated release film (red)
4. Laminate (dark red)
5. Perforated release film (red)
6. Bleeder (white)
7. Silicone caul Plate (orange)
8. Breather (white)
9. Vacuum bag (transparent)

Also shown in Figure 18: resin dam tape (yellow), vacuum bag tape (blue), vacuum ports, high temperature tape, carpenter's square, graphite knives, and scissors. Once the laminates were bagged, they were debulked for 10 minutes prior to curing. To ensure consistency, all laminates were debulked for the same amount of time. A laminate bagged and debulking is shown in Figure 19

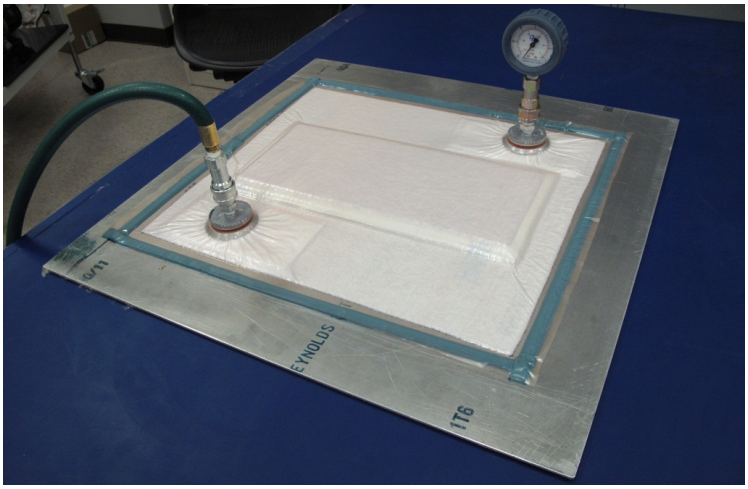

Figure 19: Each laminate was debulked for 10 minutes prior to autoclave curing.

The debulking process was included to ensure consistent compaction at room temperature before autoclave curing. With the 12 and 16 ply laminates constructed, bagged, and debulked, they were cured in the autoclave according to their specified cure schedule.

3.4 Cure Cycle

The cure cycle for each laminate was carefully chosen to induce the desired porosity concentration. Several authors in the literature concluded that the main parameter associated with inducing porosity concentration is autoclave pressure and vacuum bag pressure [6, 7]. Several authors subjected their laminates to pressures ranging from $0 \rightarrow 1$ MPa, or $0 \rightarrow 145$ psi producing laminates with porosity concentrations ranging from $0 \rightarrow 11\%$ [6–8, 10, 19]. Inside the autoclave, the laminate is subjected to the autoclave pressure, and compaction pressure from the vacuum bag, as shown in Figure 20.

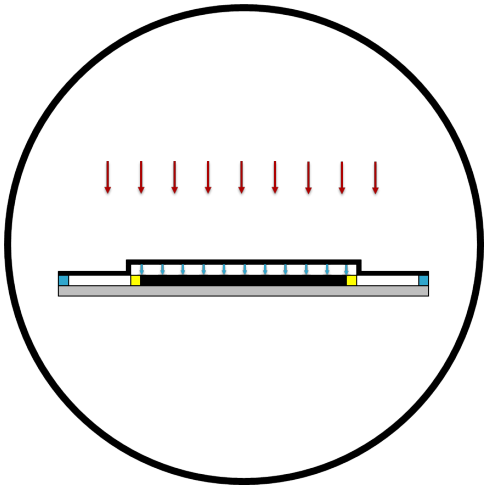

Figure 20: The laminate sees pressure from the autoclave (red arrows) and vacuum bag (blue arrows).

The vacuum bag pressure was not adjustable; it was on or off throughout the duration of the cure. The autoclave pressure and vacuum bag pressure were systematically adjusted to change the pressure seen by the laminate. The autoclave and vacuum bag pressures used for the six cures are shown in Table 4.

Table 4: Cure conditions

	100	200	300	400	500	600
$P_{autoclave}, psi$	0	0	10	20	30	45
P_{bag}, psi	0	15	15	15	15	15
P_{total}, psi	0	15	25	35	45	60

The six cure conditions were chosen to construct laminates of varying porosity content. In addition, the two extremes represent real world conditions. The 100 series panels were subjected to 0 hydrostatic pressure. Although most panels are cured inside a vacuum bag, the bag may rupture during vent. This situation is closely related to a laminate curing inside an oven. At the other extreme condition, the 600 series panels were subjected to a total

hydrostatic pressure equal to 60 psi, a common pressure for curing carbon/epoxy composites.

With the autoclave pressures determined, rheological curves were used to find the temperature to apply autoclave pressure. The rheology curve for the UF3352 resin can be found in Figure 21.

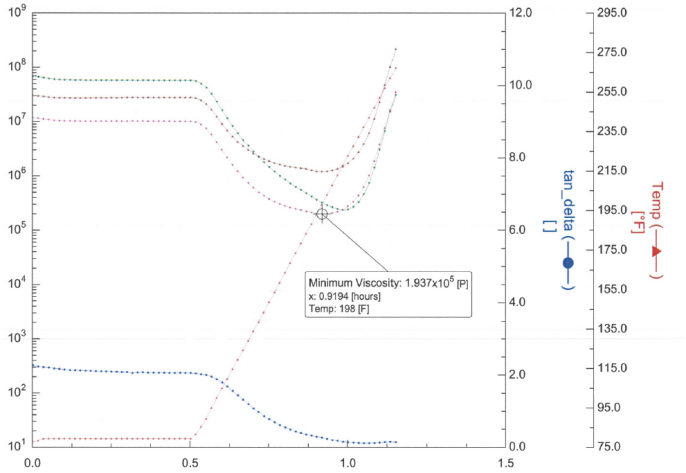

Figure 21: The rheology curve was used to find at what temperature pressure should be applied.

As temperature increases and viscosity decreases, the void pressure is high. Since this combination greatly increases the possibility for void formations, autoclave pressure must be applied prior to the minimum viscosity where gellation and polymerization occur soon after [5]. If pressure is not applied prior to minimum viscosity, gellation and polymerization will cause voids to become trapped inside the resin. From the rheology curve in Figure 21, it was determined that pressure should be applied when the part reaches 135 °F. Rheology and manufacturer supplied parameters were used to construct the cure cycle described in Figure 22.

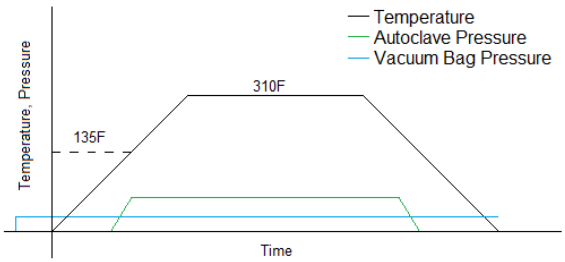

Figure 22: The quality of a part is highly dependent on the cure cycle. Pressure application point and vacuum bag cycles were determined using rheology and manufacturer supplied information.

4 Porosity Determination

4.1 Introduction

In order to derive empirical relationships between porosity and strength properties, the porosity concentration of each laminate must be accurately measured. Several methods exist in the literature, both destructive and non-destructive.

4.2 Analytic Methods

The following sections outlines the analytic methods used to measure porosity concentration using various techniques.

4.2.1 Destructive

Destructive methods include resin digestion and sectioning with optical analysis. Resin digestion uses a strong acid or extreme heat to remove the matrix from the fibers. The remaining fibers are weighed and constituent contents can be calculated. For sectioned samples, specimens are sliced and optical software is used to gather pixel intensity. Pixels under a certain threshold are determined to be pores and tabulated to estimate porosity concentration in a representative slice.

4.2.1.1 Resin Digestion

Porosity determination by resin digestion aims to separate the resin from the fibers and use their corresponding mass and densities to compute void volume. Voids are assumed to consist of volume with negligable mass. Thus, the total volume of the composite can be written as the sum of three major constituents,

$$V_c = V_m + V_f + V_v \tag{4}$$

where the subscripts c, m, f, and v correspond to composite, matrix, fibers, and voids respectively. Dividing each term by the composite volume yields the mass, fiber, and void

fraction,

$$\%V_v = 1 - \frac{1}{V_c}\left(V_m + V_f\right) \tag{5}$$

Mass density can be used to equate the volume of the fiber and matrix to their mass since mass is directly measured. The porosity concentration becomes,

$$\%V_v = 1 - \frac{\rho_c}{m_c}\left(\frac{m_m}{\rho_m} + \frac{m_f}{\rho_f}\right) \tag{6}$$

where m is the mass and ρ is the mass density of each constituent. The porosity concentration can be determined with the mass and density of the composite, matrix, and fibers. Densities of the matrix and fibers are manufacturer supplied, while the density of the composite must be accurately measured. Density was measured in accordance with ASTM D792 by measuring the weight of an object immersed in 2 different fluids (water and air). The density of the composite is calculated by,

$$\rho_c = \frac{1}{\rho_{water}}\left(\frac{m_{air}}{m_{air} + m_{water}}\right) \tag{7}$$

where m_{air} is the apparent mass of the composite in air and m_{water} is the apparent mass of the composite submersed in water.

4.2.1.2 Sectioning/Optical Analysis

Sectioned samples were imaged using an optical microscope at 50x magnification. The images were post-processed with the freeware ImageJ to distinguish voids from composite. All pixels with an intensity below a certain threshold were tabulated and divided by the total pixel count to estimate porosity concentration,

$$\%V_v = \frac{\sum \text{Pixel}_{I>T}}{\sum \text{Pixel}} \tag{8}$$

4.2.2 Nondestructive

Destructive methods for the measurement of porosity is commonly conducted in the literature, however, nondestructive techniques were employed to gain further confidence in measurements.

4.2.2.1 X-ray Computed Tomography

X-ray Computed Tomography, or CT, scans were conducted on pre-impact specimens. The analytic method for calculating porosity from CT scans is identical to the method outlined in Section 4.2.1.2, Equation (8). The Defect Analysis feature in myVGL was used to create a threshold corresponding to voxel intensity. All voxels with an intensity below a threshold were summed and divided by the total number of voxels,

$$\%V_v = \frac{\sum \text{Voxel}_{I>T}}{\sum \text{Voxel}} \tag{9}$$

4.3 Experimental Methods

The following sections outline the experimental procedure for each porosity determination experiment.

4.3.1 Destructive

4.3.1.1 Resin Digestion

Resin digestion consisted of three separate experiments. Seven procedures are outlined in ASTM D3171. Resin digestion in a nitric acid bath, sulfuric acid and hydrogen peroxide bath, and muffle furnace is compatible with epoxy resin composite composites. Samples were cut to 1" $\times$ 1", dried in a drying oven, and weighed. The density of each specimen was measured by the procedure outlined in Section 4.2.1.1, Equation (7).

1. **Nitric Acid** A nitric acid bath was mixed containing 1400 mL of 100% nitric acid and 600 mL dionized water. The bath was heated and held at a constant temperature of 75 °C. Specimens were encased in a mesh container and suspended in nitric acid bath for 6 hours. Shorter times are dependent on the composite system. The matrix is fully digested if there is no remaining matrix. The contents were washed and rinsed with water until a pH between 6 and 7 was measured. The specimens were placed in a drying oven at 50 °C. If conducted properly, only fibers should remain. The dry fibers were then weighed to the nearest 0.00001 g.

2. **Sulfuric Acid & Hydrogen Peroxide** Each specimen was placed into a beaker containing 50 mL of sulfuric acid. The acid was heated on a hot plate until the mixture began to fume and turned black. Hydrogen peroxide was slowly added down the side of the beaker to oxidize the matrix. Once the mixture turned clear, water was added to neutralize the acid. The mixture was rinsed and filtered several times until the pH was between 6 and 7. The remaning fibers were dried and weighed to the nearest 0.00001 g.

3. **Muffle Furnace** A small muffle furnace was used to heat the composite to a temperature above the resin ignition point. Each sample was preweighed and placed into tared crucibles. The crucibles were cleaned by heating to 500 °C for one hour. The composite samples were individually placed in a preheated furnace at 550 °C for one hour. After an hour, the samples cooled to room temperature in a desiccator, and weighed to the nearest 0.00001 g.

4.3.1.2 Sectioning/Optical Analysis

A representative sample corresponding to each porosity concentration was sectioned using a diamond tipped wet saw blade. Each sample was potted in an epoxy canister and polished using a state-of-the-art, proprietary polishing technique. With the surface of the composite smooth to within $0.02\mu m$, each sample was optically imaged under a digital microscope. Images were taken at 50×, 100×, and 200× magnification. The images were analyzed using ImageJ and MATLAB to count pixel frequencies corresponding to an intensity below a threshold.

4.3.2 Nondestructive

In situations where destructive testing is not suitable for porosity determination, the experimenter must turn to nondestructive testing to determine porosity concentration. X-ray computed tomography uses scattered X-rays to reconstruct a 3-dimensional model of the

sample. Commercial software is available to calculate and perform defect analysis by thresholding voxels.

4.4 Results and Discussion

The results for porosity determination for all techniques are discussed in the following sections.

4.4.1 Destructive

4.4.1.1 Resin Digestion: Nitric Acid

Porosity measurements in accordance to ASTM D3171 Procedure A was ineffective and failed to separate matrix from fibers. After 8 hours submerged in a heated nitric acid bath, the matrix had yet to fully dissolve. A drastic color change appeared in the bath, indicating the presence of a chemical reaction, however the digestion remained incomplete. Images of the nitric bath at 0, 2, and 6 hour intervals are shown in Figure 23.

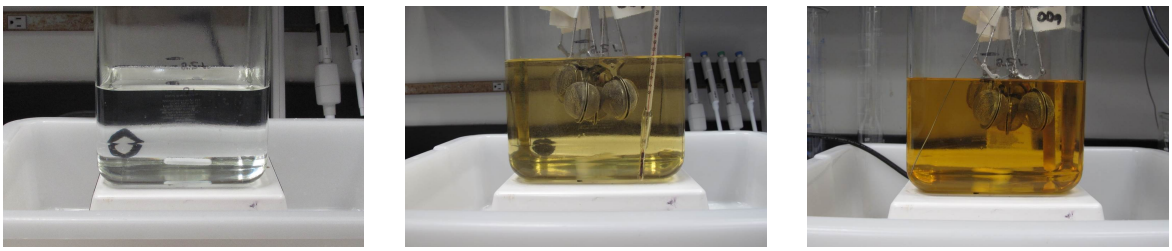

Figure 23: The heated nitric acid bath was ineffective in complete digestion of epoxy matrix. Notice the color change at time 0 (left), 2 (middle), and 6 (right) hours.

Figure 24 shows all six porosity samples after 8 hours in the heated nitric bath.

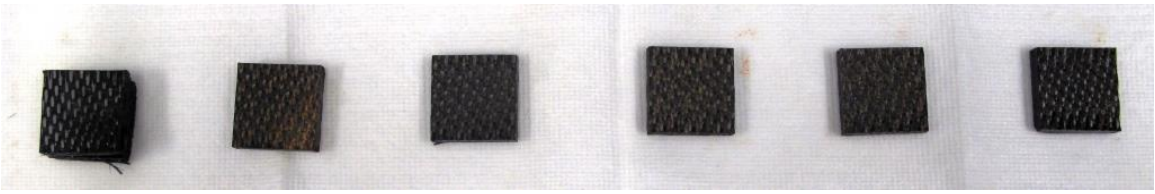

Figure 24: Incomplete digestion for samples 100-600 (left to right).

Since the nitric bath did not fully digest the matrix, fiber mass measurements were impossible. Thus, porosity was impossible to calculate using ASTM D3171 Procedure A, heated nitric acid bath. Nitric acid is an excellent solvent to clean and etch metals and organic materials, however is not strong enough to fully digest the epoxy matrix of a 6 mm thick laminate.

4.4.1.2 Resin Digestion: Sulfuric Acid & Hydrogen Peroxide

A sulfuric acid and hydrogen peroxide mixture successfully digested the epoxy matrix. Figure 25 shows the sample in a heated sulfuric acid bath. The color change of the sulfuric acid indicates the presence of a chemical reaction, helping dissolve the matrix.

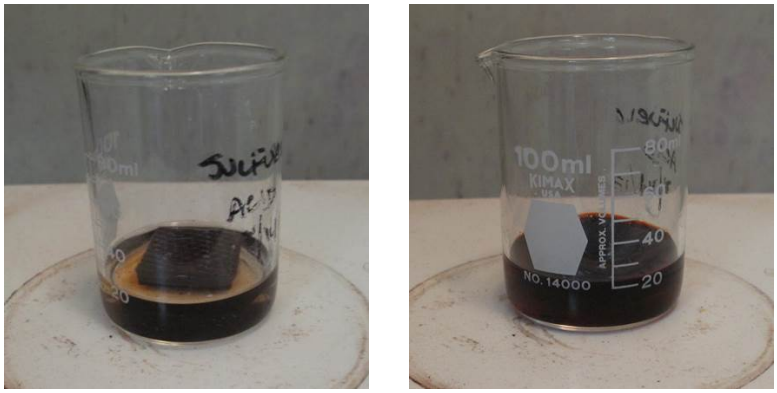

Figure 25: Composite sample in a heated sulfuric acid bath. Note the color change after 20 minutes.

Once hydrogen peroxide was added to the sulfuric acid, a violent reaction ensued. Due to the extreme fumes, hydrogen peroxide was added one drop at a time with a pipette, shown in Figure 26.

Figure 26: Hydrogen peroxide was added to the sulfuric acid, oxidizing the matrix.

Once the mixture returned clear and fuming subsided, the digestion was complete and only fibers remained. However, the mixture was highly acidic and instantaneously ignite if it came in contact with an organic substance. The fibers were rinsed and filtered several times, neutralizing the mixture to a pH between 6 and 7. The fibers were dried and weighed; the resulting mass measurements were used to calculate porosity. Table 5 displays the pre and post digestion mass measurements and corresponding porosity concentrations.

Table 5: Porosity Results by Sulfuric Acid & Hydrogen Peroxide Digestion

Sample	$m_c[g]$	$m_f[g]$	Porosity
100	2.8206	1.7178	40.32%
200	3.4316	2.1905	5.28%

Although sulfuric acid and hydrogen peroxide were successful in complete digestion of the epoxy matrix, it was not used as the primary porosity determination technique. The risk and length of each experiment was too great to justify conducting multiple experiments. Each experiment produced over a liter of toxic waste and took 2 hours to perform. Financially, resin digestion by sulfuric acid and hydrogen peroxide was not a viable option.

4.4.1.3 Resin Digestion: Muffle Furnace Burnoff

Resin digestion in a muffle furnace was the simplest, safest, fastest, and cheapest porosity determination technique. The samples were placed in a preheated muffle furnace and left to bake for an hour. Once ignition completed, they samples were cooled and weighed. Muffle furnace setup can be seen in Figure 27.

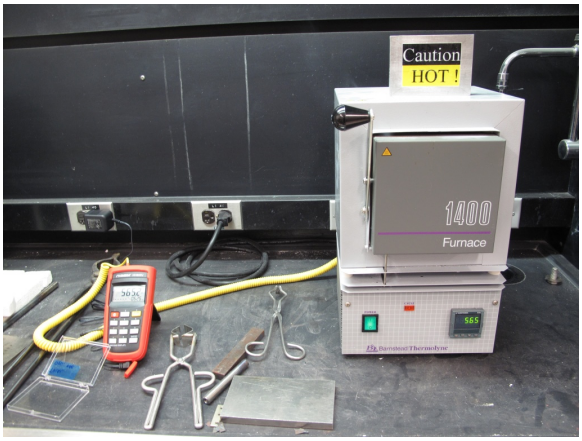

Figure 27: Test setup for resin digestion in a muffle furnace.

Resin burnoffs using the muffle furnace were conducted twice for each porosity concentration. The initial and final masses, density, and porosity for each test is given in Table 6.

Table 6: Porosity Results by Muffle Furnace Burnoff

Sample	$m_c, [g]$	$m_f, [g]$	Density, $[g/cm^3]$	Porosity
100	6.1605	3.3252	0.9062	38.59%
	6.2644	3.3122	0.9177	37.55%
200	5.9518	3.7752	1.4260	6.74%
	6.1147	3.6319	1.4036	6.79%
300	5.2755	3.3440	1.4460	3.47%
	6.1632	3.6340	1.4381	4.34%
400	6.0954	3.9207	1.4873	3.08%
	6.1423	3.3886	1.4759	1.23%
500	6.0757	3.8811	1.5058	1.71%
	6.0442	3.6710	1.5053	0.55%
600	6.1760	3.6807	1.5006	0.42%
	6.0115	3.8358	1.5056	1.69%

The muffle furnace successfully removed all matrix from the fibers, however the accuracy of the measurements is directly related to the accuracy of the density measurements. Fiber and matrix densities were supplied by the manufacturer and were assumed to be correct. The density of the composite proved to be difficult to precisely measure. A change in ± 0.02 g/cm^3 can affect the porosity by up to 0.5%. Therefore, extreme precision went into density measurements.

Density was measured using a custom apparatus to measure the weight of a sample immersed in a fluid. The apparatus is shown in Figure 28.

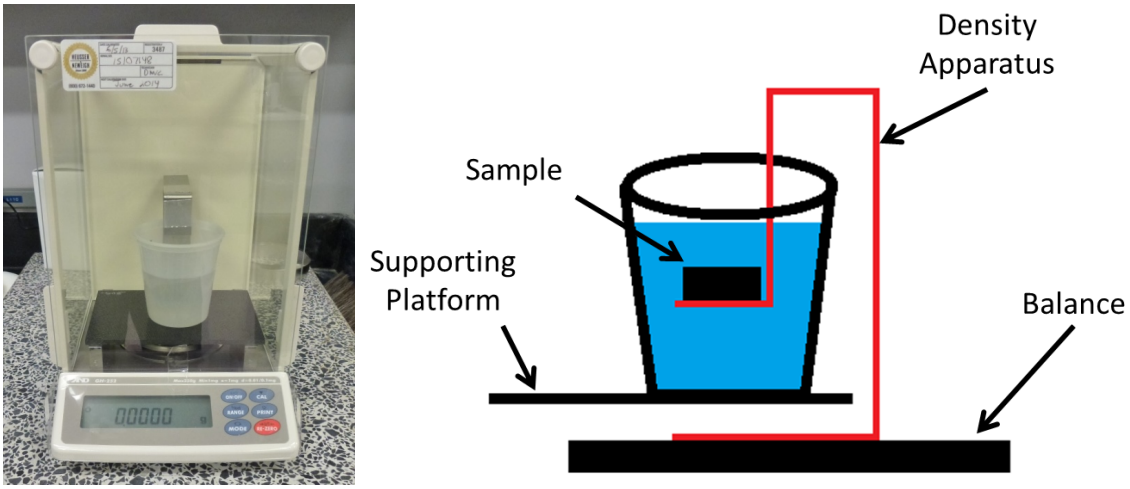

Figure 28: Test setup for density measurements (left) and schematic of density apparatus (right).

Mass measurements for samples submerged in water and measured in air are tabulated in Table 7.

Table 7: Density Results by Water Submersion

Sample	$m_{air}, [g]$	$m_{H_2O}, [g]$	Density, $[g/mm^3]$
	4.6659	1.4104	1.4318
200	5.9520	1.7828	1.4271
	4.8419	1.4327	1.4188
	5.2757	1.7050	1.4760
300	5.9902	1.9192	1.4699
	4.6589	1.4910	1.4691
	5.1711	1.6804	1.4799
400	5.9866	1.9739	1.4904
	6.0954	2.0584	1.5083
	5.1321	1.6837	1.4867
500	5.9086	1.9056	1.4745
	6.0757	2.0449	1.5058
	6.0075	1.9615	1.4833
600	7.7215	2.5984	1.5056
	4.6689	1.5257	1.4839

Density measurements for 100 samples were not calculated by submersion due to their ability to float in water. Weights could be added to the sample to ensure it sinks, however precise measurements of the density of the 100 sample was not a point of great concern. Density measurements reveal inhomogeneity throughout each laminate. Even though all specimens were cut from the same laminate, the random porosity distribution affects the specimen density. Thus, caution must be taken to ensure the correct density is used to calculate the porosity. Figure 29 shows the amount of variation in density for 5 samples from each laminate.

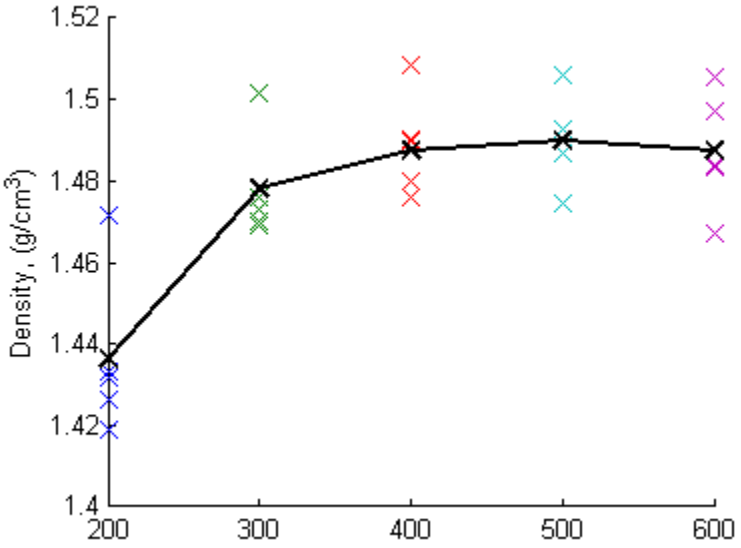

Figure 29: The spread in density measurements can be attributed to random porosity distributions within each laminate.

As previously mentioned, small changes in density can drastically affect the resulting porosity calculations.

4.4.1.4 Sectioning/Optical Analysis

Before image processing applications can be used to calculate porosity, the threshold must be properly calibrated. Porosity calculated using optical analysis is highly dependent on the threshold. The appropriate threshold for sectioned samples was calibrated using optical inspection. The threshold corresponds to pixel intensity. For an 8-bit grayscale image, there are 256 different possible intensities. If a pixel's intensity is greater than the threshold, it is considered a pore and replaced with the intensity 255. If a a pixel's intensity is less than the threshold, it is replaced with the intensity 0. This creates a bi-modal histogram distribution. Representative images of 200 and 400 samples to be used in sectioning optical analysis are shown in Figure 30.

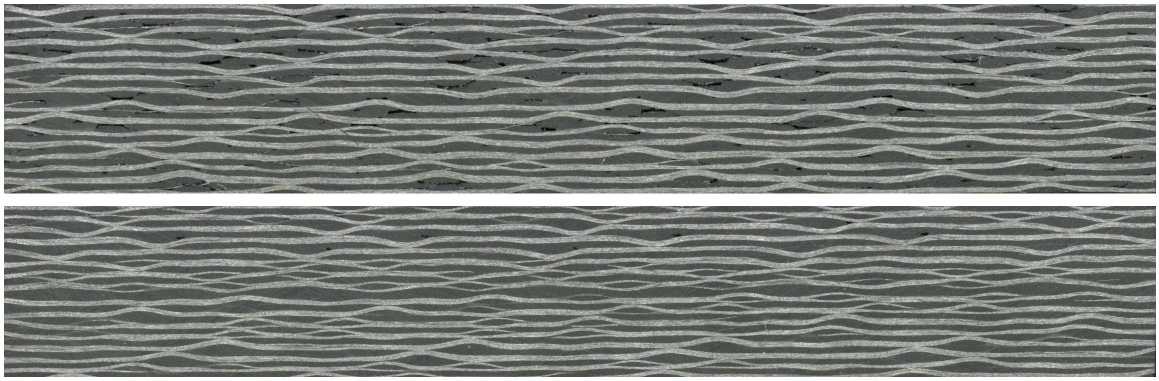

Figure 30: Sectioned samples of high porosity (200 sample, top) and low porosity (400 sample, bottom) used in optical analysis.

Notice the similarites between the matrix (gray) and pores (dark black). Since both have similar pixel intensities, the threshold must be set very high to differentiate between the two. Thus, a threshold of 210 was used to distinguish which pixels are part of a pore and which pixels are part of the matrix. Each image was transformed into an 8-bit image, and the histogram threshold was set at the previously determined value of 210. The adjusted images highlighting each pore in black and composite in white are shown in Figure 31.

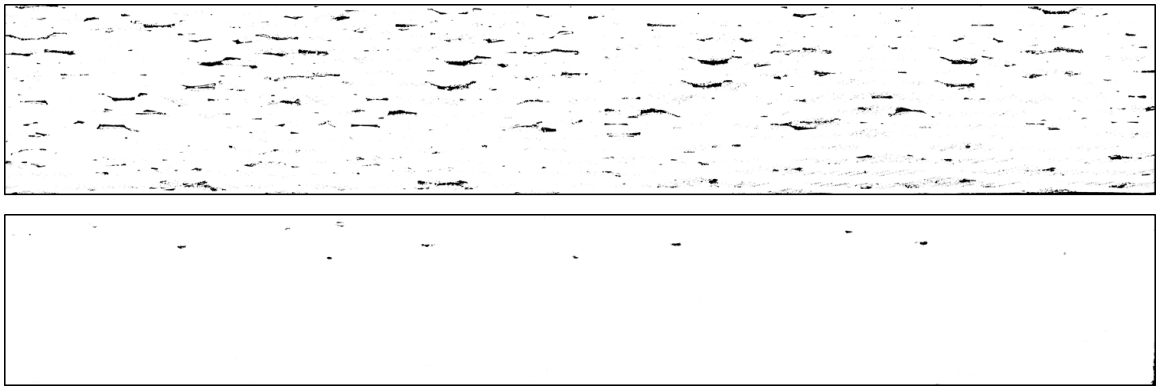

Figure 31: Adjusted images of high porosity (200 sample, top) and low porosity (400 sample, bottom) used in optical analysis.

The histogram for each image was used to count the number of black and white pixels. The tabulated values are shown in Table 8.

Table 8: Porosity Results by Sectioning

Sample	Color	Pixel Count	Porosity
	0	123293	
100	255	678066	35.48%
	Total	1911000	
	0	12428032	
200	255	341075	2.67%
	Total	12769107	
	0	11243061	
300	255	66255	0.59%
	Total	11309316	
	0	11914461	
400	255	8415	0.07%
	Total	11922876	
	0	11528973	
500	255	5297	0.06%
	Total	11534270	
	0	11214487	
600	255	0	0.00%
	Total	11214487	

4.4.2 Nondestructive

As quality verification, porosity concentration was measured using X-ray computed tomography (CT) scanning. This allows the experimenter to estimate porosity without damaging and compromising the integrity of the material.

4.4.2.1 X-ray Computed Tomography Scanning

The Defect Analysis toolbox in myVGL was used to determine a threshold corresponding to voxel intensity. The following table outlines all parameters used in CT scanning.

Table 9: CT Scanning Setup Parameters

Paramater	Value
keV	160
Target Power	70 W
Magnification	1.3x
Filter	1 mm Cu
Frame Average	16
Projections	1999
Effective Pixel Size	99.7 μm
Detector Type	Varian 2520-14 bit
X-ray Head	Yxlon 225
Acquisition Software	NSI-multipoint corrections

The experimental test setup can be seen in Figure 32.

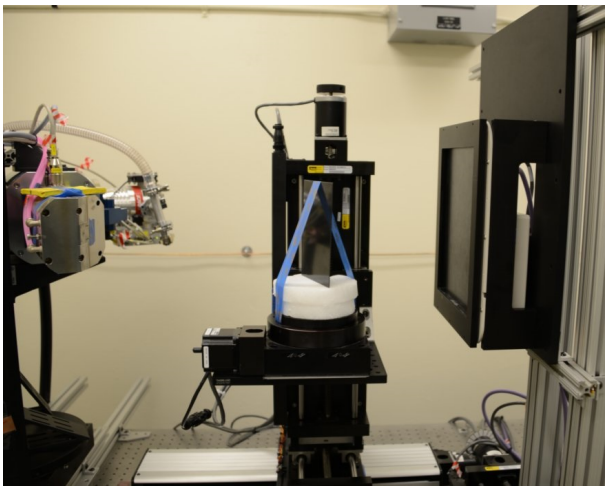

Figure 32: Test setup for CT scanning.

The X-ray output from the X-ray source is not mono-energetic. Different materials and thicknesses of those materials were used to filter out lower energy spectrums to get more useful X-rays and reduce scatter (lower energy X-rays that are not strong enough to penetrate the part can only add scatter). Frame averaging is to reduce static noise; any imperfections in the scintillator or the detector pixels can be averaged out by using frame averaging. The number of projections (samples) is the number of images taken through the 360 degree rotation. The more projections, the more accurate the 3-dimensional representation. This number is generally governed by the Nyquist sampling criteria, but under sampling can be used in some cases where detectability is more important than accuracy and time is critical. Keeping the number of projections high reduces artifacts, producing a more realistic 3-dimensional image.

The Defect Analysis Toolbox works by setting a threshold which distinguishes voids from material. All voxels below the threshold intensity were summed and divided by the total number of voxels. Table 10 displays the void volume, total volume, and void percent by volume for results analyzed using the Defect Analysis toolbox.

Table 10: Porosity Results Using Defect Analysis Toolbox

Sample	Total Volume, $[mm^3]$	Void Volume, $[mm^3]$	% Porosity
100	120000	15000	10.77%
200	77788	5332	6.41%
300	75677	2298	2.95%
400	75000	910	1.21%
500	73000	410	0.57%
600	70000	250	0.37%

Clearly, the porosity calculation for the 100 sample is incorrect. Optical analysis and resin digestion estimate the porosity of the 100 samples to be approximately 40%. Since the material was so porous, it was difficult to distinguish one void from another. However, the

other porosity concentrations are within the expected range. Porosity concentrations merely as percentages are difficult to visualize. Since CT scanning produces a 3D representation of the laminate, cut planes can be created to extract images of the interior faces. In addition to porosity calculations using the Defect Analysis Toolbox, optical analysis was used on these still images taken throughout the width of each sample. The images in Figure 33 show a side view of midplane of each laminate used in optical analysis.

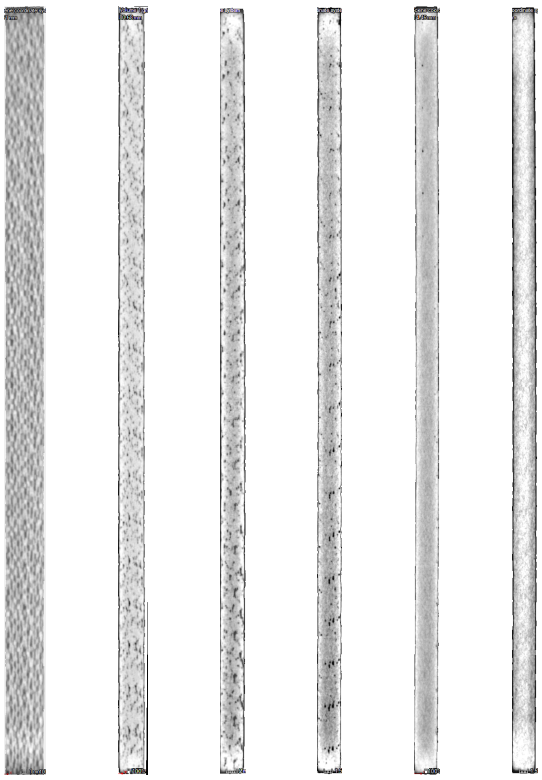

Figure 33: CT scans taken from midplane of samples 100-600 (left to right). Pores show up black, composite is white/gray.

The side cut planes shown in Figure 33 provide some insight as to why the porosity measurements for the 100 sample proved to be inaccurate; each pore is not well defined, making pores difficult to distinguish. Moving from left to right, the 200, 300, and 400 samples are clearly riddled with pores. Samples 500 and 600 show very few (if any) pores. These images help to relate porosity concentrations to visual inspection. Optical analysis described in the previous section was used to determine the porosity from these "sectioned" samples.

As mentioned in earlier sections, porosity measurements determined by optical analysis are highly dependent on the threshold. Thus, the threshold must be properly calibrated to produce accurate and meaningful porosity concentrations. Minor adjustments in the threshold can greatly influence the overall porosity calculation. Figure 34 shows four different threshold values set for images taken from a cut plane of the 200 sample.

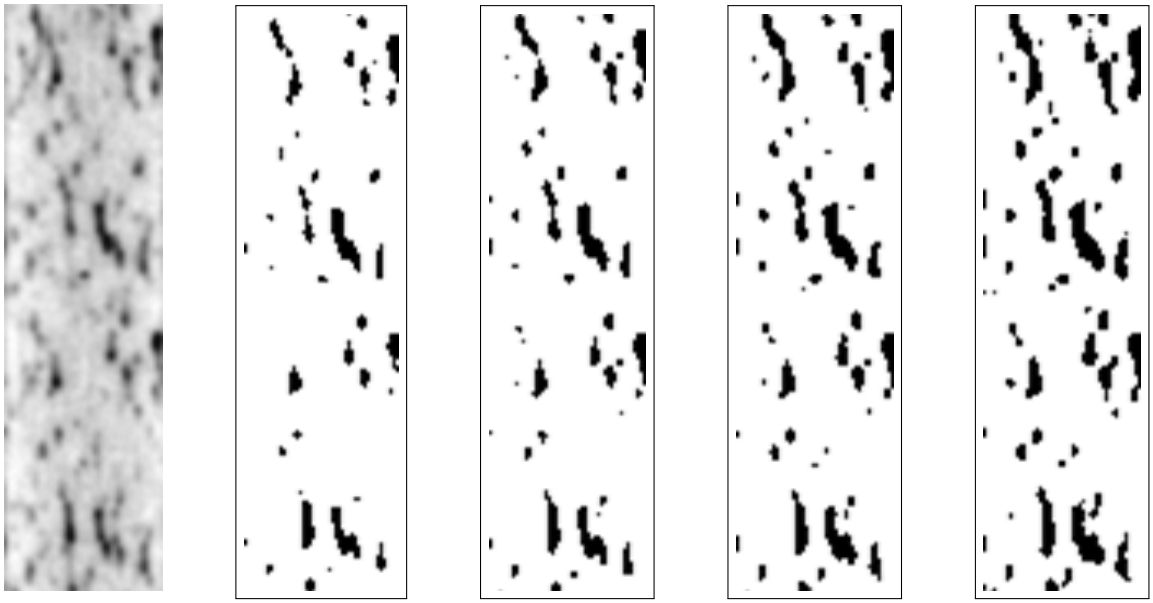

Figure 34: Threshold levels set at 130, 140, 150, and 160 (second left to right). If too many pixels are counted as pores, optical analysis will overestimate porosity concentration.

From the images in Figure 34, it is apparent how adjusting the threshold affects the overall porosity concentration. A higher threshold would count more pixels as pores, creating larger porosity concentrations. The porosity results for each threshold level are tabulated in Table 11.

Table 11: Threshold's Effect on Porosity Concentration

Threshold	Intensity	Pixel Count	Porosity
	0	71840	
130	255	5200	6.75%
	Total	77040	
	0	70267	
140	255	6773	8.79%
	Total	77040	
	0	68540	
150	255	8500	11.03%
	Total	77040	
	0	65850	
160	255	11190	14.52%
	Total	77040	

The 200 sample was used as calibration since it contained a large porosity concentration and its porosity via optical analysis is shown in Table 11. As shown in Table 6, the porosity of the 200 samples was approximately 6.5 %, indicating a threshold of approximately 130 is the appropriate value. Thus, 130 was used as the threshold for optical analysis using images from CT scan cut planes.

Using the calibrated threshold value, the resulting porosity concentration using pixel thresholding for CT scanning are tabulated in Table 12.

Table 12: Porosity Results Using Optical Analysis From CT Cut Planes

Sample	Porosity
100	41.06%
200	6.75%
300	4.83%
400	3.47%
500	0.09%
600	0.04%

Samples 100, 200, and 300 strongly agree with porosity concentrations calculated by resin burnoff. This indicates the threshold was properly calibrated and the CT scans can differentiate between pores and composite. However, as porosity concentrations decrease, the ability for the CT scans to differentiate between pores and composites decrease. CT scans reveal very few pores for 500 and 600 samples, producing a porosity concentration too low to accurately measure using resin digestion/burnoff. Sectioned samples and CT scan slices of 500 and 600 samples indicate the porosity concentration is below 1 %. Since resin digestion is accurate to within $\pm 0.5\%$, the measured porosity is on the order of the uncertainty for low porosity samples. Thus, the 500 and 600 samples were assumed to be nearly equal in porosity with a concentration $< 1\%$. Table 13 displays all porosity calculations from various measurement techniques, along with the final porosity measurements used in the remainder of the analysis.

Table 13: Porosity Results Using All Porosity Determination Methods

Sample	Resin Burnoff	Sectioning	CT Defect Analysis	CT Optical	Final
100	38.59%	35.48%	10.77%	41.06%	$\sim 38.00\%$
200	6.75%	2.67%	6.41%	6.75%	$\sim 6.50\%$
300	3.75%	0.59%	2.95%	4.83%	$\sim 3.75\%$
400	2.16%	0.07%	1.21%	3.47%	$\sim 2.25\%$
500	1.13%	0.06%	0.57%	0.09%	$< 1.00\%$
600	1.06%	0.00%	0.37%	0.04%	$< 0.50\%$

4.5 Conclusions

Compared to resin digestion methods, determination by sectioning and optical analysis seem to under-calculate porosity. This discrepancy can be attributed to several factors. Porosity calculations by resin digestion used a 1" $\times$ 1" representative sample where porosity calculations by sectioning and optical analysis looked at one edge of a 1" $\times$ 1" sample. Since resin digestion samples had a greater sample size, it is likely more representative of the entire laminate. Optical analysis is only successful if there is significant contrast between pores and composite. Poor contrast can lead to a misrepresentation of pores. The final porosity concentrations used in the reminder of the study were determined by averaging porosity from all methods with less emphasis on obvious outliers.

5 Mechanical Testing

Several papers in the literature try to relate the effect of porosity on the strength of fiber reinforced composites. However, most investigated only a few mechanical properties. This work aimed to provide a comprehensive study on the effect of porosity on multiple strength parameters, such as flexure, shear, low-velocity impact, and compressive residual strength.

5.1 Introduction

A series of mechanical tests were performed to characterize and quantify the effects of porosity. Since porosity resides within the matrix, strength parameters carried by the matrix were expected to be greatly affected. Thus, mechanical testing was performed to highlight matrix properties. Flexure, shear, drop-weight impact, and compression after impact were chosen to fully characterize the material given each induced porosity concentration. The following text matrix outlines all measured and calculated parameters for each test.

Table 14: Test Matrix

Test	Measured Quantities	Calculated Parameters
4 Point Flexure	Load	Flexural Modulus, E_{11}
		Peak Load, P_{max}
		Energy to Peak Load, E_{max}
	Displacement	Strain to Peak Load, ε_{max}
		Residual Stiffness, K_r
Short Beam Shear	Load	Interlaminar Shear Stress, ILSS
		Peak Load, P_{max}
	Displacement	Energy to Peak Load, E_{max}
		Strain to Peak Load, ε_{max}
Drop Weight Impact	Load	Stiffness, K
		Residual Stiffness, K_r
		Load to First Failure, P_{ff}
		Energy to First Failure, E_{ff}
		Strain to First Failure, ε_{ff}
		Peak Load, $P_{max\delta}$
	Time	Energy to peak load, $E_{max\delta}$
		Strain to peak load, $\varepsilon_{max\delta}$
		Energy Absorbed, E_{abs}
		Impulse, J
		Rebound Velocity, v_{reb}
Compression After Impact	Load	Peak Load, P_{max}
		Residual Compressive Strength, F_{cu}

5.2 Analytic Methods

5.2.1 Four Point Flexure

In order to determine the flexural modulus, a relationship between the applied load and displacement must be found. A schematic of the quarter point loading four point bend test setup can be found in Figure 35.

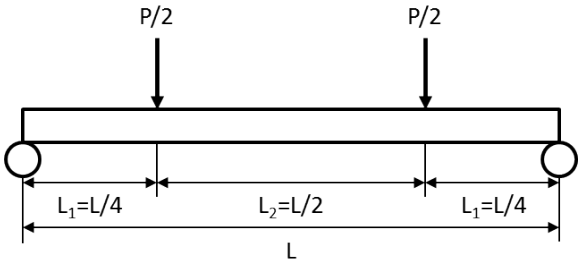

Figure 35: A simply supported beam with two vertical loads applied at the quarter points was used to model the four point bend test.

The beam was split up into two regions to be analyzed. The moment, slope, and deflection for each region was calculated and boundary conditions were used to characterize the response of the beam to four point loading. The moment throughout the left segment of the beam (region I) when $0 < x < L_1$ was found to be,

$$M_1(x) = -\frac{P}{2}x \tag{10}$$

where P is the applied load. The slope of the beam can be determined by integrating the moment throughout region I, given by,

$$\theta_1(x)EI = -\int M_1(x)\mathrm{dx} = \frac{Px^2}{4} + C_1 \tag{11}$$

where C_1 is a constant of integration. The displacement of the beam in Region I can be determined by integrating the slope,

$$\delta_1(x) = \int \theta_1(x)\mathrm{dx} = \frac{Px^3}{12} + C_1x + C_2 \tag{12}$$

where C_2 is another constant of integration. Next, Region II was analyzed when $L_1 < x < L_1 + L_2$ and $L_1 = L/4$. The moment throughout Region II was found to be constant,

$$M_2(x) = -\frac{PL_1}{2} \tag{13}$$

Since the reaction loads and applied loads are of the same magnitude but in opposite directions, the moment throughout Region II is constant and independent of position along the beam. The slope of Region II is found by integrating the moment,

$$\theta_2(x)EI = -\int M_2(x)\mathrm{dx} = \frac{PL_1x}{2} + C_3 \tag{14}$$

where C_3 is a constant of integration. The displacement is calculated by again integrating the slope,

$$\delta_2(x) = \int \theta_2(x)\mathrm{dx} = \frac{PL_1x^2}{4} + C_3x + C_4 \tag{15}$$

where C_4 is another constant of integration. Boundary conditions must be used in order to create a continuous beam and to solve for integration constants. Since there are four integration constants, four boundary conditions must be used. The four boundary conditions used for a beam subjected to four-point quarter-loading bending is found in Table 15.

Table 15: Boundary Conditions for Four Point Bend

Location	Boundary Condition	Notes
$x = 0$	$\delta_1 = 0$	0 displacement at support
$x = L_1$	$\delta_1 = \delta_2$	Displacement continuity
$x = L_1$	$\theta_1 = \theta_2$	Slope continuity
$x = L_1 + \frac{L_2}{2}$	$\theta_2 = 0$	0 slope at center of beam

With boundary conditions applied, the displacement and slope of Region I and II can be determined as a function of the applied load, geometry, and material properties,

$$\delta_1(x) = \frac{Px}{12EI}\left[x^2 - 9L_1^2\right] \tag{16}$$

$$\delta_2(x) = \frac{PL_1}{12EI}\left[3x^2 - 12L_1x + L_1^2\right] \tag{17}$$

In order to calculate the elastic modulus, the displacment at $x = L_1$ must be determined. This can be found by evaluating Equation (16) when $x = L_1$,

$$\delta_c = \delta_1(L_1) = \frac{PL_1}{12EI}\left[L_1^2 - 9L_1^2\right] = -\frac{2PL_1^3}{3EI} \tag{18}$$

where δ_c is the crosshead displacement, measured by the load frame. Note that Equation (17) could have been used, setting $x = L_1$. This reduces to

$$E = \frac{PL^3}{3Bt^3\delta_c} \tag{19}$$

where L is the total length of the beam, B is the width, and t is the thickness.

Absorbed energy is calculated by integrating the load displacement response. Although the test continued until the instantaneous load reached 20% of the peak load, energy absorption was calculated until the peak load. The following expression was used to calculate energy absorbed to peak load,

$$E_{abs} = \int_0^{\delta_{max}} P\mathrm{d}\delta \tag{20}$$

where F is the applied load and δ_{max} is the displacement at the peak load. Since the measured load-displacement response consisted of discrete points and not a continuous function, Equation (20) was approximated using numerical integration,

$$E_{abs} \approx \sum_{i=2}^{N} \frac{P_i + P_{i-1}}{2}\left(\delta_i - \delta_{i-1}\right) \tag{21}$$

where N is the index to the peak load. Residual stiffness, shown in Figure 36, was determined by calculating the slope of the load-displacement response after the first load dropoff and redistribution.

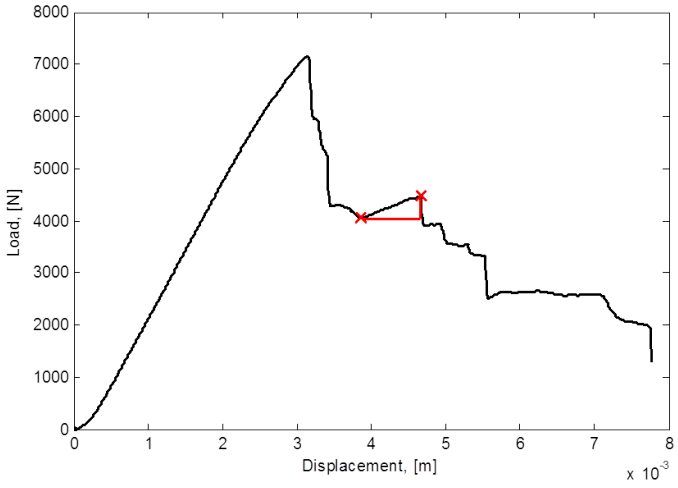

Figure 36: Residual stiffness was defined as the stiffness after first failure.

The points used to calculate the slope were determined using a custom function which looks for local maximums and minimums.

Strain to failure was calculated by dividing the displacement at first failure by the specimen thickness,

$$\varepsilon_f = \frac{\delta_f}{t} \tag{22}$$

where t is the thickness of the specimen. Many of these parameters were also calculated in shear, impact, and compression after impact testing.

5.2.2 Short Beam Shear

A beam in bending is subjected to transverse shear stress. In order to balance the transverse shear force, a longitudinal or interlaminar, shear stress is induced. The maximum interlaminar shear stress can be calculated by the well known formula,

$$\tau = \frac{VQ}{Ib} \tag{23}$$

where τ is the transverse shear stress, V is the transverse shear load, Q is the first moment of area, I is the second moment of area, and b is the section width. For a rectangular cross section, the maximum shear is found at the midplane. Equation (23) simplifies to,

$$\tau = ILSS = \frac{3V}{2bt} \tag{24}$$

where t is the beam thickness. Interlaminar shear stress can be calculated as a function of crosshead displacement, but only the maximum, or interlaminar shear strength is of concern. Thus,

$$ILSS = \frac{3P_{max}}{2bt} \tag{25}$$

where P_{max} is the maximum load recorded by the load cell during the short beam shear test. This assumes a parabolic stress variation with the maximum located at the midplane. However, since the beam is so short, the stress field is likely influenced by the local forces from the loading supports throughout the entire cross section. A standard reduction in the short beam strength from $^{3P}/_{2A}$ to $^{3P}/_{4A}$ has been adopted to account for the loading influence arising from the short loading span. This $^{3}/_{4}$ factor is widely used in the community and reported for materials specs and is found in ASTM D2344. Thus, the relationship for interlaminar shear strength, ILSS, is written as,

$$ILSS = \frac{3P_{max}}{4bt} \tag{26}$$

Energy to peak load and strain to failure were calculated using the same relationships derived for flexure.

5.2.3 Impact

Unlike flexure and shear testing, drop-weight impact testing is not displacement controlled. Since the impactor is dropped from a specified height, the displacement of the specimen is unknown. The load cell utilized during drop-weight impact testing records force as a function of time. A free body diagram of the impactor during impact is shown in Figure 37.

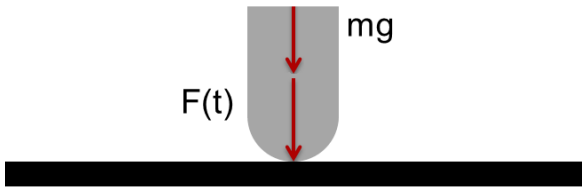

Figure 37: A free body diagram can be used to calculate the load displacement response.

A simple force balance can be conducted to calculate the displacement of the impactor as a function of time. By Newton's second law, the sum of the impactor force and weight must equal the inertial force,

$$F(t) + mg = m\ddot{a} \tag{27}$$

where $F(t)$ is the force of the imapctor, mg is the weight of the impactor, and $\ddot{a}$ is the acceleration of the impactor. Dividing my the mass and integrating with respect to time once yields,

$$v(t) = gt + \int_0^\tau \frac{F(t)}{m}\mathrm{dt} + v_0 \tag{28}$$

where $v(t)$ is the velocity, τ is the length of the impact event, and v_0 is the initial velocity. Integrating once more produces the displacement as a function of time,

$$\delta(t) = \delta_0 + v_0 t + \frac{1}{2}gt^2 + \int_0^\tau \left[\int_0^\tau \frac{F(t)}{m}\mathrm{dt}\right]\mathrm{dt} \tag{29}$$

where δ_0 is the initial displacement of the impactor, assumed to be zero. Numerical integration techniques outlined in Equations (20) and (21) were used to calculate velocity and displacement of the impactor as a function of time. With the load-displacement response, stiffness, residual stiffness, energy absorbed, energy to peak load, and strain to peak load can be calculated using the same relationships developed in earlier sections. Impulse is defined as,

$$J = \int_0^\tau F(t)\mathrm{dt} \tag{30}$$

Again, numerical techniques were employed to calculate the impulse of the impacted specimens.

5.2.4 Compression After Impact

Compression after impact was used to determine residual compressive strength after an impact event. Although the load and displacement were directly measured by the load frame, displacement values were not used in strength calculations. The maximum residual compressive strength was found by dividing the maximum load by the cross sectional area,

$$F_{cu} = \frac{P_{max}}{bt} \tag{31}$$

where b is the panel width, and t is the panel thickness. The extreme loads subjected to the panel resulted in inaccurate crosshead displacement readings. Since displacement was not measured accurately, strain, energy, and any other parameters which rely on displacement were not calculated.

5.3 Experimental Methods

5.3.1 Flexure

Flexure testing was completed on a SATEC Materials Testing load frame manufactured by Instron with a 2 kN load cell. To determine flexural properties, load and displacement were measured using a four point bend fixture in accordance with ASTM D790. The load frame and four point bend fixture are shown in Figure 38.

Figure 38: A SATEC load frame manufactured by Instron was used for all flexure, shear, and compression after impact testing.

Due to the possibility of irregular porosity distribution throughout thickness of the laminate, half of the specimens were inserted into the test fixture with the tool side up, and half of the specimens were tested tool side down. The specimen was aligned and centered such that its longitudinal axis was perpendicular to the loading nose and side supports [41]. The crosshead was lowered until it was in contact with the specimen and the load and displacement were tared. A test procedure was configured in the data recording software to perform the test at specified conditions. The crosshead displacement was set to 3mm/min and the test continued until the instantaneous load reached 20% of the peak load. Once the test concluded, several unload points were manually recorded as the crosshead returned to its home position.

5.3.2 Short Beam Shear

A similar procedure was used to determine the interlaminar shear strength of the porosity induced composites. The same SATEC load frame and data acquisition software was used to record load and displacement in accordance to ASTM D2344. A three point bend test

fixture was used with a span length determined by parameters outlined in the standard. The test fixture dimensions as called out by ASTM D2344 are shown in Figure 39.

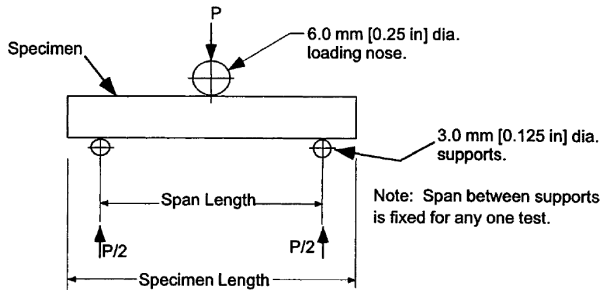

Figure 39: Loading dimensions outlined in ASTM D2344 were used for short beam shear testing.

To ensure the specimen is subjected only to shear, bending energy was eliminated by setting the supports at a thickness ratio of 4:1. With a nominal specimen thickness of 6 mm, the span length was equal to approximately 24 mm. Identical to flexure testing, the specimen was inserted into the test fixture with the tool side up for half of the tests and tool side down for half of the tests. The specimen was aligned and centered such that its longitudinal axis was perpendicular to the loading nose and side supports [41]. The crosshead was set to a load rate of 1 mm/min and ran until the instantenous load reached 20% of the peak load. At this point, the crosshead stopped and the test was completed. The instantenous load and displacement were recorded and saved for post processing.

5.3.3 Impact

All impact testing was completed using a Dynatup 8250 drop frame, shown in Figure 40.

Figure 40: Dynatup 8250 drop frame used for all impact testing.

The drop frame was outfitted with pneumatic rebound brakes to catch the impactor after first impact. This eliminates subsequent rebound impacts; ensuring the specimen is impacted only once. The rebound brakes installed on the drop frame are shown in Figure 41.

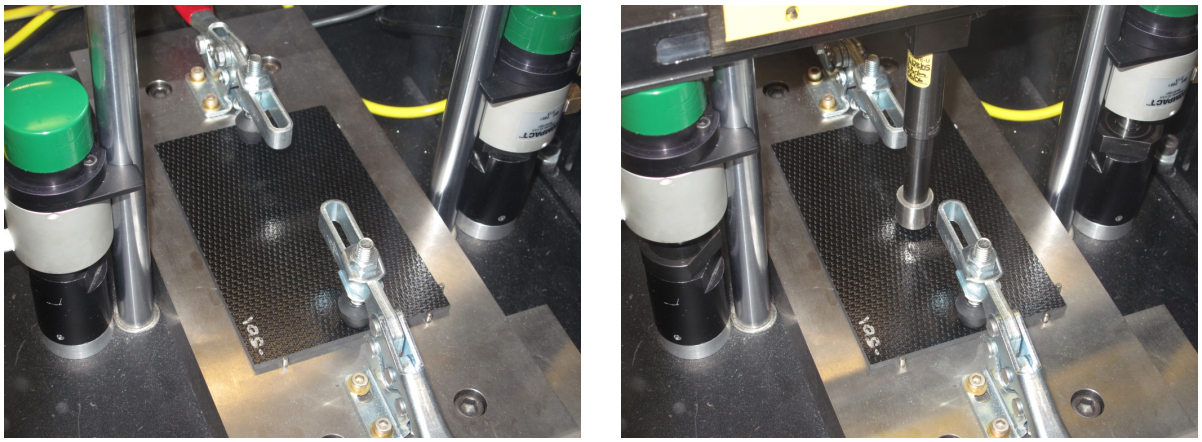

Figure 41: Rebound brakes unextended (left) and extended (right) prevented multiple rebound impacts.

The rebound brakes are activated by a metal two pronged flag passing through a photo diode, shown in Figure 42.

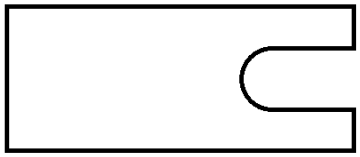

Figure 42: Flag used to trigger the rebound brakes.

Once the first prong passes through the photo diode, a timer begins. The timer ends once the second prong passes through the photo diode, and if the distance between the prongs is known, the velocity of the flag can be calculated. The flag is located on the side of the impactor and passes through the photo diode as the impact tup makes first contact with the specimen. This allows for the calculation of the impactor's initial velocity, required to integrate the force twice to calculate the displacement as a function of time. It is crucial that the photo diode are located at a height when the impact tup makes first contact with the panel. If the flag is too high, the brakes will trigger prematurely, potentially preventing the impact event. If the flag is too low, the brakes will not trigger and rebound impacts will occur. If the impact tup is changed, the photo diode height must be adjusted to ensure the brakes trigger appropriately. With the flag set at the proper height, the panel was inserted into the specimen holder at the base of the drop frame. The base consists of a 3" $\times$ 5" window with two toggle clamps, shown in Figure 43.

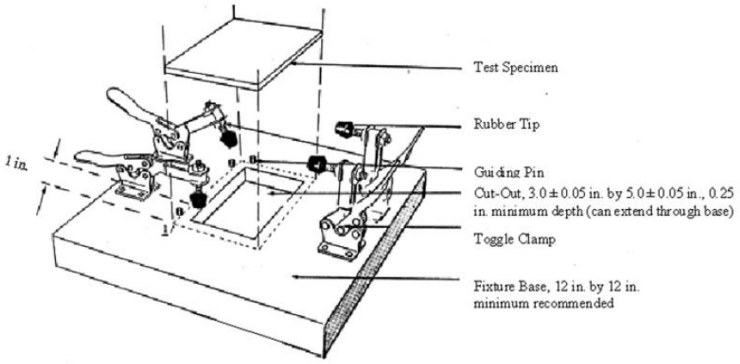

Figure 43: Impact support fixture.

The toggle claps were adjusted so the clamping pressure was zero in order to preserve simply

supported boundary conditions along all four edges. With the specimen set in place and the rebound brakes adjusted, the impactor was set to a height corresponding to the desired impact energy. Table 16 lists the drop height for each tup geometry and expected impact energy.

Table 16: Drop Conditions for Tup Geometries

	Flat Tup	Hemishperical Tup
Mass	5.42 kg	5.52 kg
Height	94 cm	55.5 cm
Impact Energy	50 J	30 J

The shape of the two tups is vastly different, inducing different degrees of damage if dropped from the same height. To maintain consistency in delamination area and damage degree, hemispherical tup impacts only imparted 30J of energy.

Previous testing indicated there was no difference between specimens tested tool side up and tool side down. Therefore, all specimens were loaded into the impact support fixture oriented with the tool side facing downward. Once the specimen was in place, rebound brakes were correctly set and activated, the doors of the drop tower were closed, and the release latch was released, allowing the impactor to fall and impact the specimen.

5.3.4 Compression After Impact

The test procedure for compression after impact testing is very similar to flexure and short beam shear procedures. The same SATEC load frame was utilized with a compression loading block. Each specimen was loaded into a specially designed compression after impact fixture to resist global buckling. The fixture is shown in Figure 44.

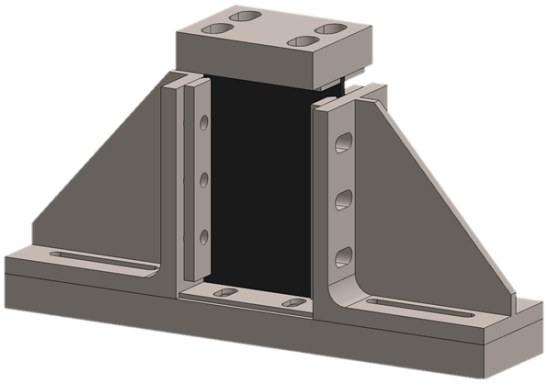

Figure 44: Compression after impact support fixture.

Each bolt located along the knife edge supports were tightened to a torque of 60 in-lbs. The fixture and specimen were loaded into the load frame directly below the loading block. The load frame was set to a displacement controlled loading rate of 1.25 mm/min and continued to run until the instantenous load reached 20% of the peak load. Most failures were violent and abrupt, often failing with little to no warning.

5.4 Results and Discussion

The results for all experimental testing will be presented in the following sections. Raw data and fracture images for each specimen is listed in the appendices.

5.4.1 Flexure

Four point flexure was conducted on specimens cut from laminates of six porosity concentrations. Ten specimens were cut from each laminate, however only eight were tested. Load and crosshead displacement were recorded and used for all post processing. A typical load-displacement response is shown in Figure 45.

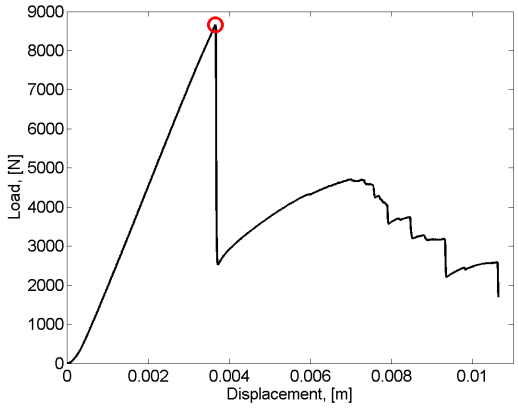

Figure 45: Typical load-displacement curve for four point flexure specimens. The red circle corresponds to the maximum load.

Load-displacement curves for samples 200-600 had the same general characteristics. The load increased linearly until it reached a threshold load. At this point, there was a sharp decrease in load. Once the specimen reaches its peak load, internal bonds rupture, and a crack is formed. Figure 46 shows a specimen before and after crack formation.

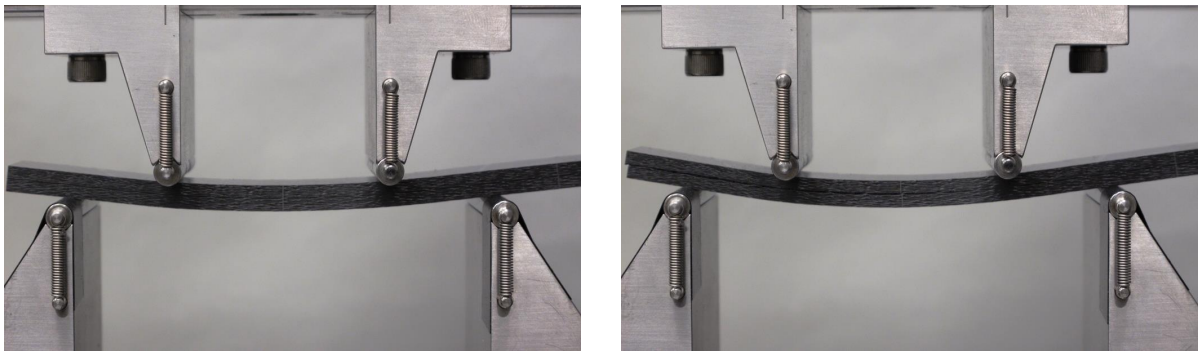

Figure 46: A crack emanating from the left end of the specimen was the first indication of failure caused by the peak load. (Sample 608)

Most samples peak load was released by a delamination crack beginning from the left end. However, some samples failed by fiber failure and crushing, shown in Figure 47.

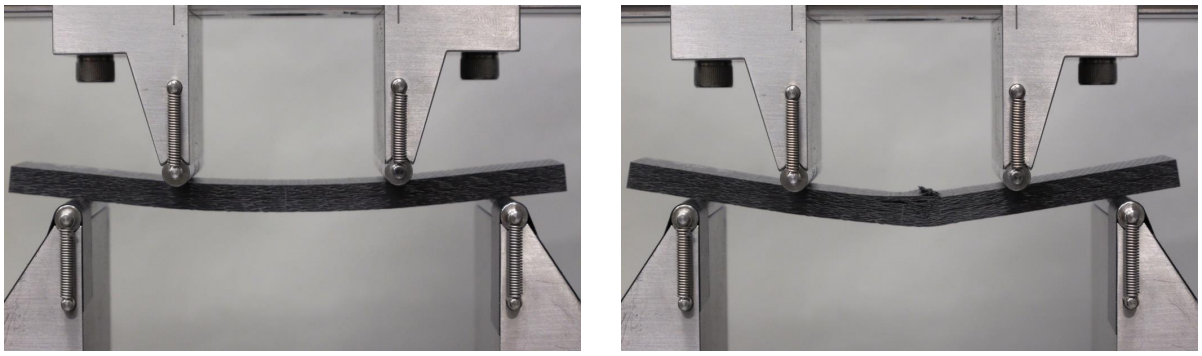

Figure 47: Fiber failure of the specimen on the upper surface was the first indication of failure caused by the peak load. (Sample 208)

Corresponding load-displacement curves at the point of maximum load are shown in Figure 48 for the two different failure modes.

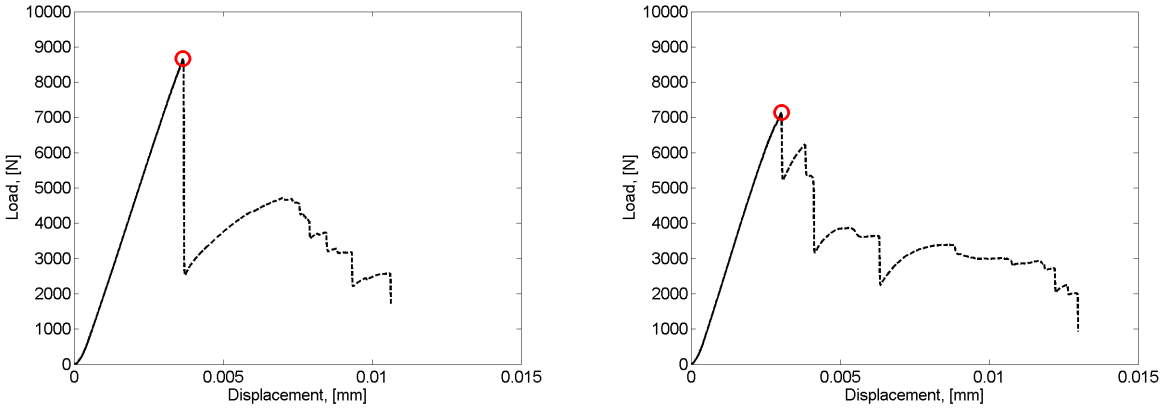

Figure 48: Delamination failure at the midplane (left, sample 608) and fiber failure of the specimen on the upper surface (right, sample 208) were two common failure modes under four-point flexure.

Failure modes for each sample were characterized and tabulated in Tables 17 and 18.

Table 17: Flexure Failure Modes, Samples 101-310

Sample	Mode	Sample	Mode	Sample	Mode
101	NF	201	FF	301	D
102	NF	202	FF	302	D
103	NF	203	FF	303	D
104	NF	204	FF	304	D
107	NF	207	D	307	D & FF
108	NF	208	D	308	D & FF
109	NF	209	FF	309	D & FF
110	NF	210	FF	310	FF

Table 18: Flexure Failure Modes, Samples 401-610

Sample	Mode	Sample	Mode	Sample	Mode
401	D	501	D	601	D
402	D	502	D	602	D
403	D	503	D	603	D
404	D	504	D	604	D
407	D	507	D	607	D
408	D	508	D	608	D
409	D	509	D	609	D
410	D	510	D	610	D

As seen in Tables 17 and 18, delamination at the midplane was the primary failure mode for low porosity samples. This indicates energy due to transverse shear is present and bending is not the primary energy mode. For beams with span to thickness ratios greater than 16:1, shear energy should be negligible. With a span equal to 100 mm and a thickness of 6.25

mm, L:t = 16:1.

Although shear energy was present, flexure tests were successful in the calculation of flexural modulus, energy to peak load, strain to peak load, and residual stiffness. Pre and post-mortem images were recorded at 50× magnification using an optical microscope. Vertical lines were etched into the thickness of the flexure specimens to capture the same window in optical images. Pre and post-mortem images for a high porosity flexure sample (6.5%) are shown in Figure 49.

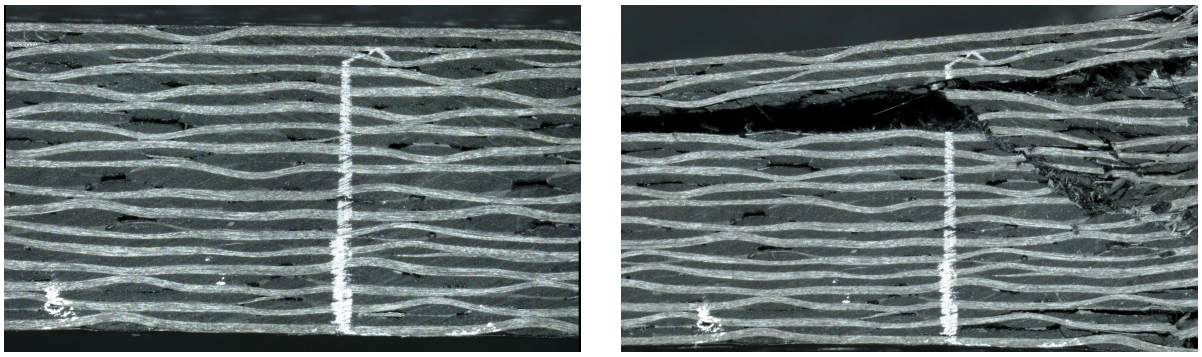

Figure 49: Pre mortem (left) and post mortem (right) images taken at 50× with an optical microscope for samples with high porosity (6.5%).

Most high porosity samples failed via fiber failure, shown in Figure 49. Optical analysis was performed on post mortem samples to determine whether or not pore sites act as crack promoters or inhibitors. Although the sample is riddled with pores, cracks do not appear to emanate or terminate at pores. Fiber failure served as the primary mode for energy release, ultimately leading to complete fracture and the termination of the experiment.

Pre and post mortem optical images were recorded for low porosity samples for comparison and are shown in Figure 50.

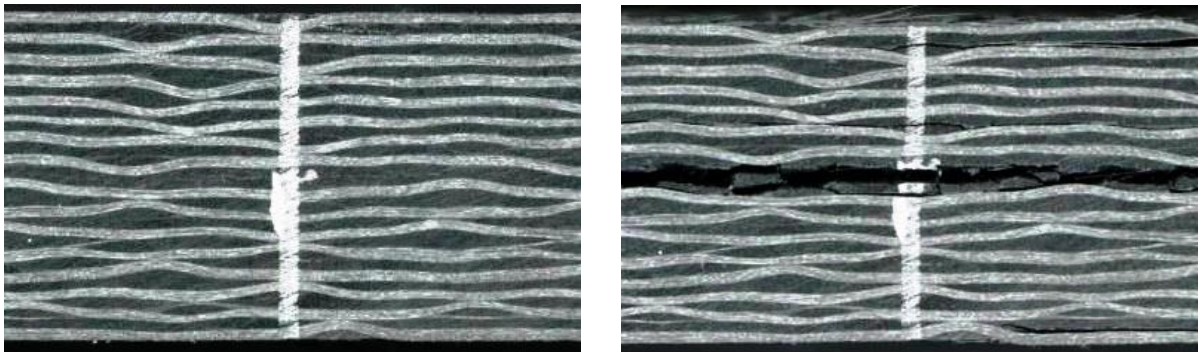

Figure 50: Pre mortem (left) and post mortem (right) images taken at 50× with an optical microscope for samples with high porosity ($< 1\%$).

In contrast with high porosity samples, laminates with low porosity failed via delamination, primarily at the midplane. Delaminations occur along the fiber-matrix interface, or where two adjacent plies are bonded together. Since interlaminar shear stress is maximum at the neutral axis, the primary delamination is expected to be seen at the midplane. The presence of delamination indicates the material is less resistant to shear than flexure. All low porosity samples (those with porosity less than 3%) failed via delamations.

Flexural modulus was calculated as a function of crosshead displacement. As listed in [42], the flexural modulus is calculated using the load and displacement corresponding to the peak load. Example graphs for high and low porosity samples are shown in Figure 51.

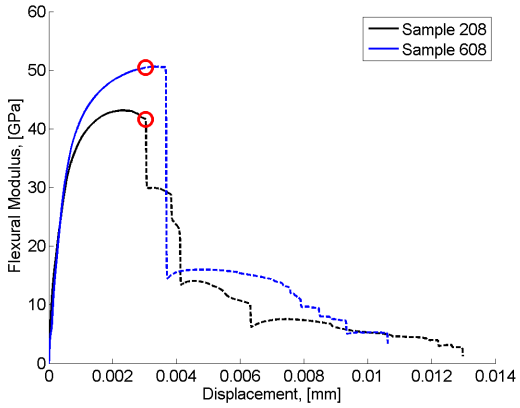

Figure 51: Flexural modulus was calculated as a function of crosshead displacement for all samples.

Flexural modulus-crosshead displacement response for all samples yielded the same characteristics. Flexural modulus increased linearly at the same slope for all samples until $\varepsilon \approx 0.15$. Beyond $\varepsilon \approx 0.15$, flexural modulus leveled off until the first primary failure, when the flexural modulus greatly decreased. The stiffness at each value of crosshead displacmeent is easily calculated using Hooke's law, dividing the load by the displacement. Stiffness as a function of crosshead displacement mirrored the shape of the flexural modulus-crosshead displacement response. Tables 19 and 20 lists the flexural modulus in GPa for each sample tested.

Table 19: Flexural Modulus, Samples 101-310

Sample	E_{11}	Sample	E_{11}	Sample	E_{11}
101	3.488	201	47.365	301	48.589
102	3.537	202	45.055	302	49.013
103	3.589	203	44.531	303	48.774
104	3.623	204	45.506	304	48.101
107	4.027	207	43.936	307	47.631
108	4.129	208	43.172	308	47.128
109	4.200	209	45.225	309	48.530
110	4.029	210	45.535	310	48.987

Table 20: Flexural Modulus, Samples 401-610

Sample	E_{11}	Sample	E_{11}	Sample	E_{11}
401	48.592	501	48.111	601	49.403
402	48.690	502	49.196	602	49.790
403	49.127	503	49.795	603	49.261
404	49.386	504	49.500	604	48.744
407	49.266	507	48.820	607	49.909
408	50.038	508	47.575	608	50.617
409	49.528	509	47.715	609	50.546
410	51.735	510	49.320	610	51.271

The flexural modulus as a function of porosity for samples 200-600 are shown in Figure 52.

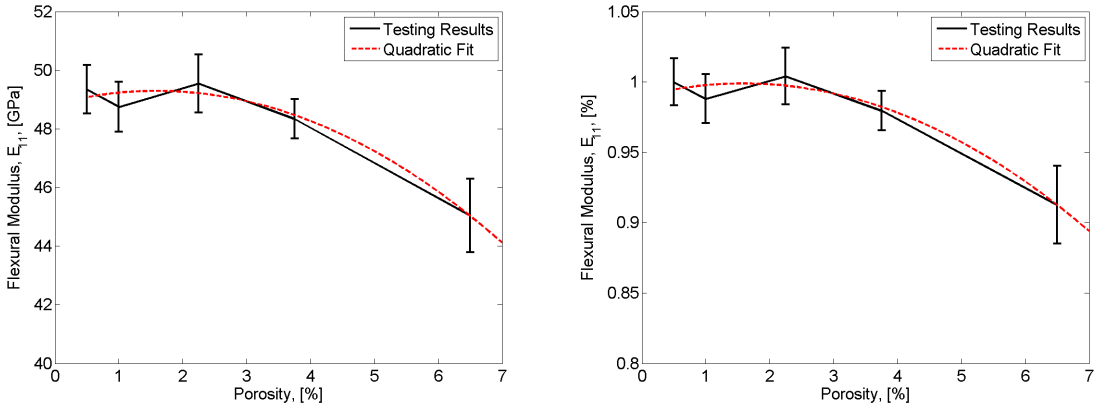

Figure 52: Flexural modulus was calculated as a function of porosity for samples 200-600. A quadratic fit is shown by a red dashed line.

The error bars in Figure 52 were generated by taking the standard deviation of each test. The right plot of Figure 52 was generated by dividing each specimen's calculated flexural modulus by the flexural modulus of the control sample, samples with porosity concentrations $< 0.5\%$. The quadratic fits allows for easy interpolation and extrapolation. For example, a sample with 7% porosity is expected to see a 10% decrease in flexural modulus. This decrease in flexural modulus is likely due to the reduced effectiveness of the matrix to transfer load from fiber to fiber. Since pores create discontinuities in the matrix, porosity reduces the load transfer capabilities.

Complete failure did not occur at the first primary failure during flexure testing. As shown in Figure 48, the load steadily increased after each energy release event. After the first failure, the specimen redistributed the load as the stiffness increased. Residual stiffness was calculated by measuring the slope of the load-displacement response after the first failure, as shown in Figure 36. Residual stiffness for representative samples from the 200 and 600 series are shown in Figure 53.

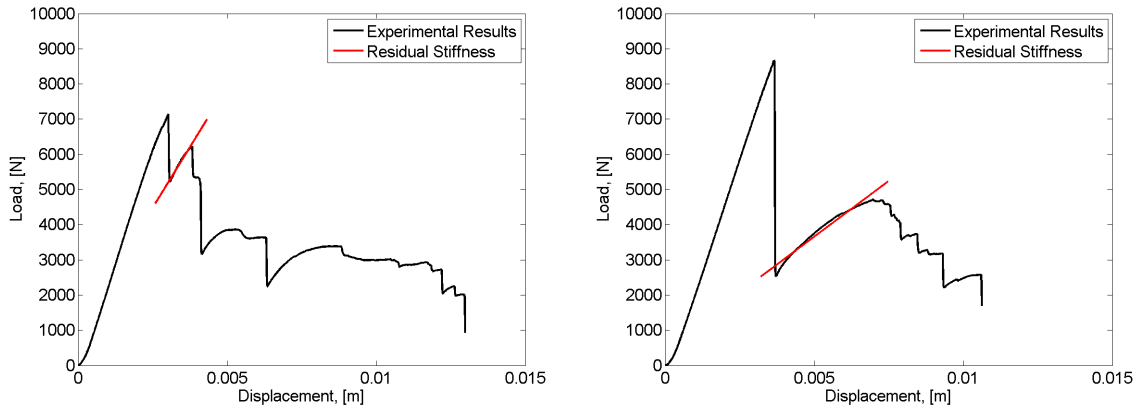

Figure 53: Residual stiffness for high porosity (left) and low porosity (right), calculated by the slope after the first peak load.

Residual stiffness for each experiment is tabulated in Tables 21, 22, and 23. All stiffness results have the units kN/mm, or N/m $\times 10^6$.

Table 21: Residual Stiffness, Samples 201-310

Sample	K_1	K_2	% Red	Sample	K_1	K_2	% Red
201	2.477	0.554	22%	301	2.497	0.659	26%
202	2.478	0.951	38%	302	2.545	0.540	21%
203	2.492	0.224	9%	303	2.574	0.573	22%
204	2.475	0.578	23%	304	2.571	0.584	23%
207	2.545	0.826	32%	307	2.606	0.475	18%
208	2.545	1.378	54%	308	2.585	0.551	21%
209	2.541	0.975	38%	309	2.624	0.468	18%
210	2.597	–	–	310	2.616	0.262	10%

Table 22: Residual Stiffness, Samples 401-510

Sample	K_1	K_2	% Red	Sample	K_1	K_2	% Red
401	2.603	0.781	30%	501	2.504	0.944	38%
402	2.586	0.688	27%	502	2.514	0.761	30%
403	2.579	0.619	24%	503	2.501	0.713	28%
404	2.563	0.649	25%	504	2.472	0.699	28%
407	2.548	0.643	25%	507	2.484	0.665	27%
408	2.558	0.619	24%	508	2.482	0.771	31%
409	2.555	0.575	23%	509	2.488	0.706	28%
410	2.573	0.610	24%	510	2.485	0.617	25%

Table 23: Residual Stiffness, Samples 601-610

Sample	K_1	K_2	% Red
601	2.595	0.524	20%
602	2.603	0.672	26%
603	2.628	0.690	26%
604	2.623	0.849	32%
607	2.510	0.550	22%
608	2.506	0.634	25%
609	2.434	0.739	30%
610	2.464	0.624	25%

The results from Tables 21, 22, and 23 were plotted with porosity to determine the effect of porosity on stiffness and residual stiffness.

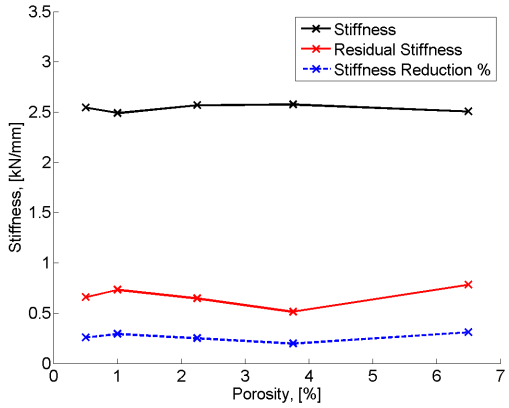

Figure 54: Porosity had little to no effect on the stiffness and residual stiffness under four-point flexure.

As shown in Figure 54, stiffness and residual stiffness was not greatly affected by porosity. This is surprising considering the effect porosity had on flexural modulus, shown in the plots of Figure 52. As shown in Eq (19), flexural modulus is highly dependent on the thickness of the specimen. Since the thickness is cubed, small variations in thickness can greatly influence the flexural modulus. Stiffness is merely P/δ, therefore changes in thickness do not affect stiffness. The influence specimen thickness plays on the flexural modulus and stiffness can be seen in Figures 52 and 54.

The area under the load-displacement curve is equal to the energy absorbed during the experiment, calculated by Eq (20). Energy absorbed as a function of displacement for high and low porosity representative samples is shown in Figure 55.

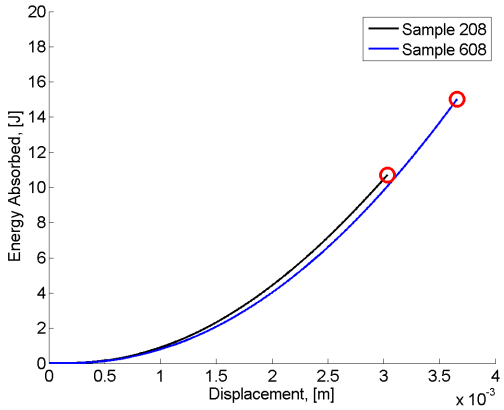

Figure 55: Energy absorbed as a function of crosshead displacement for samples 208 (black) and 608 (blue).

Energy absorbed to the peak load for all experiments had the same basic shape, concave up and quadratic. Since energy is a summed quantity, the final value is the result of the integral. The total energy absorbed to the peak load for each tested sample is shown in Table 24. Tabulated energy results are given with units of joules.

Table 24: Energy to Peak Load Results, Samples 201-610

Sample	E_{abs}	Sample	E_{abs}	Sample	E_{abs}	Sample	E_{abs}	Sample	E_{abs}
201	11.27	301	10.89	401	14.07	501	14.97	601	14.61
202	10.32	302	11.47	402	14.34	502	15.88	602	14.15
203	9.77	303	11.31	403	14.73	503	14.89	603	13.60
204	12.20	304	11.74	404	12.88	504	13.96	604	13.96
207	9.34	307	11.03	407	14.73	507	14.49	607	14.95
208	10.71	308	12.07	408	12.93	508	14.89	608	15.02
209	12.78	309	12.41	409	14.95	509	14.16	609	15.17
210	13.20	310	13.71	410	15.38	510	18.03	610	15.17

The results from Table 24 were averaged and plotted against porosity, shown in Figure 56.

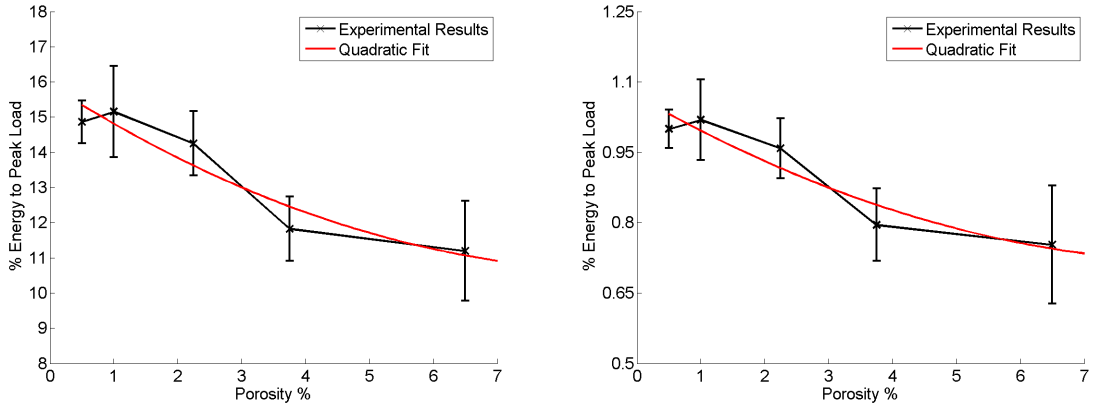

Figure 56: Energy absorbed to peak load was calculated as a function of porosity for samples 200-600. A quadratic fit is shown by a red line.

The error bars in Figure 56 were generated by taking the standard deviation of each test. To determine the reduction in energy absorbed, each value was divided by the control sample with porosity concentration $< 0.5\%$, shown in the right plot of Figure 56. The empirical fit shown by the red curves allow for easy interpolation and extrapolation. For example, a composite with approximately 7% porosity constructed of the same constituents is expected to see a 20% reduction in energy absorbed to the peak load while absorbing approximately 11 joules. The best fit quadratic curve is concave up with a decreasing slope as porosity increases unlike the quadratic fit for flexural modulus, shown in Figure 52. This indicates the energy absorbed is approaching an asymptote and will not decrease any further once porosity reaches a certain concentration. The implications of this will be further discussed when results from samples 100 with a porosity concentration of 38% are presented.

The peak load of each experiment was defined by the maximum load supported by the specimen just prior to the first failure. Peak load was a measured quantity, no calculations or post-processing was required to determine the following relationships. The maximum load experienced during each experiment is tabulated in Table 25.

Table 25: Peak Load Results, Samples 201-610

Sample	P_{max}	Sample	P_{max}	Sample	P_{max}	Sample	P_{max}	Sample	P_{max}
201	7142	301	7404	401	8514	501	8634	601	8689
202	6962	302	7462	402	8602	502	8761	602	8486
203	6786	303	7520	403	8590	503	8556	603	8422
204	7498	304	7755	404	8152	504	8238	604	8513
207	6633	307	7611	407	8629	507	8204	607	8379
208	7140	308	7785	408	8115	508	8495	608	8665
209	7677	309	8015	409	8717	509	8276	609	8560
210	7179	310	8324	410	8800	510	9010	610	8554

The results from Table 25 were averaged and plotted against porosity, shown in Figure 57.

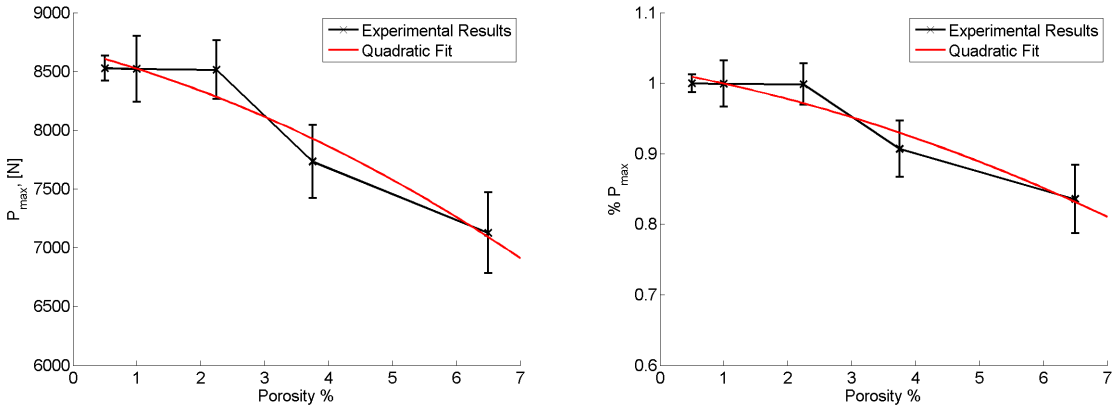

Figure 57: Peak load was calculated as a function of porosity for samples 200-600. A quadratic fit is shown by a red line.

Similar to flexural modulus, the peak load-porosity relationship decreases at an increasing rate as porosity increases, i.e., a quadratic empirical relationship is concave down. The quadratic fit, indicated by the red curve in the plots in Figure 57 falls entirely within the error bars of the experimental data and is used as a tool for interpolation and extrapolation.

A sample with 7% porosity is expected to support a peak load equal to 7000 N, or reduction of approximately 20% compared to a porosity free sample.

The strain associated with the first failure was calculated and tabulated for all experiments. Strain was calculated by dividing the crosshead displacement by the specimen thickness, nondimensionalizing the results into a quantity that is easily comparable among specimens of varying thickness. The resulting strain to failure for samples 200-600 are shown in Table 26.

Table 26: Strain to Failure Results, Samples 201-610

Sample	ε_f	Sample	ε_f	Sample	ε_f	Sample	ε_f	Sample	ε_f
201	0.4952	301	0.5125	401	0.5573	501	0.5950	601	0.5673
202	0.4724	302	0.5090	402	0.5682	502	0.6064	602	0.5568
203	0.4597	303	0.5012	403	0.5745	503	0.5881	603	0.5410
204	0.5052	304	0.5115	404	0.5429	504	0.5865	604	0.5502
207	0.4434	307	0.5139	407	0.5845	507	0.5805	607	0.5902
208	0.4673	308	0.5141	408	0.5444	508	0.5933	608	0.5986
209	0.4991	309	0.5325	409	0.5890	509	0.5785	609	0.6159
210	0.5089	310	0.5125	410	0.5802	510	0.6356	610	0.5984

The results from Table 25 were averaged and plotted against porosity, shown in Figure 58.

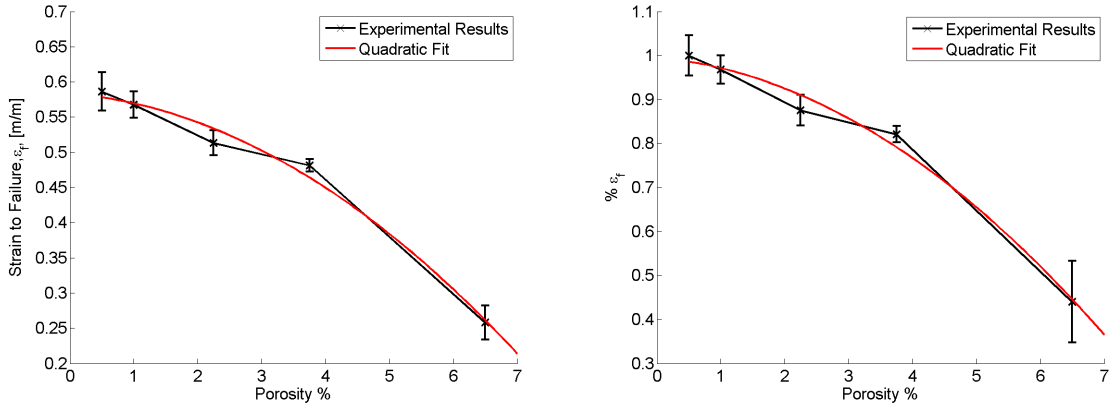

Figure 58: Strain to first failure was calculated as a function of porosity for samples 200-600. A quadratic fit is shown by a red line.

Similar to flexural modulus and peak load, the strain to failure decreases at an increasing rate as porosity increases, i.e., the resulting empirical relationships are concave down. As shown in the right plot of Figure 58, the strain to failure is reduced by nearly 60% for the sample with nearly 7% porosity. This indicates the composite has lost much of its ductility. A material exhibiting less ductility is likely to fail subjected to smaller loads, in agreement with the results shown in Figure 57.

To this point, experimental results from the samples of greatest porosity concentration have been omitted in discussion. The extreme porosity samples exhibited unusual results when subjected to flexure testing. While the samples displayed extreme elasticity, their load-displacement relationship was nonlinear. Thus, calculations were limited to those which do not require a linear stress-strain or load-displacement assumption such as the calculation of flexural modulus which assumes a linear elastic beam. The nonlinearity of the extreme porosity samples is shown in Figure 59.

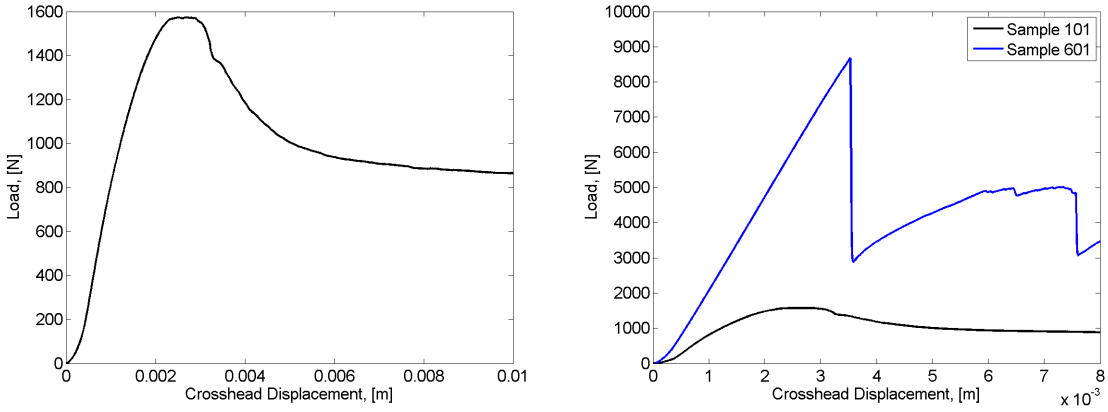

Figure 59: Samples with extreme porosity do not a exhibit linear load-displacement relationship.

In addition to its nonlinear load-displacement relationship, the magnitude of the peak load was significantly lower than those from lower porosity samples, shown in the right plot of Figure 59. This significant decrease in peak load made it difficult to see any discernible trends in quantities such as peak load, strain to failure, and energy absorbed. A visual comparison of the extreme porosity sample subjected to its peak load on the left with the control specimen on the right.

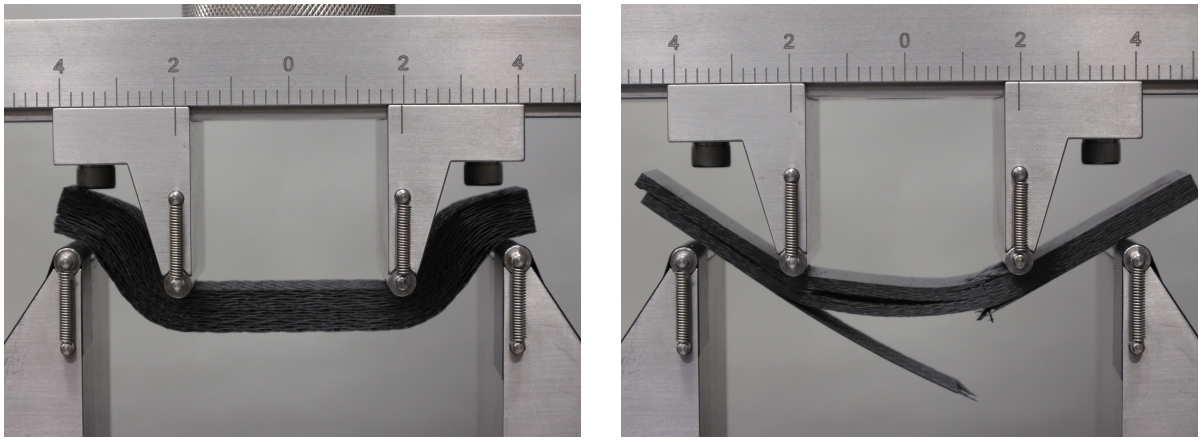

Figure 60: Specimens with extreme porosity concentration (left) exhibited an unusual visual response to the four-point load application. Low porosity sample (right) for comparison.

The post processed results from samples 100 are tabulated in Table 27 below. Flexural modulus, stiffness, and residual stiffness were not calculated since they requires a linear stress-strain or load-displacement response.

Table 27: Strain to Failure Results, Samples 201-610

Sample	P_{max}, [N]	E_{abs}, [J]	ε_f, [m/m]
101	1574	2.583	0.257
102	1493	2.576	0.259
103	1502	2.619	0.260
104	1517	2.288	0.238
107	1729	2.866	0.257
108	1769	3.063	0.265
109	1852	3.106	0.263
110	1816	3.055	0.265

The results in Table 27 were combined with those from Tables 24, 25, and 26 and plotted against porosity, shown in Figures 61, 62,and 63.

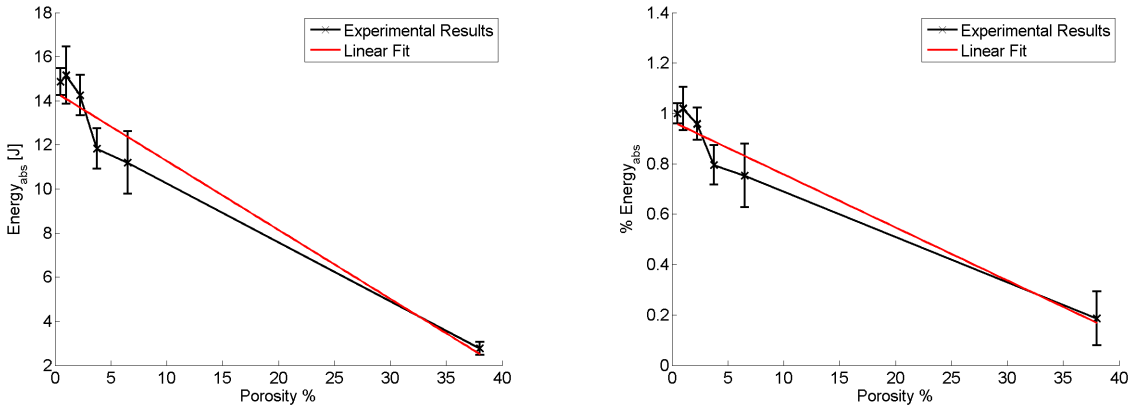

Figure 61: Energy to peak load was calculated as a function of porosity for all samples. A linear fit is shown by a red line.

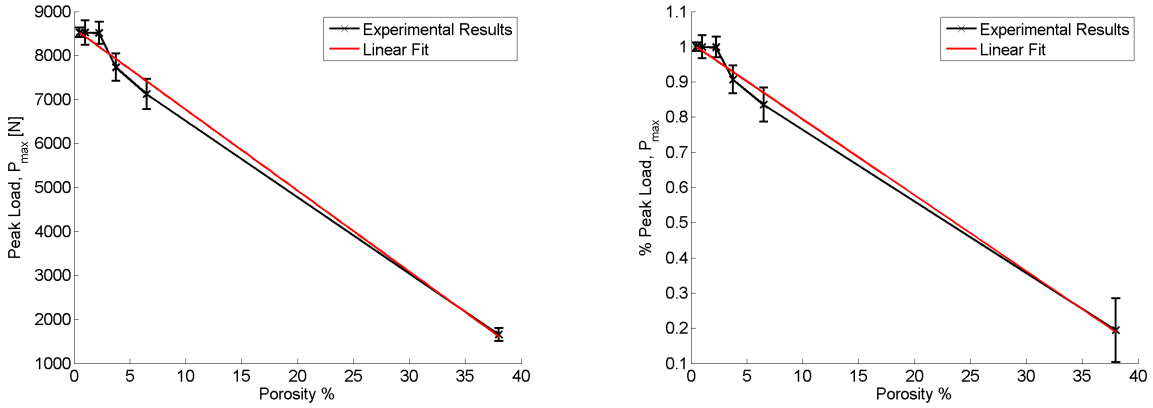

Figure 62: Peak load was calculated as a function of porosity for all samples. A linear fit is shown by a red line.

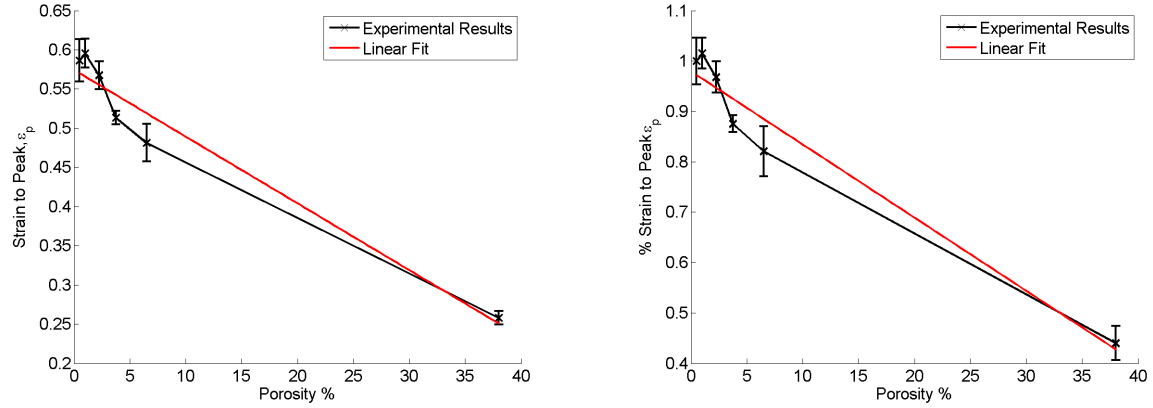

Figure 63: Strain to peak load was calculated as a function of porosity for all samples. A linear fit is shown by a red line.

By including experimental results from the extreme porosity samples, the lower porosity concentration trends are difficult to discern. The 38% porosity samples experienced an 80% reduction in peak load and energy to peak load and a 55% reduction in strain to peak load. These extreme reductions in key mechanical properties deem the material nonideal in structural applications.

5.4.2 Short Beam Shear

Short beam shear experimental testing was conducted to determine the effects of porosity on the shear carrying capabilities of the composite. The aspect ratio of the beam was reduced from 16:1 to 4:1, increasing the damage due to transverse and interlaminar shear stress. Similar to flexure testing, load and displacement were recorded and all post processing was conducted with these two parameters. The test continued until the instantenous load reached 20% of the peak load, however post processing used the first primary failure as the end point to end testing. Only samples 200-600 were subjected to short beam shear testing. The ASTM standard for short beam shear testing limits the specimen thickness to 6 mm [41], however extreme porosity samples had a thickness $>$ 10 mm. Samples thicker than 6 mm may be shear tested using an Iosipescu Shear apparatus. Iosipescu shear was not conducted to keep results consistent. Instead, three point bending with a 4:1 span-to-thickness ratio was implemented. A typical load-displacement curve for a specimen subjected to short beam shear is shown in Figure 64.

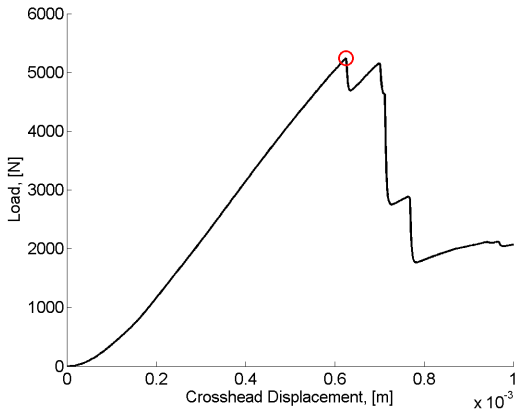

Figure 64: Typical load-displacement curve for short beam shear specimens. The red circle corresponds to the maximum load.

Load-displacement curves for samples 200-600 had the same general characteristics and looked very similar to the one shown in Figure 64. Applied load increased linearly until it reached a peak value. This was followed by a small decrease in applied load, followed

by a linear increase. A large, sudden drop in applied load occurred once the interlaminar shear strength was reached, allowing energy to escape in the form of shear cracking and delaminations. Damage and delaminations were difficult to visually inspect for low porosity samples, however was easily noticible for high porosity samples. Images of high and low porosity samples at the point of maximum interlaminar shear stress are shown in Figure 65.

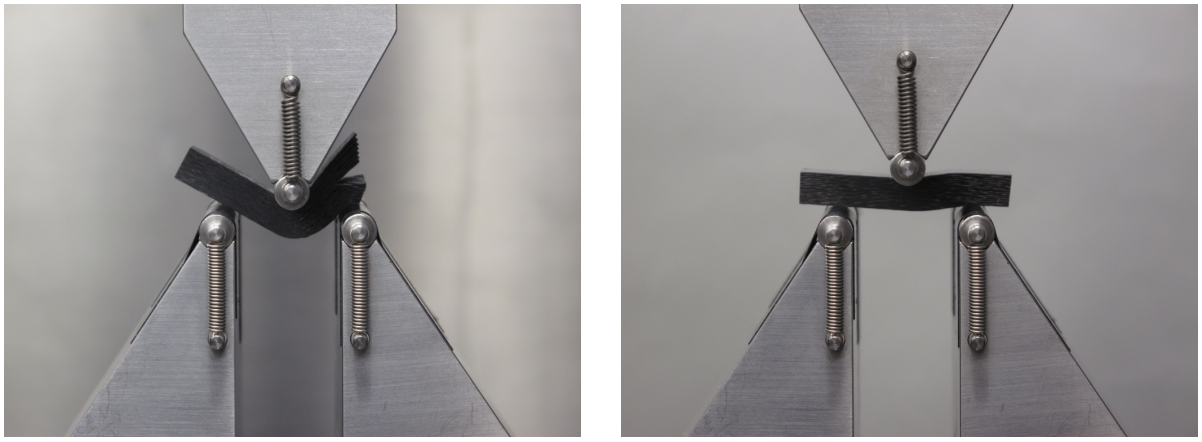

Figure 65: Delaminations were easy to visually inspect for high porosity samples (left). Damage was more difficult to visually detect for low porosity samples.

Specimens 210-210 all failed in the same manor, delaminations of plies above the midplane on the right side of the apparatus. Since every specimen failed in the same manor, it is likely there was bias of the apparatus to the right. Close investigation of the apparatus determined the central loading block was not directly in the center of the support spans. While this asymmetry is not ideal, it is not render the results meaningless. All experiments were conducted using the same apparatus and were subjected to the same asymmetry. Samples with lower porosity concentrations failed via shear and delaminations, however plies did not curl around the loading block as with the high porosity samples, shown in the right image of Figure 65. Pre and post mortem images were captured using a high powered optical microscope to compare and visually inspect the damage. Representative images of samples with high (6.5%) and low ($< 1\%$) are shown in Figures 66 and 67.

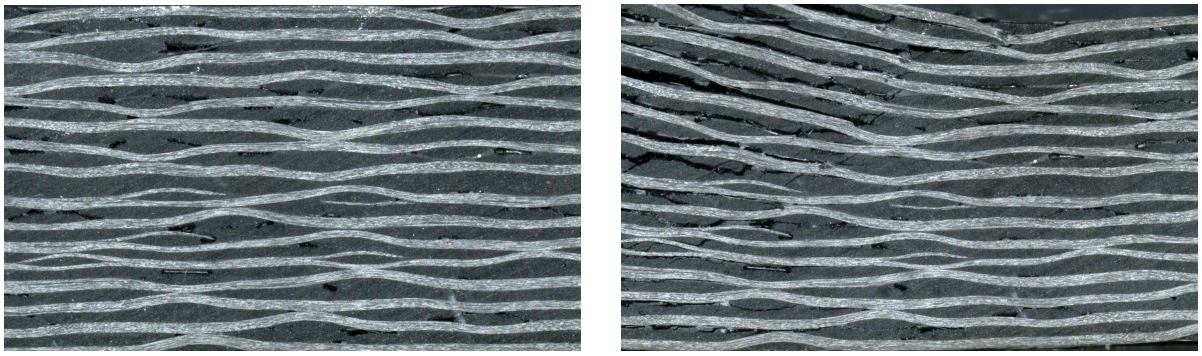

Figure 66: Pre moretem (left) and post mortem (right) images taken at 50x with an optical microscope for samples with high porosity (6.5%).

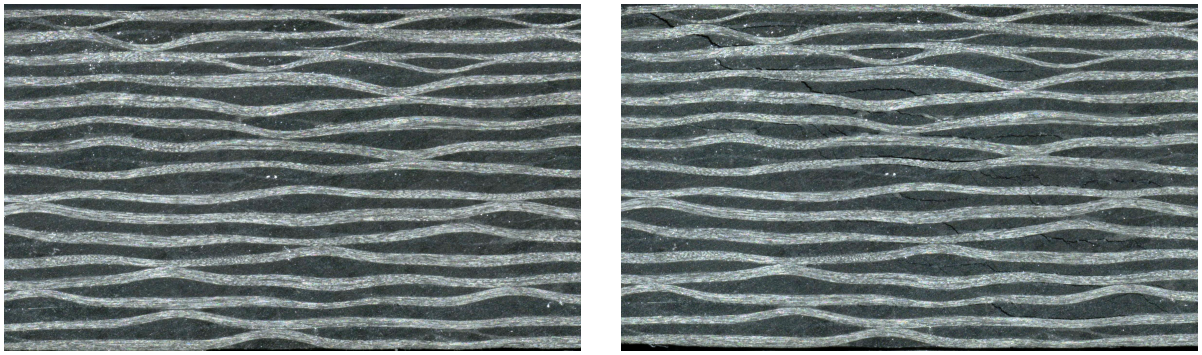

Figure 67: Pre moretem (left) and post mortem (right) images taken at 50x with an optical microscope for samples with low porosity ($< 1\%$).

The images taken in Figures 66 and 67 were taken in the same locations to determine if cracks initiated or terminated at pore locations. Several pores are the sites of matrix cracking, however it is difficult to determine whether or not pores increased the likelihood of shear cracking.

Corresponding load-displacement curves for the specimens shown in Figures 66 and 67 are shown below.

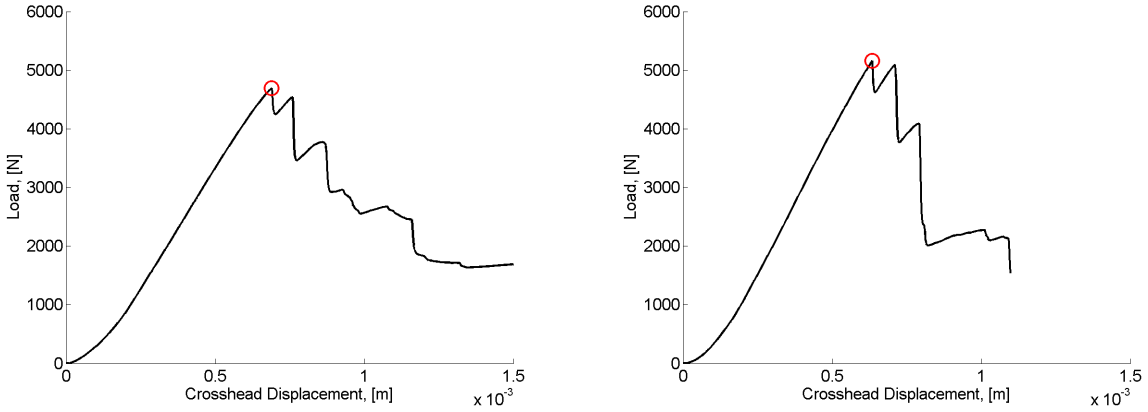

Figure 68: Load-displacement response for the high porosity (6.5%, left) and low porosity (<1%, right) samples. The red circle indicates the peak load.

Peak load, strain to peak load, energy to peak load, and interlaminar shear strength were calculated for each experiment using the same techniques developed for flexure testing. Peak load for each experiment are tabulated in Tables 28 and 29. All tabulated values are have units of N.

Table 28: Peak Load, Samples 201-410

Sample	P_{max}	Sample	P_{max}	Sample	P_{max}
201	4691	301	5250	401	5320
202	4461	302	5138	402	5909
203	4355	303	5147	403	5459
204	4669	304	5139	404	5484
207	4460	307	5148	407	5377
208	4496	308	5300	408	5385
209	4704	309	5129	409	5367
210	4531	310	5306	410	5592

Table 29: Peak Load, Samples 501-610

Sample	P_{max}	Sample	P_{max}
501	5489	601	5158
502	5431	602	5377
503	5334	603	5397
504	5476	604	5362
507	5715	607	5373
508	5598	608	5469
509	5429	609	5446
510	5572	610	5243

The values contained in Tables 28 and 29 were averaged and plotted as a function of porosity. Standard deviations were taken and used to calculate error bars to determine the spread of the measured data. The resulting plots are shown in Figure 69.

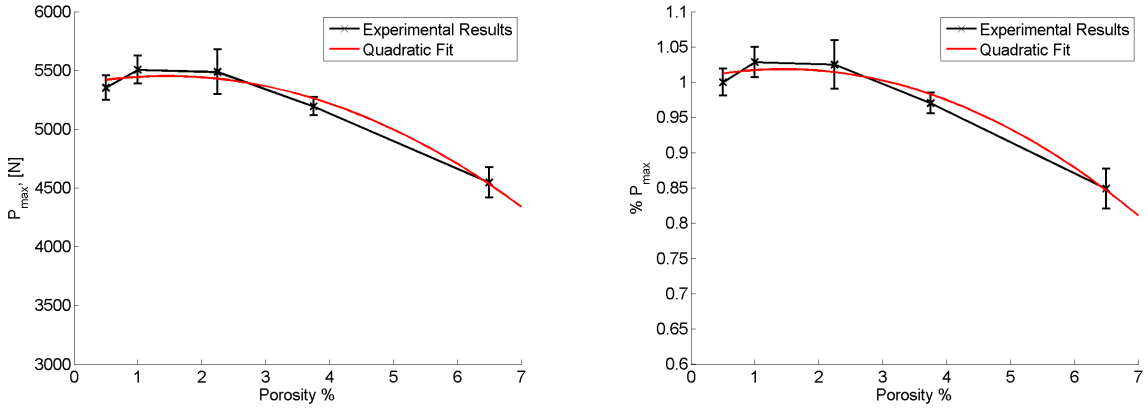

Figure 69: Peak load was calculated as a function of porosity for all samples. A quadratic fit is shown by a red line.

Similar to peak load during flexure testing shown in Figure 57, peak load decreases as a function of porosity with the same, concave down trend. For specimens with a porosity con-

centration $< 2\%$, peak load appears to be unaffected by porosity. Beyond 2%, the composite exhibits a 15% reduction in peak load. Referencing Figure 57 from flexure testing, samples with porosity concentrations of 7% also experience roughly a 15% decrease in peak load.

Porosity was expected to greatly affect mechanical properties carried through the matrix, specifically interlaminar shear stress. As noted in Eq. (25), interlaminar shear strength is a function of peak load and geometry terms. Thus, it is expected to follow the same trend as peak load shown in Figure 69. Tabulated values of interlaminar shear strength for all experiments are shown in Tables 30 and 31, with all units in MPa.

Table 30: ILSS, Samples 201-410

Sample	ILSS	Sample	ILSS	Sample	ILSS
201	22.55	301	24.84	401	24.73
202	20.51	302	24.12	402	27.58
203	19.92	303	24.08	403	25.53
204	21.40	304	24.02	404	25.81
207	20.12	307	23.83	407	25.38
208	20.09	308	24.52	408	25.44
209	21.14	309	23.75	409	25.36
210	20.38	310	24.60	410	26.60

Table 31: ILSS, Samples 501-610

Sample	ILSS	Sample	ILSS
501	25.73	601	24.08
502	25.62	602	25.23
503	25.39	603	25.17
504	26.15	604	24.94
507	26.97	607	25.49
508	26.30	608	26.13
509	25.60	609	26.32
510	26.20	610	25.20

The values contained in Tables 30 and 31 were averaged and plotted as a function of porosity. Standard deviations were taken and used to calculate error bars to determine the spread of the measured data. The resulting plots are shown in Figure 70.

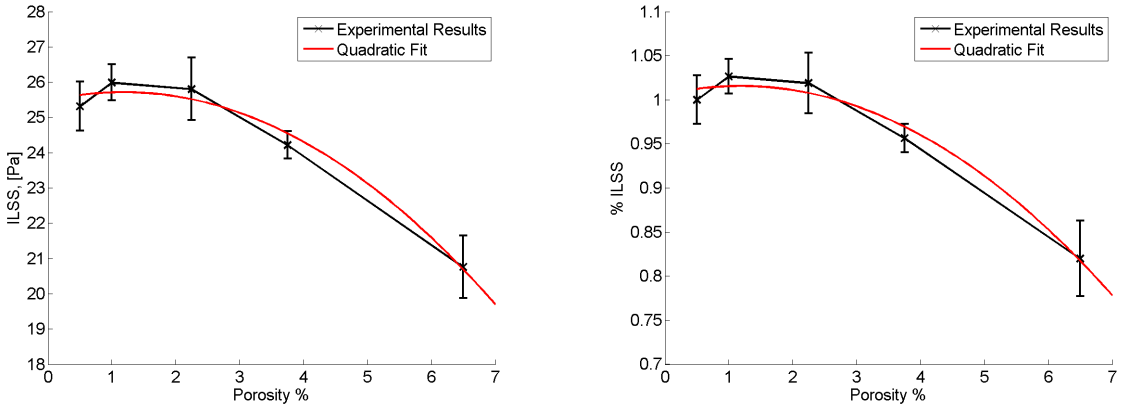

Figure 70: Interlaminar shear strength was calculated as a function of porosity for all samples. A quadratic fit is shown by a red line.

Interlaminar shear strength experiences the same unaffected region for porosity concentrations $< 2\%$. Beyond 2%, interlaminar shear strength decreases until it reaches approximately

a 17% reduction by the time the porosity reaches 7%. As expected, the same trend is present for interlaminar shear strenght as peak load.

Energy absorbed to peak load was calculated by integrating the load-displacement response with the upper limit being the displacement corresponding to the peak load. This value describes the amount of shear energy the specimen can absorb until the first major energy release. The results from all experiments are tabulated below in Tables 32 and 33. All values have units of joules.

Table 32: Energy Absorbed, Samples 201-410

Sample	E_{abs}	Sample	E_{abs}	Sample	E_{abs}
201	1.466	301	1.572	401	1.570
202	1.624	302	1.842	402	1.903
203	1.707	303	1.950	403	1.585
204	1.466	304	1.880	404	1.674
207	1.821	307	2.130	407	1.559
208	1.762	308	1.605	408	1.607
209	1.406	309	1.549	409	1.599
210	1.384	310	2.056	410	1.735

Table 33: Energy Absorbed, Samples 501-610

Sample	E_{abs}	Sample	E_{abs}
501	1.627	601	1.442
502	2.129	602	1.564
503	1.627	603	1.667
504	1.718	604	1.557
507	1.851	607	1.551
508	1.729	608	1.619
509	2.125	609	1.621
510	1.725	610	1.467

The values contained in Tables 32 and 33 were averaged and plotted as a function of porosity. Standard deviations were taken and used to calculate error bars to determine the spread of the measured data. The results are shown in Figure 71.

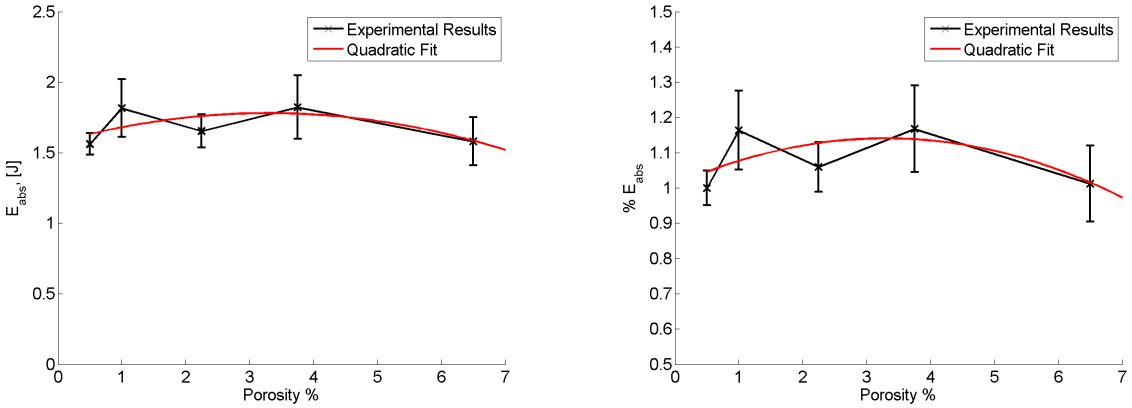

Figure 71: Energy absorbed to peak load was calculated as a function of porosity for all samples. A quadratic fit is shown by a red line.

Unlike peak load and interlaminar shear strength, there appears to be no significant affect of porosity on energy absorbed to peak load. The plots show a gradual increasing and de-

creasing trend with the maximum occurring at approximately 3%. At the peak value, only 10% additional energy has been absorbed. With error bars spanning between 10 and 30%, it is likely porosity has no affect on energy absorbed to peak load. The gradual increasing and decreasing trend present is due to experimental scatter and slight variations in porosity from specimen to specimen within a given laminate.

Strain to peak load was calculated by dividing the crosshead displacement at the peak load by the specimen thickness. By dividing out the thickness, each sample is nondimensionalized and can be compared against specimens of varying thickness. The results for each speicmen's strain to peak load is tabulated and given in Tables 34 and 35.

Table 34: Strain to Peak Load, Samples 201-410

Sample	ε_p	Sample	ε_p	Sample	ε_p
201	0.1086	301	0.1046	401	0.1031
202	0.1150	302	0.1117	402	0.1077
203	0.1198	303	0.1204	403	0.1054
204	0.1087	304	0.1168	404	0.1097
207	0.1190	307	0.1192	407	0.1028
208	0.1181	308	0.1014	408	0.1051
209	0.1013	309	0.1032	409	0.1018
210	0.1010	310	0.1185	410	0.1101

Table 35: Strain to Peak Load, Samples 501-610

Sample	ε_p	Sample	ε_p
501	0.1075	601	0.1019
502	0.1251	602	0.1011
503	0.1080	603	0.1084
504	0.1106	604	0.0994
507	0.1105	607	0.1035
508	0.1115	608	0.1056
509	0.1247	609	0.1084
510	0.1080	610	0.1027

The values contained in Tables 34 and 35 were averaged and plotted as a function of porosity. Standard deviations were taken and used to calculate error bars to determine the spread of the measured data. The resulting plots are shown in Figure 72.

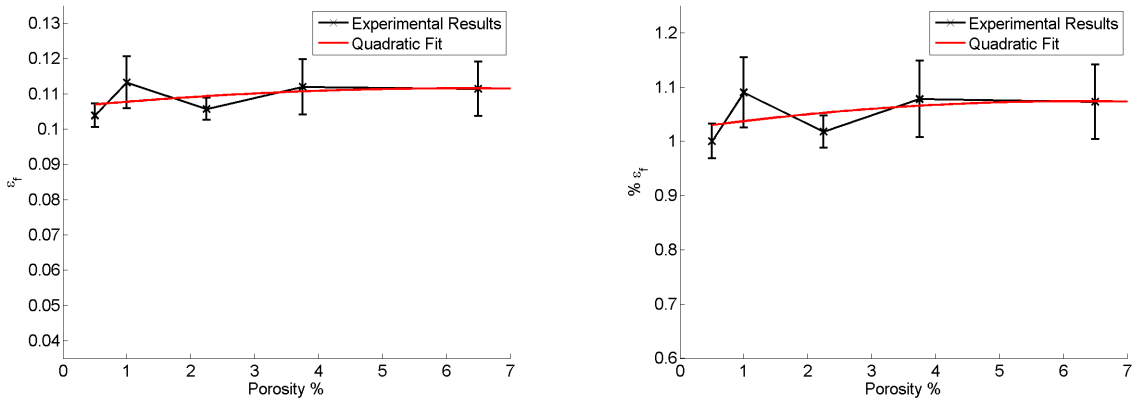

Figure 72: Strain to peak load was calculated as a function of porosity for all samples. A quadratic fit is shown by a red line.

Strain to peak load exhibited the same, unaffected trend as energy to peak load. The quadratic empirical fit can be replaced with a constant, linear relationship and produce

nearly identical results. Although there is slight variation between porosity concentrations, a constant strain to peak load falls within the spread of the data. Porosity has no major affect on the strain to peak load.

As noted in earlier sections, it was very difficult to accurately measure porosity concentrations $< 1\%$. A student T-test suggests there is no statistical difference between samples 500 and samples 600. To account for this, the same plots were generated assuming the 500 and 600 laminates were identical with $< 1\%$ porosity. Shear results for peak load, interlaminar shear strength, energy absorbed to peak load, and strain to peak load are given in Figures 73, 74, 75, and 76.

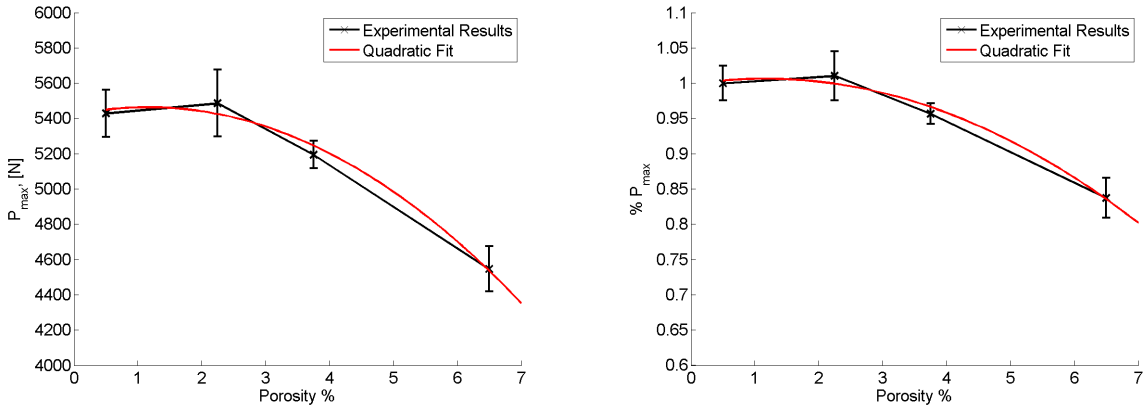

Figure 73: Peak load was calculated as a function of porosity for all samples. A quadratic fit is shown by a red line.

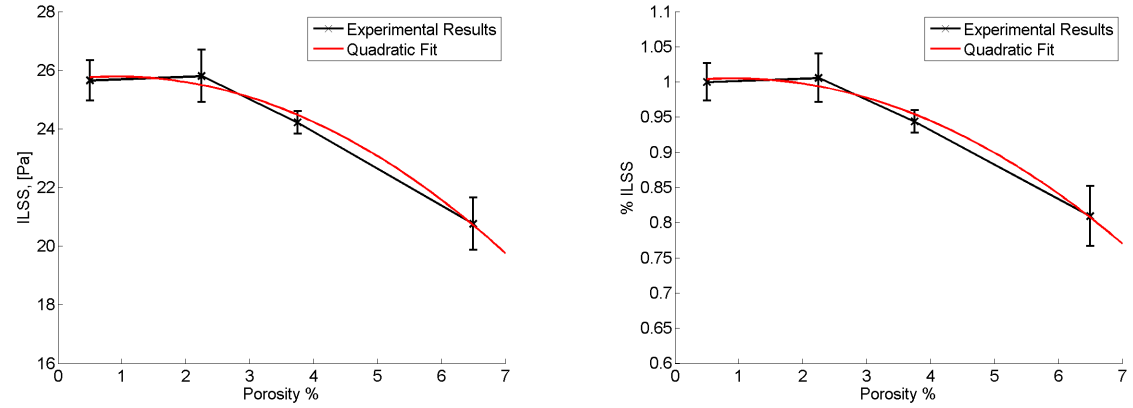

Figure 74: Interlaminar shear strength was calculated as a function of porosity for all samples. A quadratic fit is shown by a red line.

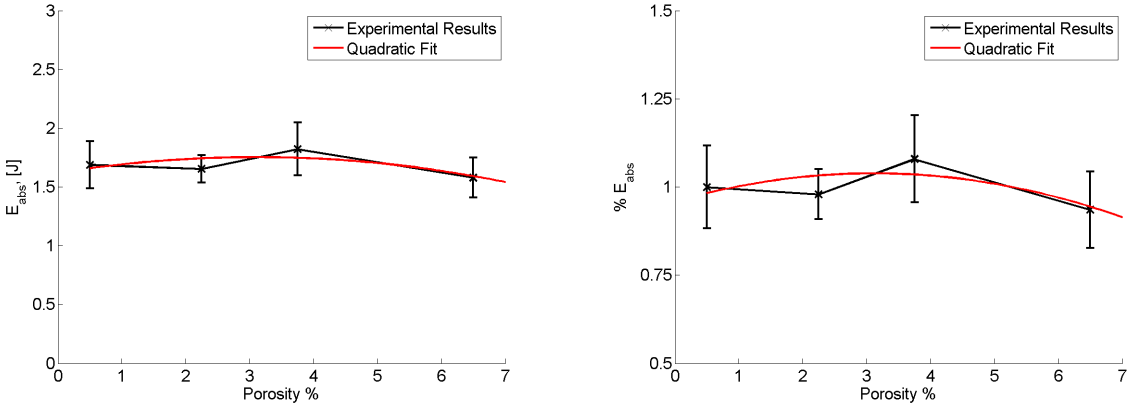

Figure 75: Energy absorbed to peak load was calculated as a function of porosity for all samples. A quadratic fit is shown by a red line.

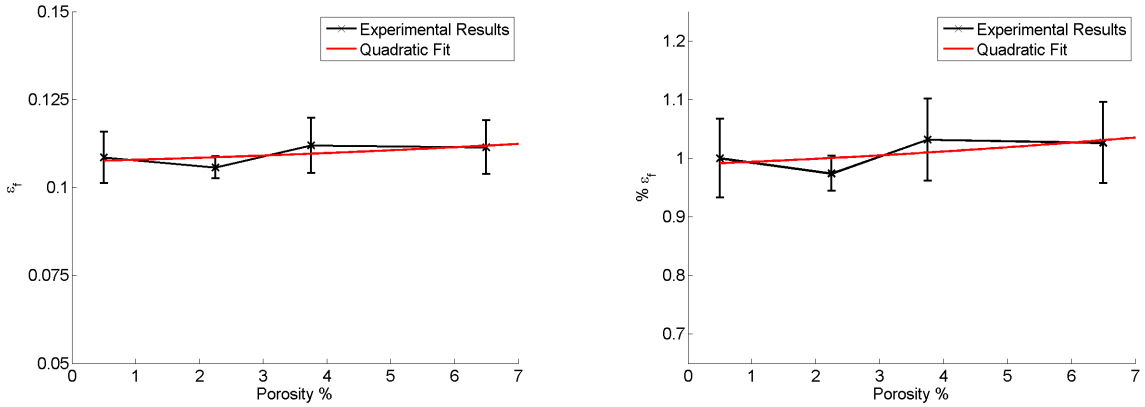

Figure 76: Strain to peak load was calculated as a function of porosity for all samples. A quadratic fit is shown by a red line.

The same general trend is present using four or five porosity concentrations. To reduce the number of similar plots and remain consistent, all five porosity concentrations will be used in porosity characterization for the rest of the study.

5.4.3 Impact

Low-velocity, drop-weight impact testing was conducted on a Dynatup 8250 drop tower. Load and time were measured from the load cell. Two tup geometries were used in drop weight testing–a blunt, flat tup, and a round, hemispherical tup. In order to ensure consistent damage, impact energy was reduced from 50J to 30J for for hemispherical tup testing. Post processing and comparisions for each tup geometry were treated separately.

5.4.3.1 Flat Tup

The load-time response shown below in Figure 77 was taken directly from the output of the load cell. Load-time response curves were created for each experiment. A representative curve for high porosity (6.5%) and low porosity (<1%) are shown below.

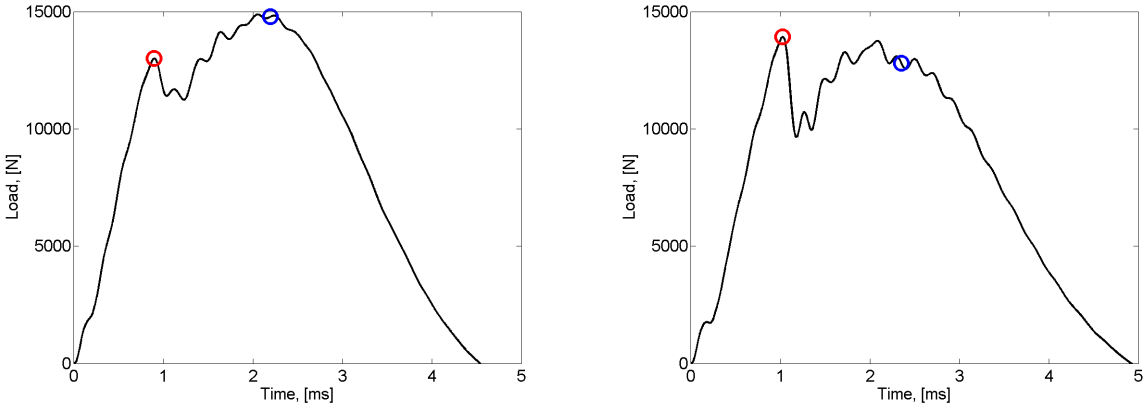

Figure 77: Representative load-time response for high porosity (left) and low porosity (right) samples. The red circle corresponds to the first failure, blue circle corresponds to maximum displacement.

More information can be gathered from a load-displacement curve, thus displacement must be calculated from the load-time response. Using Newton's second law and a simple force balance shown in 37 and Equation (29), load as a function of displacement can be calculated. A typical load-displacement curve for an impacted specimen is shown in Figure 78 below.

To fully characterize the effect of porosity, several points along the load-displacement curve were analyzed. These points are outlined and described in the following figures.

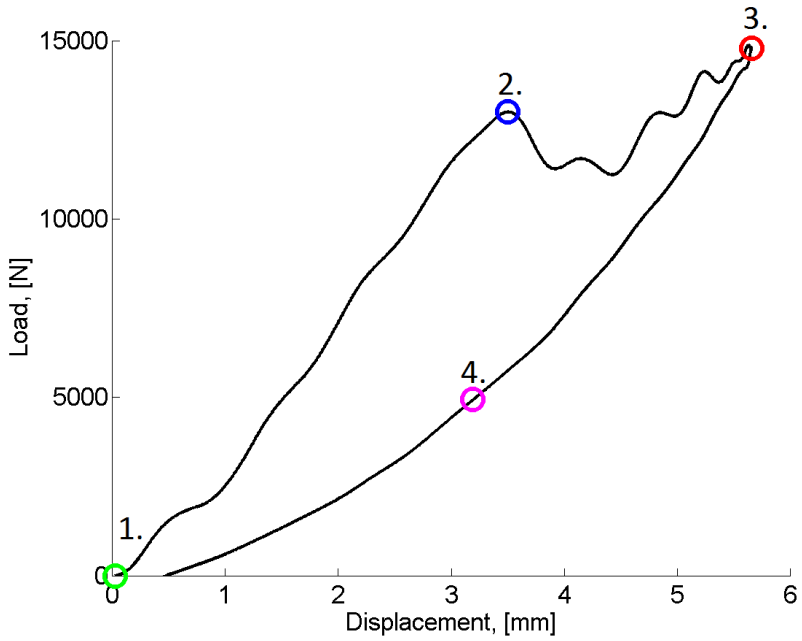

Figure 78: Four important points were investigated throughout the impact event.

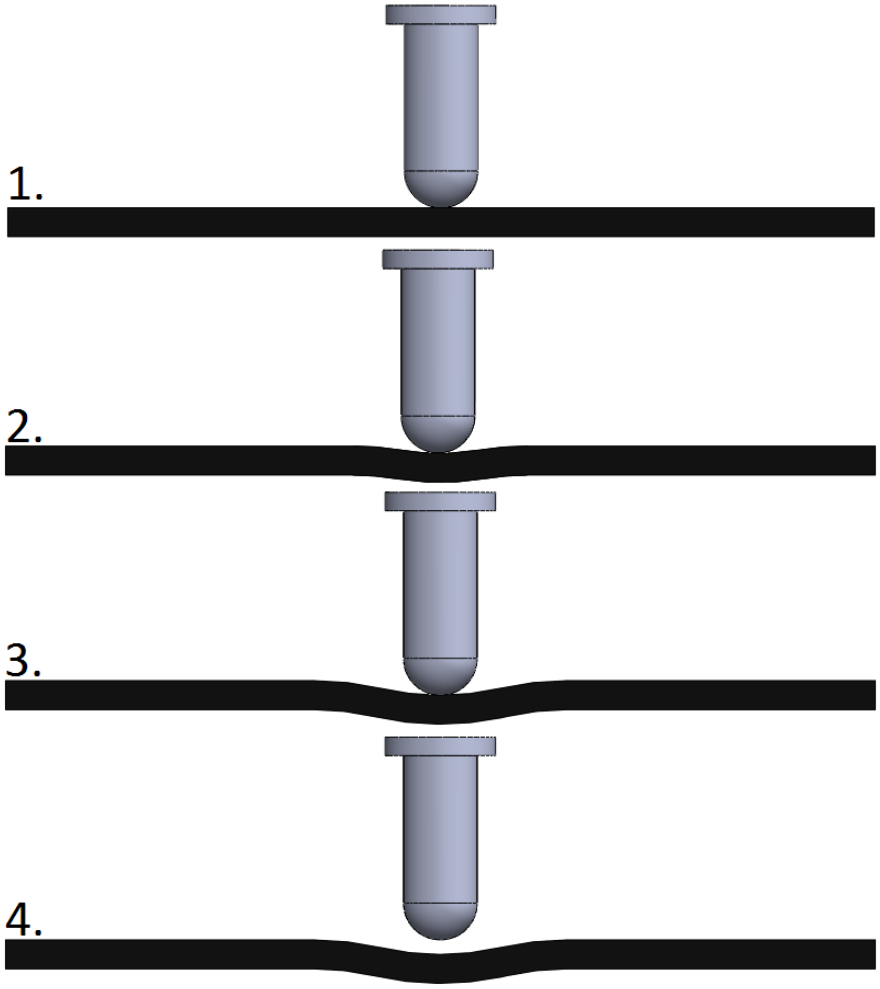

Figure 79: Four important points were investigated throughout the impact event, corresponding to the points on the load-displacement response in the figure above.

Data collection begins as the impactor makes first contact with the specimen, shown by the green circle at point 1. The momentum and kinetic energy of the impactor causes deformation at the site of impact. The impactor continues to travel downward until it the load is too great for the specimen to support without damaging the material in the form of fiber breakage or ply delaminations. The first failure, shown by the blue circle at point 2, is the point where permanent has begun to accumulate. Once the load redistributes along broken fibers or delaminated plies, the specimen is able to support greater load. The momentum of the impactor, while decreasing, brings the impactor and the specimen to its maximum vertical

deflection, indiacted by the red circle at point 3. The specimen acts as a spring with stored elastic energy, forcing the impactor upward, off the part and through the velocity detector. The curved portion of the load-displacement response between points 3 and 4 is equivalent to a mass converting kinetic energy into potential energy by moving upward against gravity. It is important to note the load-displacement response shown in Figure 78 is of the impactor, not the specimen itself.

The load, strain, and absorbed energy at points 2 and 3 in Figure 78 were extracted to determine the effects of porosity. The first failure load and peak load for experiments 201-610 are shown in Tables 36 and 37. All values have units of N.

Table 36: Peak Load at Max Deflection, Load to First Failure, Samples 201-410

Sample	P_{ff}	$P_{max\delta}$	Sample	P_{ff}	$P_{max\delta}$	Sample	P_{ff}	$P_{max\delta}$
201	12996	14783	301	13551	14087	401	14113	13146
202	NA	NA	302	12583	13532	402	13822	13391
203	12286	14294	303	12600	12365	403	13918	12392
204	12247	14851	304	12630	13049	404	13490	11995

Table 37: Peak Load at Max Deflection, Load to First Failure, Samples 501-610

Sample	P_{ff}	$P_{max\delta}$	Sample	P_{ff}	$P_{max\delta}$
501	13947	12972	601	13917	12801
502	13879	13393	602	12885	12110
503	13432	14914	603	12784	11943
504	12638	12996	604	12898	13673

The values contained in Tables 36 and 37 were averaged and plotted as a function of porosity. Standard deviations were taken and used to calculate error bars to determine the spread of the recorded data. The resulting plots are shown in Figures 80 and 81.

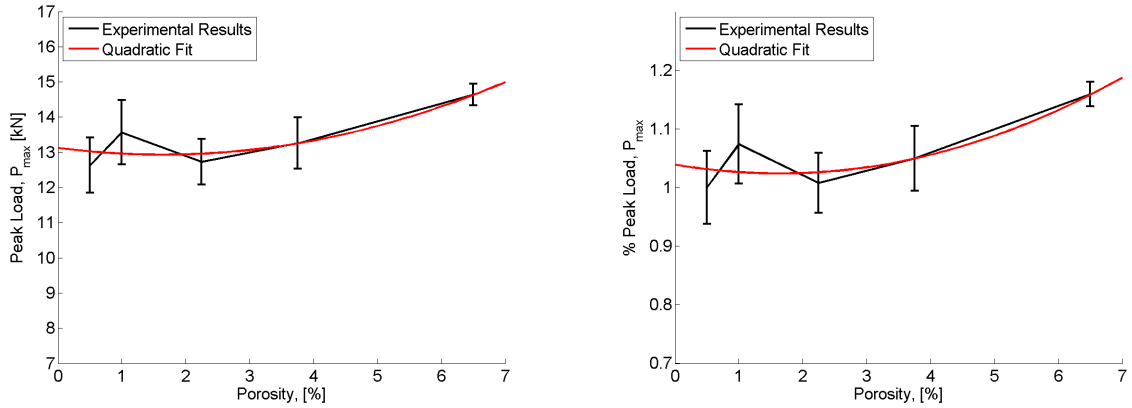

Figure 80: Peak load at maximum deflection was calculated as a function of porosity for all samples. A quadratic fit is shown by a red line.

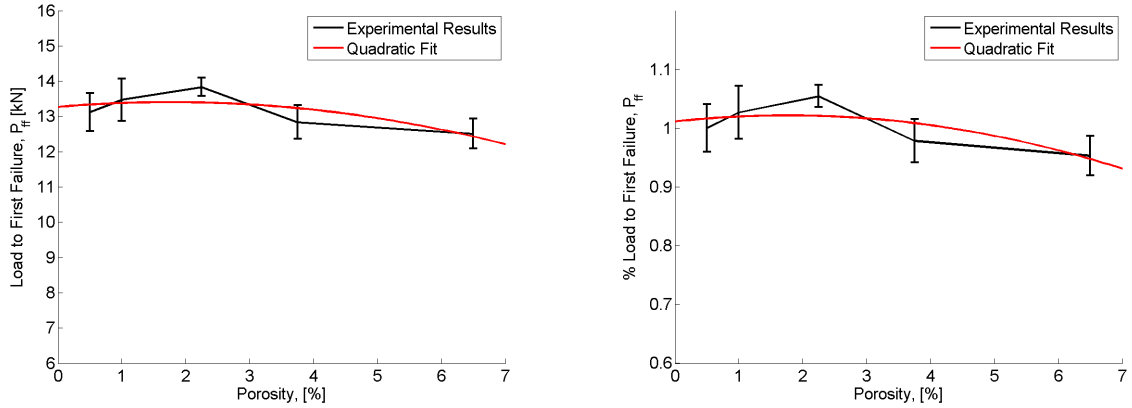

Figure 81: Load to first failure load was calculated as a function of porosity for all samples. A quadratic fit is shown by a red line.

It should be noted that $P_{max\delta}$ was defined as the load corresponding to the maximum deflection, not necessarily the maximum load seen during the experiment. For those specimens, the maximum load occurred at the first failure. Redistributing the load created residual stiffness, allowing the specimen to increase its load carrying capability, but not to a point greater than the first failure load. An example can be seen in Figure 82 for sample 501.

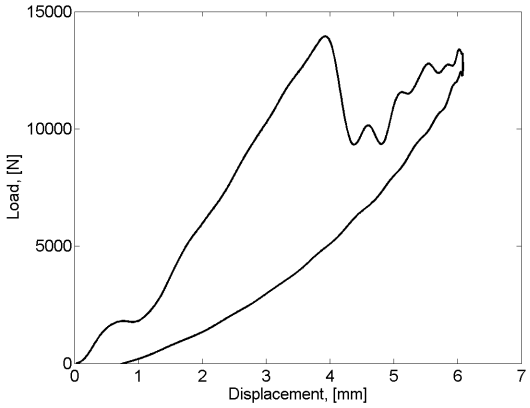

Figure 82: The load corresponding to the first failure was greater than the load at maximum deflection for sample 501.

As seen in Figure 80, peak load at maximum deflection slightly increases as porosity increases. Results indicate little to no change in samples with porosity $< 2\%$. Peak load to maximum deflection increased by 10% with a composite containing approximately 7% porosity. Load to first failure, shown in Figure 81, remained nearly constant with increasing porosity. The curved quadratic fit can be replaced with a constant, horizontal line and nearly fall within all error bars.

Strain to first failure and strain to maximum displacement was calculated for each experiment and the results are given in Tables 38 and 39.

Table 38: Strain, Flat Tup, Samples 201-410

Sample	ε_{ff}	$\varepsilon_{max\delta}$	Sample	ε_{ff}	$\varepsilon_{max\delta}$	Sample	ε_{ff}	$\varepsilon_{max\delta}$
201	0.703	1.1373	301	0.801	1.220	401	0.838	1.241
202	NA	NA	302	0.774	1.258	402	0.813	1.243
203	0.7183	1.1694	303	0.794	1.299	403	0.836	1.264
204	0.7095	1.1577	304	0.812	1.287	404	0.835	1.299

Table 39: Strain, Flat Tup, Samples 501-610

Sample	ε_{ff}	$\varepsilon_{max\delta}$	Sample	ε_{ff}	$\varepsilon_{max\delta}$
501	0.846	1.3117	601	0.845	1.286
502	0.911	1.3422	602	0.823	1.333
503	0.876	1.299	603	0.832	1.349
504	0.828	1.3409	604	0.846	1.326

The values contained in Tables 38 and 39 were averaged and plotted as a function of porosity. Standard deviations were taken and used to calculate error bars to determine the spread of the calculated and recorded data. The resulting plots are shown in Figures 83 and 84.

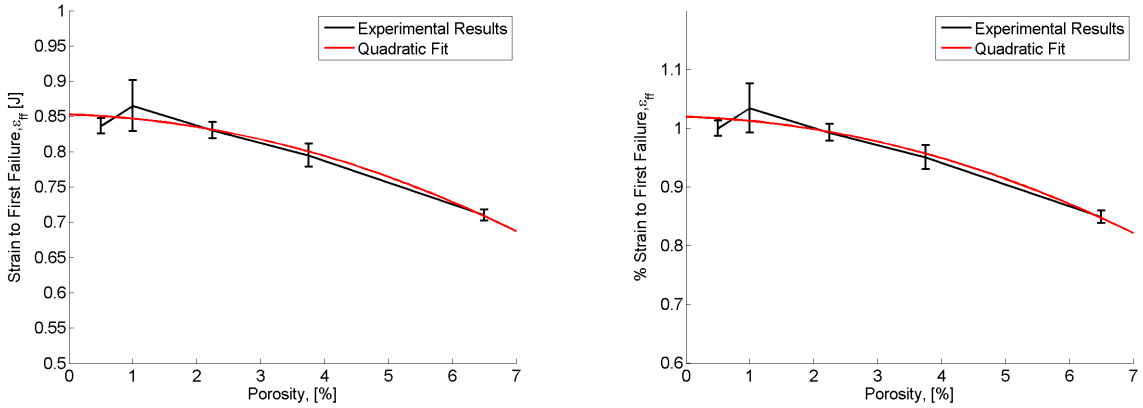

Figure 83: Strain to first failure was calculated as a function of porosity for all samples. A quadratic fit is shown by a red line.

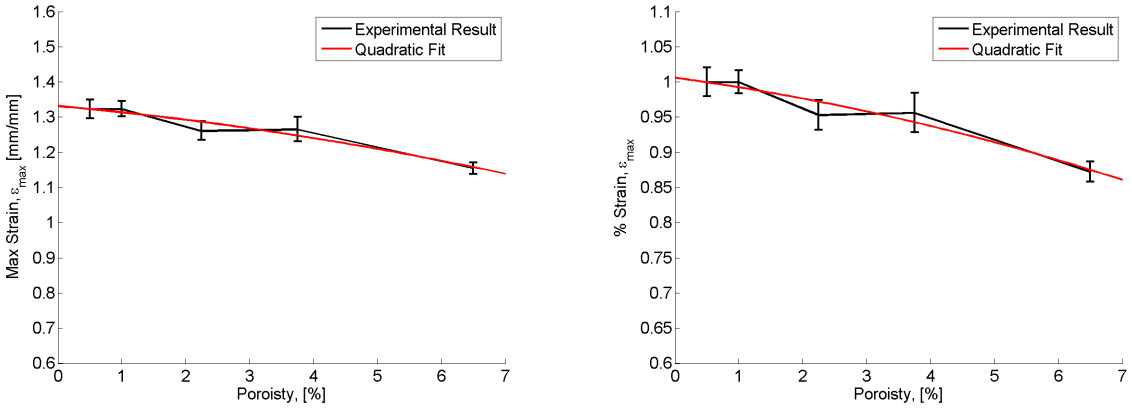

Figure 84: Maximum strain was calculated as a function of porosity for all samples. A quadratic fit is shown by a red line.

Strain to first failure and strain to maximum displacement both decreased as a function of increasing porosity. Similar to the trends for absorbed energy, load to first failure, and load to maximum displacement, strain remained nearly constant for porosity concentrations less than 2%. For porosity concentrations greater than 2%, strain decreased nearly linearly until reaching approximately a 10% reduction for porosity concentrations equal to 7%. For simplicity, the quadratic fit could be replaced with a linear fit, reducing the complexity of the empirical relationship without compromising much accuracy.

Absorbed energy is calculated by integrating the load-displacement curve, using the same algorithm implemented during flexure and shear testing. An example energy-displacement curve is shown for reference in Figure 85.

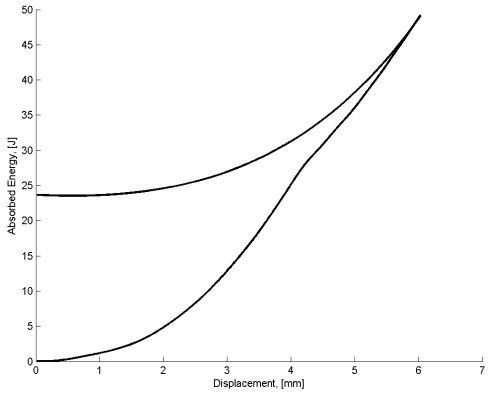

Figure 85: Absorbed energy was calculated by integrating the load-displacement curve.

Since absorbed energy is calculated by integrating load with respect to displacement, the graph shown in Figure 85 is a running total of the absorbed energy at each point. Therefore, the total energy absorbed during the impact event is the last point on the graph. The impact event begins and ends when displacment = 0, creating a cyclic graph when plotted as a function of displacement. Starting at the origin, the absorbed energy increases quadratically until it reaches 50 J, or the total impact energy. Energy accumulation ends when the impactor's kinetic energy reaches zero, and decreases as it moves upward. If the specimen behaved like a perfectly elastic spring, the absorbed energy would increase and decrease along the same curve, ending with no energy absorption. Conversely, if the impactor completely penetrated through the specimen, the event would end with full energy absorption. The difference between the impact energy and the final energy is the amount of energy absorbed by the specimen. This energy is to deform the specimen in the form of broken fibers are broken ply delaminations. Any kinks in the energy-displacement curve can be attributed to sudden decreases in load, caused by sudden fiber failure or delaminations.

Absorbed energy and strain to the first failure and peak load at maximum displacement were also calculated. Results from all experiments for absorbed energy to the first failure and peak load at maximum displacement were tabulated in Tables 40 and 41. All values

have units J.

Table 40: Absorbed Energy, Samples 201-410

Sample	E_{ff}	$E_{max\delta}$	Sample	E_{ff}	$E_{max\delta}$	Sample	E_{ff}	$E_{max\delta}$
201	21.70	49.03	301	23.91	49.23	401	25.30	49.45
202	NA	NA	302	20.18	49.28	402	24.07	49.43
203	20.26	48.72	303	20.32	49.23	403	24.41	49.22
204	20.26	49.21	304	20.88	49.28	404	23.07	49.30

Table 41: Absorbed Energy, Flat Tup, Samples 501-610

Sample	E_{ff}	$E_{max\delta}$	Sample	E_{ff}	$E_{max\delta}$
501	24.39	49.17	601	24.63	49.23
502	24.62	49.52	602	21.08	49.34
503	23.73	49.22	603	20.83	49.06
504	20.12	49.34	604	21.42	49.21

The values contained in Tables 40 and 41 were averaged and plotted as a function of porosity. Standard deviations were taken and used to calculate error bars to determine the spread of the calculated and recorded data. The resulting plots are shown in Figures 86.

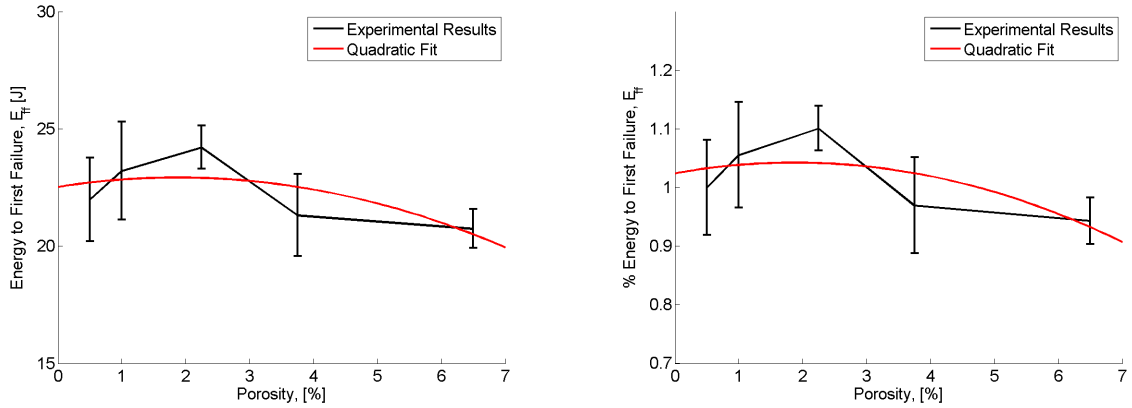

Figure 86: Absorbed energy to first failure was calculated as a function of porosity for all samples. A quadratic fit is shown by a red line.

Based on the relationship between energy to first failure and porosity in Figure 86, there appears to be an ideal porosity concentration to maximize the amount of absorbed energy to first failure at approximately 2%. Again, the increasing trend seen with porosity concentrations below 2% can be replaced with a constant, unchanging line. For composites with porosity greater than 2%, a decreasing, concave up curve can be used to create empirical relationships. There is only a 5% decrease in absorbed energy to first failure for samples with 7% porosity.

Absorbed energy to maximum displacement was not averaged and plotted as a function of porosity because it is equivalent to the impact energy, a set parameter. All energy values are approximately 50 or 30 J (depending on tup geometry), indicating the drop height was calculated correctly using conservation of energy principles.

Total absorbed energy was calculated for each experiment. The final value of the energy-displacement response was extracted and tabulated in Tables 42 and 43. Again, all tabulated results have units of J.

Table 42: Absorbed Energy, Flat Tup, Samples 201-410

Sample	E_{abs}	Sample	E_{abs}	Sample	E_{abs}
201	20.65	301	21.04	401	24.32
202	NA	302	23.23	402	22.66
203	20.41	303	25.37	403	25.33
204	19.40	304	23.84	404	26.23

Table 43: Absorbed Energy, Flat Tup, Samples 501-610

Sample	E_{abs}	Sample	E_{abs}
501	24.85	601	23.70
502	24.83	602	25.61
503	23.47	603	25.44
504	23.74	604	21.75

The values contained in Tables 40 and 41 were averaged and plotted as a function of porosity. Standard deviations were taken and used to calculate error bars to determine the spread of the calculated and recorded data. The resulting plots are shown in Figures 87.

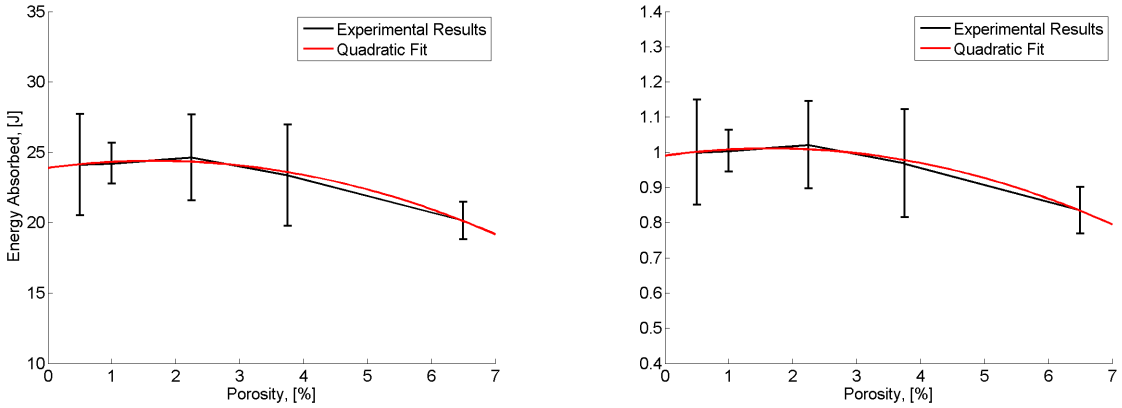

Figure 87: Absorbed energy was calculated as a function of porosity for all samples. A quadratic fit is shown by a red line.

Continuing with the same trend, total absorbed energy remained constant for specimens with porosity concentrations below 2%. For specimens with porosity concentrations greater than 2%, less energy was absorbed during each impact event. As absorbed energy increases, the amount of damage in the form of fiber failure and ply delaminations increases. From the results in Figure 87, low porosity samples should exhibit greater damage than low porosity samples. Subjecting the impacted specimens to ultrasonic, thermography, and X-ray computed tomography scanning produces visuals to characterize the internal damage imparted during the impact event.

Similar to flexure testing, stiffness and residual stiffness were calculated for impacted samples. Figure 88 shows the points used to calculate stiffness and residual stiffness.

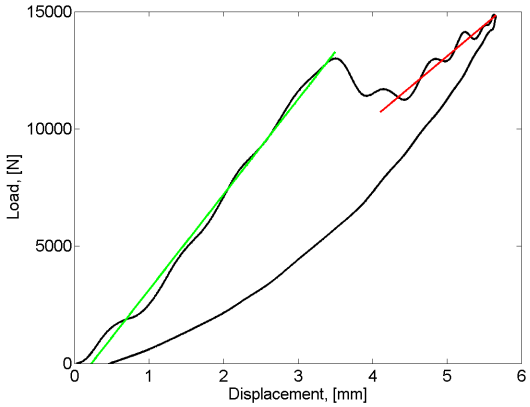

Figure 88: Stiffness (green) and residual stiffness (red) were determined by calculating the slope of a linear lines for the initial and residual load carrying capability.

Stiffness and residual stiffness were calculated for all experiments. The results were tabulated and shown in Tables 44, 45 and 46. All values have the units N/mm.

Table 44: Flat Tup Residual Stiffness, Samples 201-310

Sample	K_1	K_r	% Red	Sample	K_1	K_r	% Red
201	4056	2652	65%	301	3823	2063	54%
202	N/A	N/A	N/A	302	3659	3253	89%
203	3814	1750	46%	303	3589	2574	72%
204	3849	1781	46%	304	3551	3121	88%

Table 45: Flat Tup Residual Stiffness, Samples 401-510

Sample	K_1	K_r	% Red	Sample	K_1	K_r	% Red
401	3871	2079	54%	501	3809	2431	64%
402	3869	2223	57%	502	3542	NA	NA
403	3840	2543	66%	503	3649	2419	66%
404	3709	2380	64%	504	3479	1890	54%

Table 46: Flat Tup Residual Stiffness, Samples 601-610

Sample	K_1	K_r	% Red
601	3797	2599	68%
602	3596	2410	67%
603	3565	3257	91%
604	3501	1536	44%

The values contained in Tables 44, 45, and 46 were averaged and plotted as a function of porosity. Standard deviations were taken and used to calculate error bars to determine the spread of the calculated and recorded data. The resulting plots are shown in Figures 89.

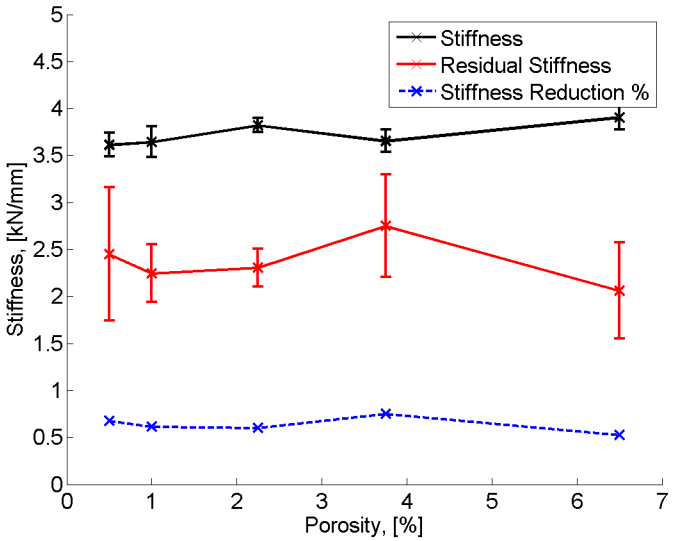

Figure 89: Stiffness (black) and residual stiffness after first failure (red) were measured as a function of porosity. The blue line represents the reduction in stiffness after first failure.

As shown in Figure 89, stiffness slightly increases but residual stiffness decreases as porosity increases. Beyond 4% porosity, the reduction in stiffness decreases from approximately 60% to 50%. Porosity had a minimal effect on the stiffness and residual stiffness throughout both flexure (Figure 54) and impact testing.

Impulse is defined as the integral of the magnitude of the applied force with respect to time for a non constant force. The load applied by the momentum of the impactor causes acceleration of the specimen and impactor while the two are in contact. Impulse is a vector quantity which quantifies the change in momentum of the impactor. Impulse was calculated for each experiment and the results were tabulated in Tables 47 and 48. All tabulated values have units N s.

Table 47: Total Impulse, Flat Tup, Samples 201-410

Sample	J	Sample	J	Sample	J
201	40.58	301	40.56	401	39.66
202	NA	302	39.90	402	40.14
203	40.48	303	39.17	403	39.16
204	41.07	304	39.68	404	38.90

Table 48: Total Impulse, Flat Tup, Samples 501-610

Sample	J	Sample	J
501	39.33	601	39.73
502	39.53	602	39.17
503	39.77	603	39.06
504	39.75	604	40.35

The values contained in Tables 47 and 48 were averaged and plotted as a function of porosity. Standard deviations were taken and used to calculate error bars to determine the spread of the calculated and recorded data. The resulting plots are shown in Figures 90.

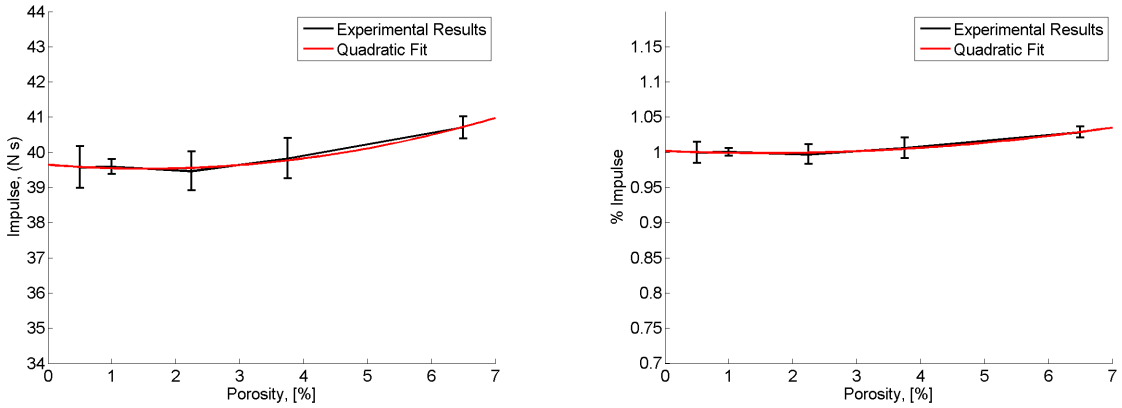

Figure 90: Impulse was calculated as a function of porosity for all samples. A quadratic fit is shown by a red line.

As seen in Figure 90, impulse slightly increases with increasing porosity beyond porosity concentrations greater than 4%. However, the increase is minimal, less than 5%. As shown in Figure 80, load to maximum deflection increases with increasing porosity, however the total impact duration decreases with increasing porosity. This creates a minimal change in total impulse throughout the impact event, indicating impulse is not greatly influenced by porosity concentration.

As the impactor travels downard toward the specimen, potential energy is transferred into kinetic energy. Once the impactor makes contact with the specimen, kinetic energy is transferred into elastic energy. The specimen builds up elastic energy until the impactor comes to rest. A fraction of the elastic energy is released in the form of fiber failure and ply delaminations. The remaining elastic energy is used to propel the impactor upward, similar to a trampoline. The impactor accelerates vertically until it is caught by the pneumatic rebound brakes. The velocity-time curve is calculated by integrating the force balance equation once, as shown in Eq (28). A representative velocity-time response for a high and low porosity sample is shown in Figure 91.

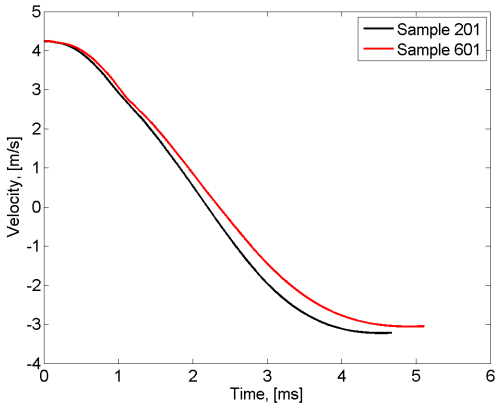

Figure 91: Velocity as a function of time was calculated by integrating a force balance with respect to time, shown for a high porosity sample (6.5%, black line) and a low porosity sample (<1%, red line).

The rebound velocity of the impactor was defined as the velocity of the impactor as it passed through the $\delta = 0$ datum after impact. The velocity-time response for each experiment was calculated and tabulated in Tables 49 and 50. All values are in units m/s.

Table 49: Rebound Velocity, Flat Tup, Samples 201-410

Sample	v_{reb}	Sample	v_{reb}	Sample	v_{reb}
201	3.223	301	3.212	401	3.036
202	NA	302	3.090	402	3.129
203	3.219	303	2.959	403	2.957
204	3.303	304	3.057	404	2.908

Table 50: Rebound Velocity, Flat Tup, Samples 501-610

Sample	v_{reb}	Sample	v_{reb}
501	2.986	601	3.057
502	3.010	602	2.945
503	3.074	603	2.942
504	3.066	604	3.175

The values contained in Tables 49 and 49 were averaged and plotted as a function of porosity. Standard deviations were taken and used to calculate error bars to determine the spread of the calculated and recorded data. The resulting plots are shown in Figures 92.

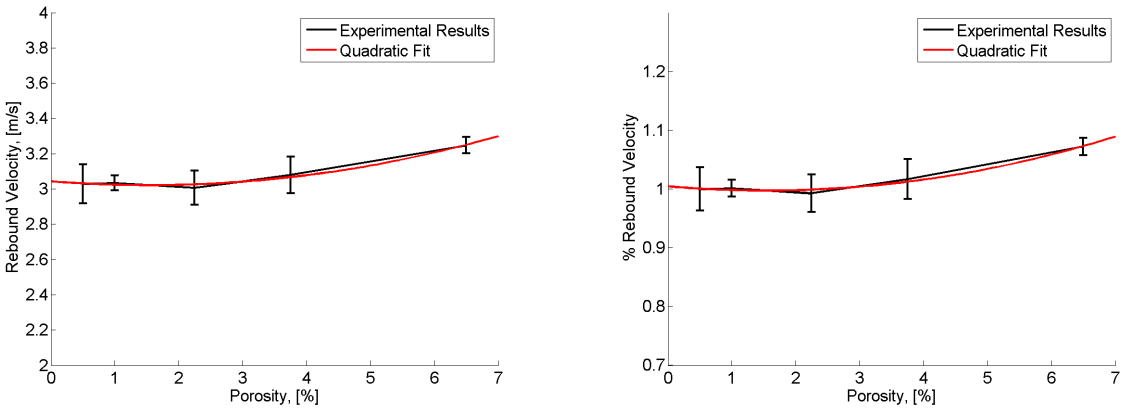

Figure 92: Rebound velocity was calculated as a function of porosity for all samples. A quadratic fit is shown by a red line.

Rebound velocity slightly increases as porosity increases once the porosity concentration reaches approximately 4%. The increase is minimal; rebound velocity of high porosity samples is only 5% greater than rebound velocity of low porosity samples. Rebound velocity is marginally affected by porosity concentration.

5.4.3.2 Hemispherical Tup

Impact testing was also conducted using a hemispherical tup on the impactor, shown in Figure 93 below.

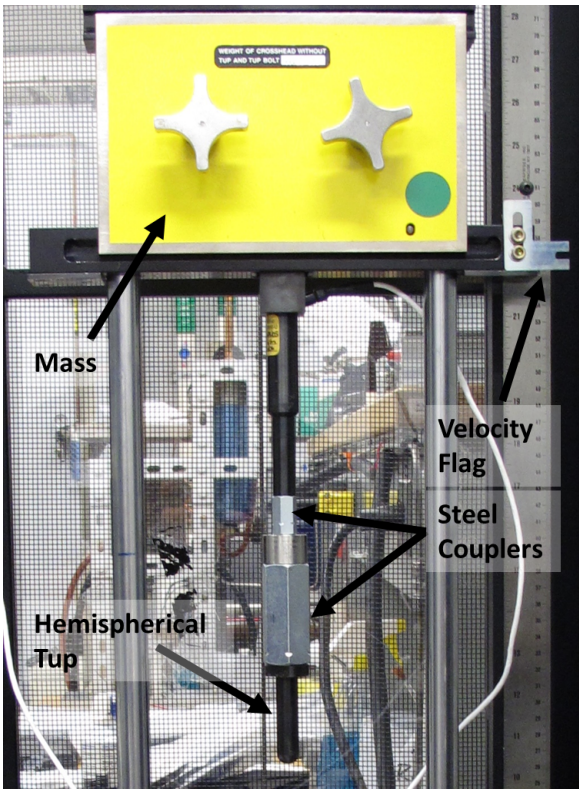

Figure 93: The hemispherical tup was connected to the load cell using two steel couplers.

Trial runs were conducted to determine the appropriate drop height to match the level of damage from flat tup impact events. Due to the sharper tup, the drop height was reduced, lowering the impact energy from 50 J to 30 J. Samples impacted with the flat and hemispherical tup cannot be directly related due to a difference in impact energy, however comparisons can be made between each group.

With a drop height set to induce a 30 J impact, porosity panels were subjected to impact events to determine the effect of porosity on specific impact parameters. Figure 94 shows a typical load-time response from an impacted sample.

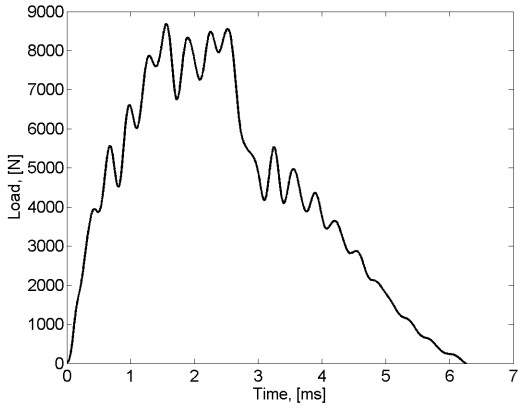

Figure 94: The load-time response for hemispherical tup impacted samples was riddled with load oscillations.

Clearly, the load-time response for each sample looks dramatically different than those from flat tup impacted samples. Literary research indicate the source of the oscillations is due to resonance vibrations in the impactor. Once the impactor contacts the sample, vibrations travel up and down the tup, passing through the load cell. The path between the tup and the load cell is greater and travels through several different materials such as plain steel and stainless steel couplers for the hemispherical tup, possibly inducing resonance vibrations that show up in the data in the form of oscillations. The constant periodicity of the oscillations indicate they are caused by vibrations and are not caused by breakage and redistribution of load in the impact sample. The vibrations add unwanted noise to load data, and were removed with statistical techniques. Figure 95 shows the load-time response with and without statistical techniques to remove unwanted oscillations.

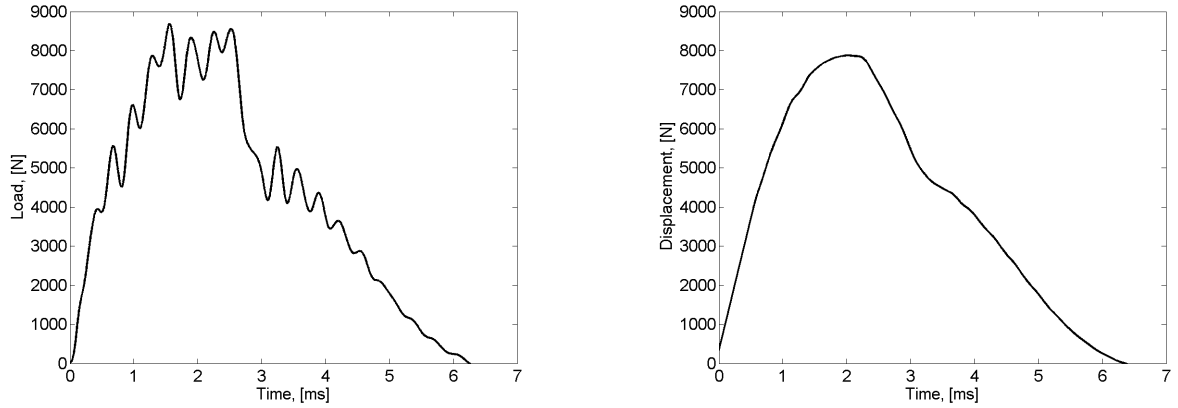

Figure 95: A simple moving algorithm was employed to remove unwanted oscillations from resonance vibrations between the load cell and the hemispherical tup.

The load-time response was integrated twice to produce the load-displacement response used to calculate all other mechanical properties. The raw and adjusted load-displacement curves for sample 210 are shown in Figure 96.

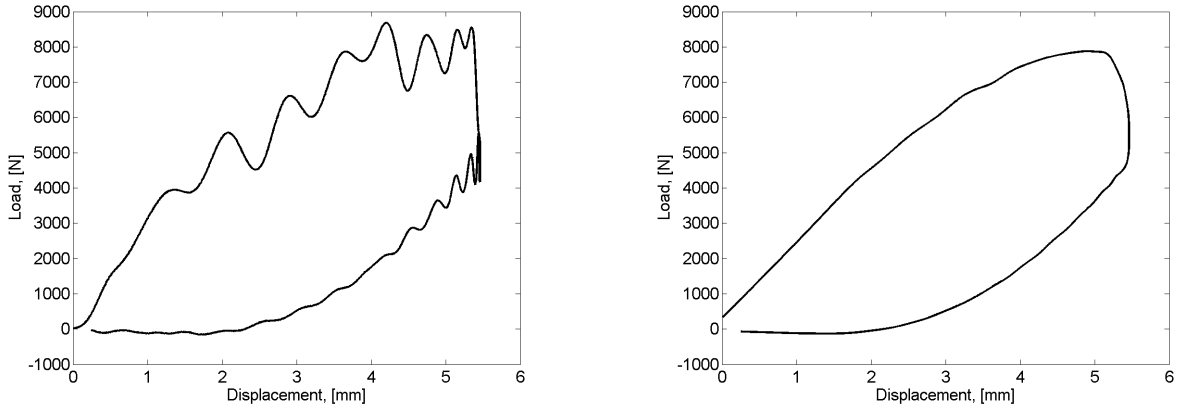

Figure 96: Load-time response was integrated twice to calculate the displacement as a function of load. A simple moving average algorithm was used to remove oscillations.

The results from the hemispherical tup impact events closely matched those from the flat tup impact events. With a sharper tup geometry, damage was more localized when impacted with the hemispherical tup. There was no distinctive first failure damage, clearly seen in the

load-time response of flat tup impact events. Thus, load, strain, and energy to first failure load were not calculated for hemispherical tup impact events.

To eliminate duplicate and repetitive graphs, all results from hemispherical tup impact events can be found in the conclusions.

5.4.4 Nondestructive Evaluation

Three nondestructive evaluation techniques were employed to visually inspect a representative impacted sample prior to compression after impact testing. Each sample was scanned using ultrasonic transmission, thermography, and X-ray computed tomography. The results are shown below.

5.4.4.1 Ultrasonic Transmission

Each panel was scanned using the Mistras UPK-T24 system with a 5 MHz transducer, an immersion tank capable of scanning samples up to 24" × 18", shown in Figure 97.

Figure 97: The immersion tank was used to conduct ultrasonic transmission testing, creating visuals of the damage incurred during impact.

Several transducers were used to determine the optimal image, ranging from 10 Mhz to 0.5 Mhz. A 5 MHz, 0.5" diameter transducer with a 2" focal length was used for all ultrasonic testing. A diagram outlining the concept behind ultrasonic transmission testing is shown in Figure 98.

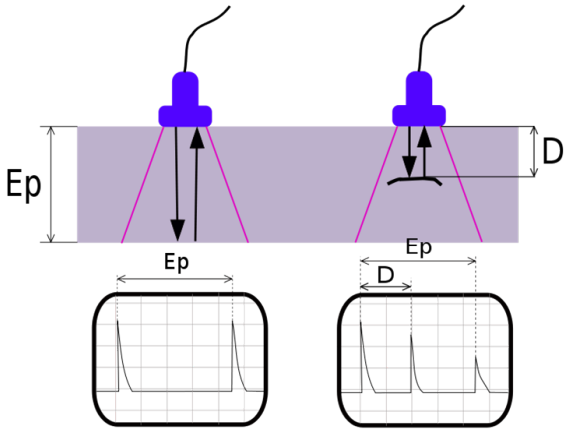

Figure 98: Ultrasonic pulses are sent through a material and the reflected signal is used to detect defects or flaws through the thickness.

The transducer sends an ultrasonic pulse through a material submerged in a tank of water. The signal reflects off back wall of the sample and picked up by the transducer, shown on the left of Figure 98. The time until the refelcted signal returns to the transducer, or time of flight, is directly proportional to thickness and density of the material. A defect in the material will cause the signal to return earlier than expected with back face amplitude loss, shown on the right of Figure 98. The transducer moves to the next point, sends a pulse, and records the reflection. An A-scan (shown in Figure 98) is created for each point scanned throughout the test. The maximum amplitude of the returned signal at each point is used to create a color map to show where amplitude losses occur in the sample, called a C-scan. By properly calibrating the scanning depth, it is easy to determine whether or not a sample has been damaged. An undamaged and damaged sample is shown in Figure 99.

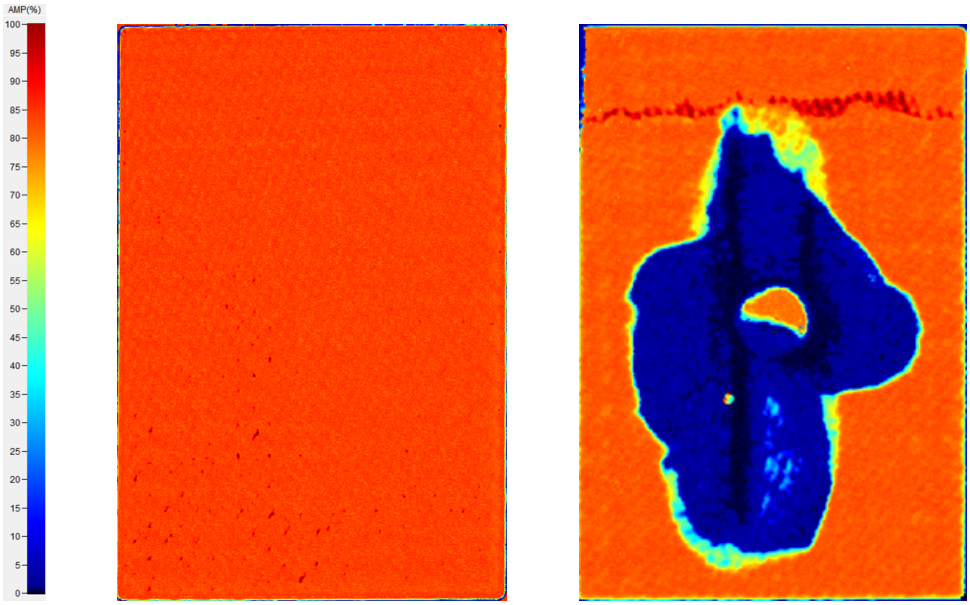

Figure 99: Undamaged samples have a 100% return signal (left), damaged samples have amplitude loss in areas of flaws (right).

With the transducer focused to the back wall, regions of red/orange correspond to full returned signal to the transducer after reflection off the back face. If the pulse fails to reach the back wall and return to the transducer with full amplitude, it is colored blue/yellow, depending on the strength of the return signal. By creating a color map of amplitude strengths, it is very easy to determine where the material is damaged. Figure 99 shows an undamaged and damaged control specimen with <1% porosity.

With the ultrasonic transmission scanning properly calibrated, all panels were scanned together to visually inspect the impact damage. One representative sample was scanned from each porosity concentration. C-scans from all six scans are shown in Figure 100 below.

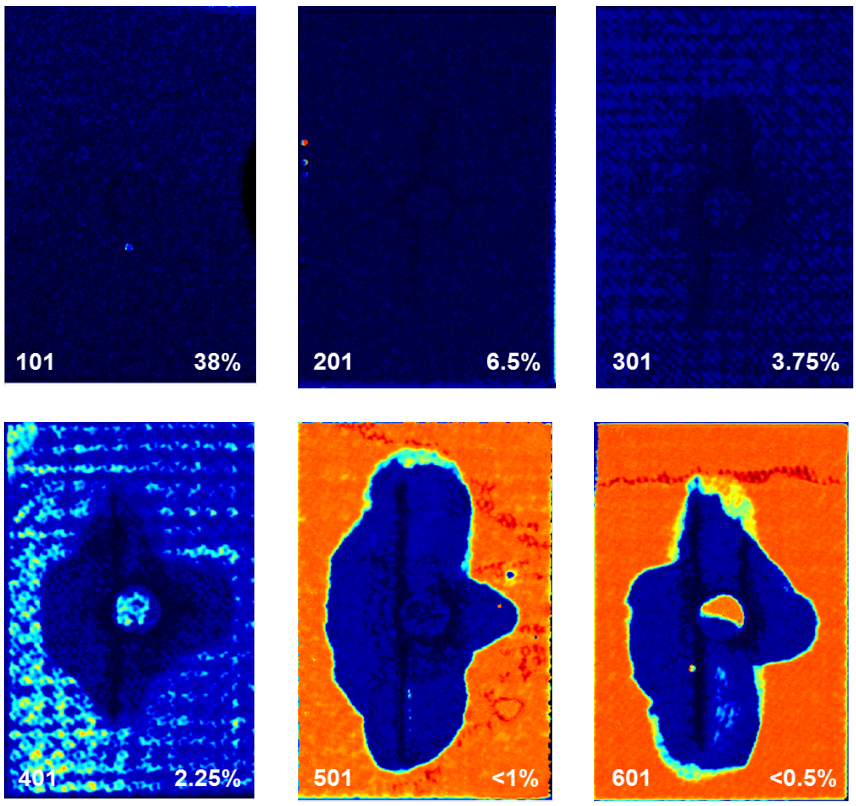

Figure 100: Ultrasonic transmission scanning with focus to the back wall. Red indicates full reflection/transmission, blue indicates no reflection/transmission.

The C-scans generated by focusing the transducer on the back wall indicate the reflected signal from samples 101-401 is not reaching the transducer. An imprint of the round, flat tup can clearly be seen in the center of all images. The poor transmission through samples 101-401 indicate the porosity concentration is too great for transmission in undamaged areas of the sample. This is undesirable since it is difficult to determine the extent of the damage during impact events for high porosity samples. Several different transducers were utilized to penetrate through the porosity and reach the back face, however none were powerful enough. Focusing the transducer to a point near the midplane of the sample would reduce the distance the pulse must travel to reflect off of delaminated plies within the sample. C-scans from the refocused scans are shown in Figure 101 below.

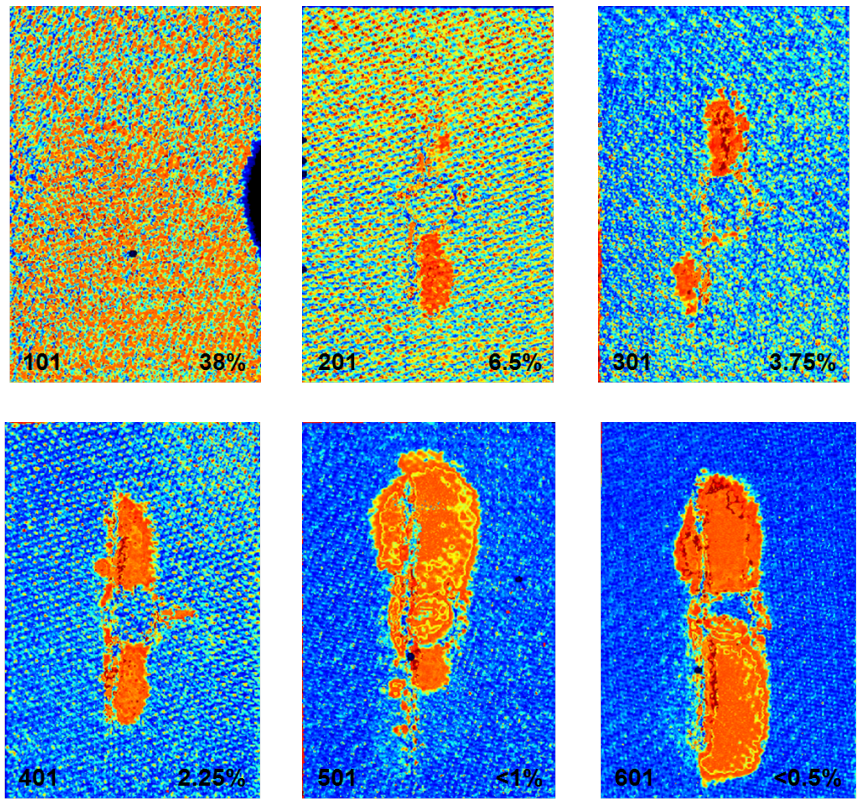

Figure 101: Ultrasonic transmission scanning with focus to the midplane. Red indicates full reflection/transmission, blue indicates no reflection/transmission.

By refocusing, or gating, the signal to the midplane, damage is visible in high porosity samples. By the C-scans in Figures 100 and 101, it is clear delamination area increases as porosity decreases. Thus, low porosity, pristine samples poses the greatest damage. This is in agreement with the energy absorption relationships found during impact testing, shown in Figure 87. The additional absorbed energy went into breaking bonds between plies, creating greater delamination area.

A common damage threshold used in the aerospace industry is at -6dB. The color map was adjusted to 2-bit, and generated the following C-scans, shown in Figure 102.

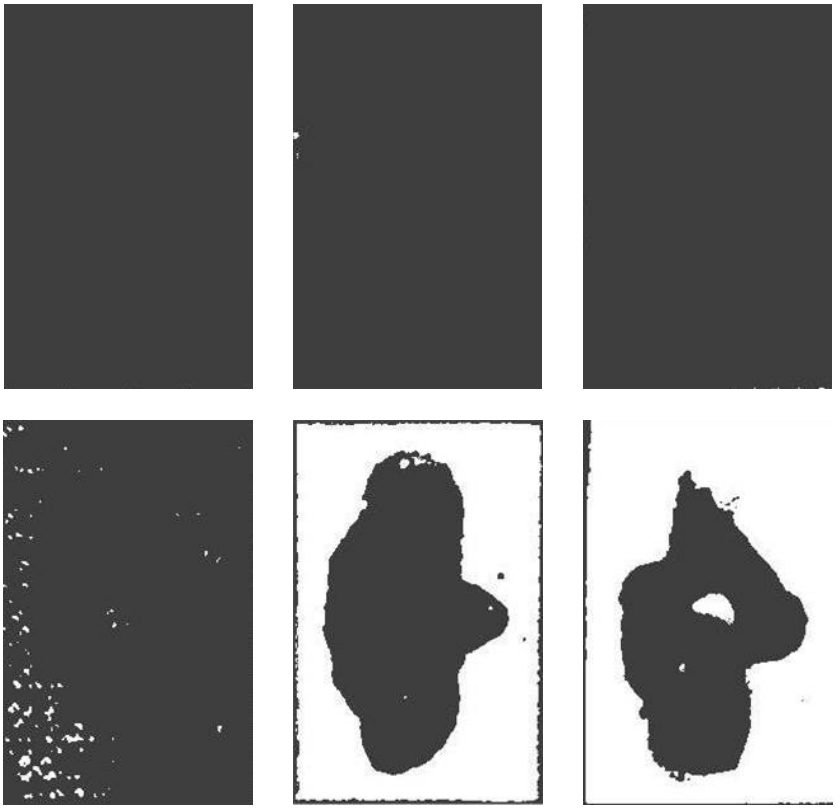

Figure 102: Ultrasonic transmission scanning with focus to the back face and threshold set to -6 dB. Light gray indicates full reflection/transmission, dark gray/black indicates no reflection/transmission.

The second gate was moved to the same position to focus the pulse to the midsurface. The resulting C-scans are shown in Figure 103.

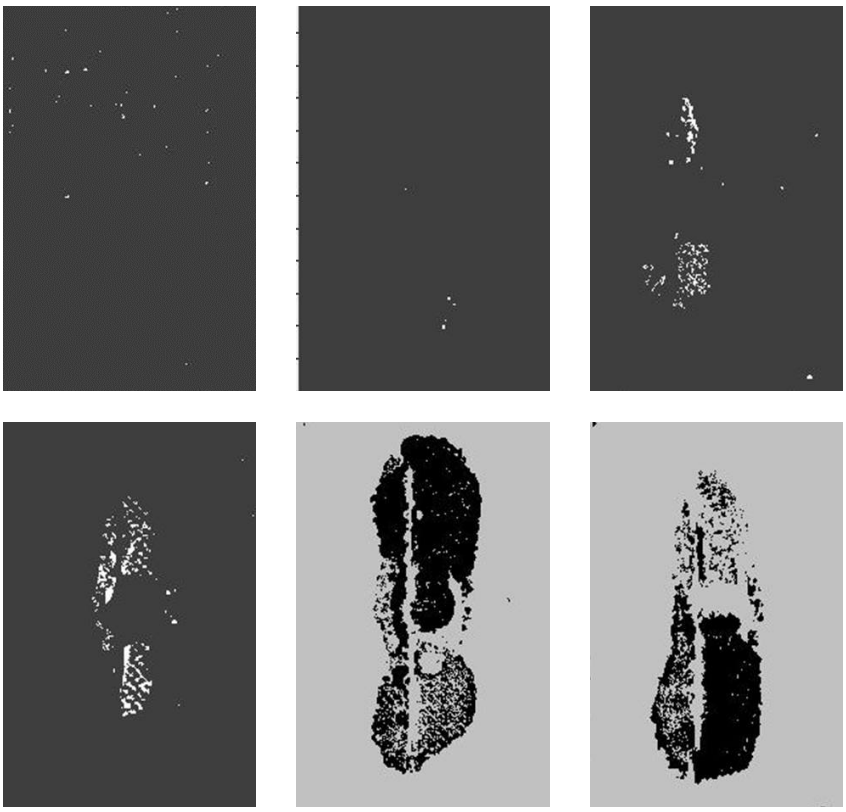

Figure 103: Ultrasonic transmission scanning with focus to the midplane and threshold set to -6 dB. White indicates full reflection/transmission, gray indicates no reflection/transmission.

The results of this study indicate ultrasonic transmission scanning does not accurately predict damage of panels with porosity concentrations greater than 2%. Ultrasonic transmission works exceptionally well characterizing the damage and delamination areas of very low porosity composite specimens. The pulse is unable to reach the back wall and reflect to the transducer for high porosity panels. Trapped air inside the panel scatters the ultrasonic pulse and prevents it from reflecting back into the transducer. Thus, ultrasonic transmission should only be used on low porosity composite panels. If the user is interested in the porosity concentration, a 5 MHz flat focus transducer is unable to reach the back face for composite panels with porosity concentrations greater than 1-2%. Thus, if a panel is scanned and the resulting C-scan shows no through transmission, the porosity concentration is greater than 2%. This detection threshold can be very useful when trying to quantify the quality of

composite parts.

5.4.4.2 Thermography

Each panel was thermally flashed and recorded using an infrared (IR) camera. Active Thermography (AT) uses a source to rapidly heat the surface of a part. IR cameras are used to watch as heat dissipates and the part cools. Delaminations heat and cool more quickly than undamaged areas, making it clearly visible which parts of a composite part are damaged. A schematic of the test setup used is shown in Figure 104.

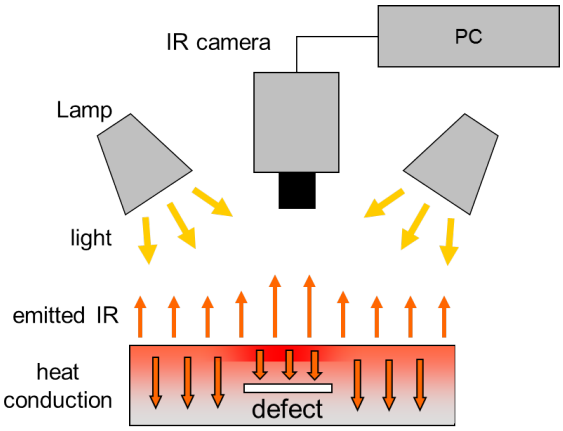

Figure 104: Each specimen was rapidly heated and recorded with an IR camera.

As time progresses, the heat flash moves through the thickness of the part. By recording the heat signature, the user has the ability to see the damage as it moves through the thickness. Areas of high temperature are shown as white, areas of low temperature are gray and black. Delaminations heat and cool faster than undamaged sections due to the reduced heat capacity of air with respect to the composite. Thus, damaged areas appear white, undamaged areas appear gray. An example of an undamaged and damaged sample is shown in Figure 105.

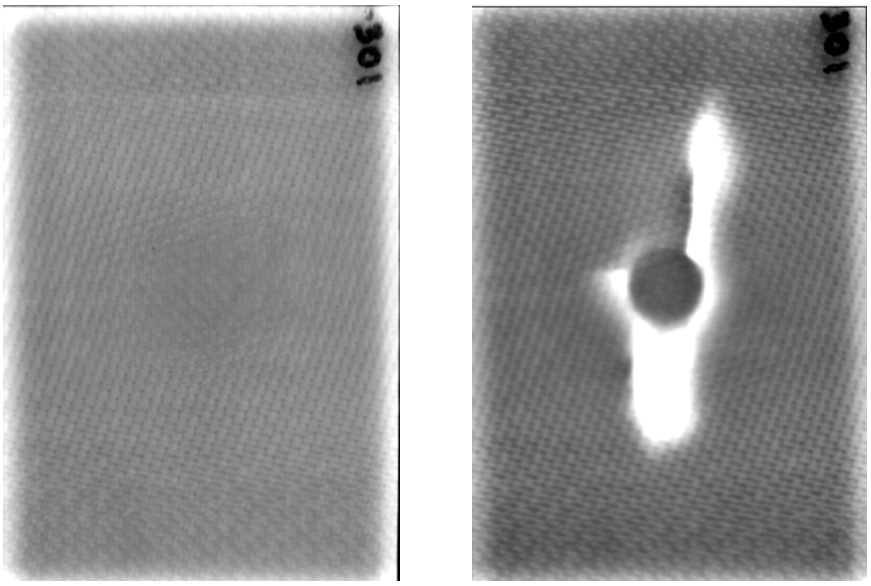

Figure 105: Damaged areas appear white (right) while undamaged areas appear gray(left) when flashed with a heat source and recorded with an IR camera.

For consistency, still images were extracted from each sample at the same time throughout the test. By dividing the total number of frames by the thickness of the specimen, an estimate for the depth of each image can be approximated. The following images shown in Figure 106 were taken from the midplane of the specimen.

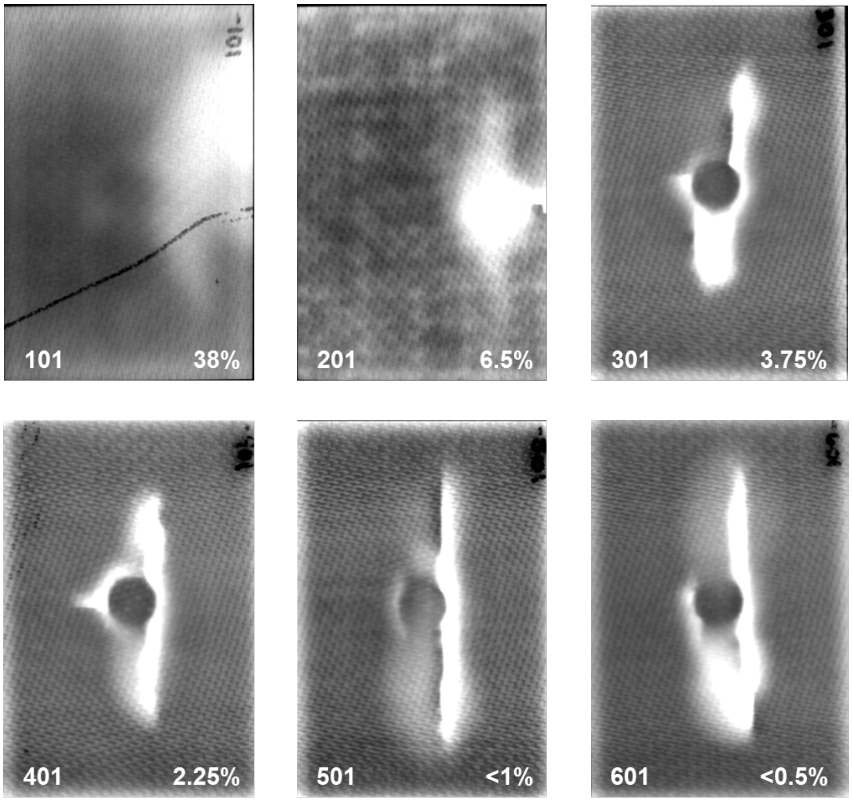

Figure 106: Still images were extracted corresponding to the midplane of each panel after pulsed with a heat source and recorded with an IR camera.

Similar to ultrasonic transmission scanning, thermography was unable to produce accurate visual representations of damaged high porosity composite panels. However, themrography captured damage in panels 301 and 401, where ultrasonic transmission scanning was unable to penetrate deep enough into the composite. The bright spots in on the right sides of samples 101 and 201 in Figure 106 is merely a reflection of the heat pulse, not delamanations in the composite. Due to the trapped pockets of air, thermography was unable to detect damage in composite samples with a porosity concentration greater than 4%. Unfortunately, pre-impacted high and low porosity samples looked identical when flashed and recorded with an IR camera, indicating thermography is unable to determine porosity concentration.

5.4.4.3 X-ray Computed Tomography

X-ray Computed Tomography (CT) was used as the final nondestructive evaluation technique to characterize impact damage of composite samples with various concentrations of porosity. The specimens were scanned using the setup parameters listed in Table 9 with the test setup shown in Figure 32. CT scanning allows the user to recreate a 3-dimensional image of the part with the ability to create cut planes throughout the model. An undamaged and damaged specimen are shown in Figure 107 for comparison.

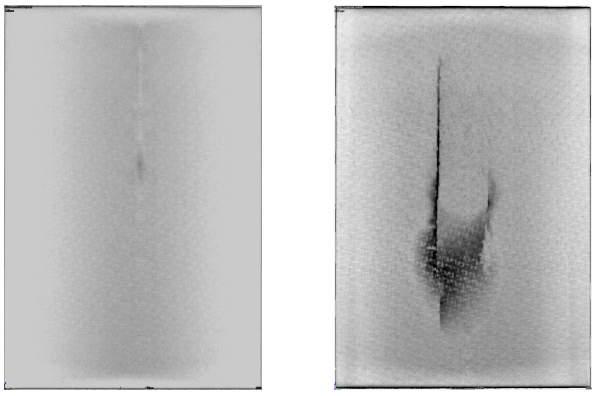

Figure 107: An undamaged (left) and damaged (right) impacted composite specimen scanned using X-ray computed tomorgraphy.

While it may be difficult to determine delamination area or the extend of the impact damage, it is very clear that damage is present. Images taken from a cut plane at the midsurface of the damaged composite panels are shown in Figure 108.

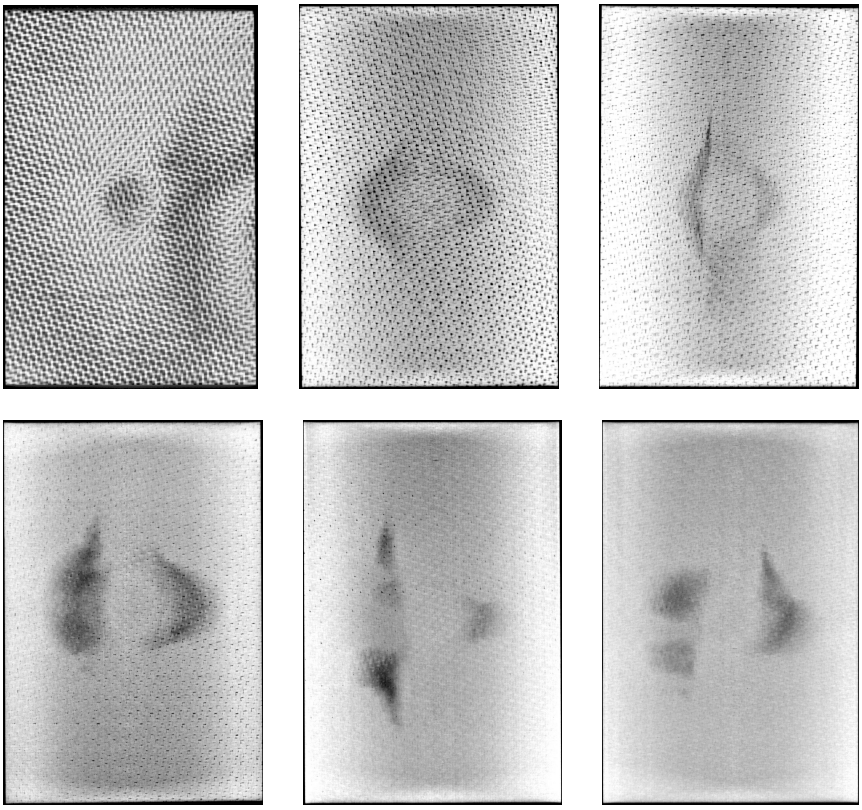

Figure 108: Still images were extracted corresponding to the midplane of each panel after CT scanning.

CT scanning characterized impact damage of all specimens, regardless of porosity concentration. The Defect Analysis Toolbox was used to estimate the porosity concentration by summing voxels with an intensity below a user specified threshold. While it is difficult to quantify the extent of delaminations, CT scanning excels in defect detection. CT scanning is able to detect cracks and flaws within a material. Longitudinal cracks were easily visible using CT scanning, shown in Figure 109.

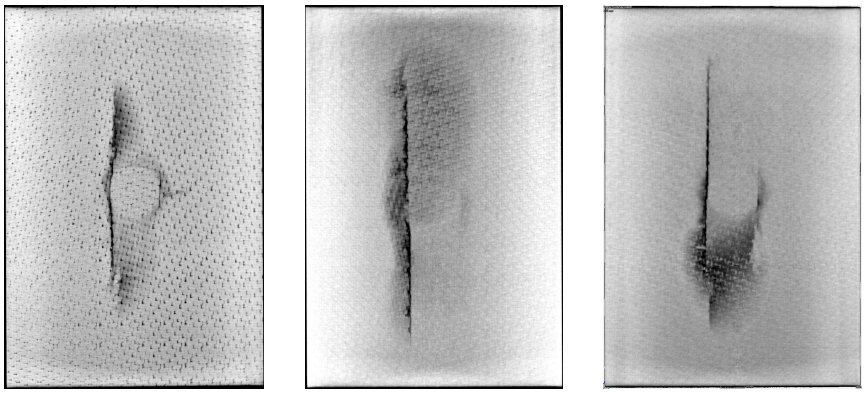

Figure 109: Cracks were easily discernible throughout the thickness of impacted composite sampless 401-601, left to right, using CT scanning.

The ability of CT scanning to characterize impact damage makes it an attractive method of nondestructive evaluation, however its expensive equipment, lengthy setup and test time, and technician expertise deem it less desirable.

5.4.5 Compression After Impact

Once impact testing was complete, all specimens were subjected to compression testing. Compression after impact testing was conducted to determine the residual strength properties after an impact event since delaminations greatly reduce the composites ability to withstand and transfer compressive loads. Under uniaxial compression, delamations can result in three types of buckling:

a Local Buckling

b Mixed-Mode Buckling

c Global Buckling

The specially designed compression after impact fixture utlizes knife edges, shown in Figure 110 to resist global buckling modes (b & c shown in Figure 111) while preserving a pinned boundary condition.

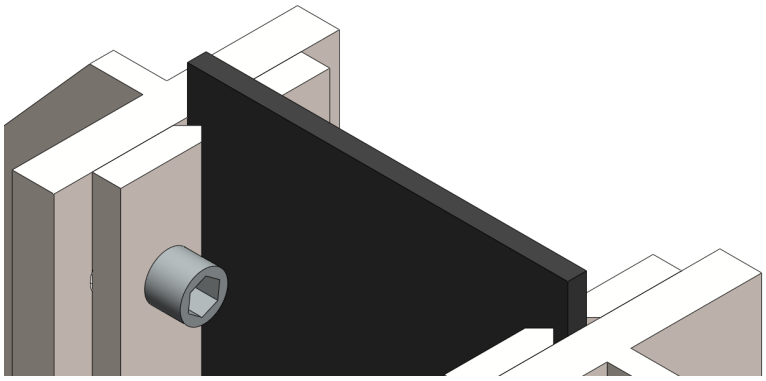

Figure 110: Knife edge supports eliminates global buckling modes during compression after impact testing.

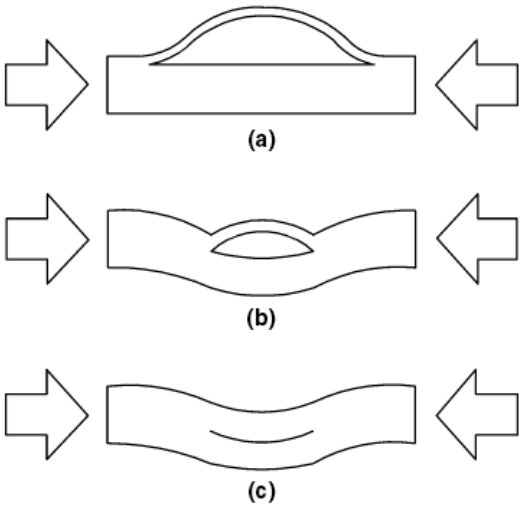

Figure 111: A laminate can buckle via local buckling (top), mixed-mode buckling (middle), or global buckling (bottom).

Each specimen was loaded into the compression after impact fixture and all bolts were torqued to 60 in-lbs. The fixture was loaded into the load frame and each test began with approximately 150N of compressive load applied. Although load and displacement were recorded, only load was utilized in all post processing. The measured displacement from the crosshead does not directly correlate to the displacement of the specimen due to the compliance of the load frame itself. With maximum loads approaching 100 kN, the compliance

of all components in the load frame must be considered. Since the crosshead displacement does not account for displacements and deformations of the internal components of the load frame, crosshead displacement was recorded but not used in calculations. Thus, only peak load was measured and used for post processing. The crosshead moved vertically at a rate of 1.25 mm/min until the instantaneous load reached 20% of the peak load. Samples xx1 were not subjected to compression after impact testing in order to examine impacted specimens using ultrasonic transmission, themrography, and X-ray computed tomography.

Figure 112 shows a representative high porosity (6.5%) and low porosity (<1%) sample at failure.

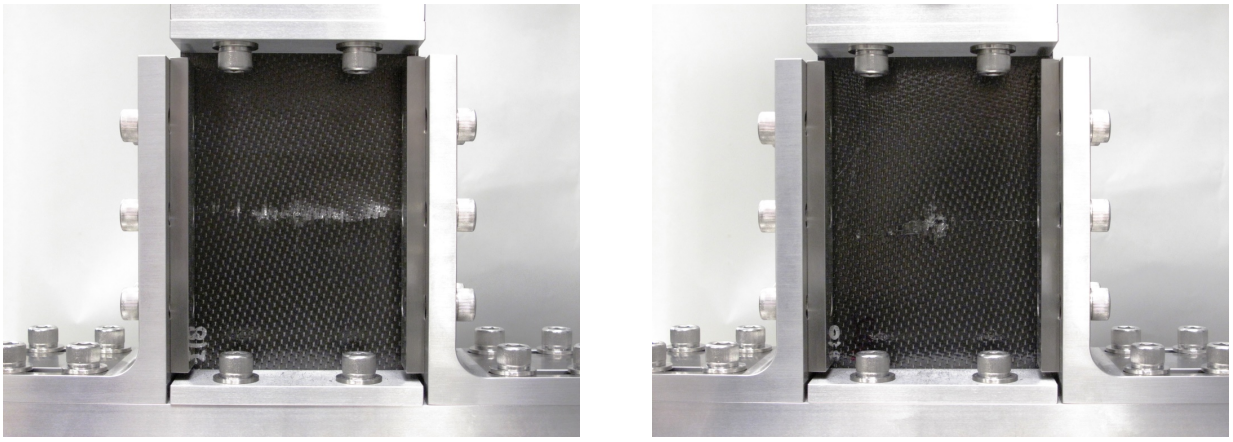

Figure 112: High (left) and low (right) porosity samples at failure when subjected to compression after impact testing.

Peak load and ultimate compressive strength for flat and hemispherical impacted experiments were recorded and tabulated in Tables 51 and 52 below. All values tabulated loads are in units kN and stress are in units MPa respectively.

Table 51: Compression After Impact, Flat Tup, Samples 201-404

Sample	P_{max}	F_{cu}	Sample	P_{max}	F_{cu}	Sample	P_{max}	F_{cu}
201	NA	NA	301	NA	NA	401	NA	NA
202	NA	NA	302	62.51	125.6	402	64.02	129.6
203	64.00	124.5	303	79.94	161.4	403	79.81	163.8
204	72.60	141.2	304	81.08	163.7	404	72.41	147.5

Table 52: Compression After Impact, Flat Tup, Samples 501-604

Sample	P_{max}	F_{cu}	Sample	P_{max}	F_{cu}
501	NA	NA	601	NA	NA
502	79.17	164.3	602	82.72	169.7
503	66.15	137.3	603	89.67	185.6
504	80.41	165.3	604	77.64	159.9

The values contained in Tables 49 and 49 were averaged and plotted as a function of porosity. Standard deviations were taken and used to calculate error bars to determine the spread of the calculated and recorded data. The resulting plots are shown in Figures 113 and 114.

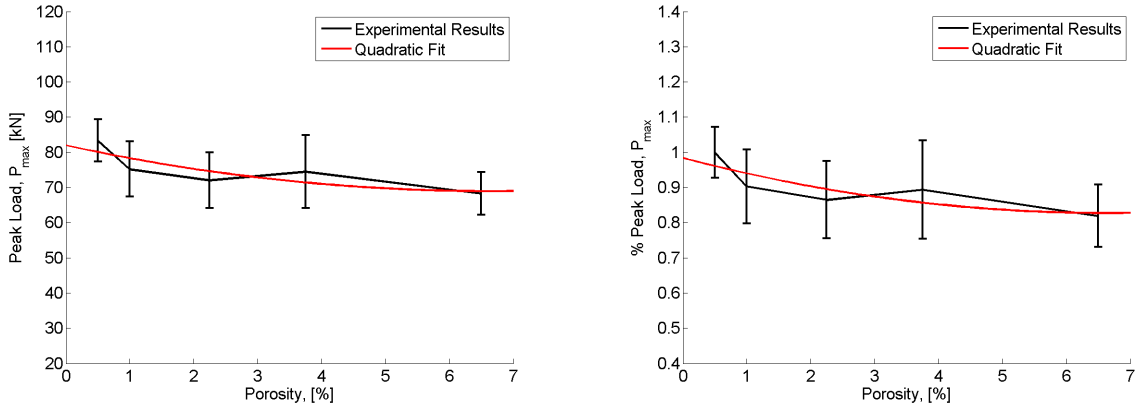

Figure 113: Peak load was calculated as a function of porosity for all samples. A quadratic fit is shown by a red line.

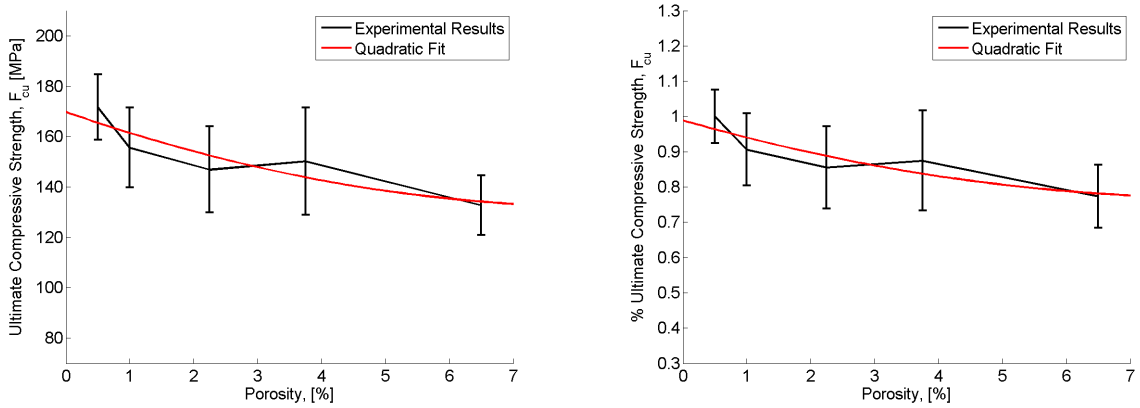

Figure 114: Ultimate compressive residual strength was calculated as a function of porosity for all samples. A quadratic fit is shown by a red line.

Since compressive residual strength is a function of peak load, it is expected that both yield the same trend. As expected and in agreement with all other mechanical testing, peak load decreases as porosity increases. At approximately 7% porosity, the ultimate compressive strength has been reduced by approximately 20%, a significant reduction that should not be ignored.

5.5 Summarized Results

The previous sections present several trends of mechanical strength properties with increasing porosity. The results from extreme porosity samples (38%) were omitted from discussion and trends due to the extreme differences in results; a nonlinear stress-strain relationship prevented accurate and meaningful comparisons. Due to the obvious physical differences, it is highly unlikely that one could falsely identify the extreme porosity laminate for a less porous laminate. The exclusion of the extreme porosity laminate led to general increasing or decreasing trends of mechanical strength properties with respect to increasing porosity.

Summarized results for flexure testing are found in Table 53. The percentage change was determined by calculating the percent difference between high porosity (6.5%) and low porosity (less than 0.5%) laminates. A bilinear relationship was employed to accurately characterize the change in mechanical properties with increasing porosity. The threshold where porosity plays an influential role was found to be approximately 2.25%. Thus, the porosity spectrum was divided into two regions—one where laminates contain high porosity ($2.25\% \leq x \leq 6.5\%$) and one where laminates contain low porosity ($0.5\% \leq x \leq 2.25\%$). An example of a bilinear relationship with high and low porosity regions can be seen in Figure 115.

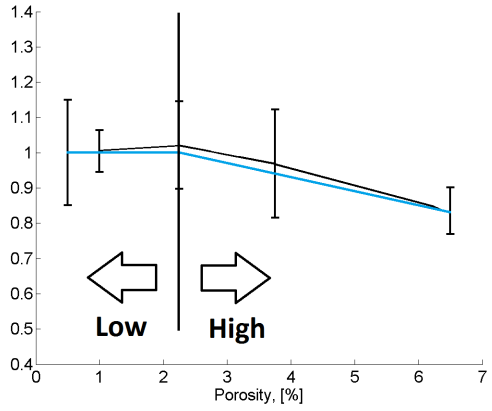

Figure 115: A bilinear relationship was calculated to characterize the affect of porosity on strength properties. The threshold between low and high porosity was approximately 2.25%.

The total percent difference between maximum and minimum porosity and percentage of increase or decrease for each percent porosity in each region of flexure testing are shown in Table 53.

Table 53: Flexure Mechanical Testing Summary

	$\%_d$	0.5% - 2.25%	2.25% - 6.5%
P_{max}	-15%	-2.31%	-2.31%
E_{11}	-8%	0.00%	-3.53%
E_{abs}	-20%	0.00%	-4.71%
ε_f	-60%	-5.33%	-11.29%

All flexural mechanical strength properties decreased with increasing porosity, as expected. Strain to first failure possessed the greatest reduction—approximately 60% for laminates containing 6.5% porosity. The quantities in column 3 of Table 53 indicate the minimal role porosity plays in strength reduction, however laminates with porosity concentrations greater than 2.25% possess dramatic reductions in all calculated strength properties. Structures subjected to flexural loads should not contain greater than 2% porosity.

The total percent difference between maximum and minimum porosity and percentage of increase or decrease for each percent porosity in each region of short-beam shear testing are shown in Table 54.

Table 54: Shear Mechanical Testing Summary

	$\%_d$	0.5% - 2.25%	2.25% - 6.5%
P_{max}	-15%	0.00%	-3.53%
ILSS	-17%	0.00%	-4.00%
E_{abs}	0%	0.00%	0.00%
ε_f	0%	0.00%	0.00%

Porosity provided no significant increase or decrease in absorbed energy and strain to failure during short-beam shear testing. Laminates with low porosity exhibited no change in maximum load, interlaminar shear strength, absorbed energy, or strain to failure. High porosity laminates featured maximum load and interlaminar shear strength reductions of approximately 3.5% and 4% per percent porosity. Structures subjected to shear loading should not contain greater than 2% porosity.

The total percent difference between maximum and minimum porosity and percentage of increase or decrease for each percent porosity in each region of drop-weight impact testing are shown in Table 55.

Table 55: Impact Mechanical Testing Summary

	Flat			Hemispherical		
	$\%_d$	0.5% - 2.25%	2.25% - 6.5%	$\%_d$	0.5% - 2.25%	2.25% - 6.5%
P_{ff}	-2%	0.00%	-0.47%	NA	NA	NA
ε_{ff}	-15%	-2.31%	-2.31%	NA	NA	NA
E_{ff}	-5%	5.71%	-3.53%	NA	NA	NA
$P_{max\delta}$	15%	0.00%	3.53%	200%	0.00%	47.06%
$\varepsilon_{max\delta}$	-15%	-2.31%	-2.31%	-20%	0.00	-4.71%
E_{abs}	-12%	0.00%	-2.82%	-30%	-4.62%	-4.62%
J	3%	0.00%	0.71%	20%	3.08%	3.08%
v_{reb}	5%	0.00%	1.18%	247%	38.00%	38.00%

Strain to first failure, strain to maximum displacement, and total absorbed energy exhibited the greatest reduction when subjected to flat tup impact events. A linear reduction in strain to first failure and maximum displacement of 2.31% per percent porosity was calculated across low and high porosity laminates. The typical bilinear relationship is present in total energy absorbed—low porosity laminates are unaffected while high porosity laminates pos-

sess a 2.82% reduction per percent porosity. An increasing, bilinear response is present in peak load to maximum displacement, impulse, and rebound velocity. Due to the linearity of the flat tup impact results, the slight increase in peak load, impulse, and rebound velocity do not outweigh the reductions in all other strength properties. Laminates subjected to blunt impact events should not contain any porosity.

Since first failure was not well defined for hemispherical impact events, first failure quantities were not calculated. A dramatic linear increase in peak load to maximum displacement was observed in high porosity laminates. Peak load to maximum displacement increased by approximately 47% per percent porosity for high porosity laminates. Similarly, rebound velocity increased linearly by approximately 38% per percent porosity for both high and low porosity laminates. The drastic increase of peak load to maximum displacement, rebound velocity, and impulse suggest porosity should be induced when structures are expected to be subjected to hemispherical impact events. If peak load, impulse, and rebound velocity are desired quantities, reductions in strain to maximum displacement and total energy absorbed can be tolerated and high porosity laminates should be considered.

The total percent difference between maximum and minimum porosity and percentage of increase or decrease for each percent porosity in each region of compression after impact testing are shown in Table 56.

Table 56: Compression After Impact Mechanical Testing Summary

	Flat			Hemispherical		
	$\%_d$	0.5% - 2.25%	2.25% - 6.5%	$\%_d$	0.5% - 2.25%	2.25% - 6.5%
P_{max}	-12%	-6.86%	0.00%	15%	5.71%	1.18%
F_{cu}	-20%	-8.57%	-1.18%	8%	4.57%	0.00%

Peak load and ultimate compressive strength decreased bilinearly with porosity when sub-

jected to flat tup impact events. Significant reductions were observed within low porosity laminates. For high porosity laminates, no further reduction in peak load or ultimate compressive strength was calculated. Laminates subjected to compressiona fter blunt impact events should not contain any porosity.

Peak load and ultimate compressive strength increased bilinearly with porosity when subjected to hemispherical tup impact events. A significant increase was observed within low porosity laminates. For high porosity laminates, no substantial increase in peak load or ultimate compressive strength was calculated. Although the data suggests laminates subjected to hemispherical impact events should induce porosity, it is unlikely the increase in peak load or ultimate compressive strength after impact will outweigh the reductions in remaining strength properties listed above.

5.6 Conclusions and Recommendations

Porosity determination was a crucial step in order to detemrine the affect of porosity on mechanical properties. However, not all porosity techniques produced equal results. All papers researched for this study performed porosity determination using the ASTM standard. While the ASTM standard produced accurate and repeatable results, it can only be used for simple, two part composites. Any composite system that contains a third constituent cannot be used unless its mass and density are known quantities.

There is nothing new or novel regarding the porosity threshold equal to approximately 2%. Numerous aerospace and defense companies set an upper limit of acceptable porosity at 2%. However, it is extremely important to note that all of the calculations and experiments conducted in this study are only valid for laminates constructed of Hexcel AS4C fibers woven into an 8-harness satin weave pre-impregnated with a UF3352 TCR resin system.

The UF3352 resin system is extremely viscous with a viscosity similar to peanut butter at its minimum viscosity during cure. The extreme viscosity of this resin system was desirable for this study to trap volatiles during laminate construction to induce porosity. If laminates are construed with less viscous resin systems, different porosity concentrations should be observed given the same cure conditions.

Appendix A: Flexure

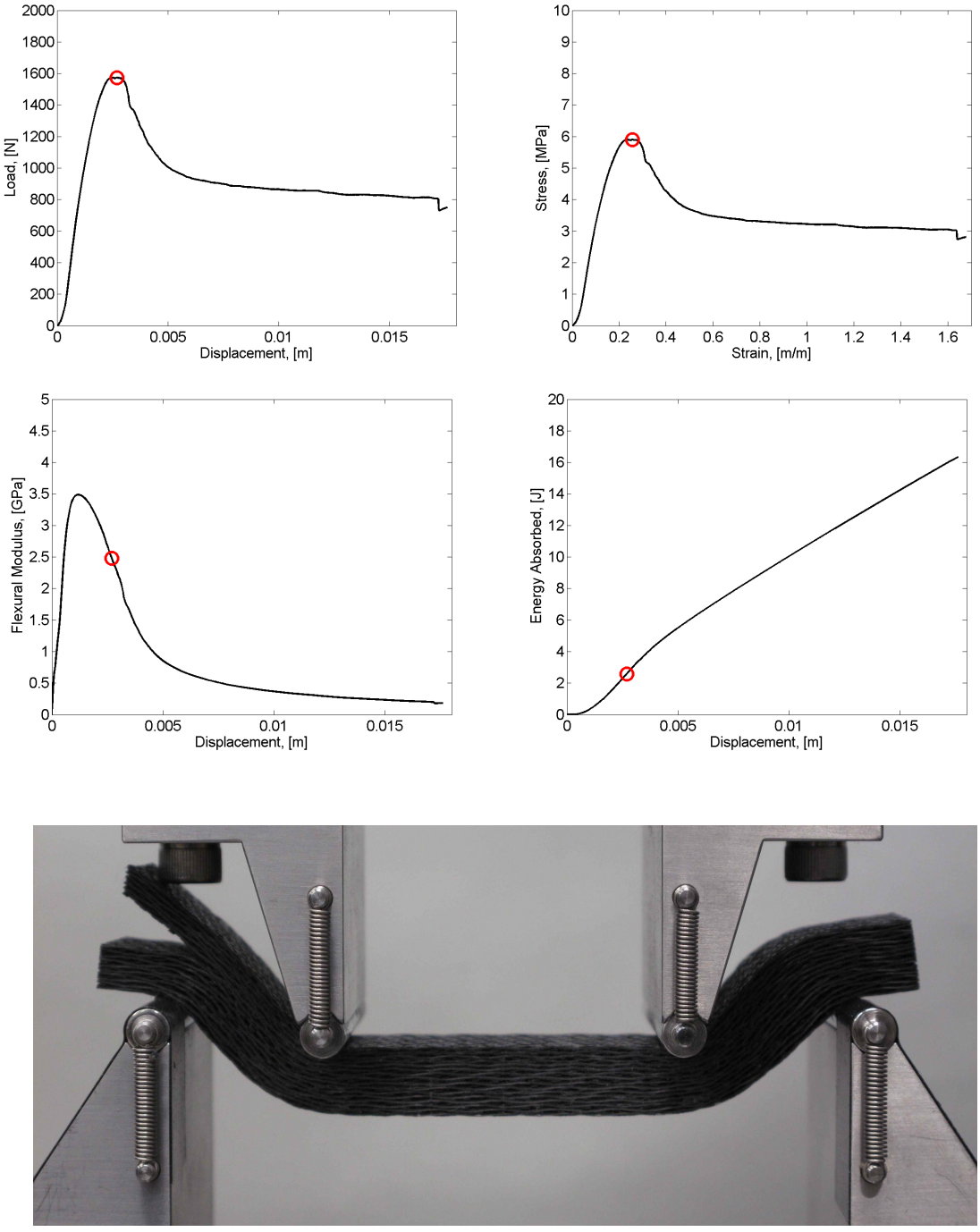

Figure 116: Measured and calculated response of Sample 101 subjected to four point bend testing. Red circle indicates maximum load.

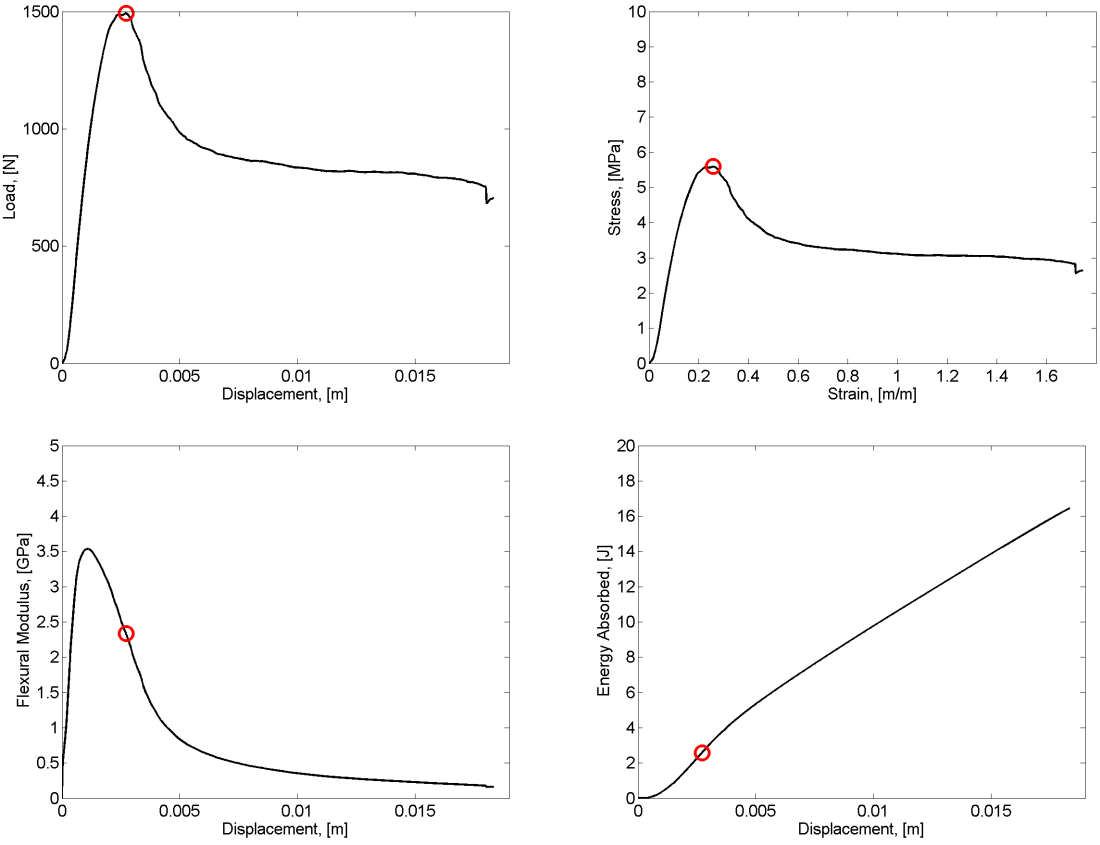

Figure 117: Measured and calculated response of Sample 102 subjected to four point bend testing. Red circle indicates maximum load.

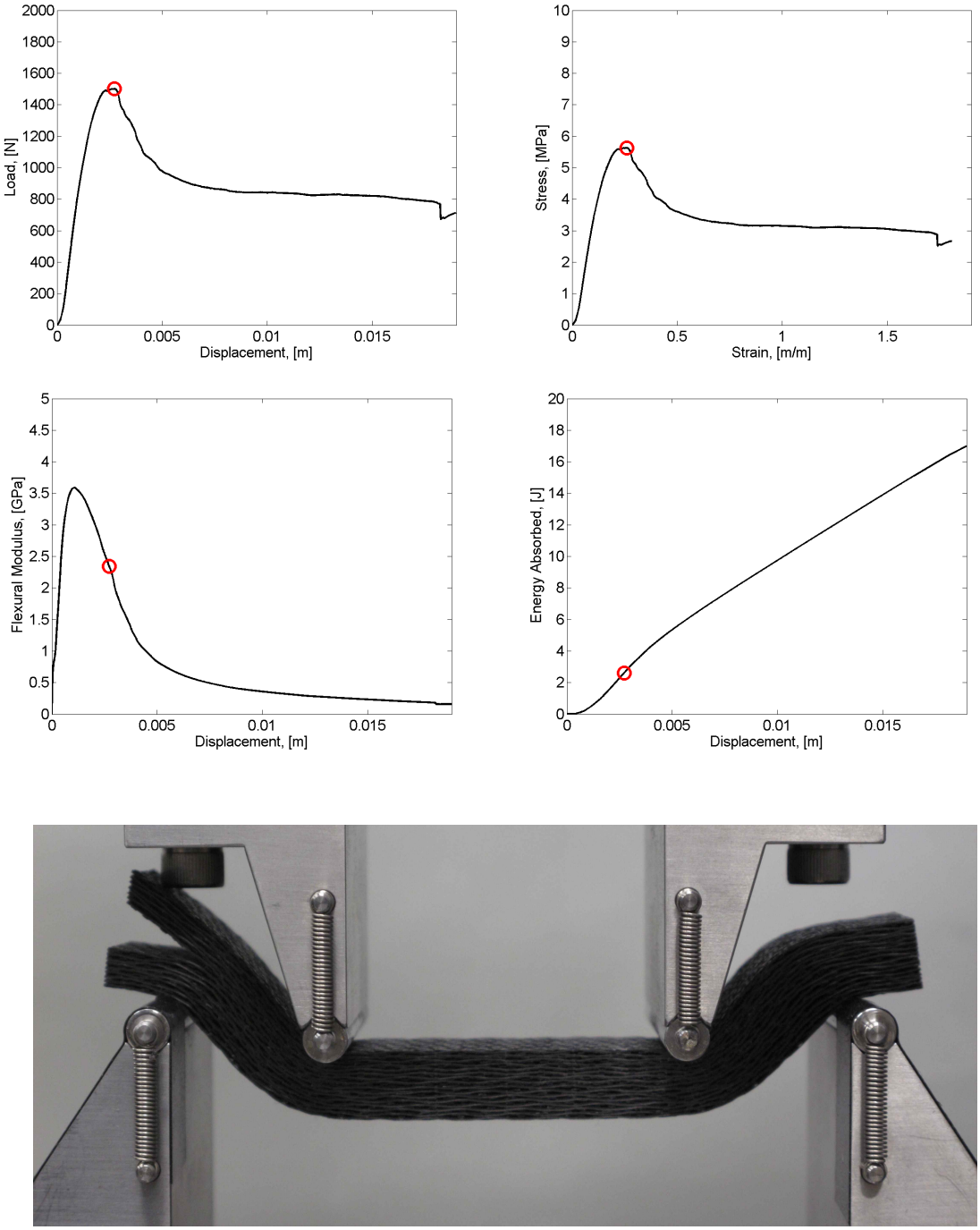

Figure 118: Measured and calculated response of Sample 103 subjected to four point bend testing. Red circle indicates maximum load.

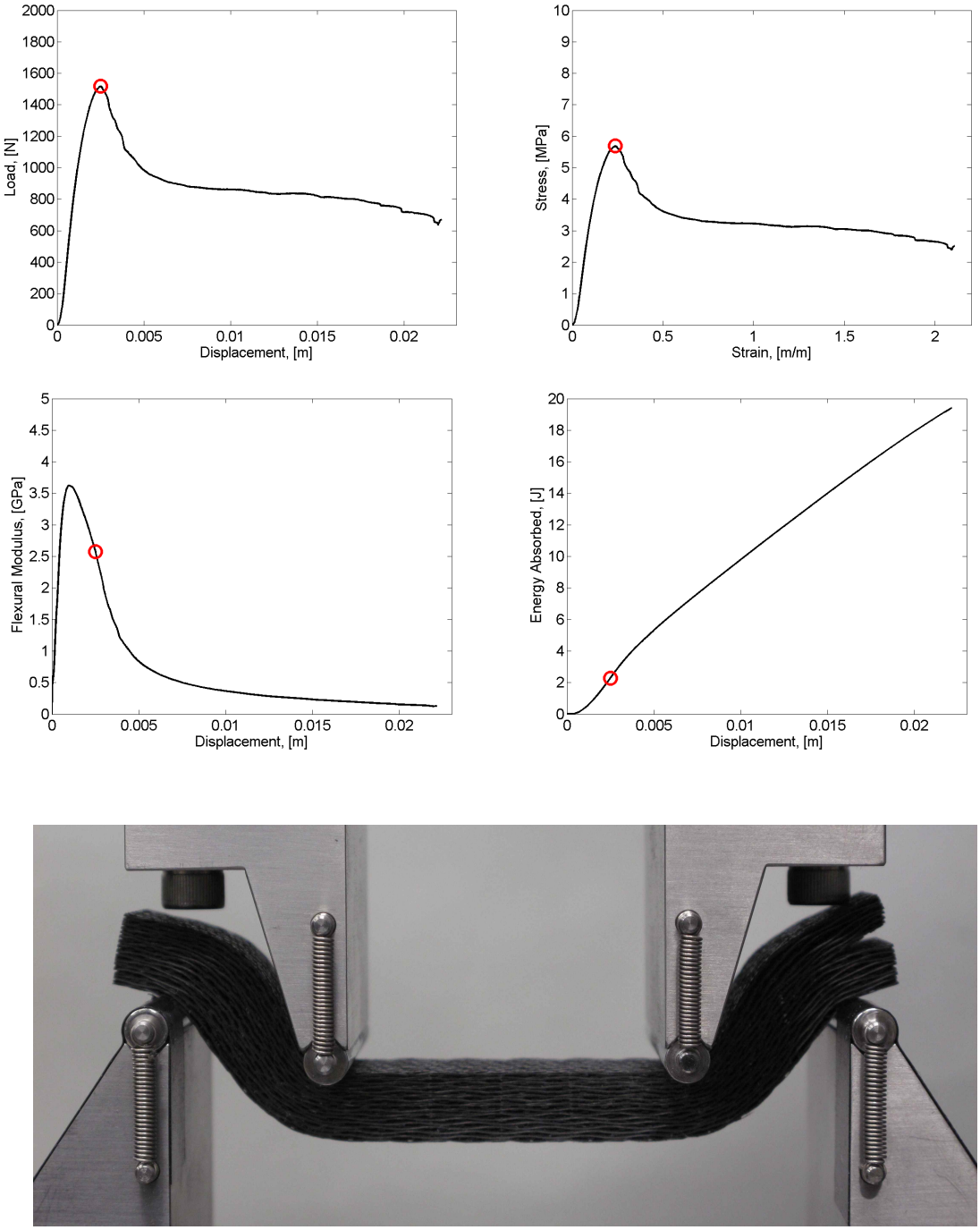

Figure 119: Measured and calculated response of Sample 104 subjected to four point bend testing. Red circle indicates maximum load.

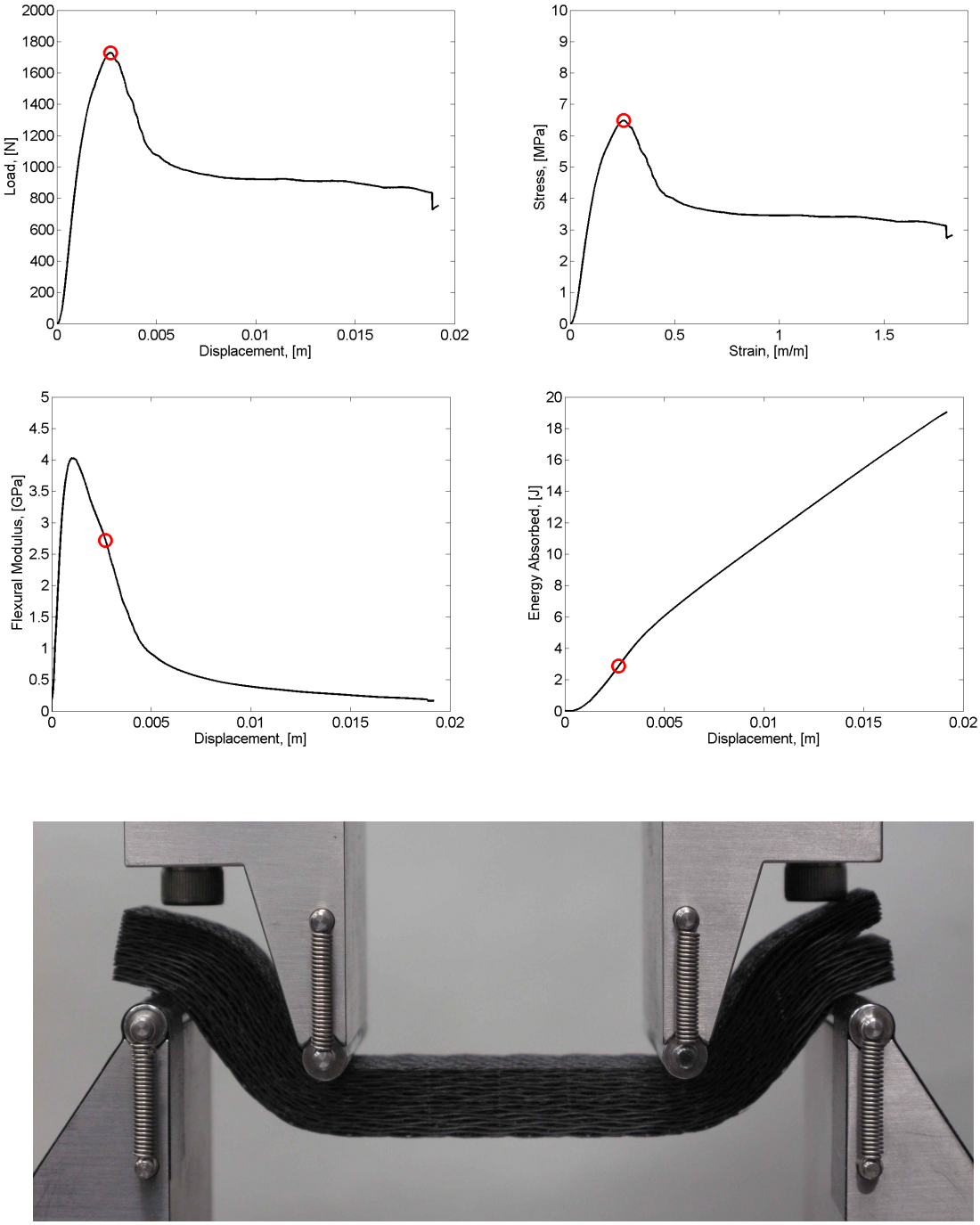

Figure 120: Measured and calculated response of Sample 107 subjected to four point bend testing. Red circle indicates maximum load.

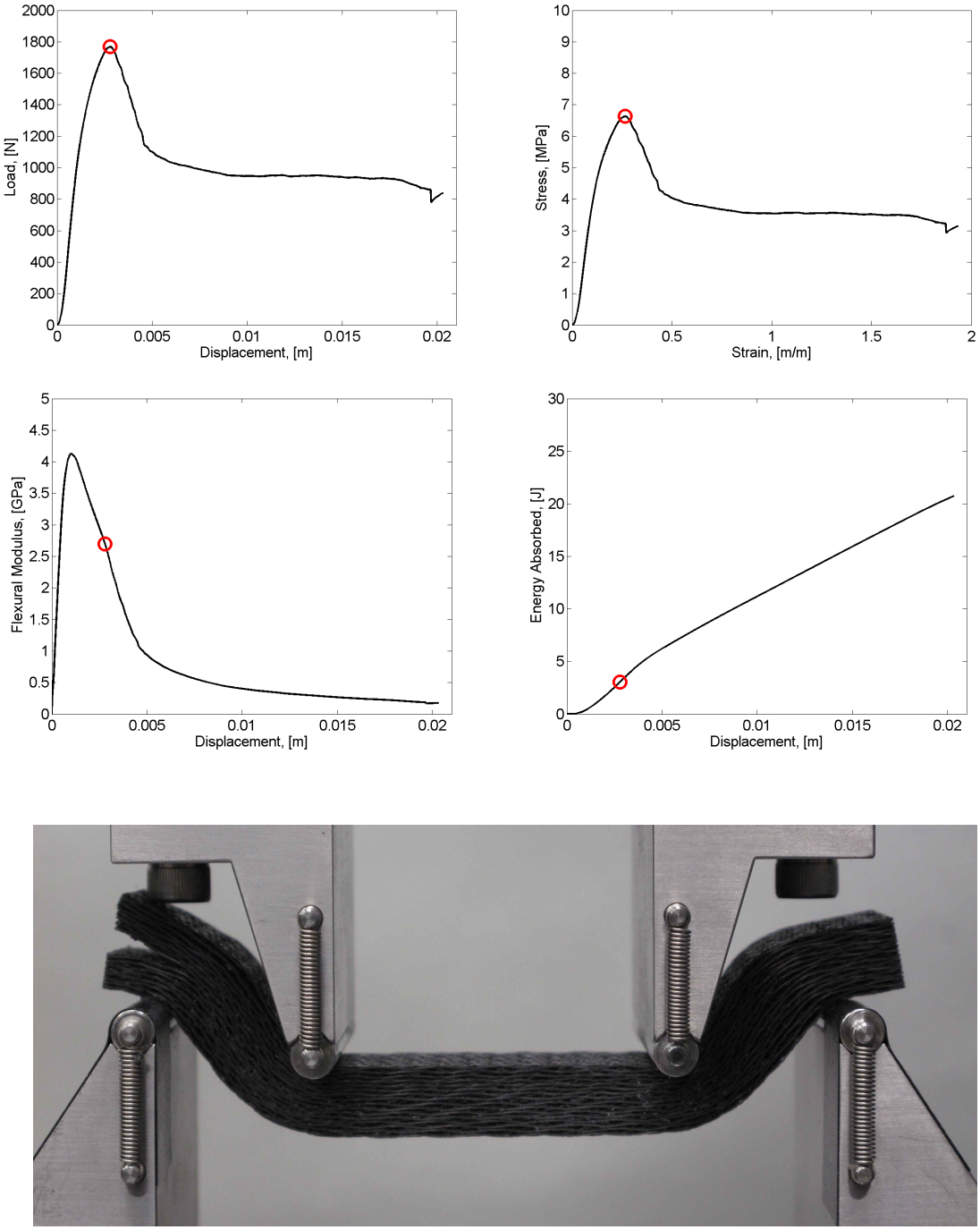

Figure 121: Measured and calculated response of Sample 108 subjected to four point bend testing. Red circle indicates maximum load.

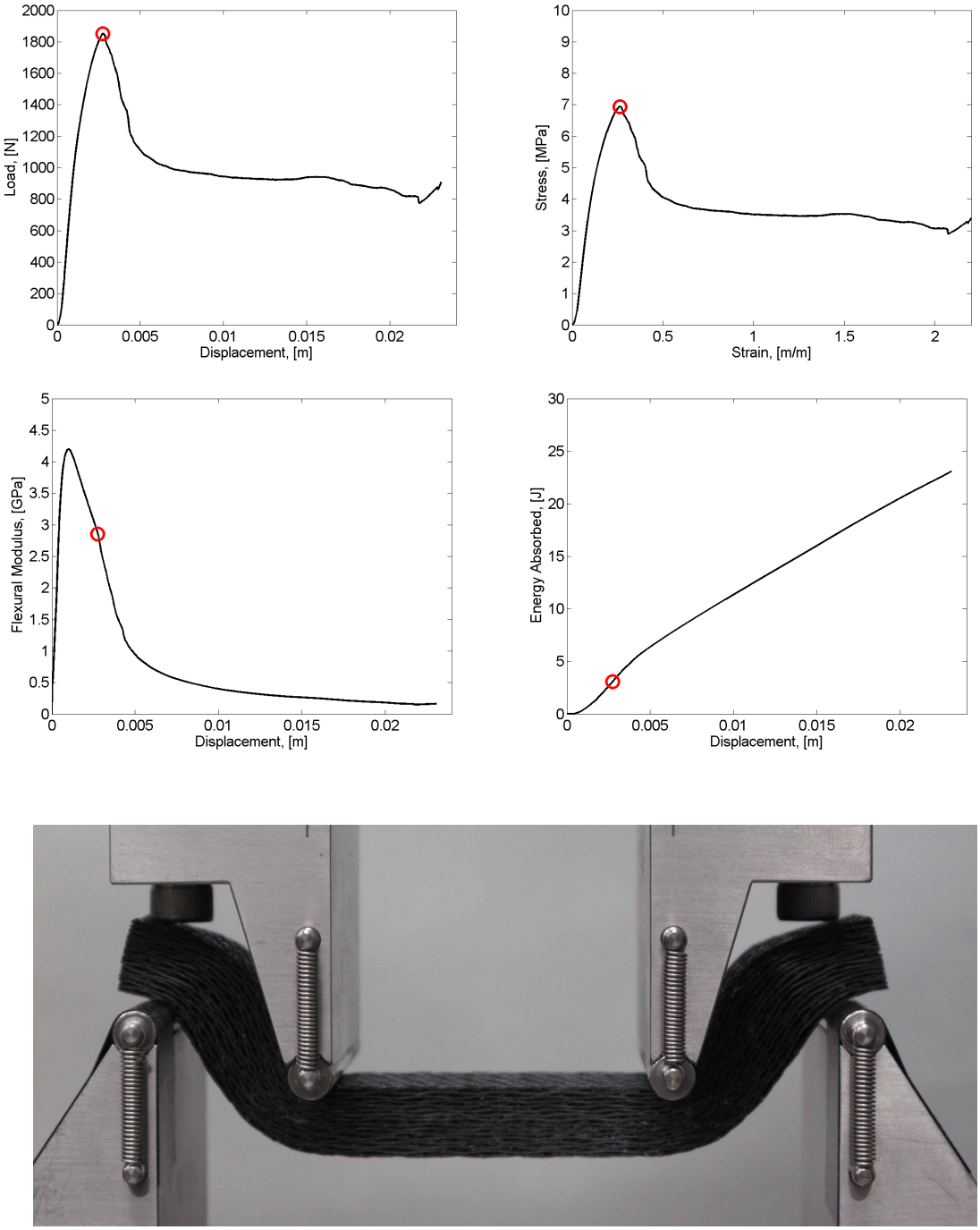

Figure 122: Measured and calculated response of Sample 109 subjected to four point bend testing. Red circle indicates maximum load.

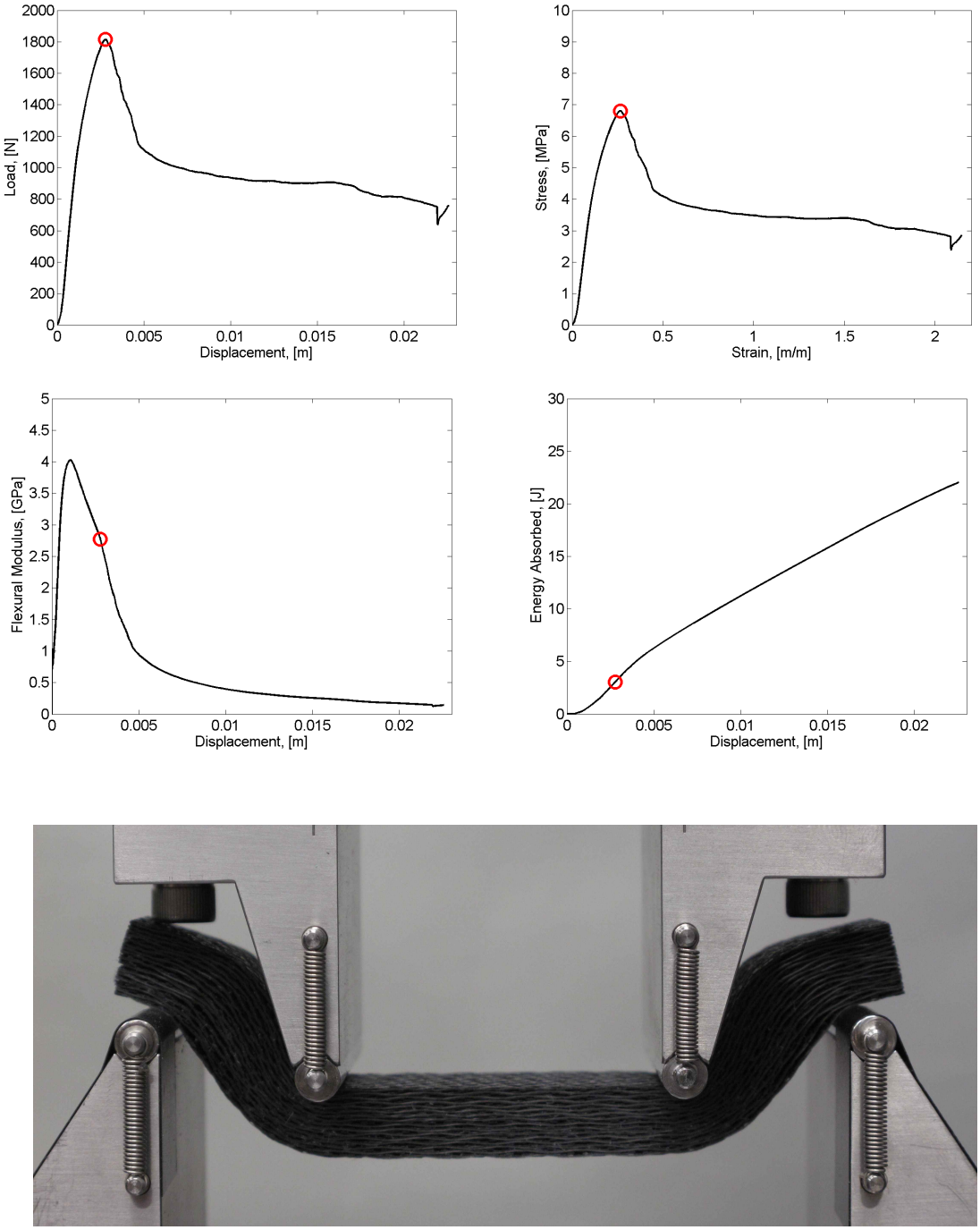

Figure 123: Measured and calculated response of Sample 110 subjected to four point bend testing. Red circle indicates maximum load.

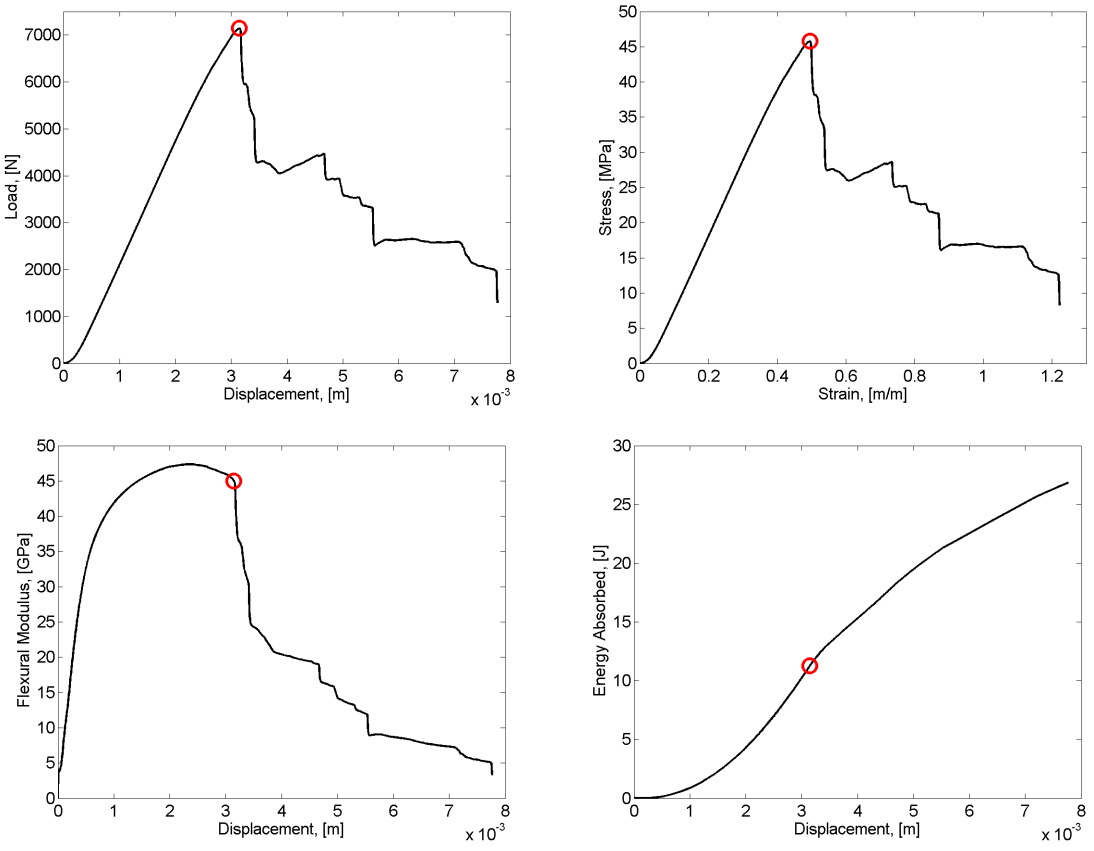

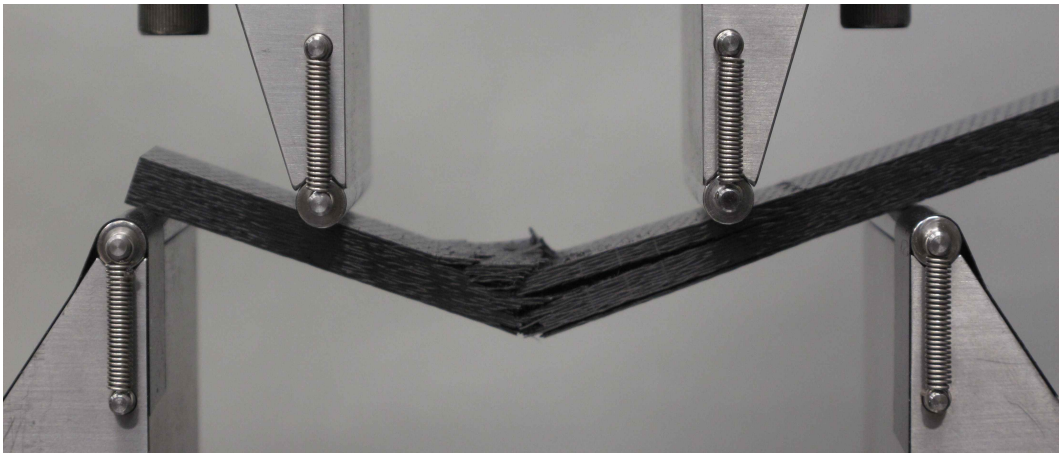

Figure 124: Measured and calculated response of Sample 201 subjected to four point bend testing. Red circle indicates maximum load.

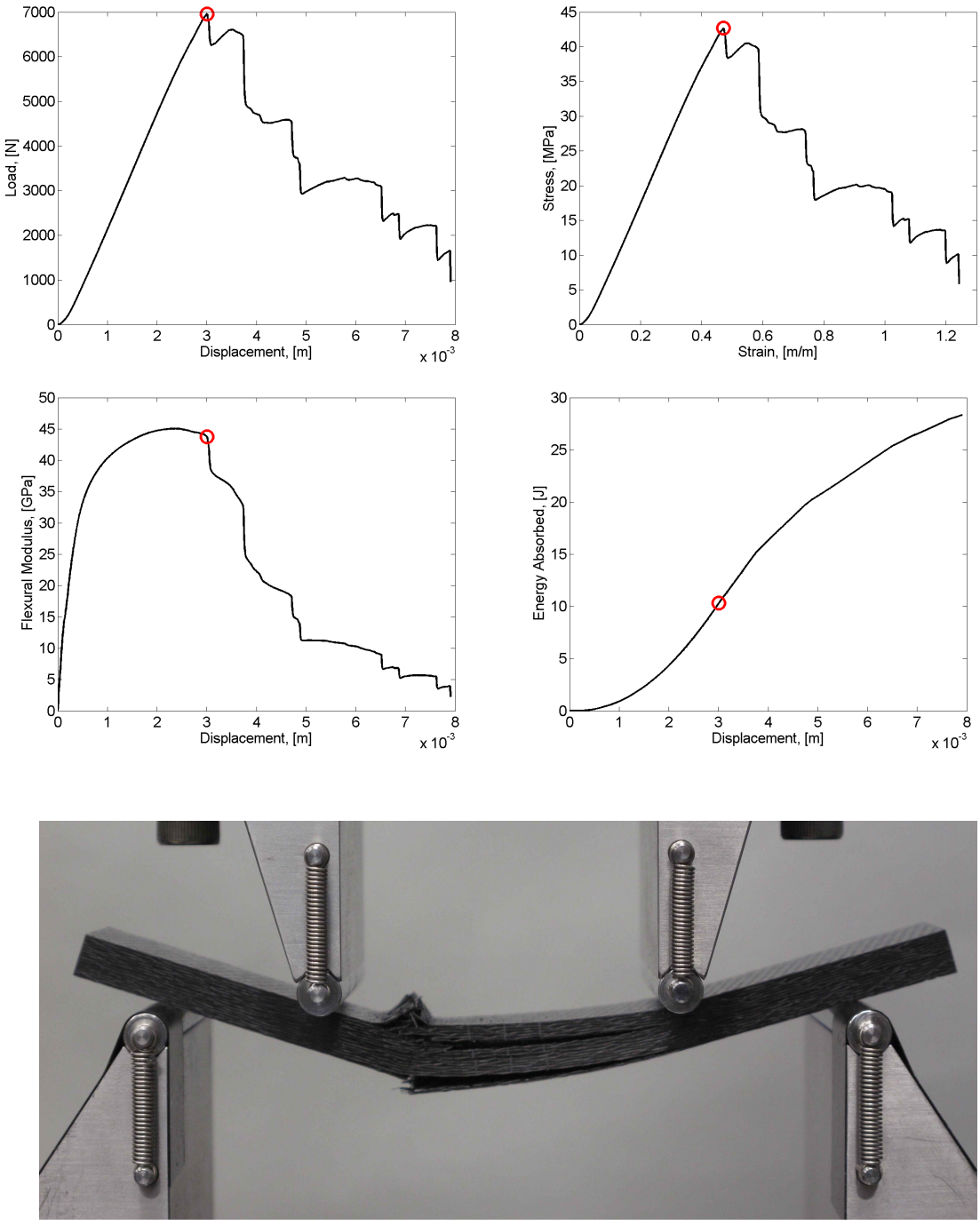

Figure 125: Measured and calculated response of Sample 202 subjected to four point bend testing. Red circle indicates maximum load.

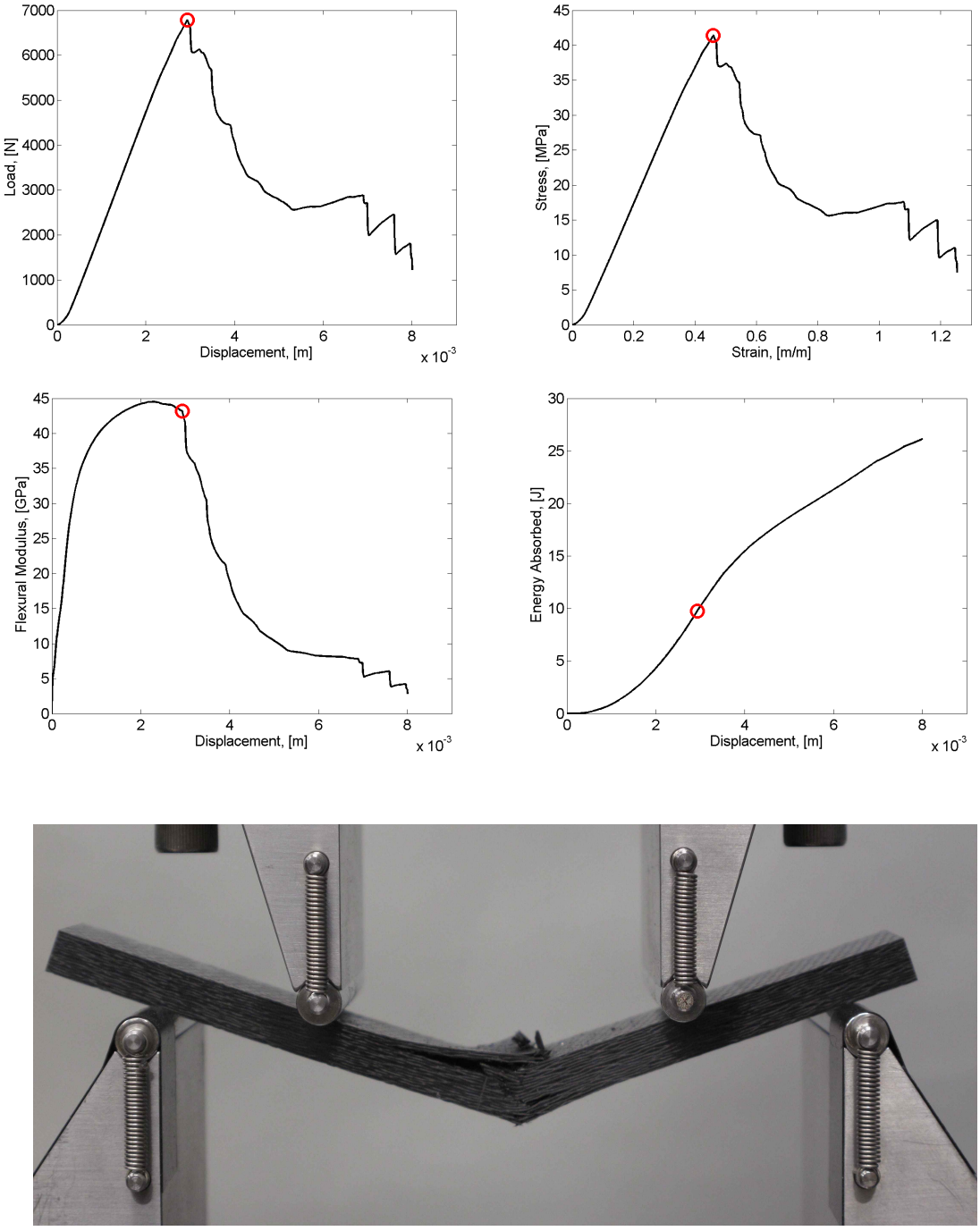

Figure 126: Measured and calculated response of Sample 203 subjected to four point bend testing. Red circle indicates maximum load.

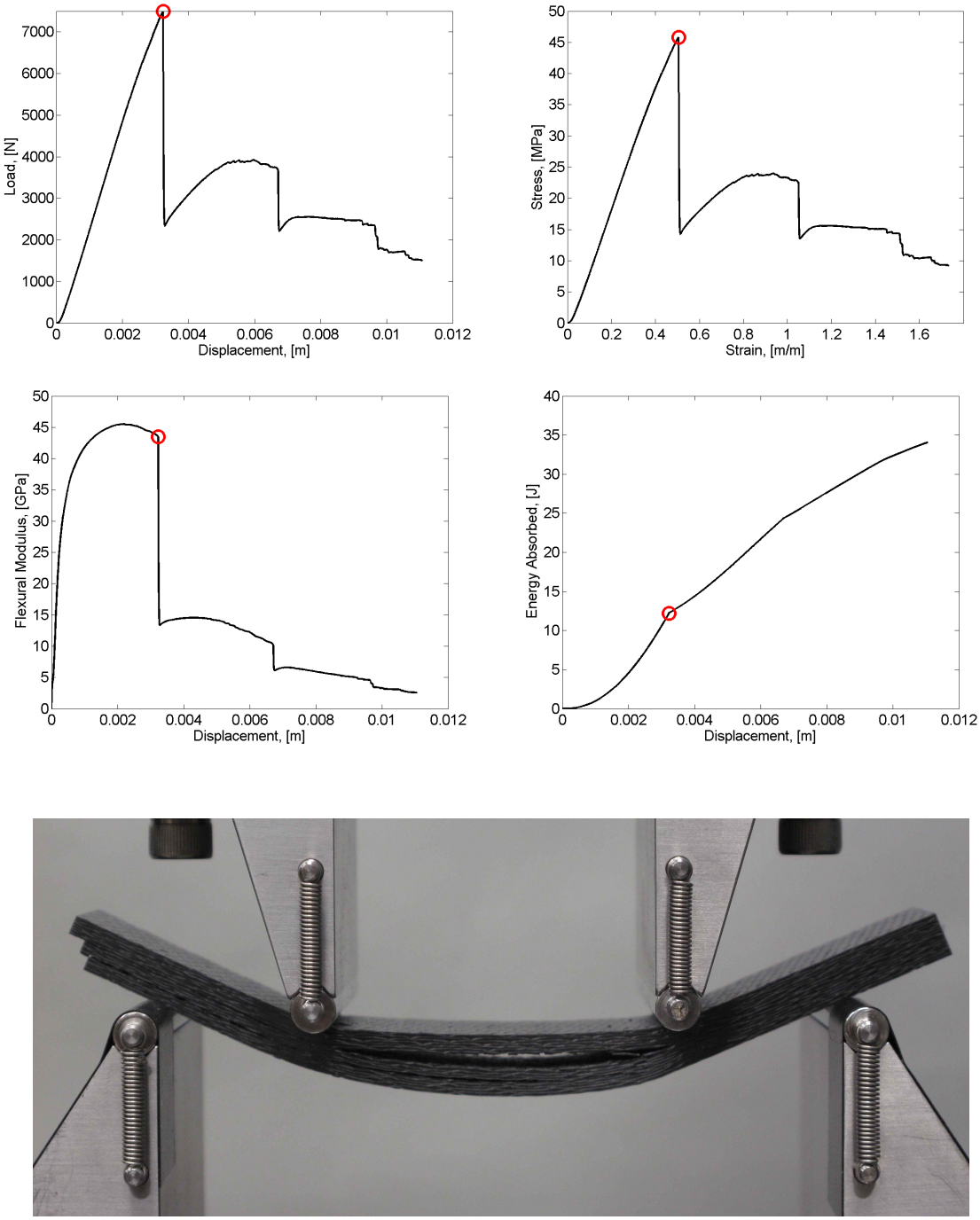

Figure 127: Measured and calculated response of Sample 204 subjected to four point bend testing. Red circle indicates maximum load.

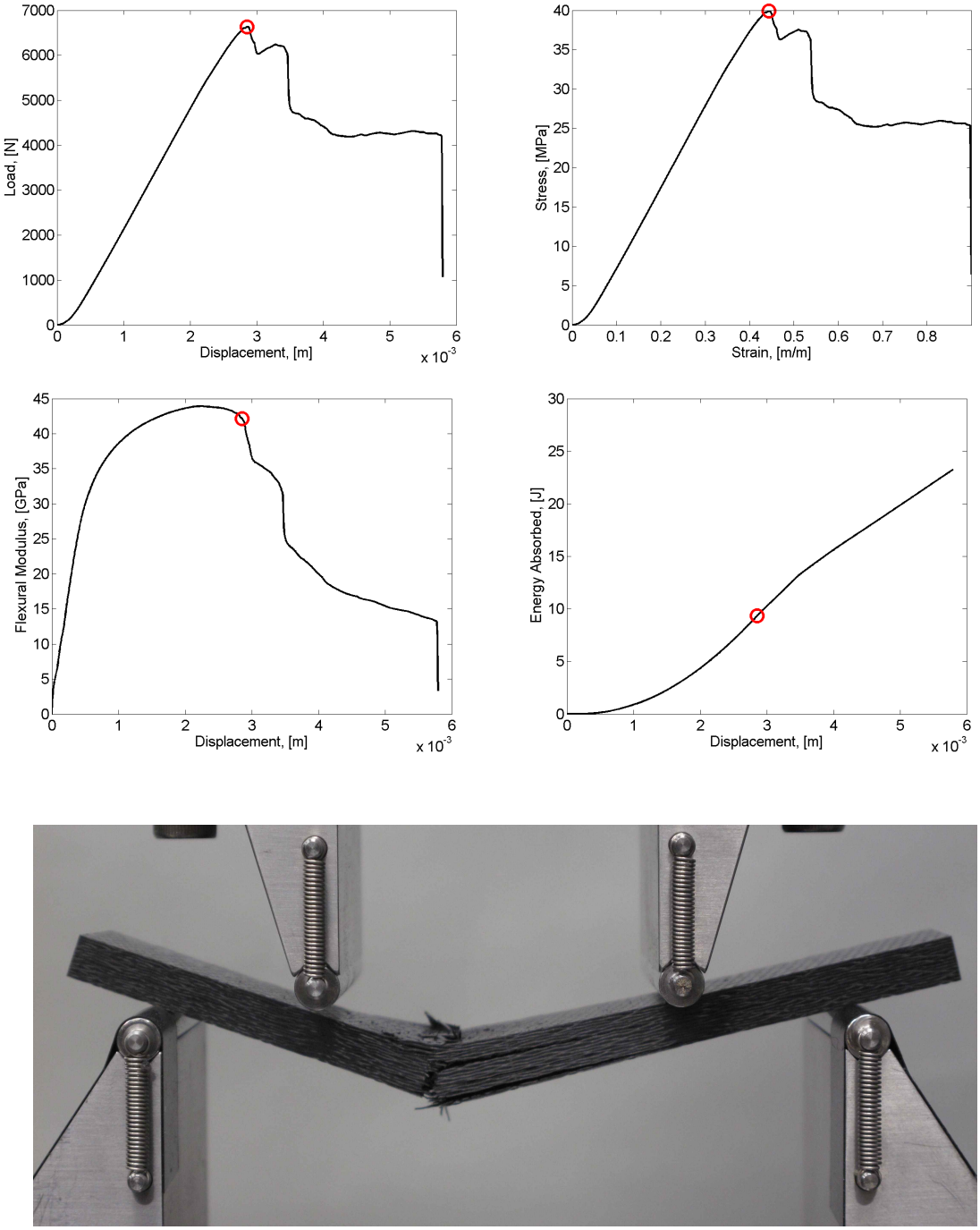

Figure 128: Measured and calculated response of Sample 207 subjected to four point bend testing. Red circle indicates maximum load.

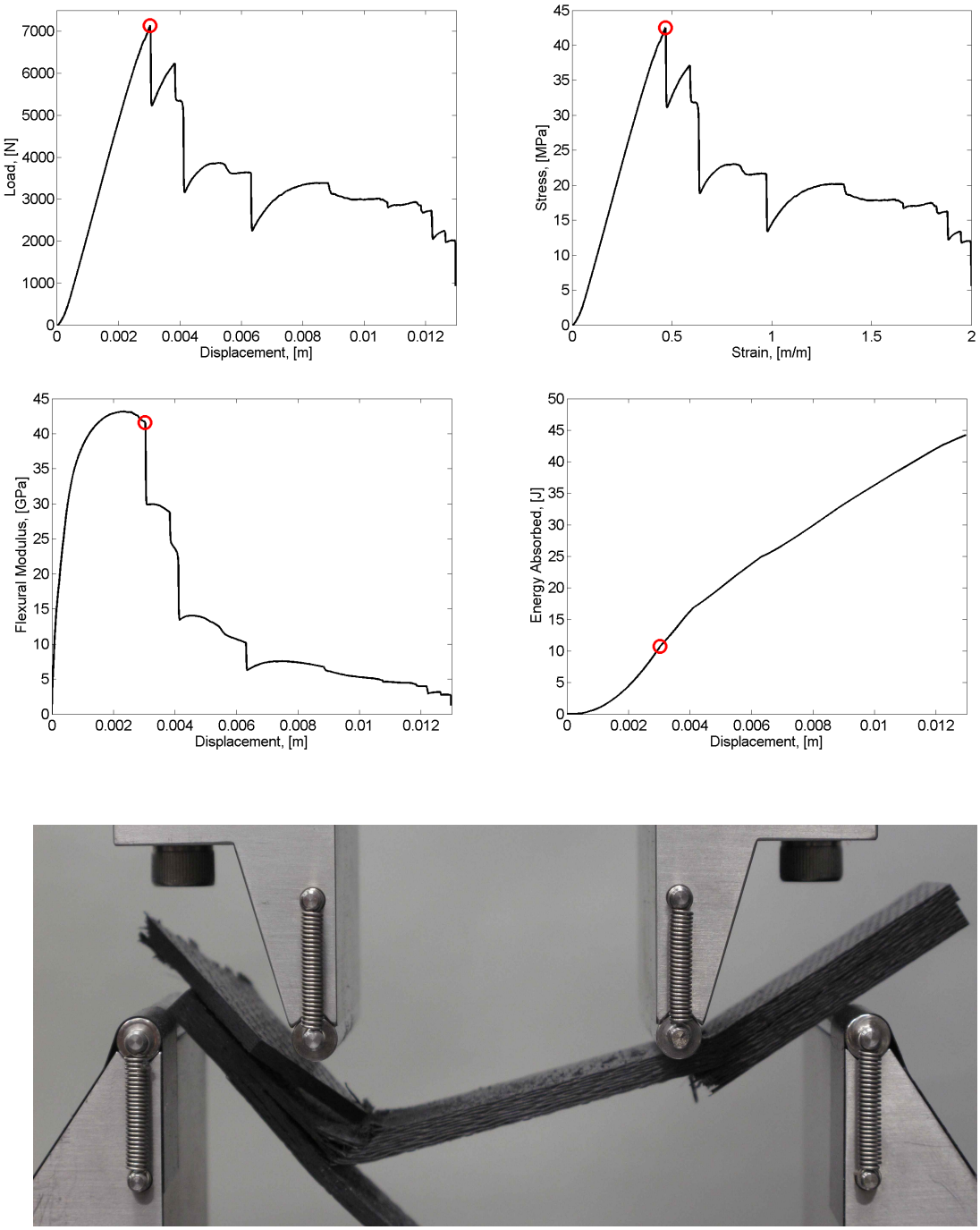

Figure 129: Measured and calculated response of Sample 208 subjected to four point bend testing. Red circle indicates maximum load.

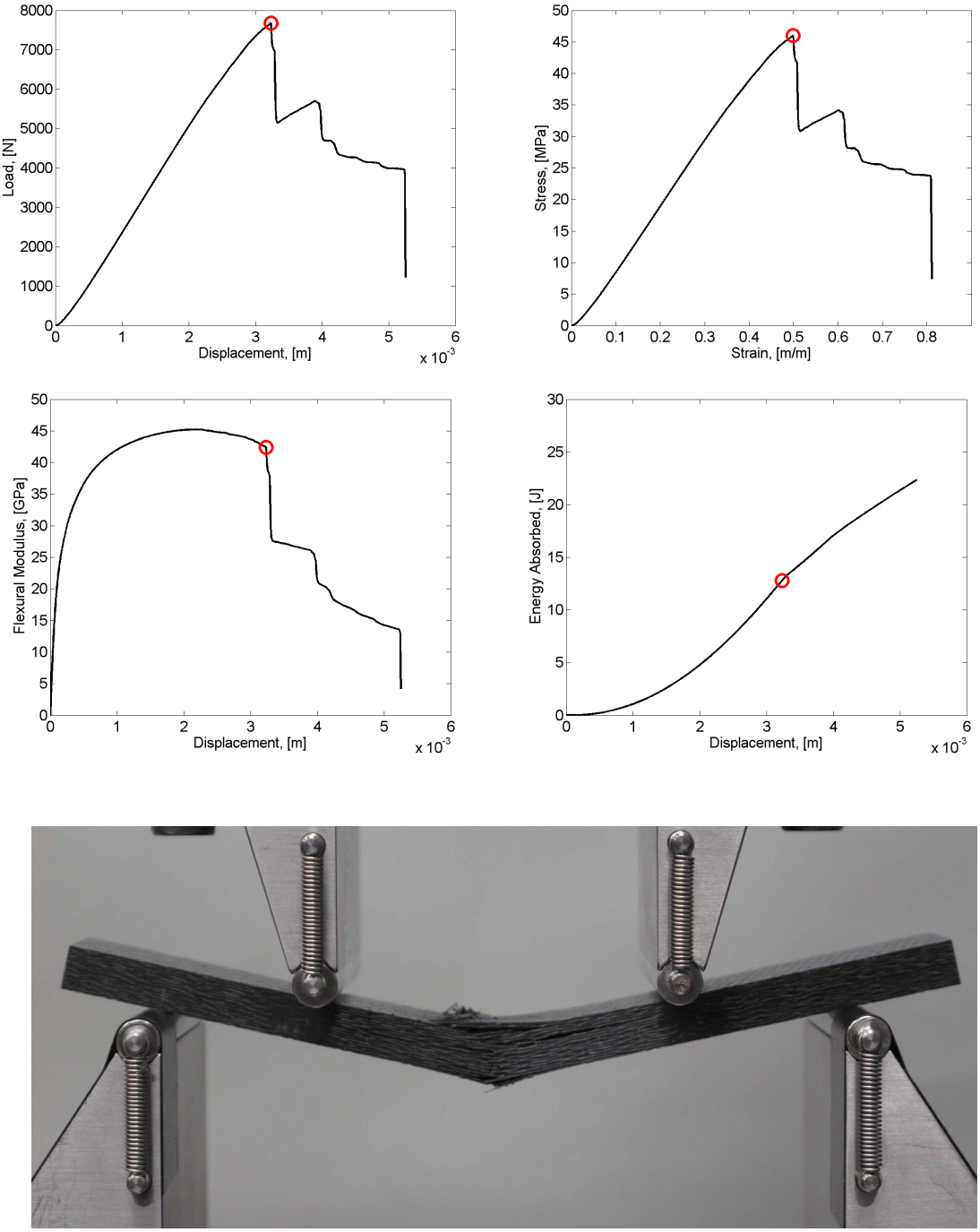

Figure 130: Measured and calculated response of Sample 209 subjected to four point bend testing. Red circle indicates maximum load.

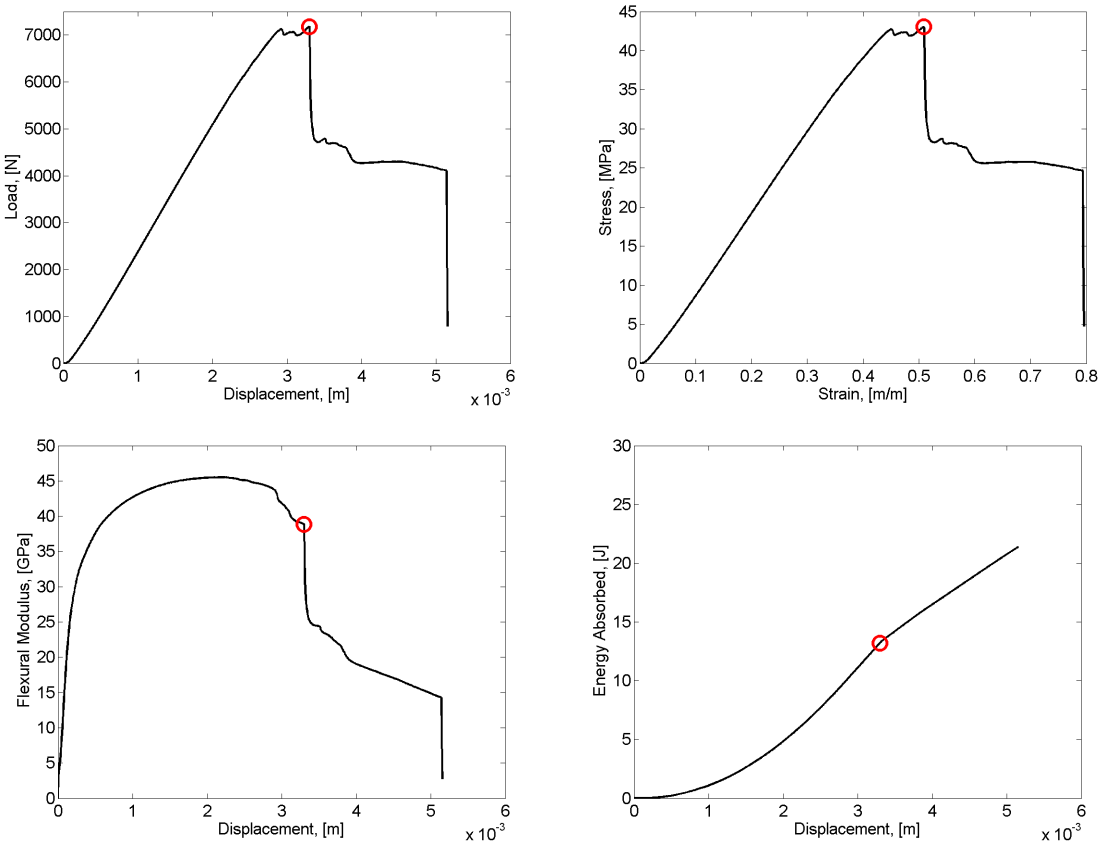

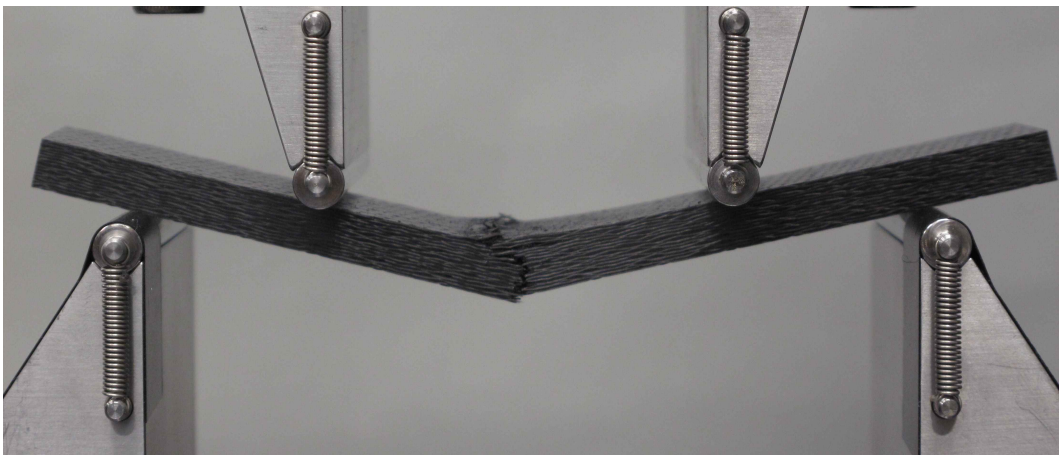

Figure 131: Measured and calculated response of Sample 210 subjected to four point bend testing. Red circle indicates maximum load.

Sample 301

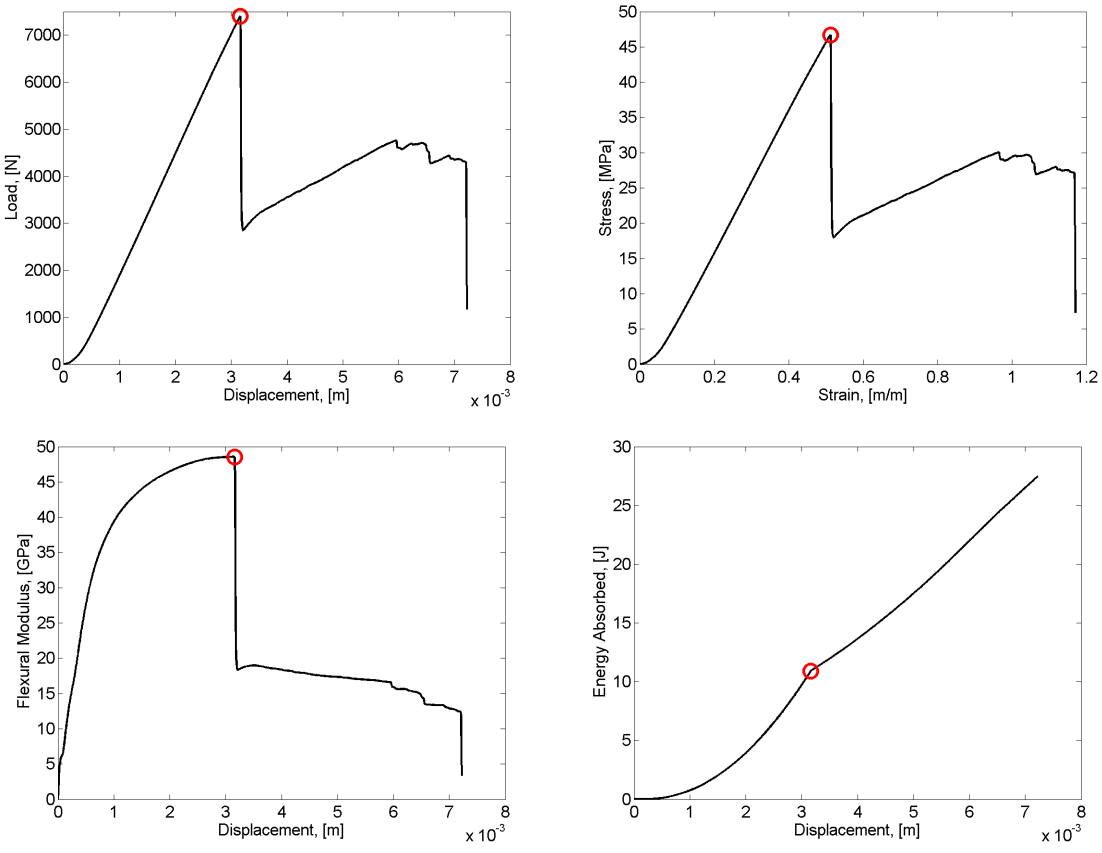

Figure 132: Measured and calculated response of Sample 301 subjected to four point bend testing. Red circle indicates maximum load.

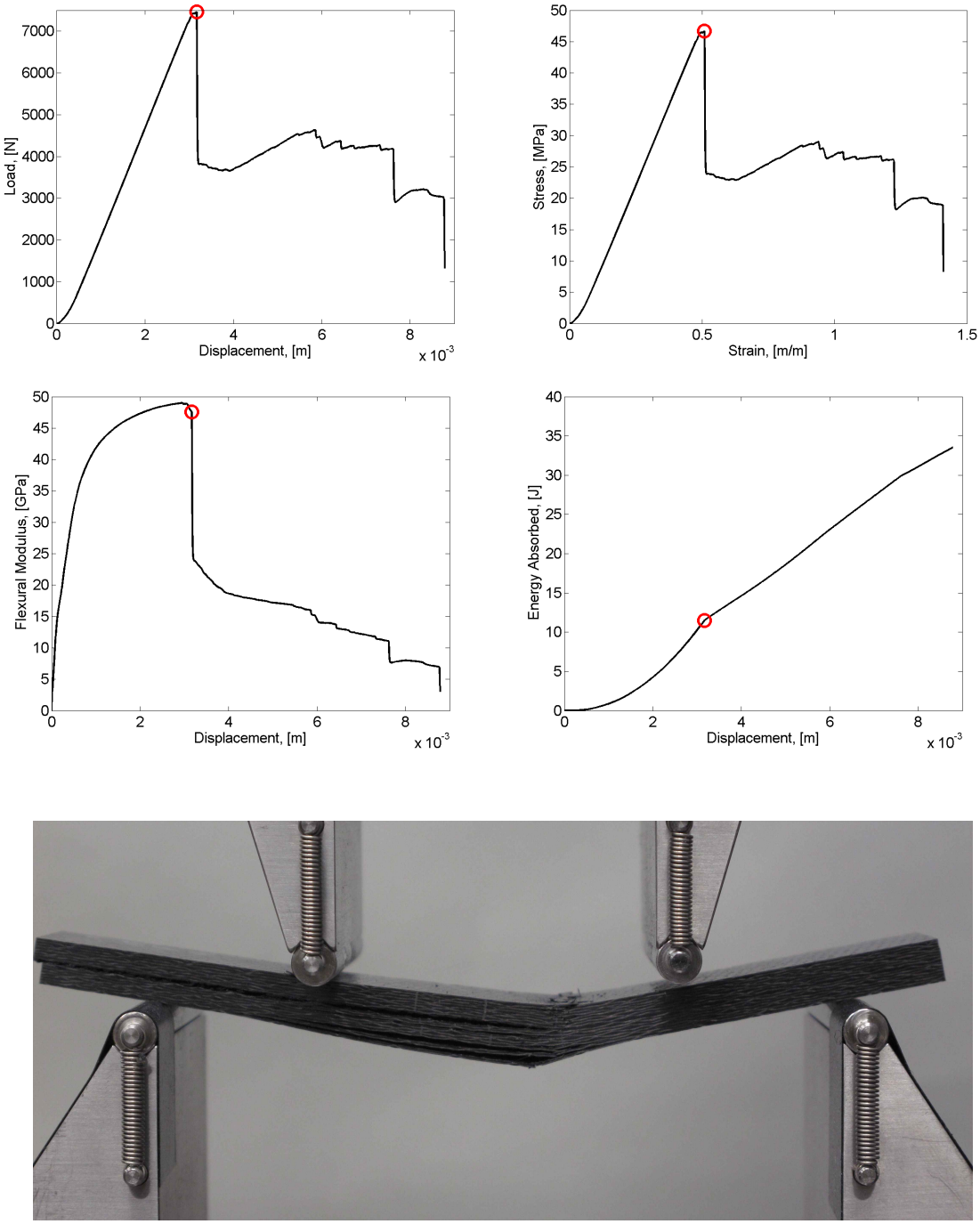

Figure 133: Measured and calculated response of Sample 302 subjected to four point bend testing. Red circle indicates maximum load.

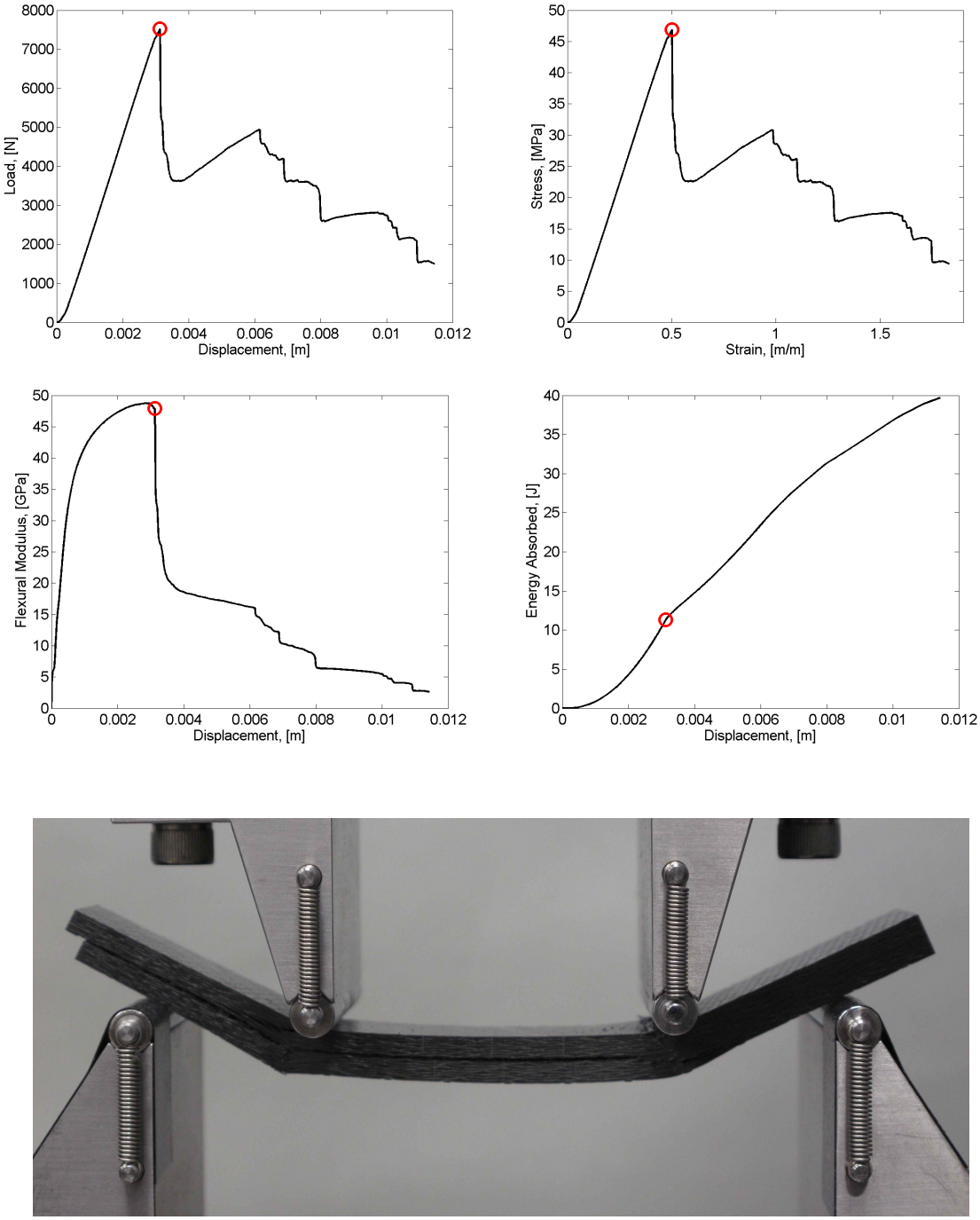

Figure 134: Measured and calculated response of Sample 303 subjected to four point bend testing. Red circle indicates maximum load.

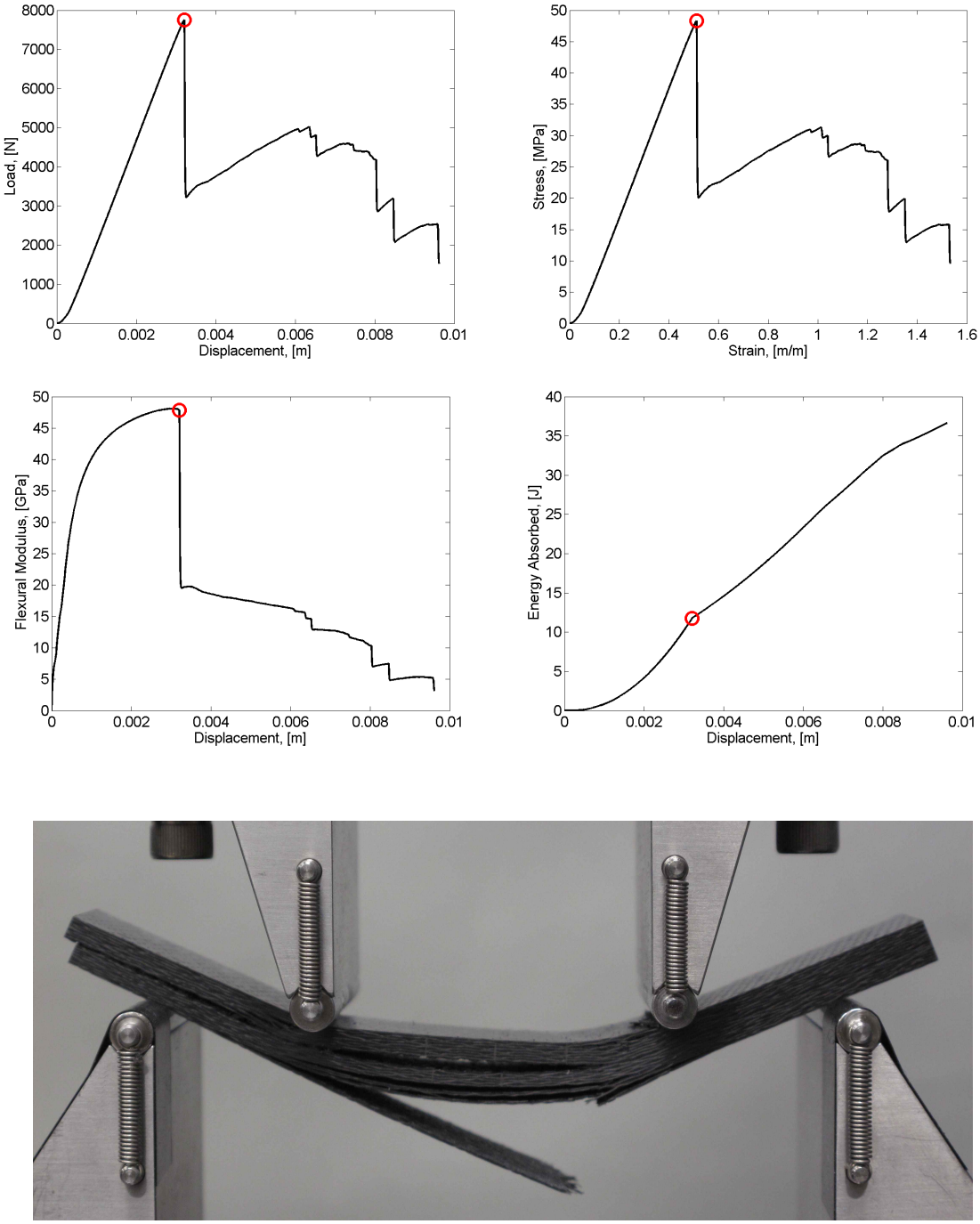

Figure 135: Measured and calculated response of Sample 304 subjected to four point bend testing. Red circle indicates maximum load.

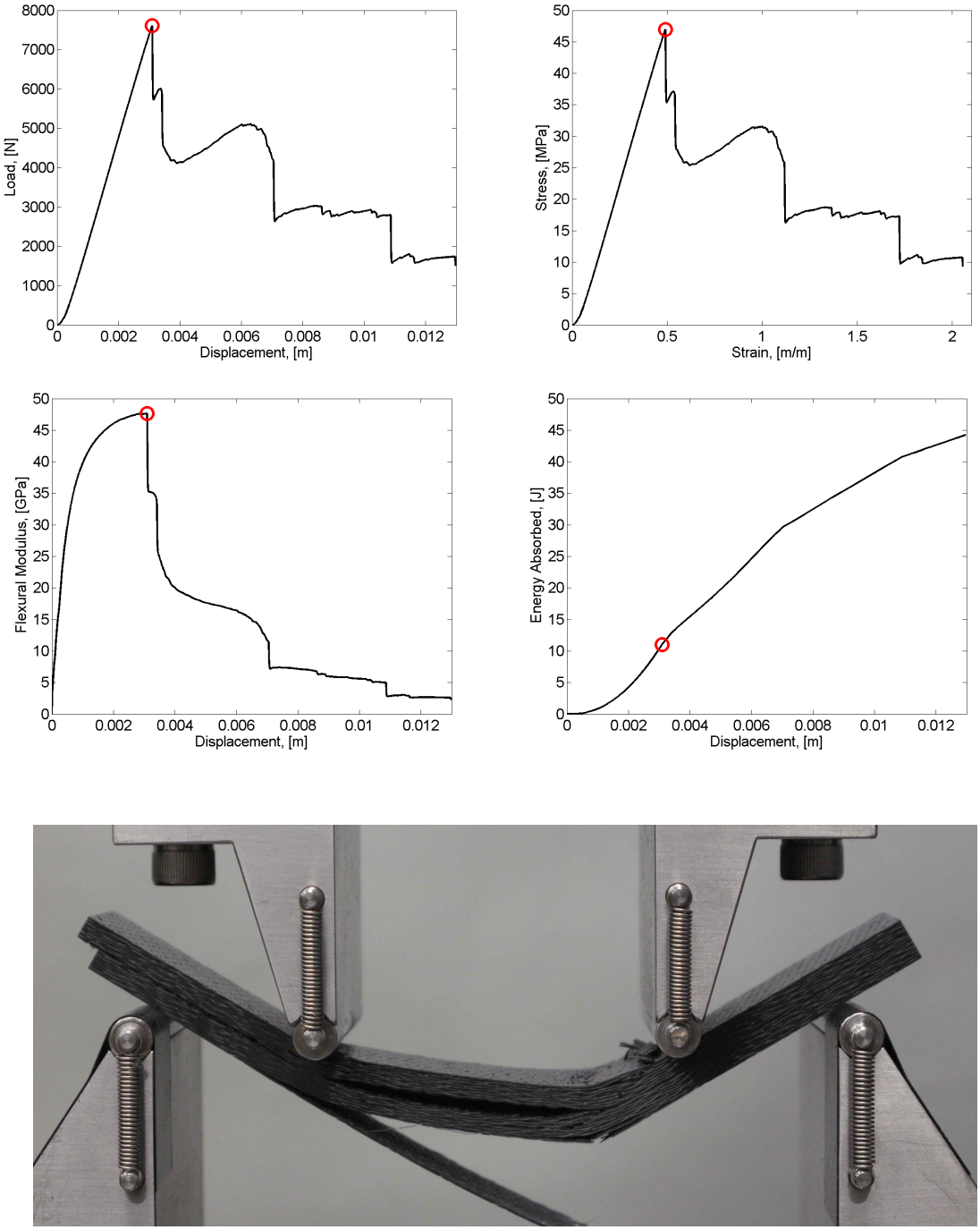

Figure 136: Measured and calculated response of Sample 307 subjected to four point bend testing. Red circle indicates maximum load.

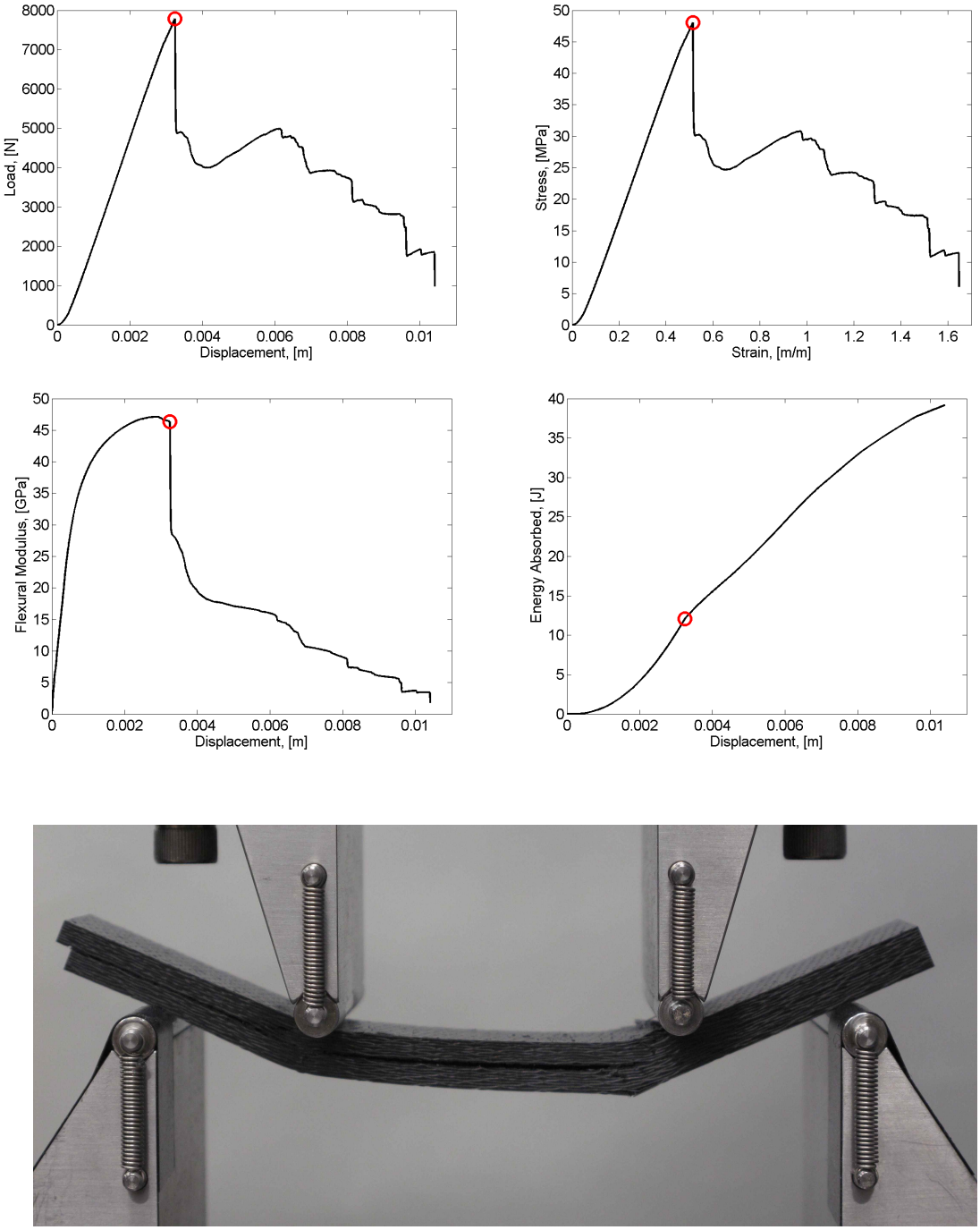

Figure 137: Measured and calculated response of Sample 308 subjected to four point bend testing. Red circle indicates maximum load.

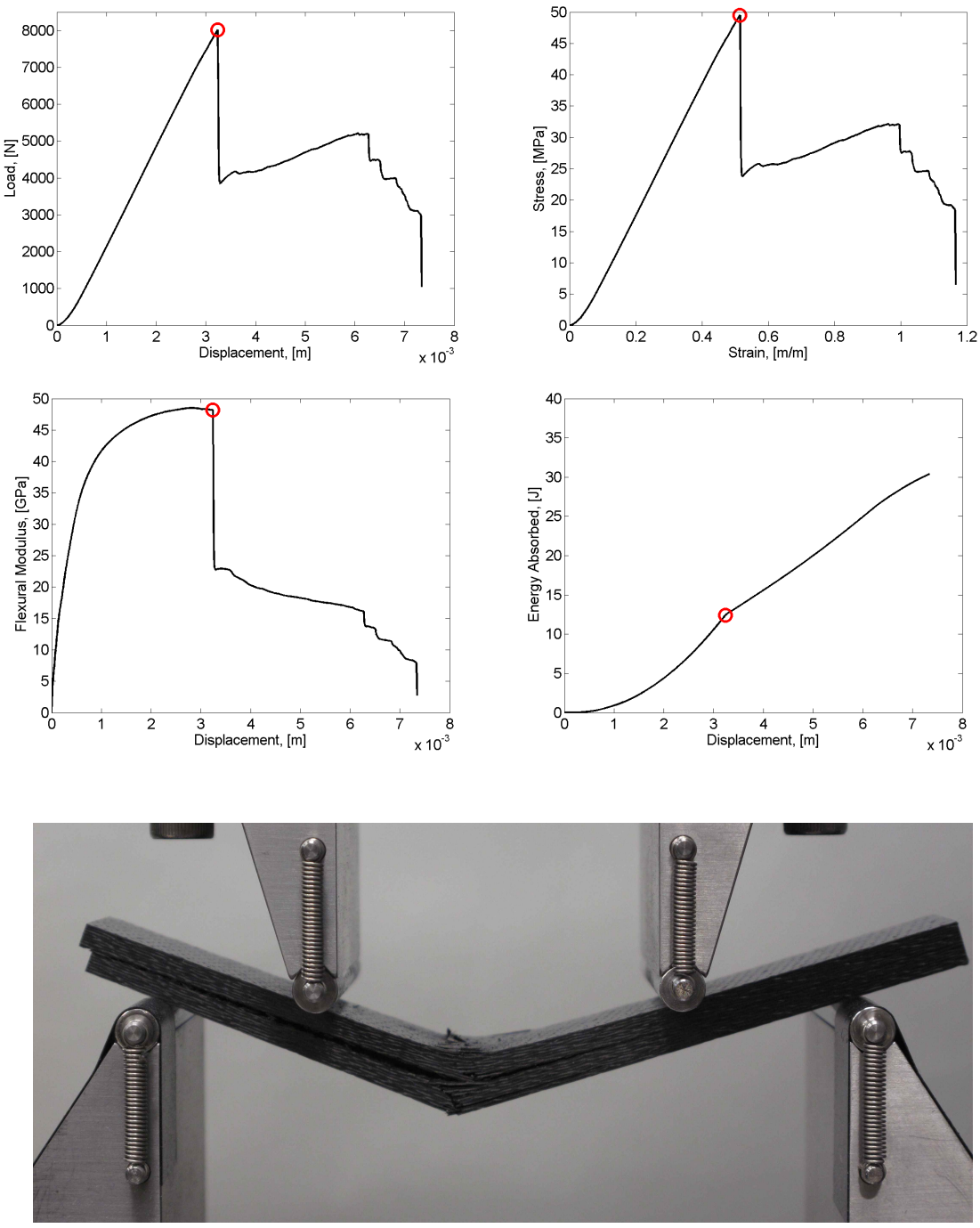

Figure 138: Measured and calculated response of Sample 309 subjected to four point bend testing. Red circle indicates maximum load.

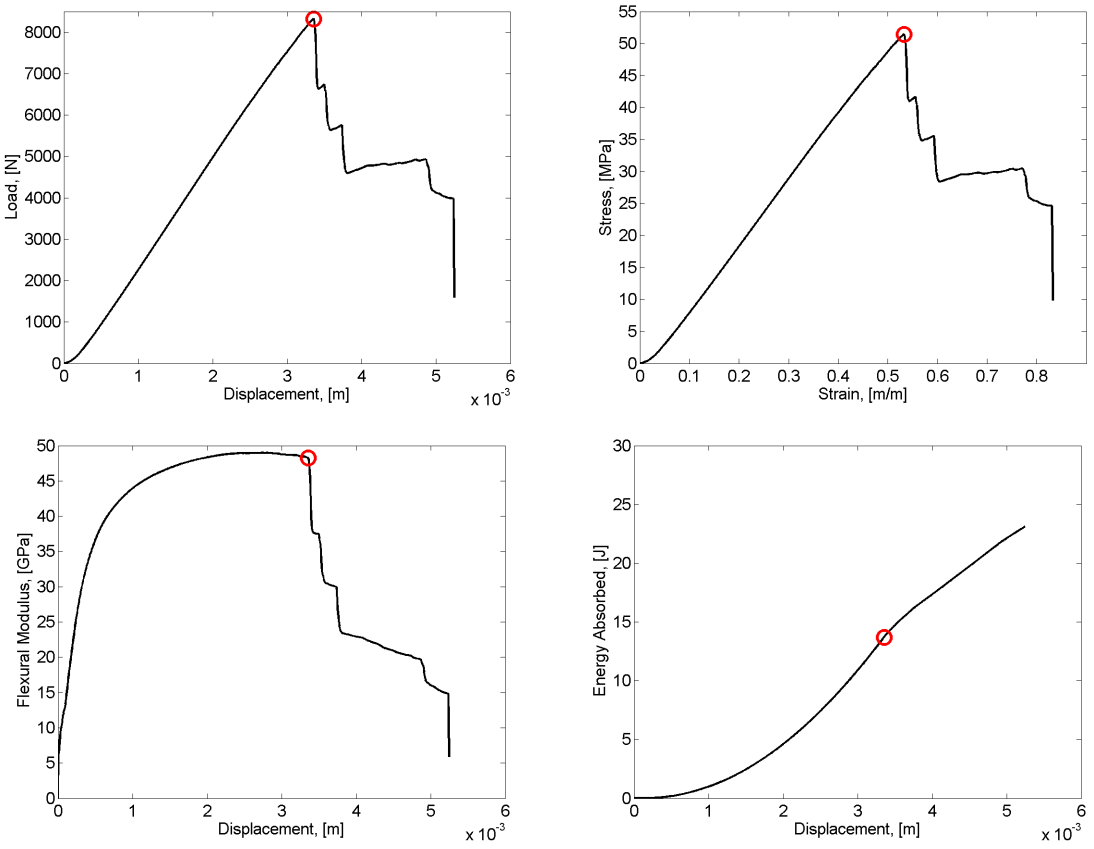

Figure 139: Measured and calculated response of Sample 310 subjected to four point bend testing. Red circle indicates maximum load.

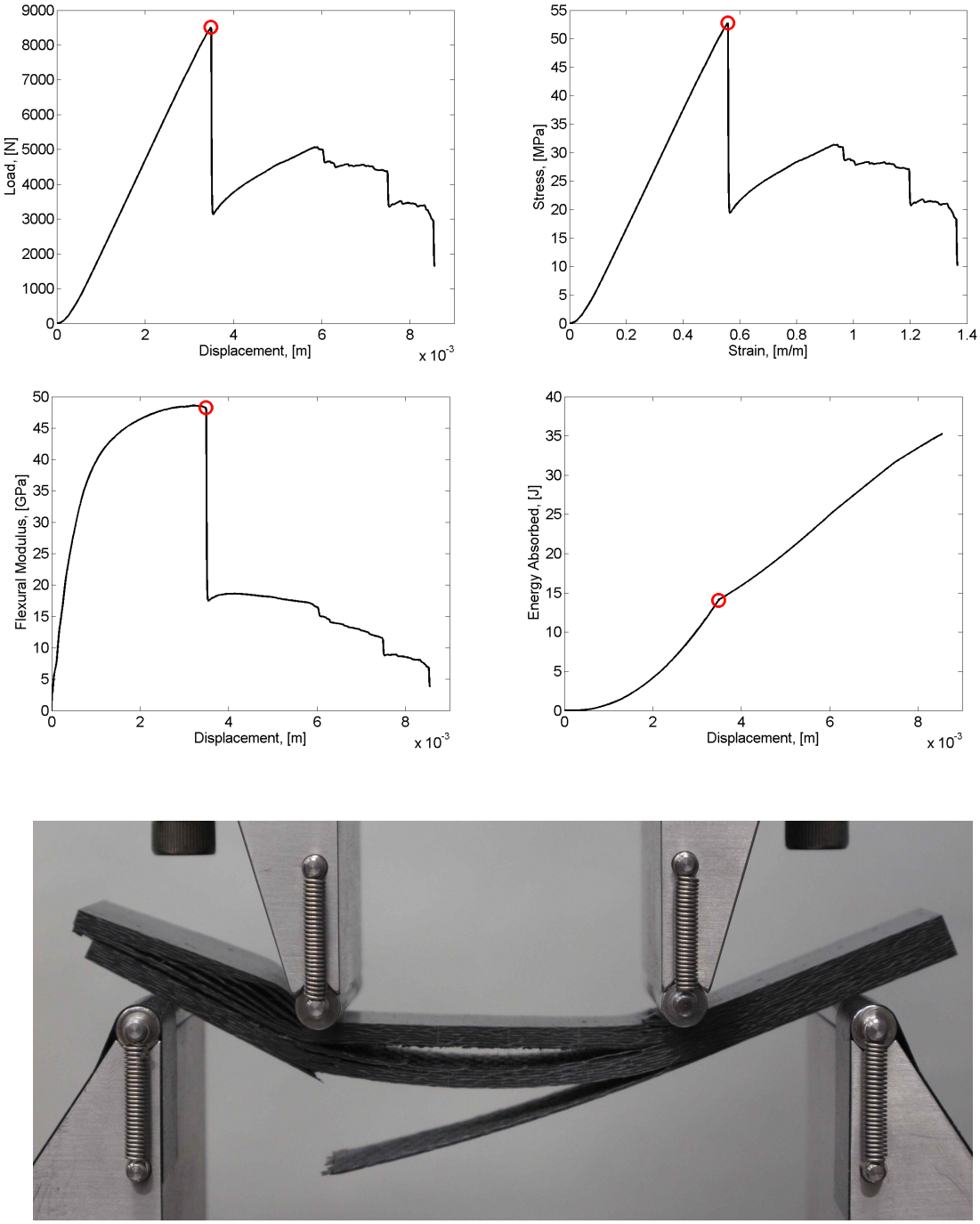

Figure 140: Measured and calculated response of Sample 401 subjected to four point bend testing. Red circle indicates maximum load.

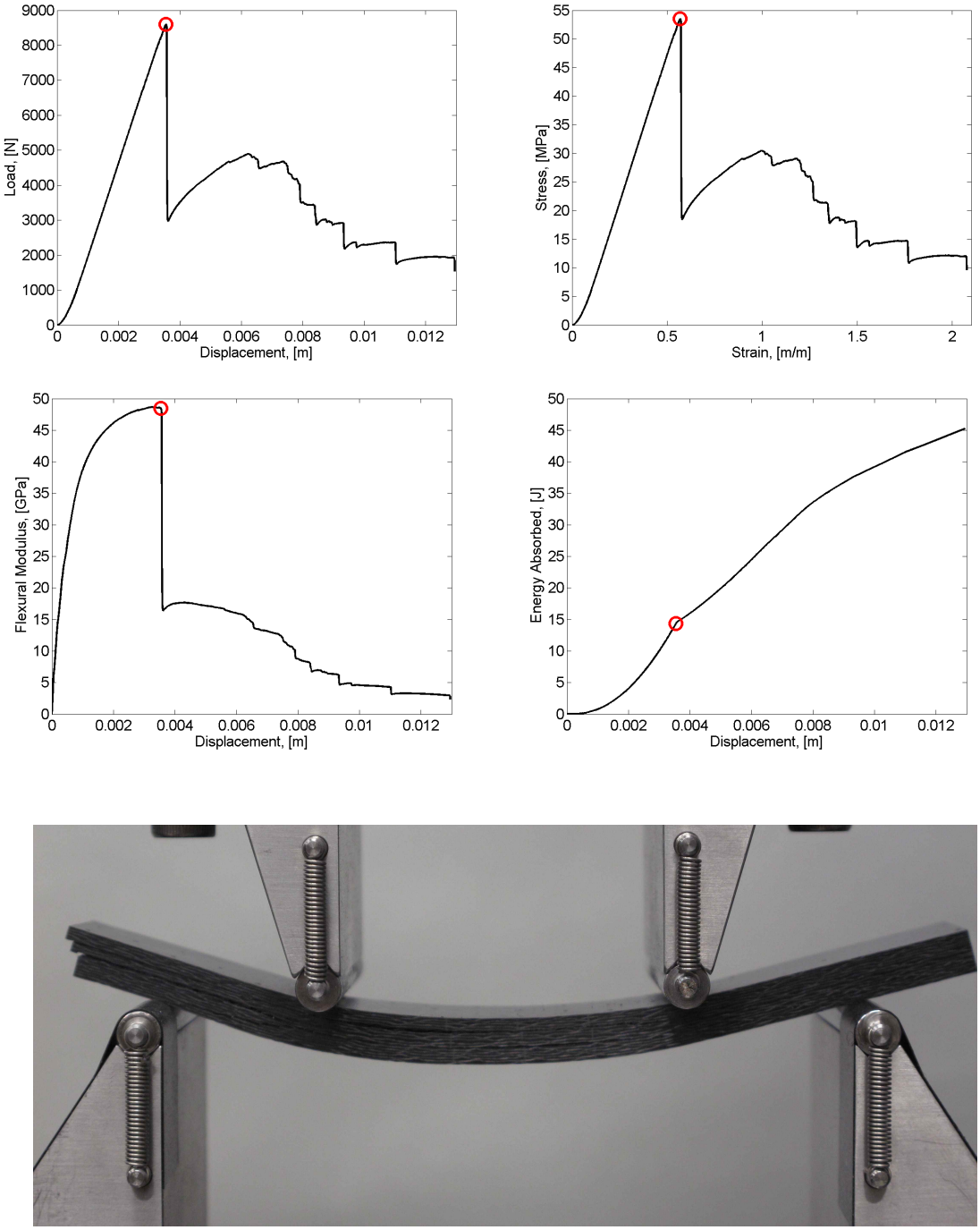

Figure 141: Measured and calculated response of Sample 402 subjected to four point bend testing. Red circle indicates maximum load.

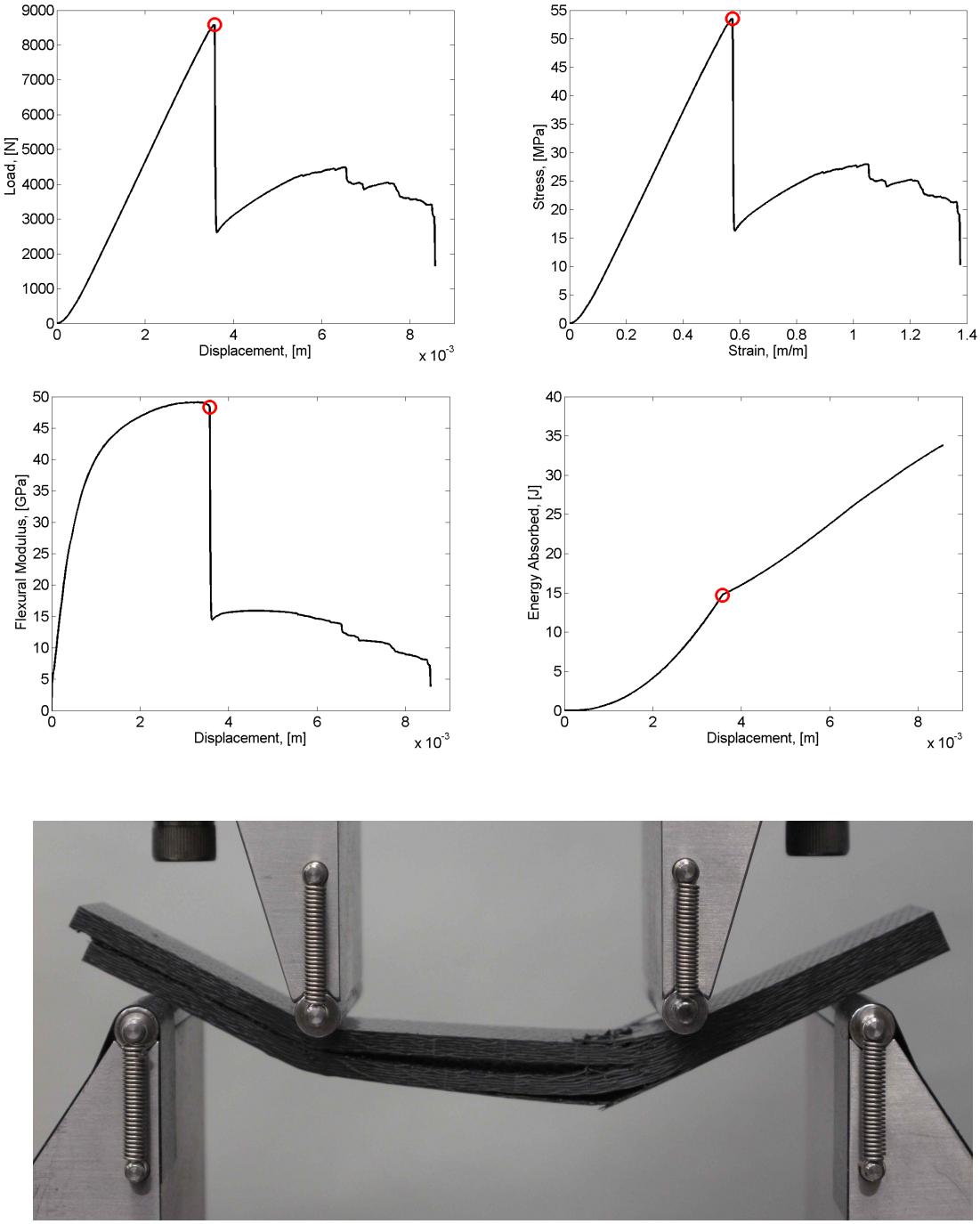

Figure 142: Measured and calculated response of Sample 403 subjected to four point bend testing. Red circle indicates maximum load.

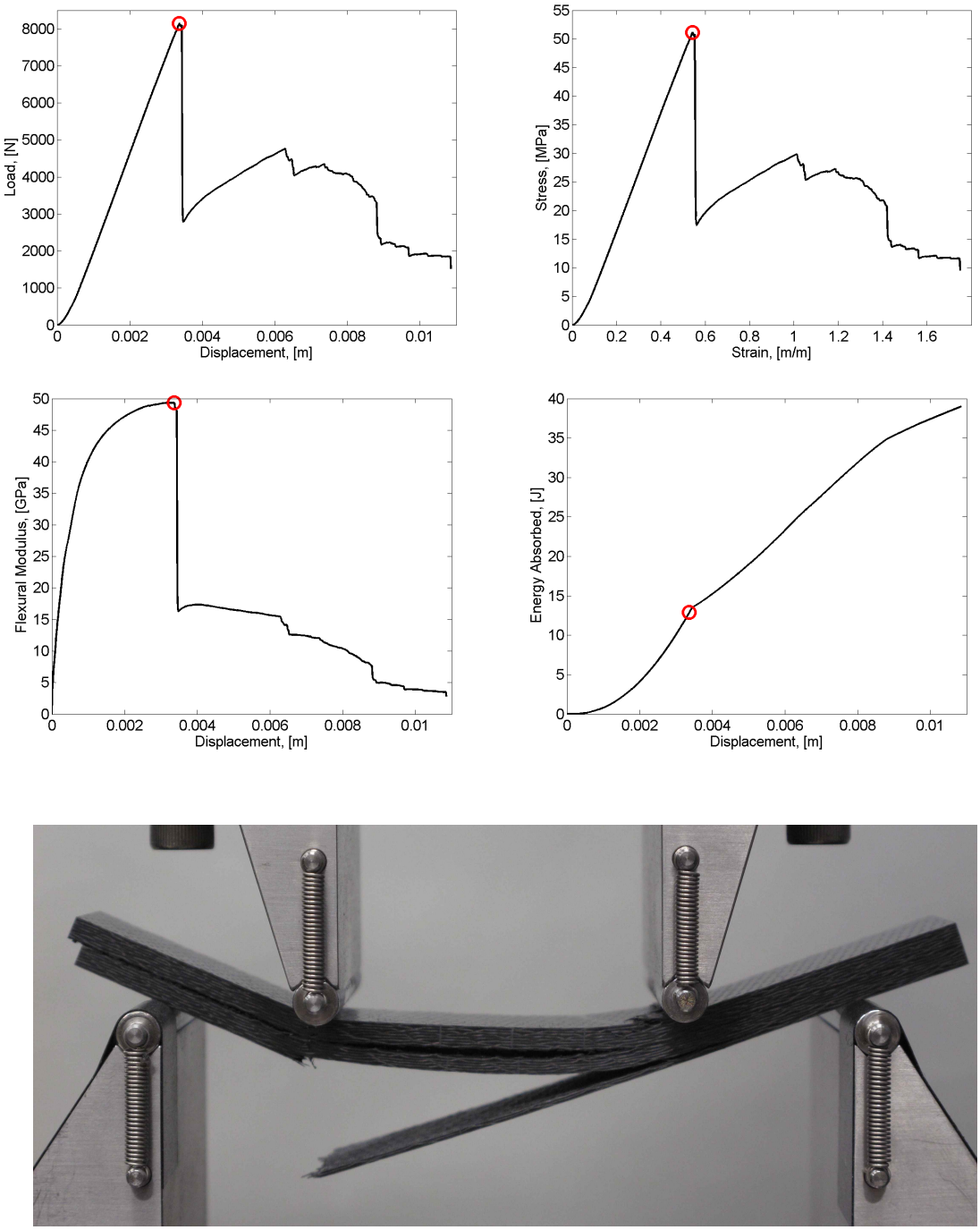

Figure 143: Measured and calculated response of Sample 404 subjected to four point bend testing. Red circle indicates maximum load.

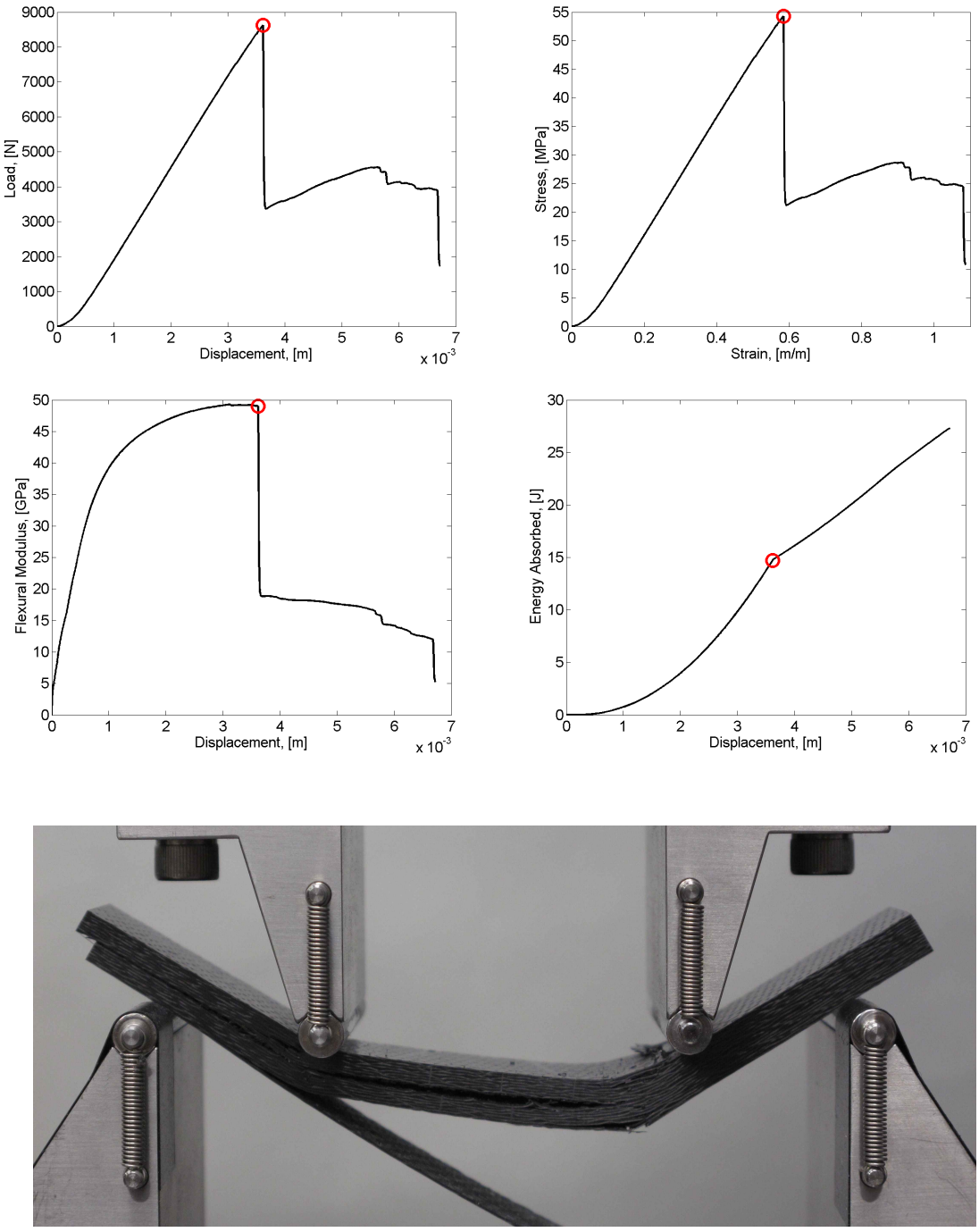

Figure 144: Measured and calculated response of Sample 407 subjected to four point bend testing. Red circle indicates maximum load.

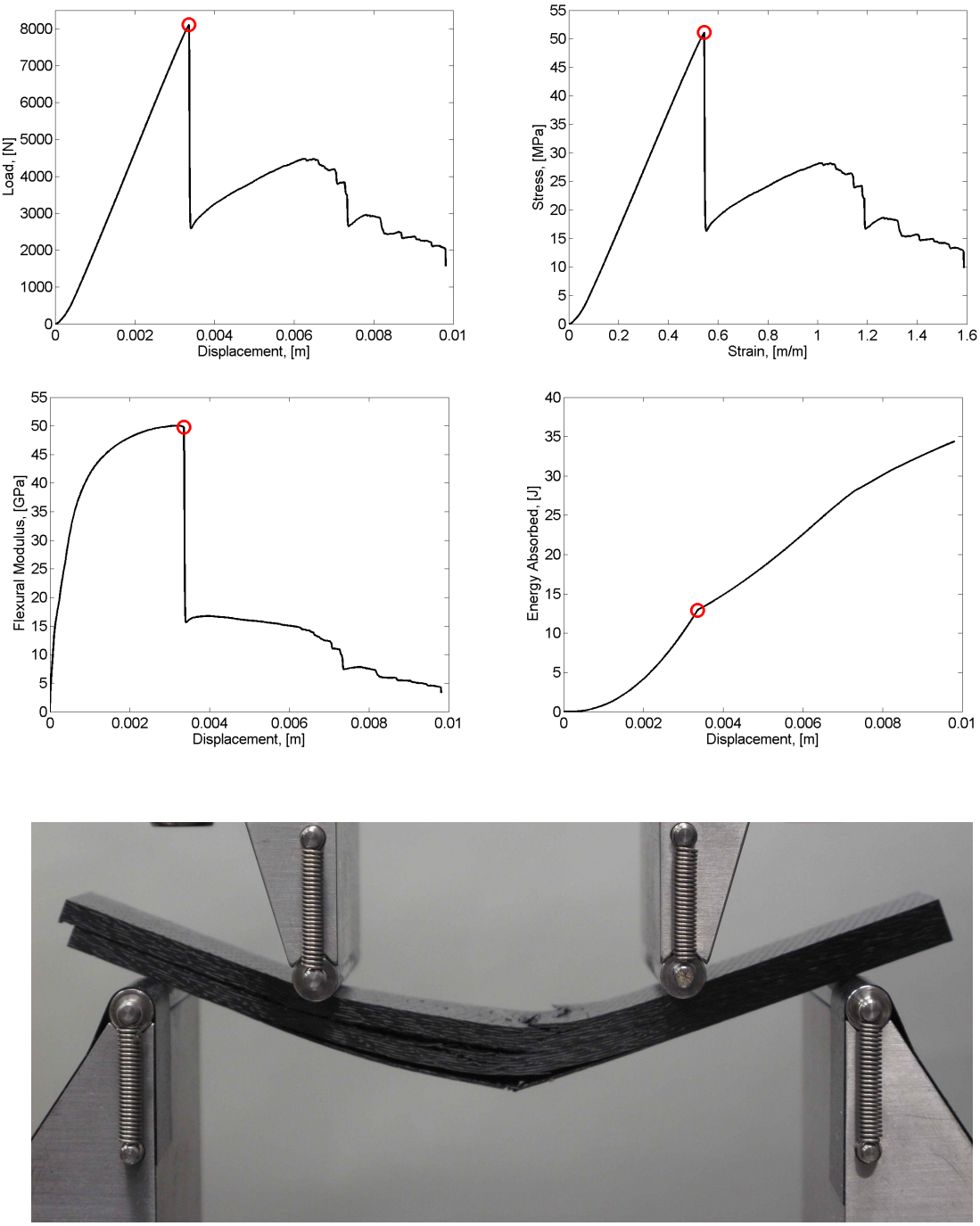

Figure 145: Measured and calculated response of Sample 408 subjected to four point bend testing. Red circle indicates maximum load.

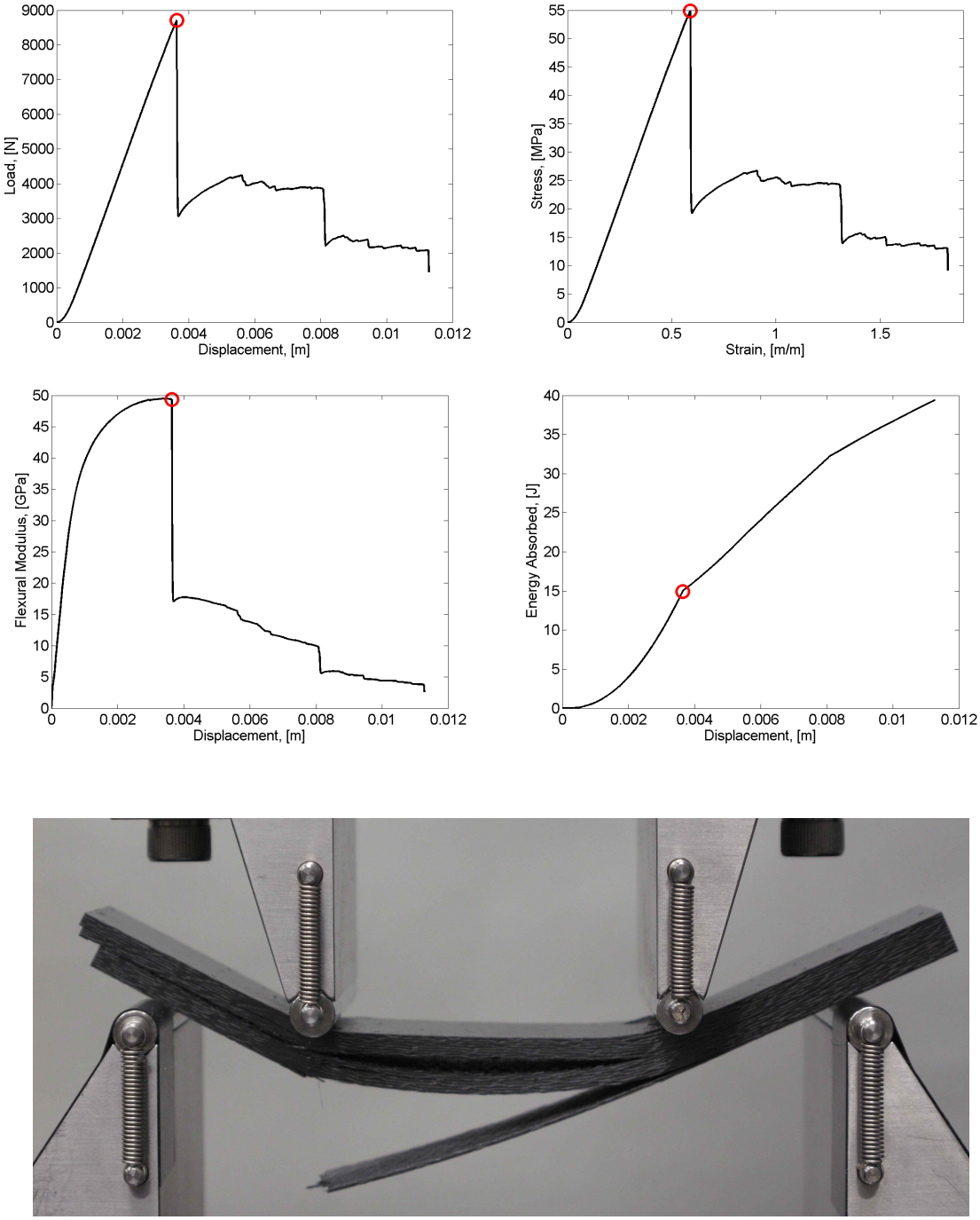

Figure 146: Measured and calculated response of Sample 409 subjected to four point bend testing. Red circle indicates maximum load.

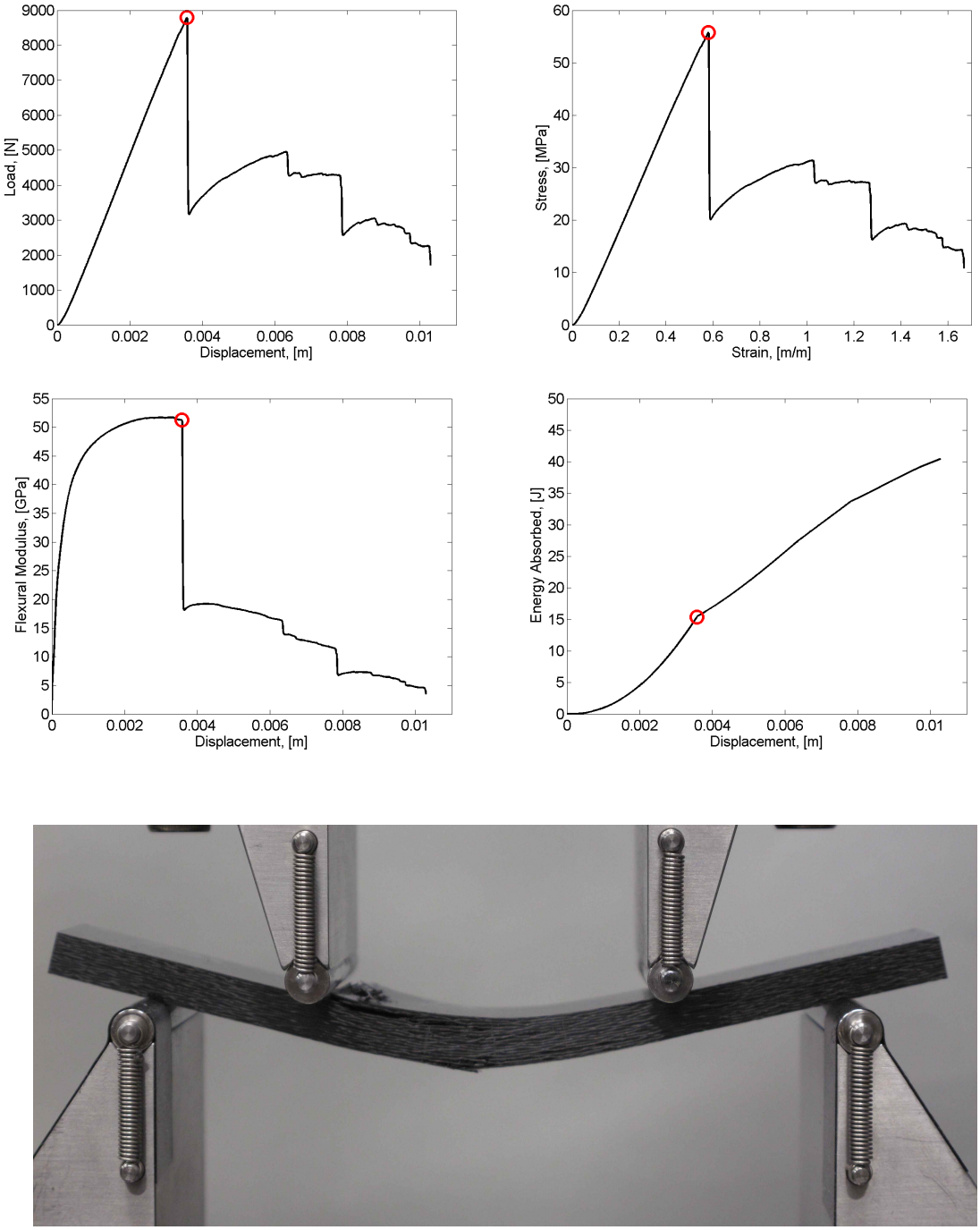

Figure 147: Measured and calculated response of Sample 410 subjected to four point bend testing. Red circle indicates maximum load.

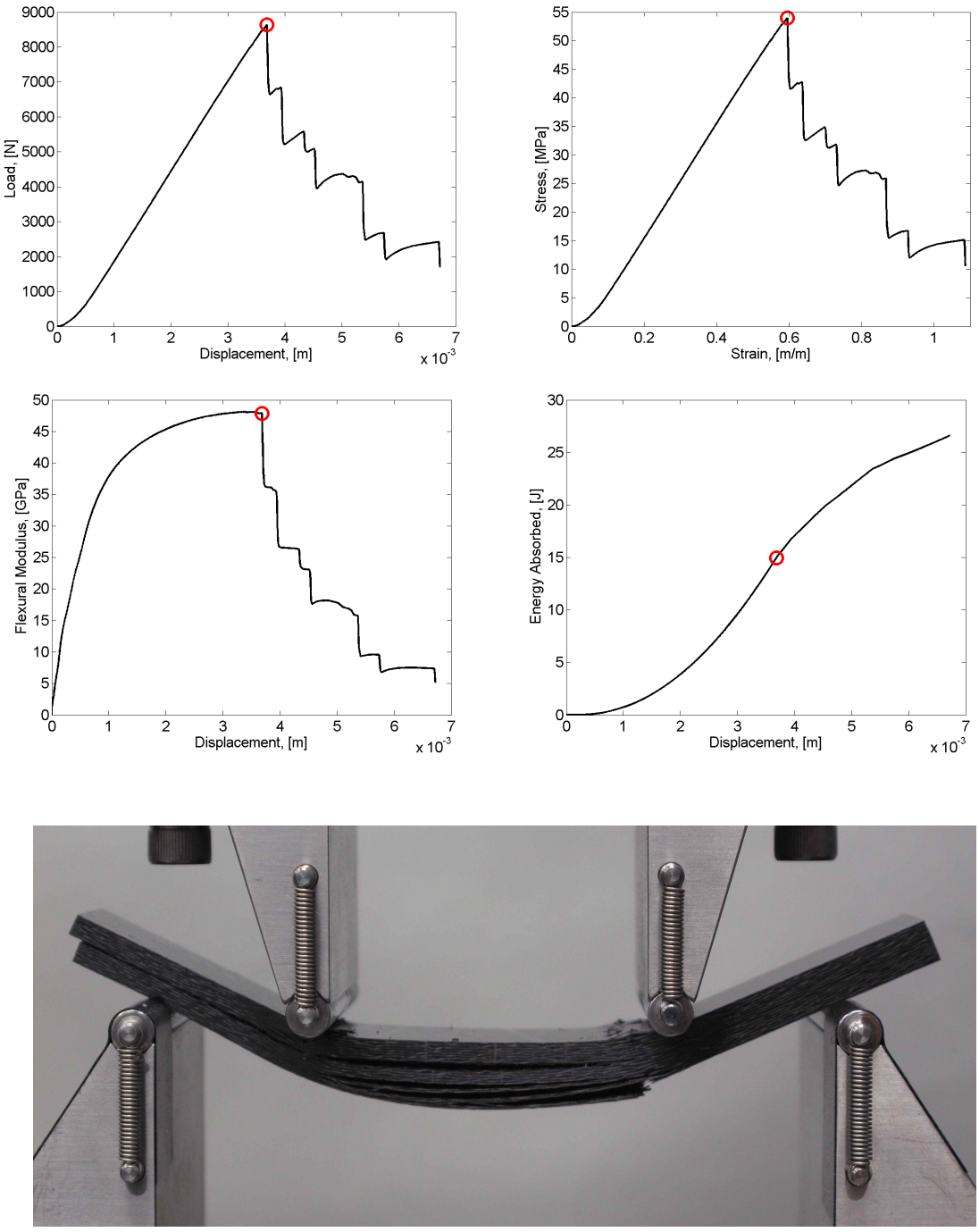

Figure 148: Measured and calculated response of Sample 501 subjected to four point bend testing. Red circle indicates maximum load.

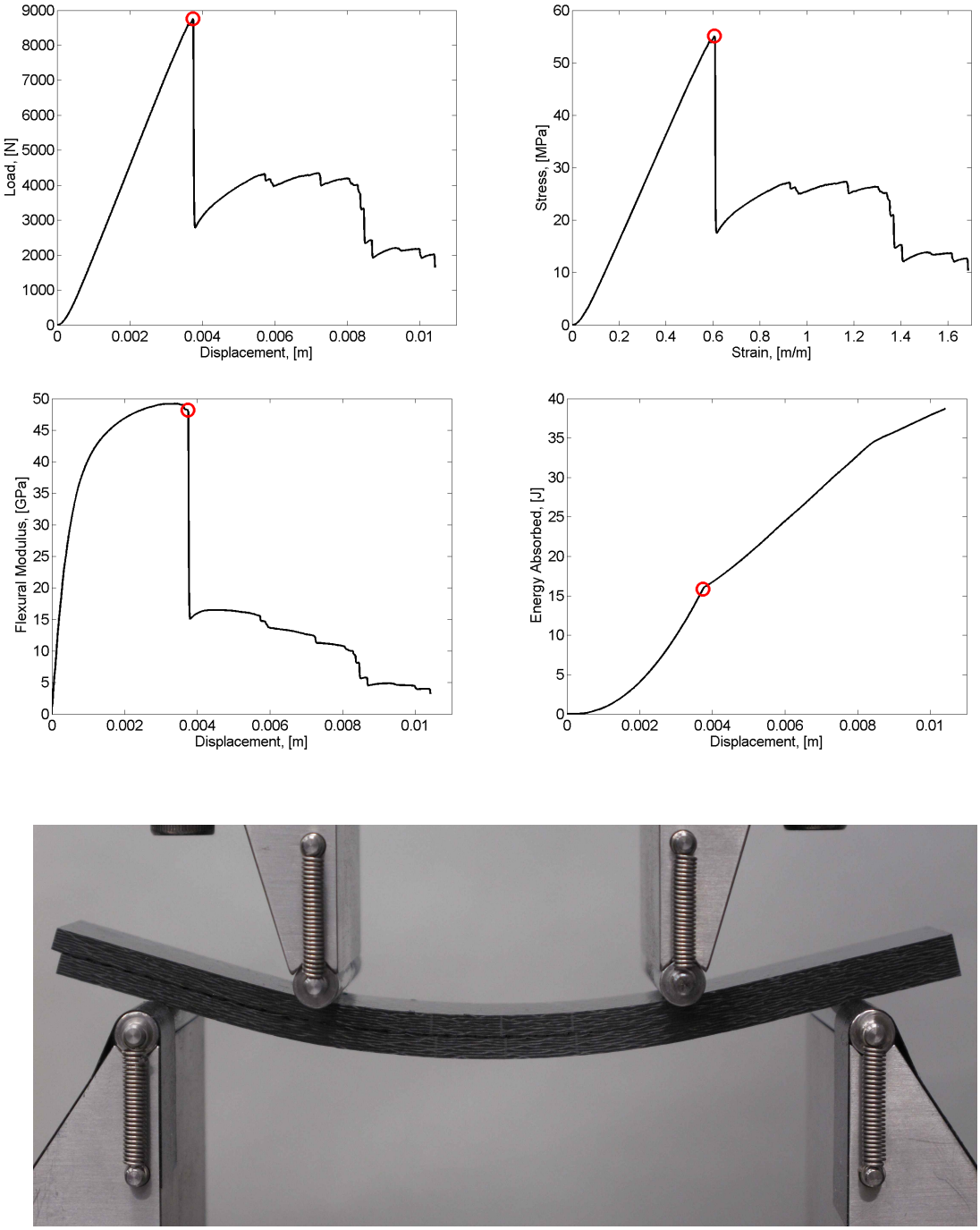

Figure 149: Measured and calculated response of Sample 502 subjected to four point bend testing. Red circle indicates maximum load.

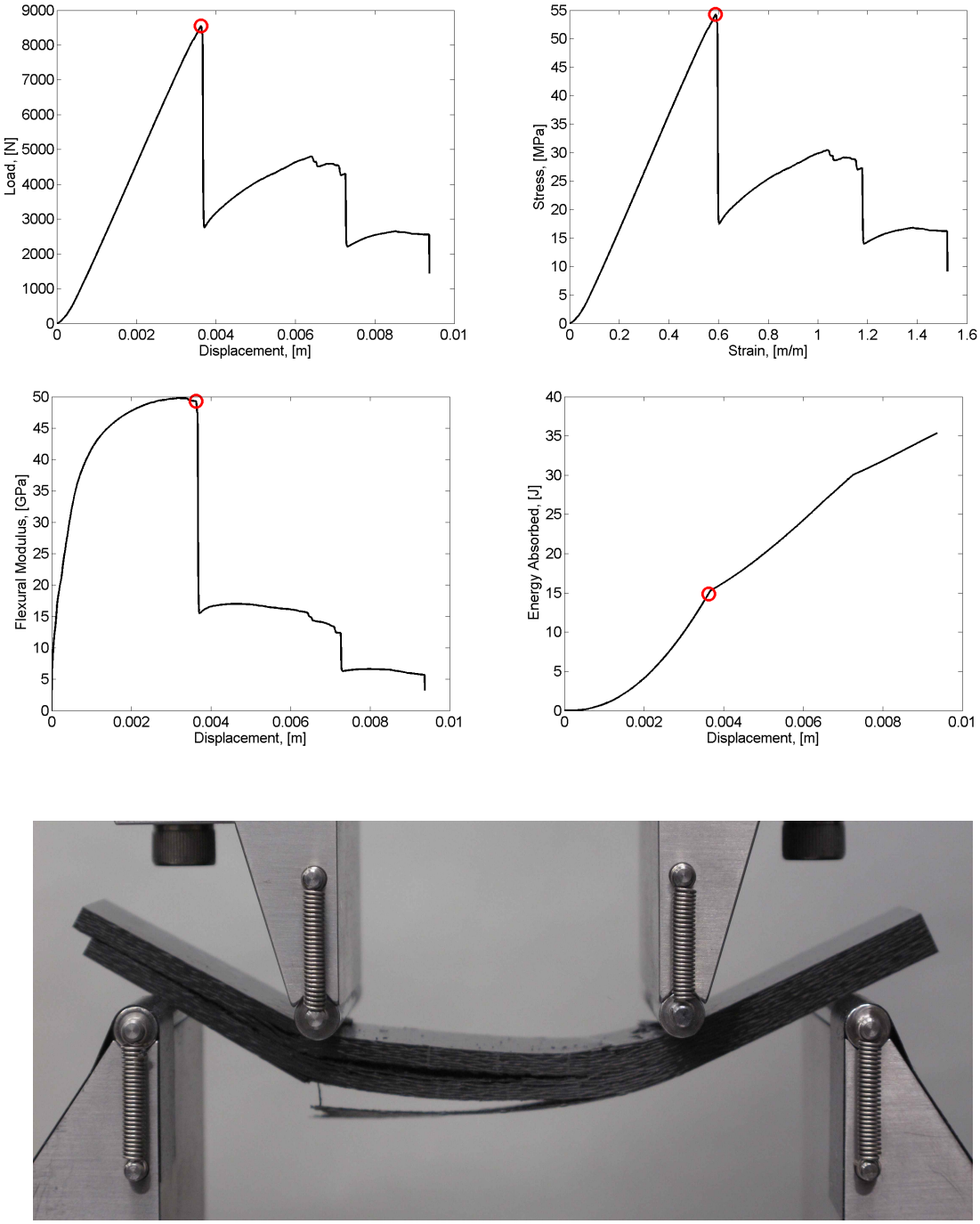

Figure 150: Measured and calculated response of Sample 503 subjected to four point bend testing. Red circle indicates maximum load.

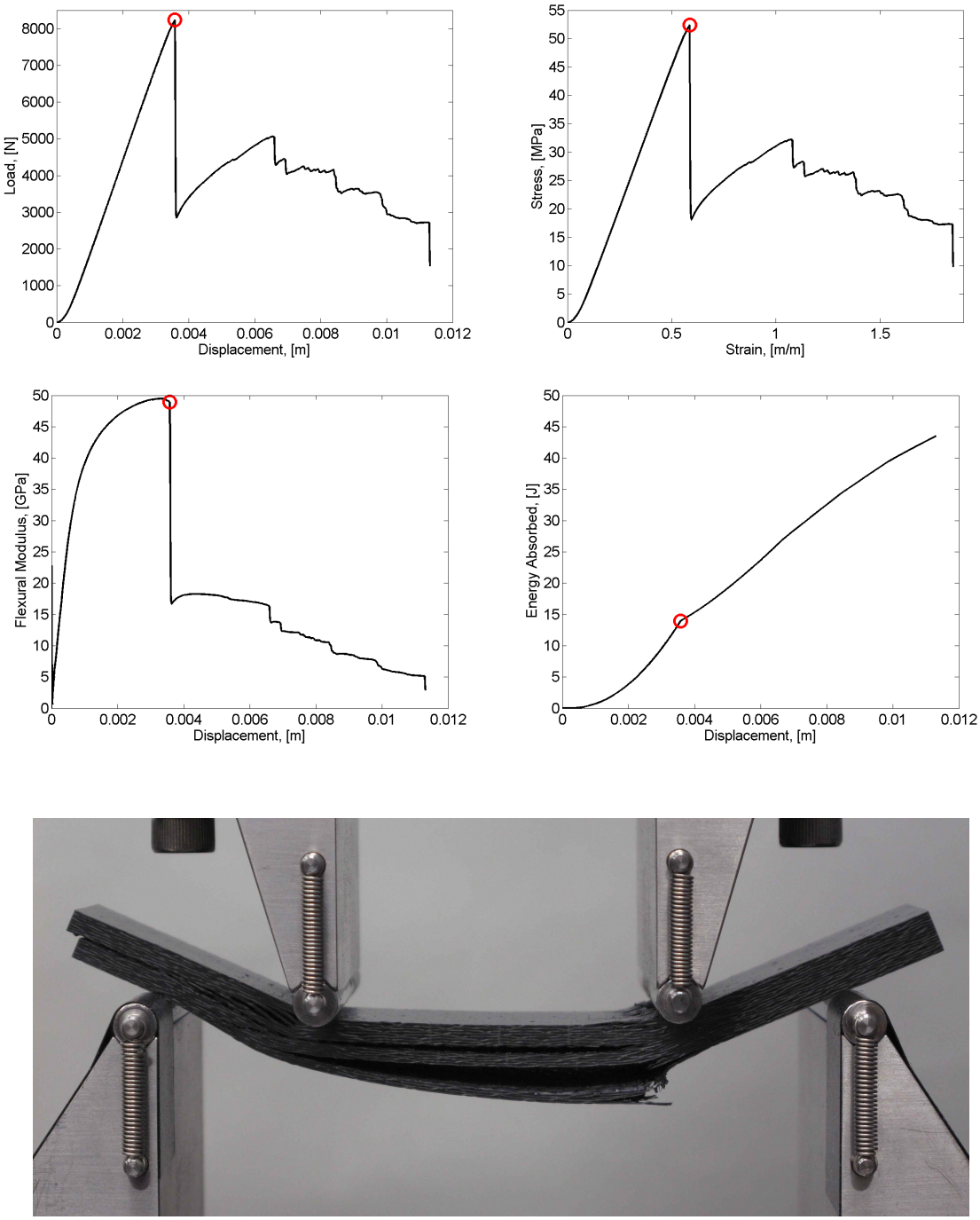

Figure 151: Measured and calculated response of Sample 504 subjected to four point bend testing. Red circle indicates maximum load.

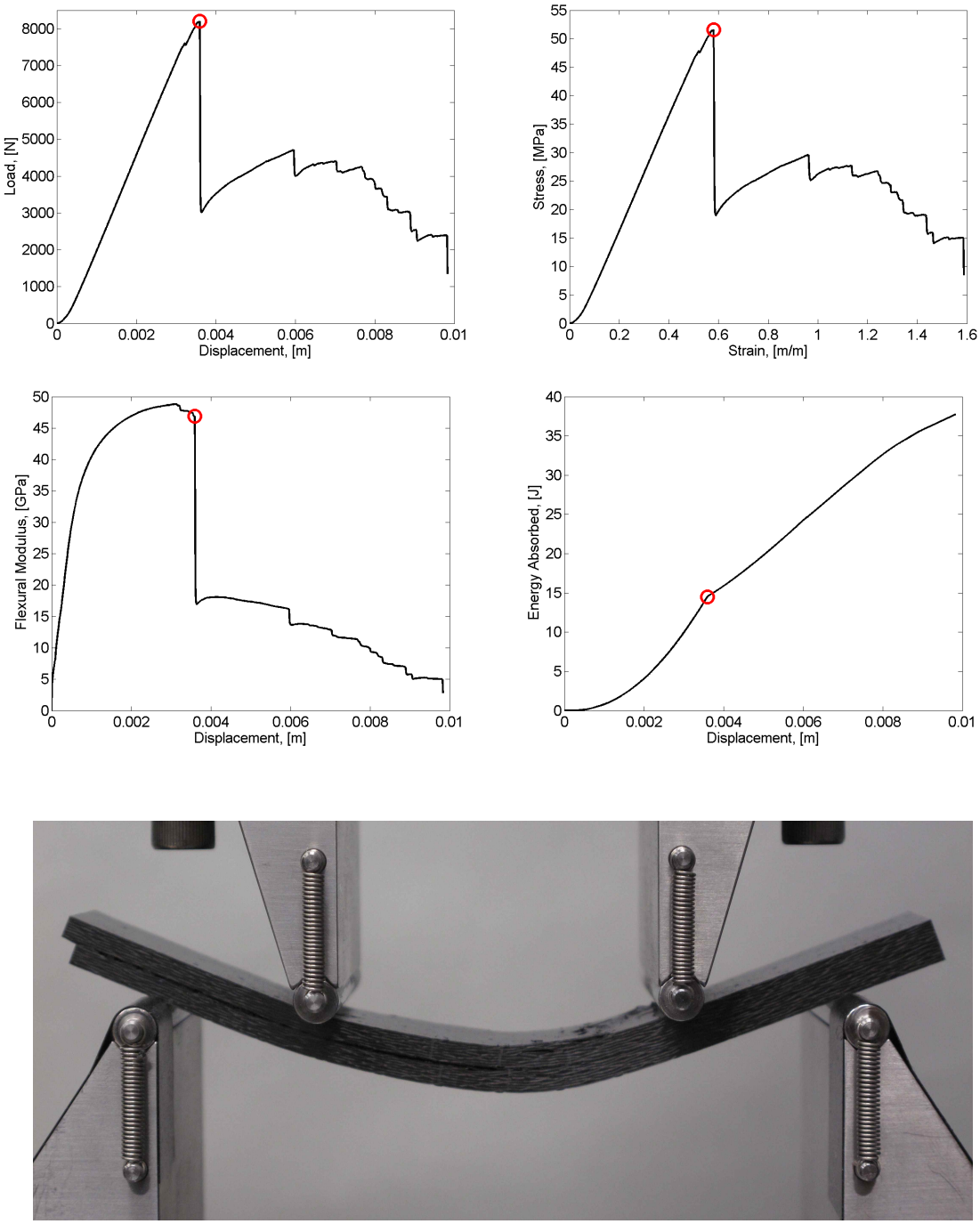

Figure 152: Measured and calculated response of Sample 507 subjected to four point bend testing. Red circle indicates maximum load.

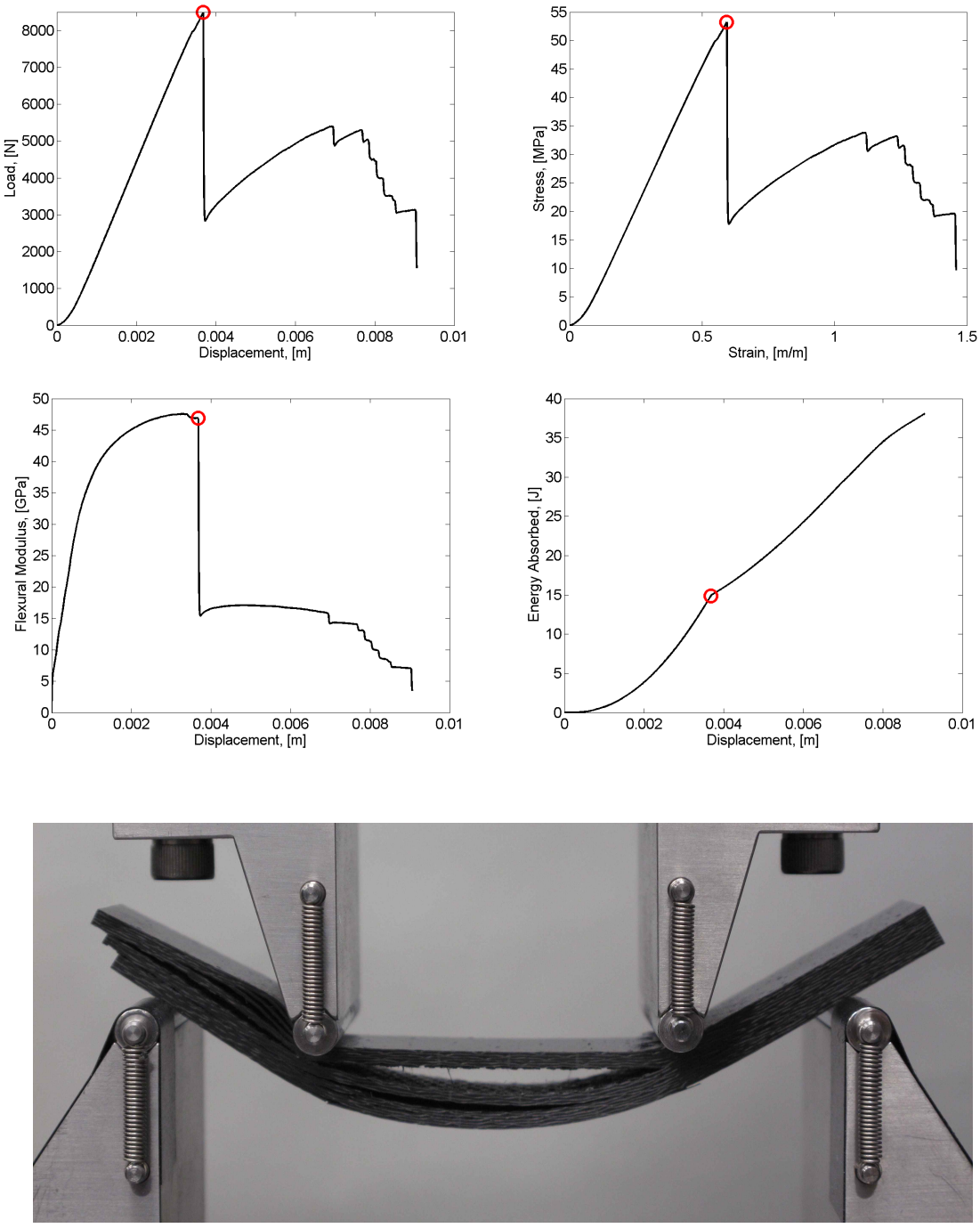

Figure 153: Measured and calculated response of Sample 508 subjected to four point bend testing. Red circle indicates maximum load.

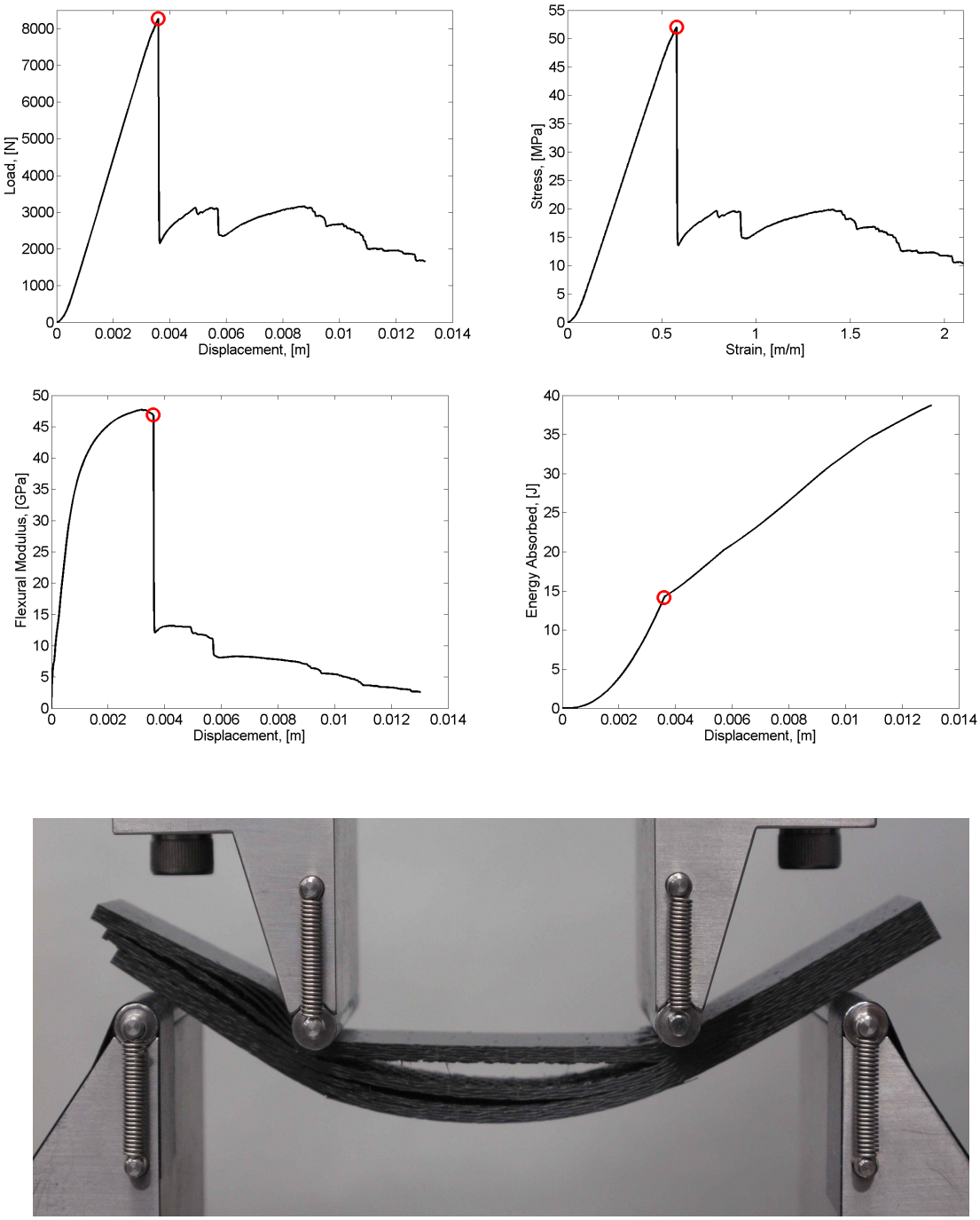

Figure 154: Measured and calculated response of Sample 509 subjected to four point bend testing. Red circle indicates maximum load.

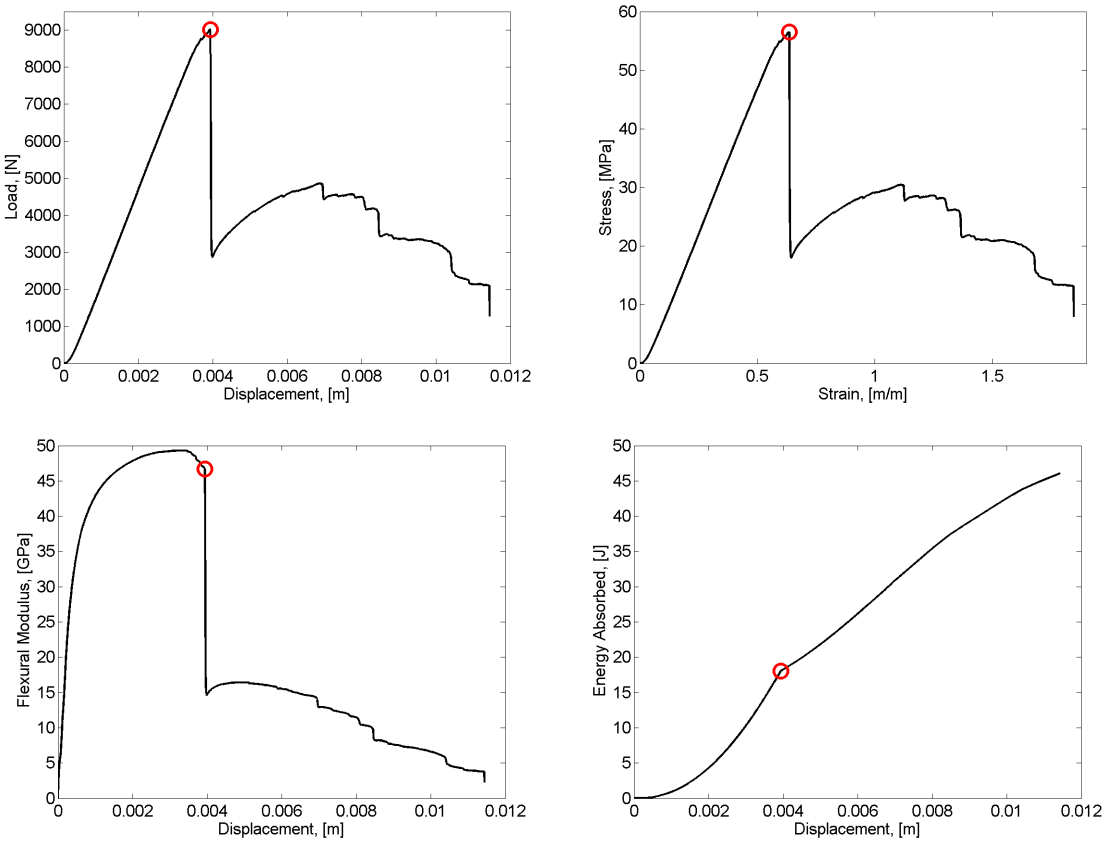

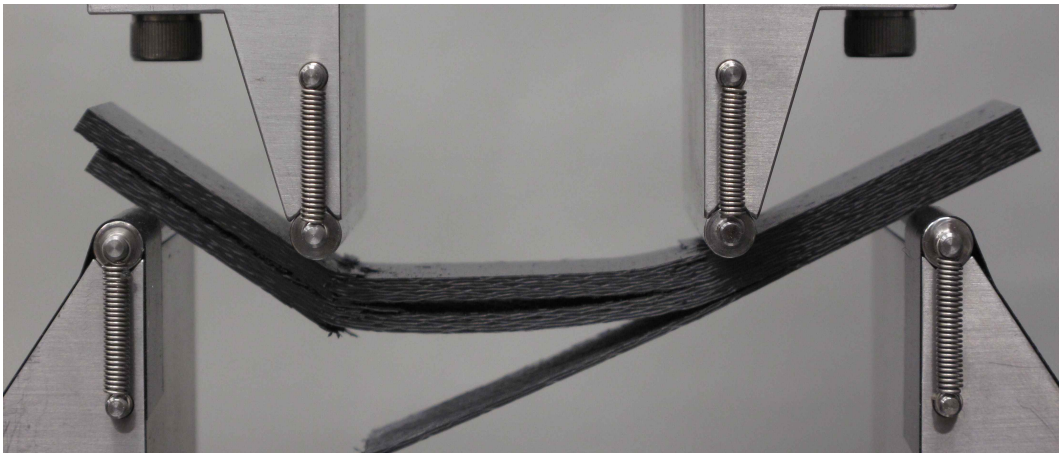

Figure 155: Measured and calculated response of Sample 510 subjected to four point bend testing. Red circle indicates maximum load.

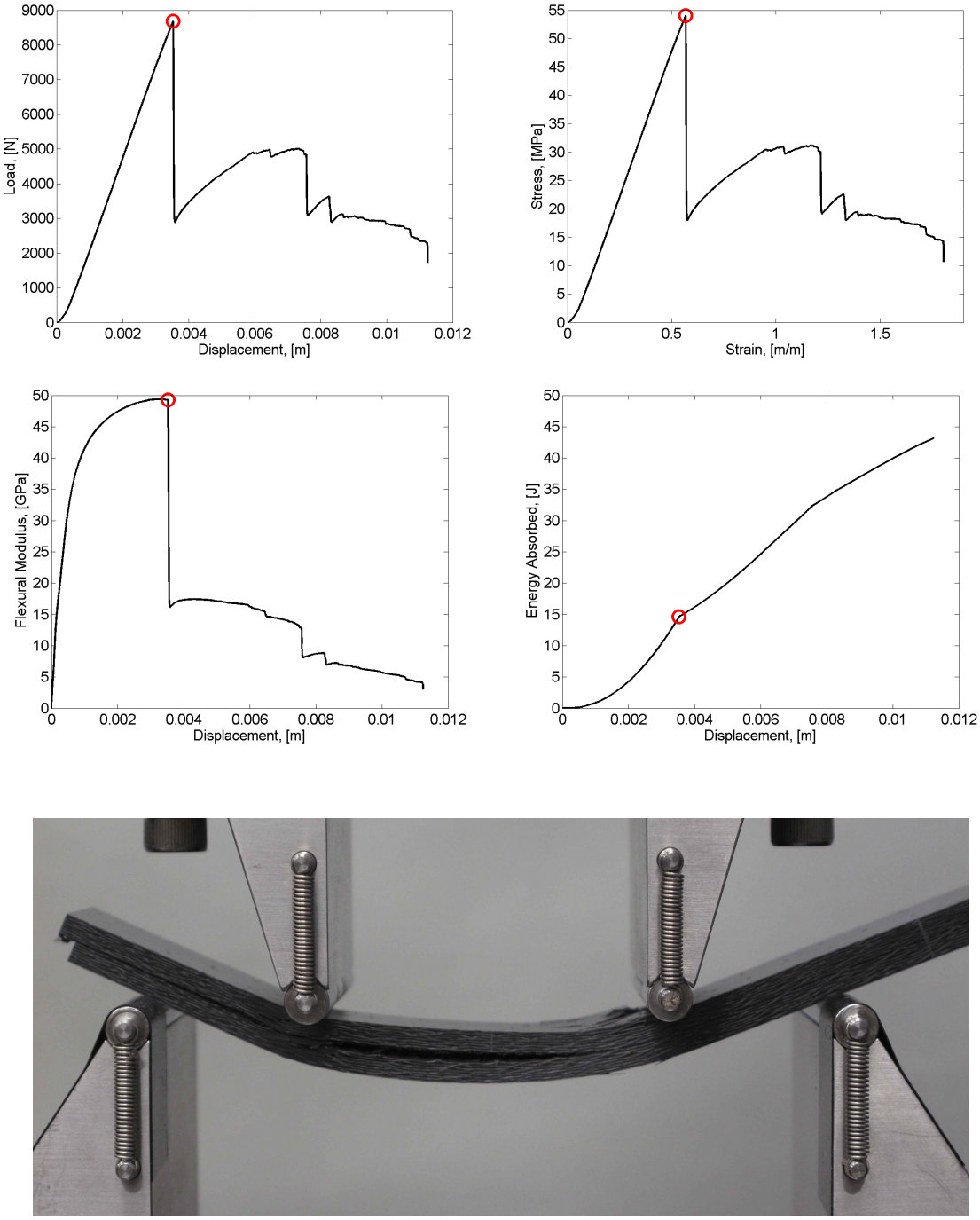

Figure 156: Measured and calculated response of Sample 601 subjected to four point bend testing. Red circle indicates maximum load.

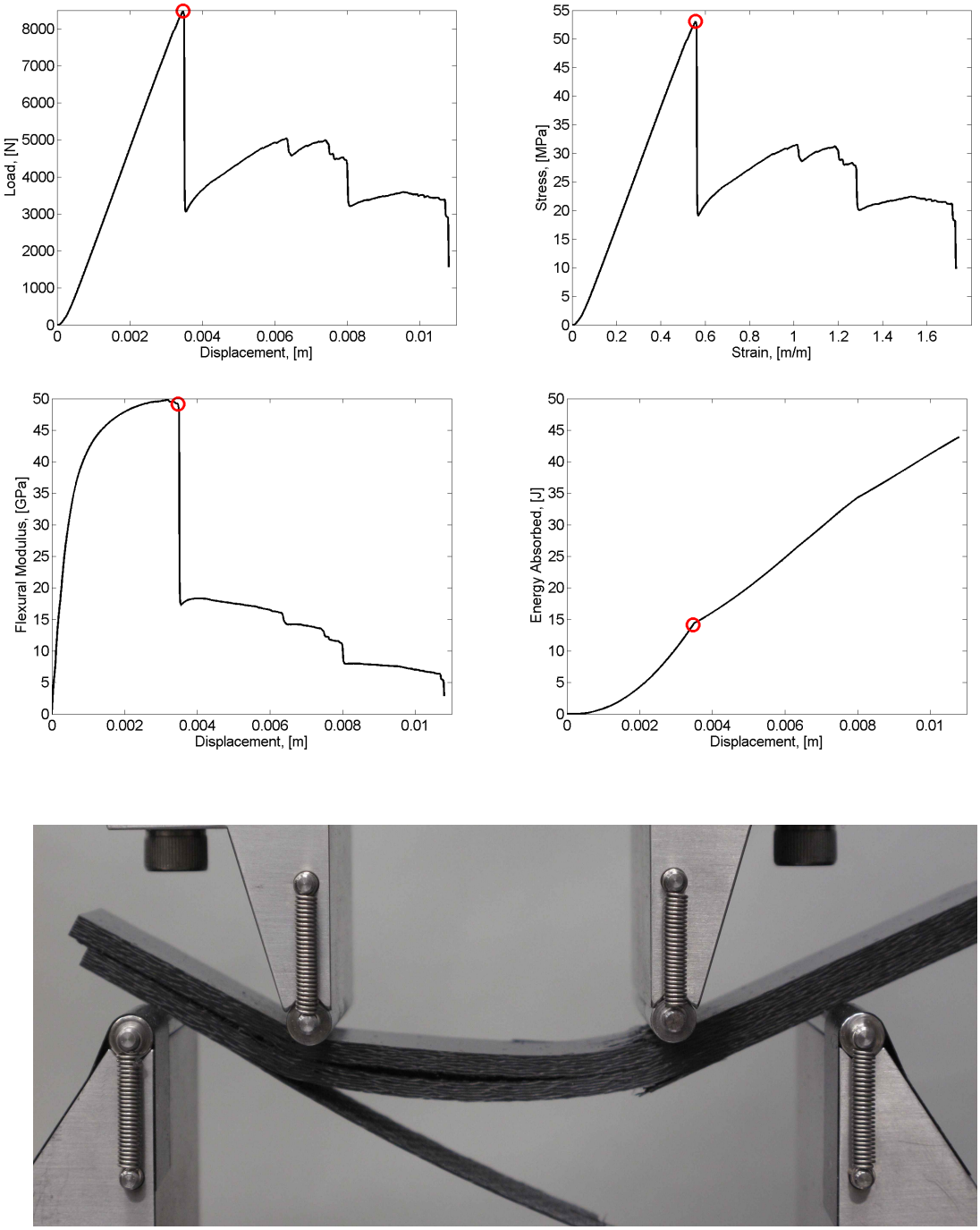

Figure 157: Measured and calculated response of Sample 602 subjected to four point bend testing. Red circle indicates maximum load.

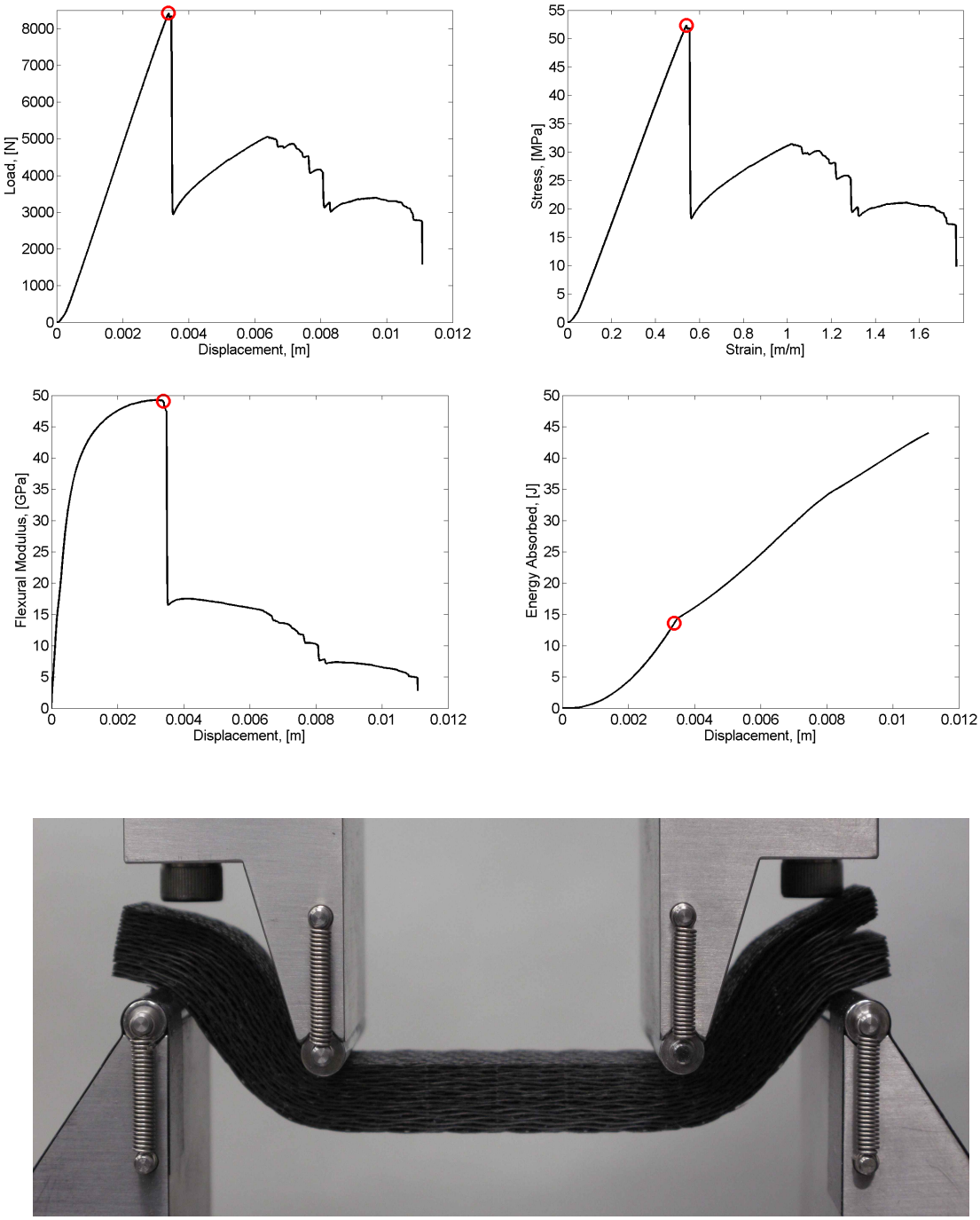

Figure 158: Measured and calculated response of Sample 603 subjected to four point bend testing. Red circle indicates maximum load.

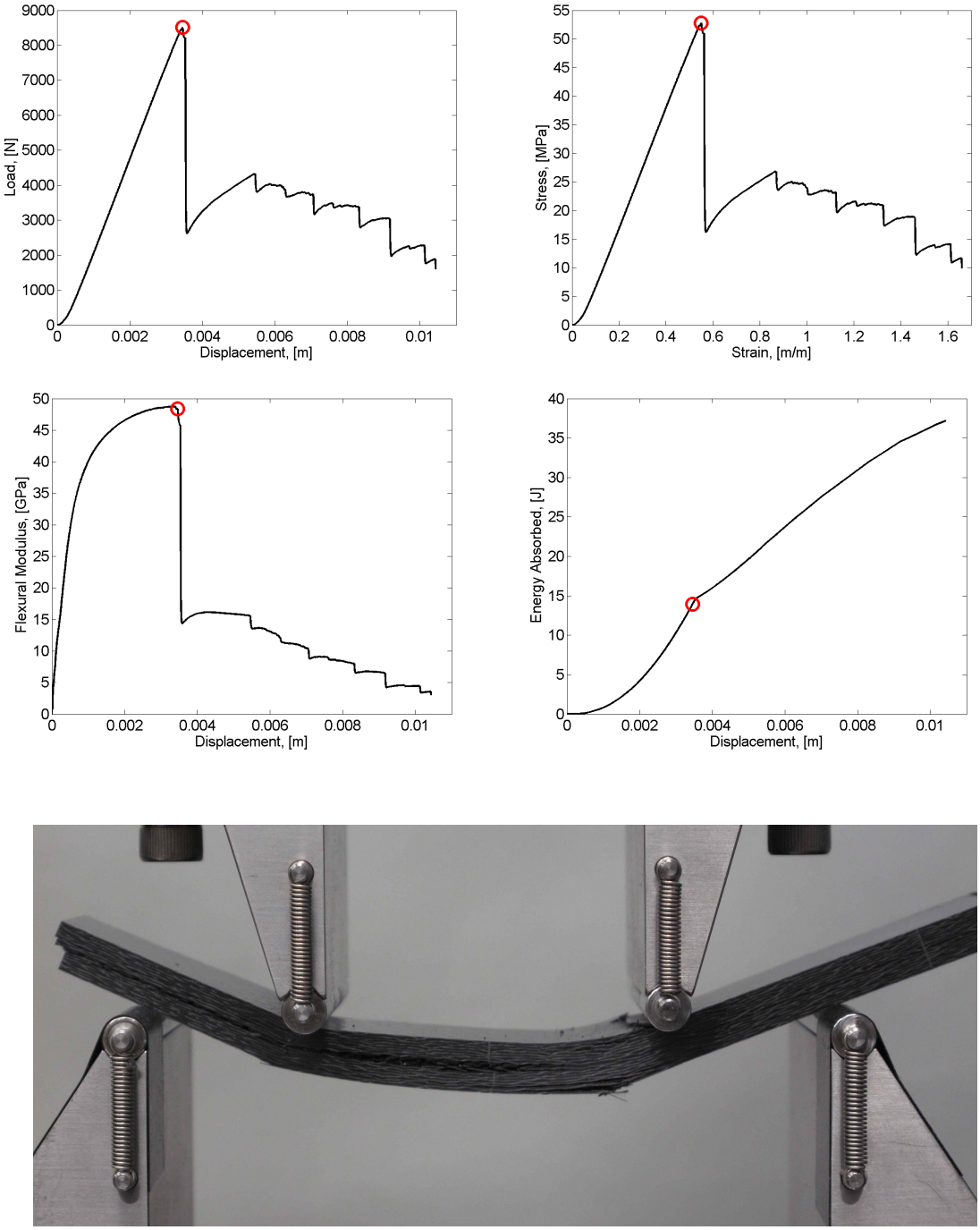

Figure 159: Measured and calculated response of Sample 604 subjected to four point bend testing. Red circle indicates maximum load.

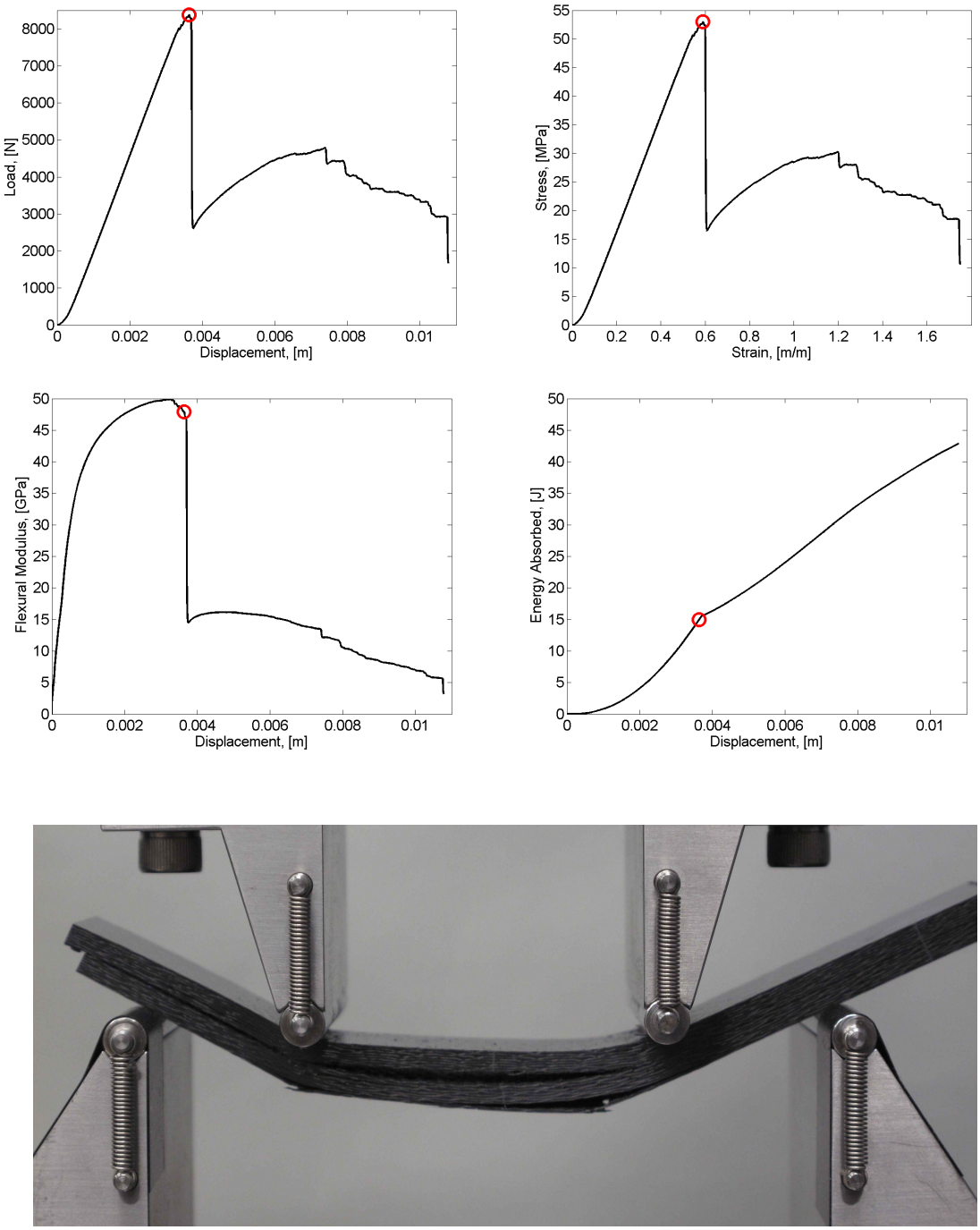

Figure 160: Measured and calculated response of Sample 607 subjected to four point bend testing. Red circle indicates maximum load.

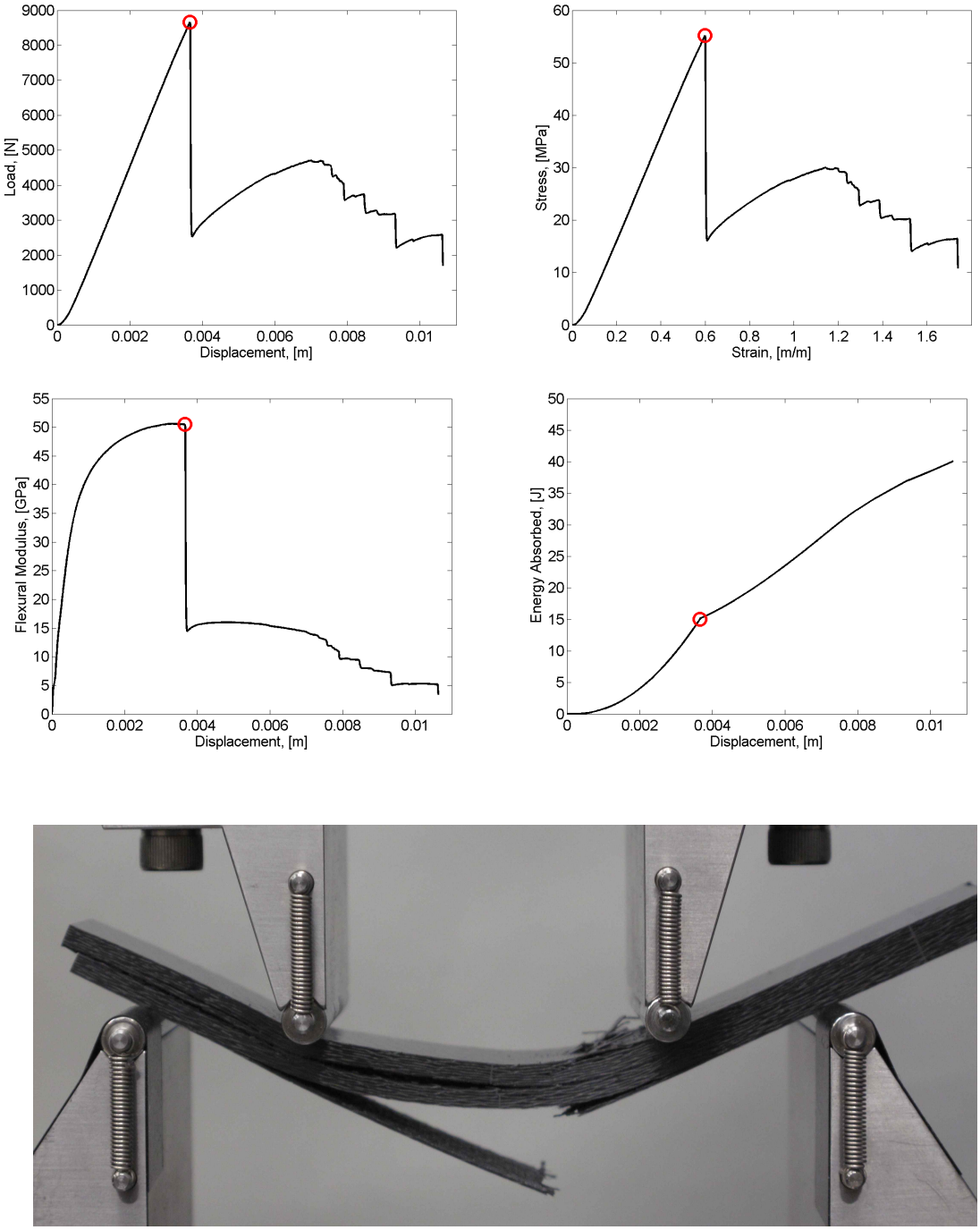

Figure 161: Measured and calculated response of Sample 608 subjected to four point bend testing. Red circle indicates maximum load.

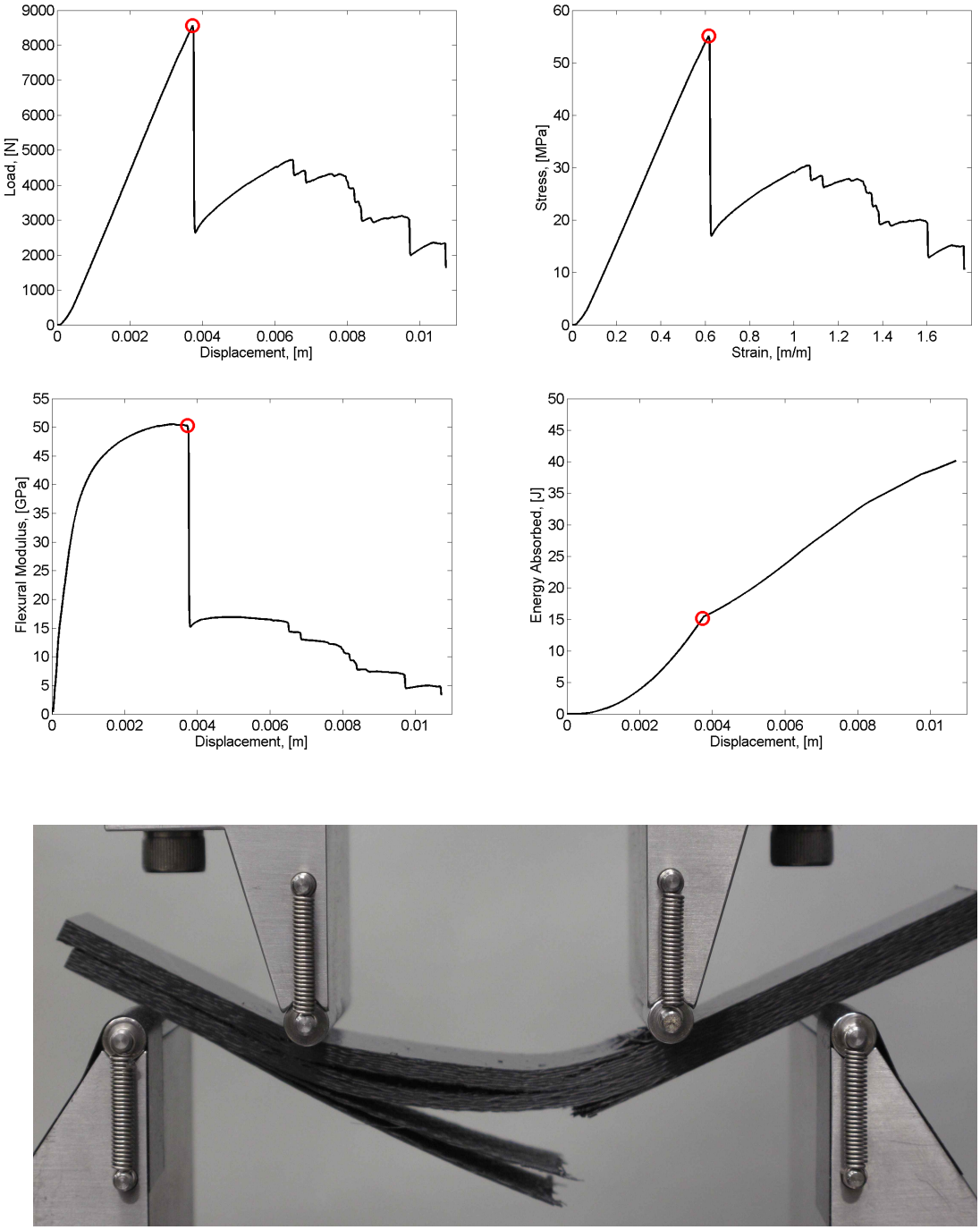

Figure 162: Measured and calculated response of Sample 609 subjected to four point bend testing. Red circle indicates maximum load.

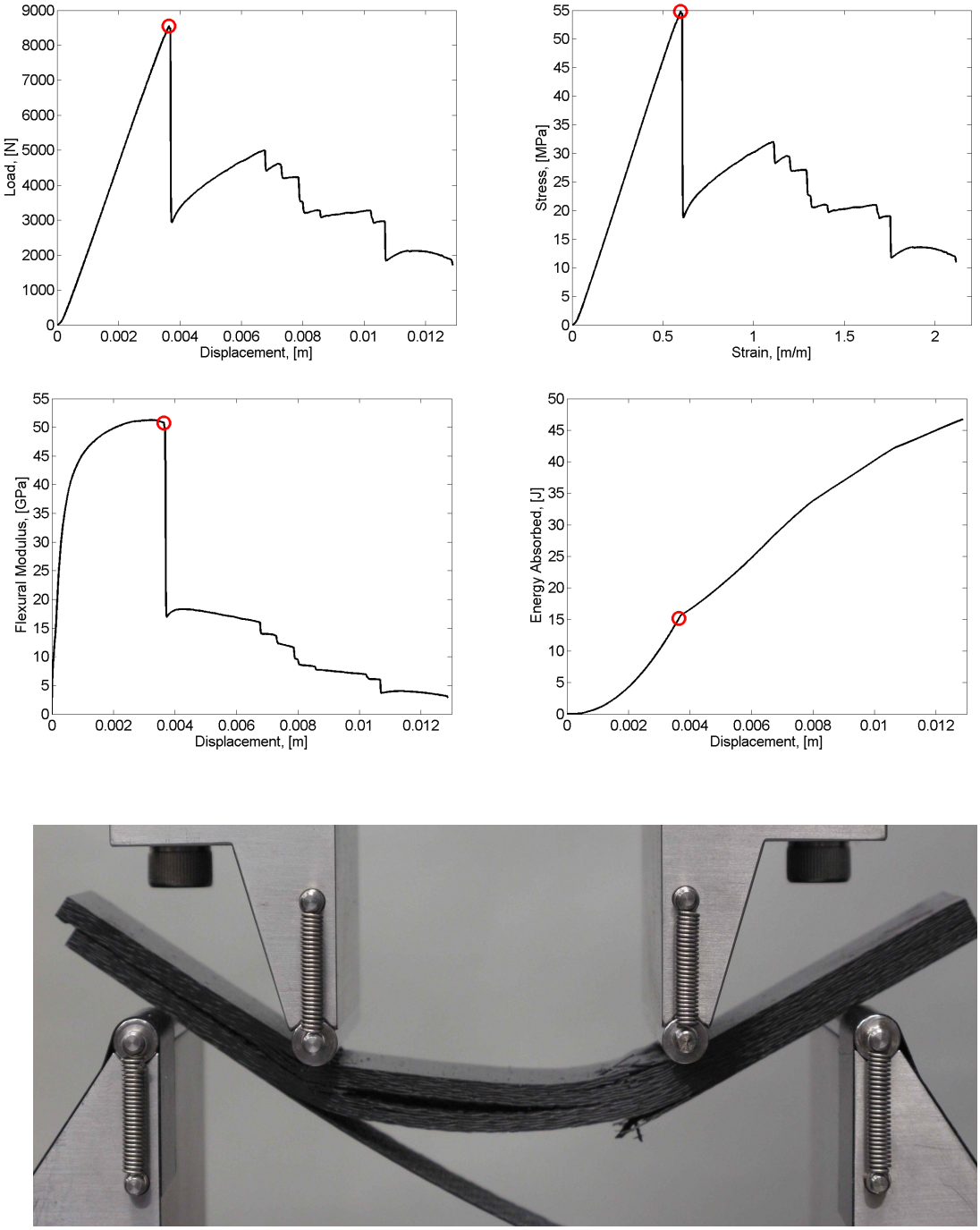

Figure 163: Measured and calculated response of Sample 610 subjected to four point bend testing. Red circle indicates maximum load.

Appendix B: Short Beam Shear

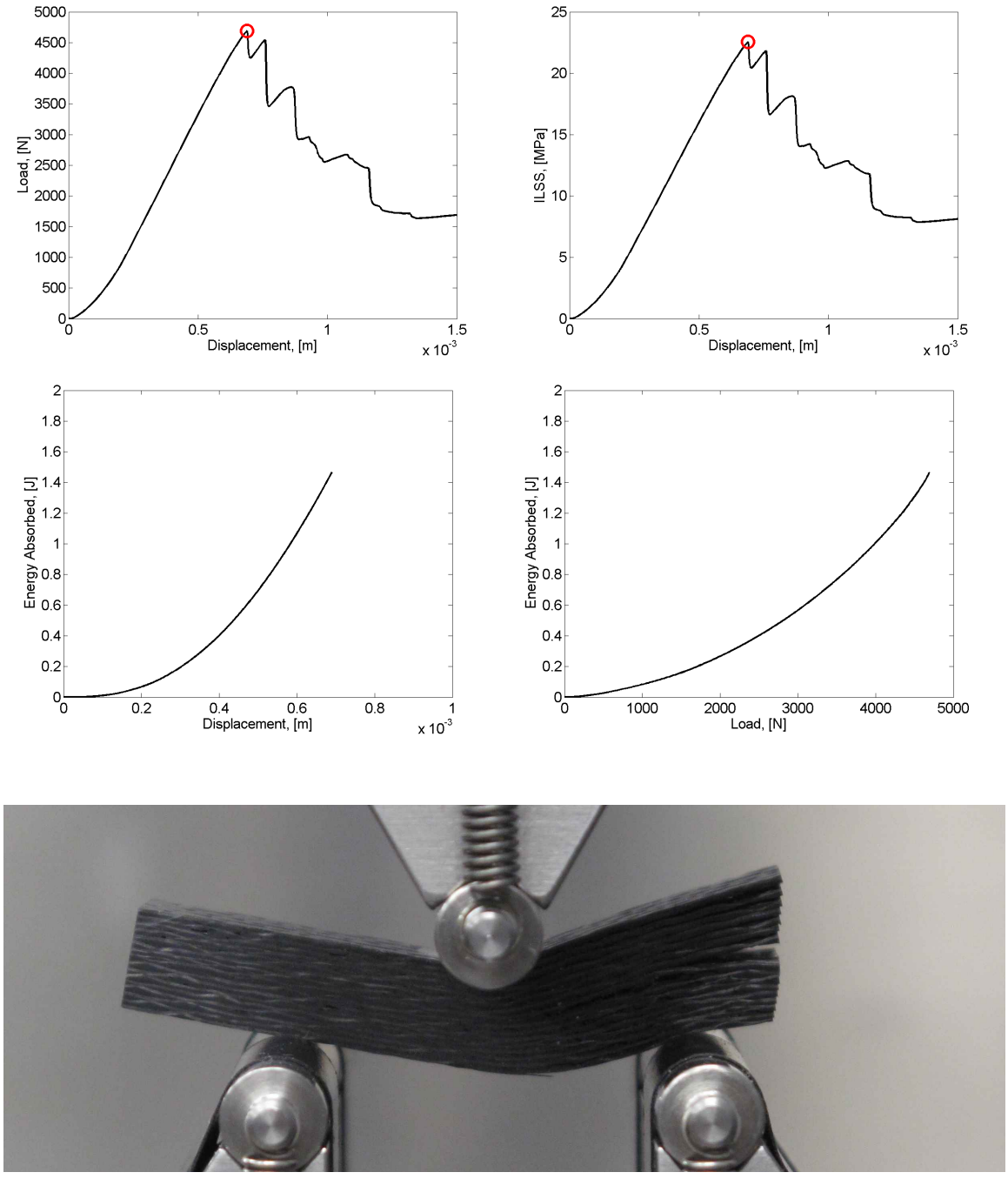

Figure 164: Measured and calculated response of Sample 201 subjected to short beam shear testing. Red circle indicates maximum load.

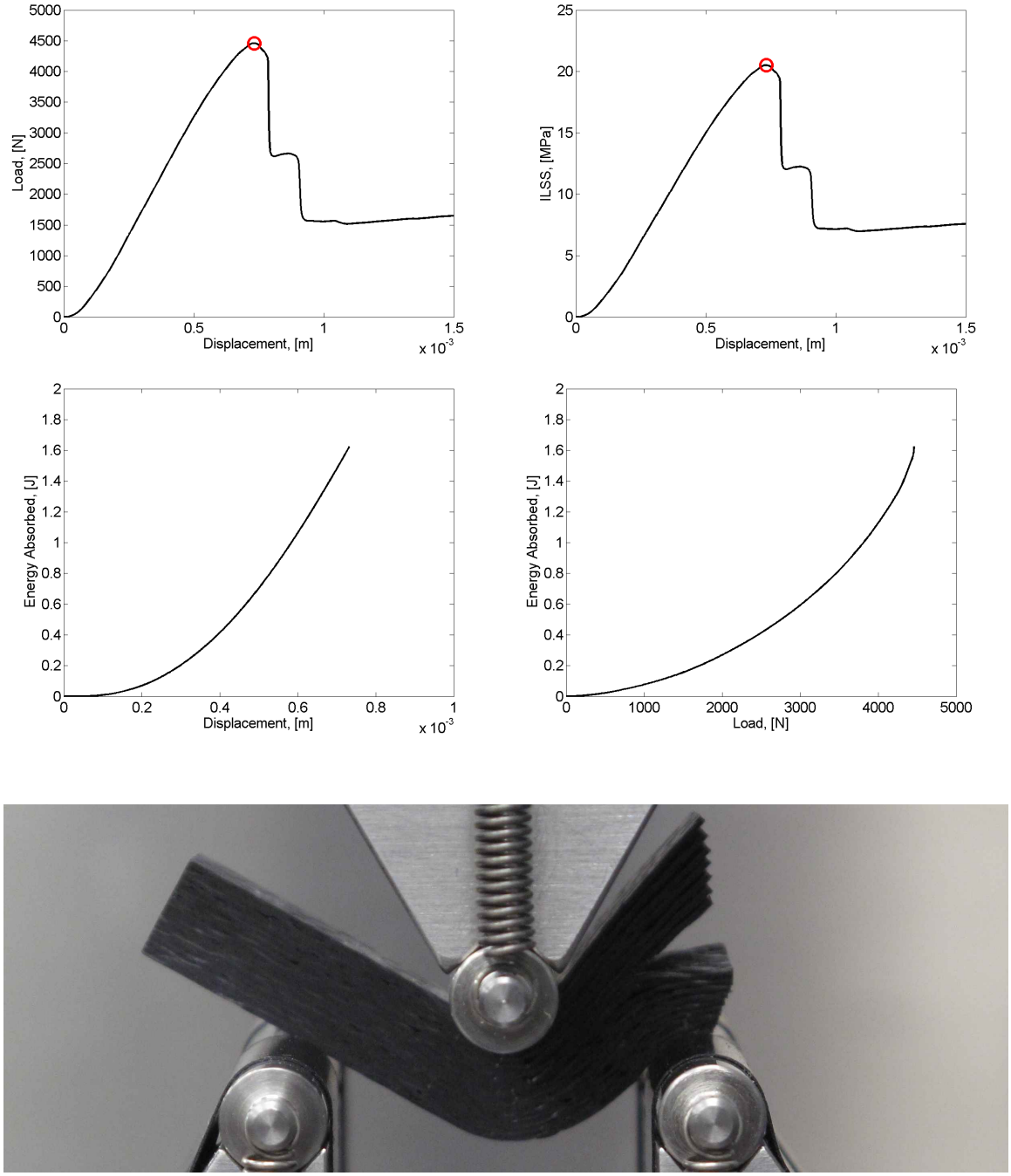

Figure 165: Measured and calculated response of Sample 202 subjected to short beam shear testing. Red circle indicates maximum load.

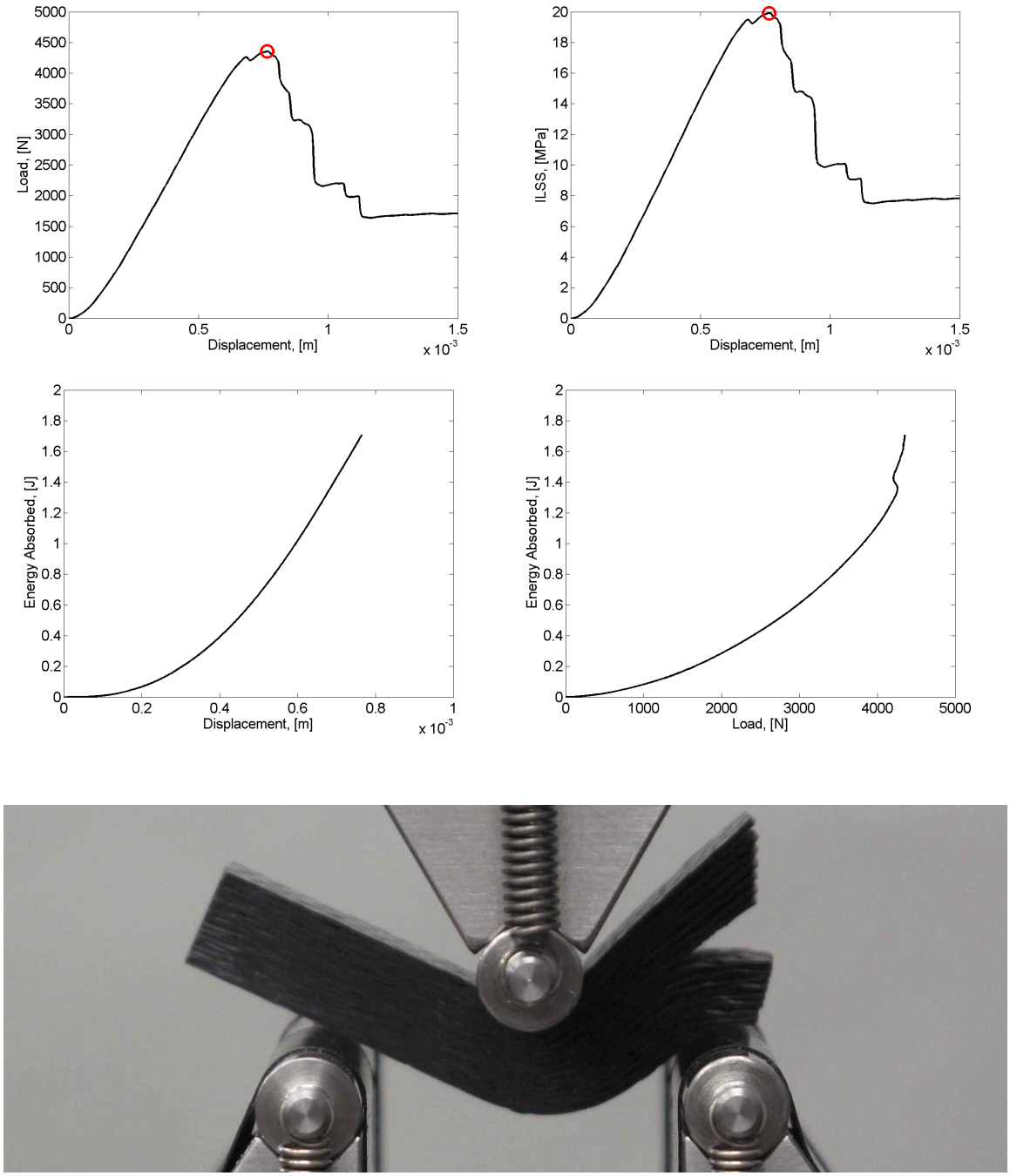

Figure 166: Measured and calculated response of Sample 203 subjected to short beam shear testing. Red circle indicates maximum load.

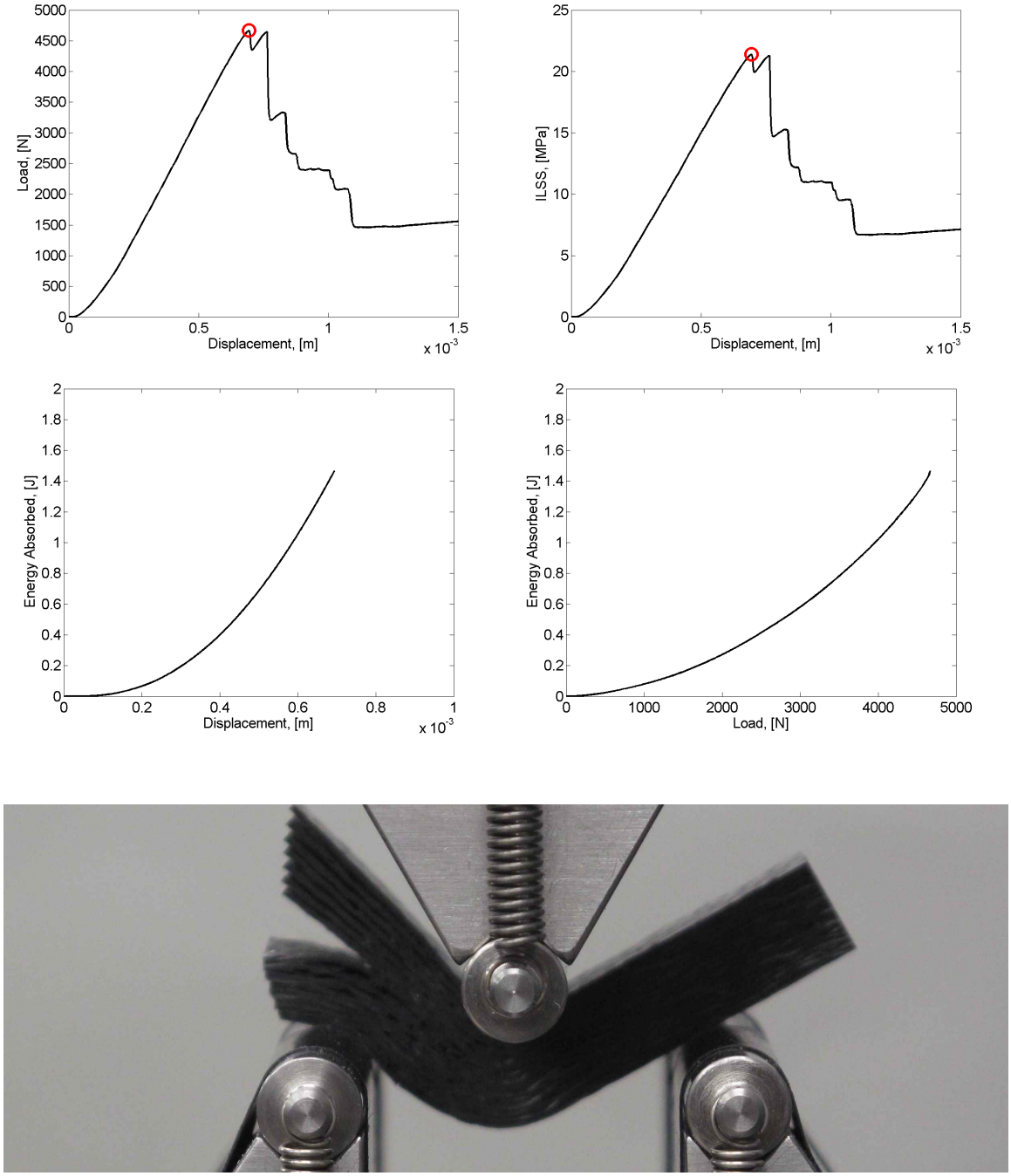

Figure 167: Measured and calculated response of Sample 204 subjected to short beam shear testing. Red circle indicates maximum load.

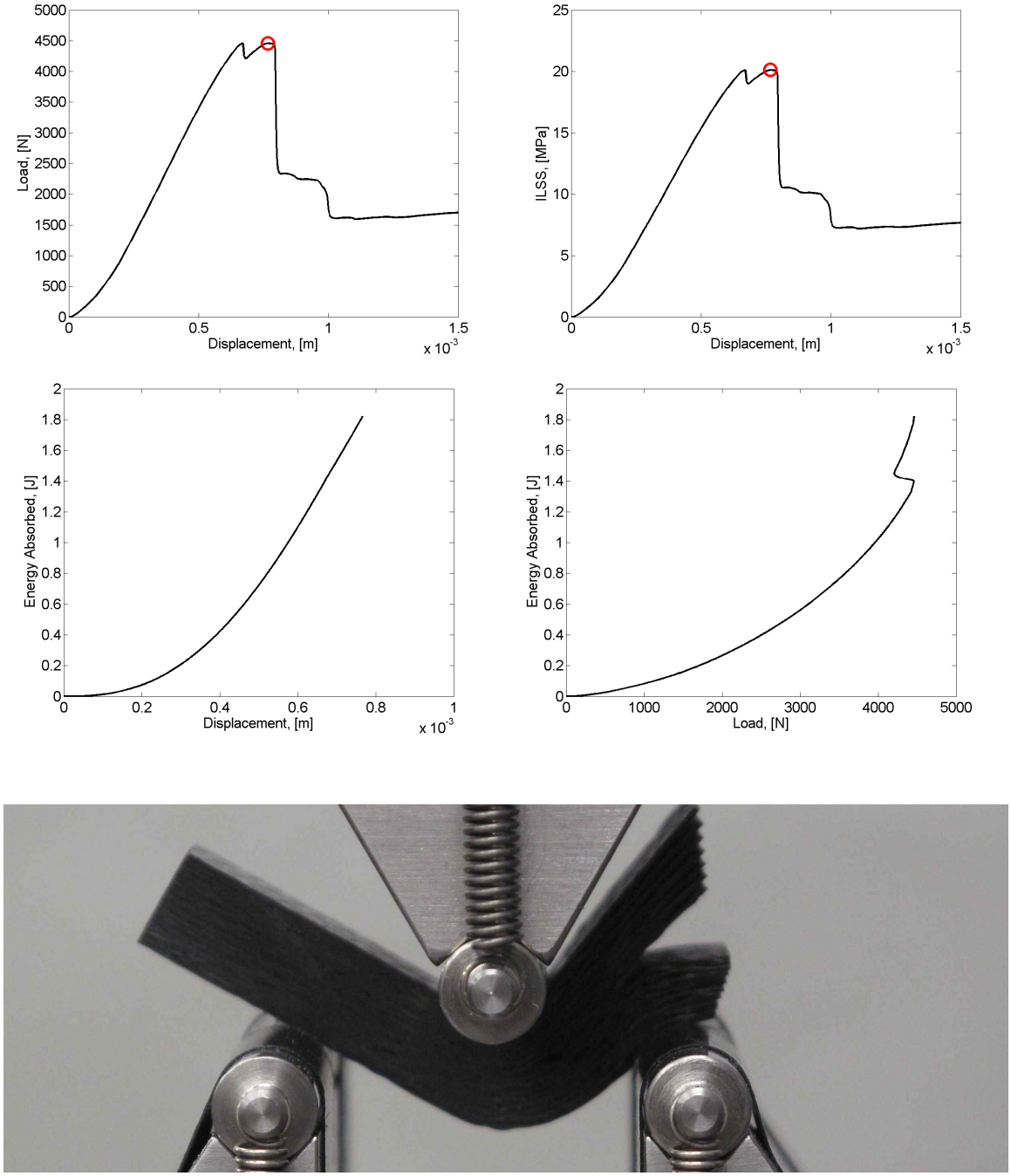

Figure 168: Measured and calculated response of Sample 207 subjected to short beam shear testing. Red circle indicates maximum load.

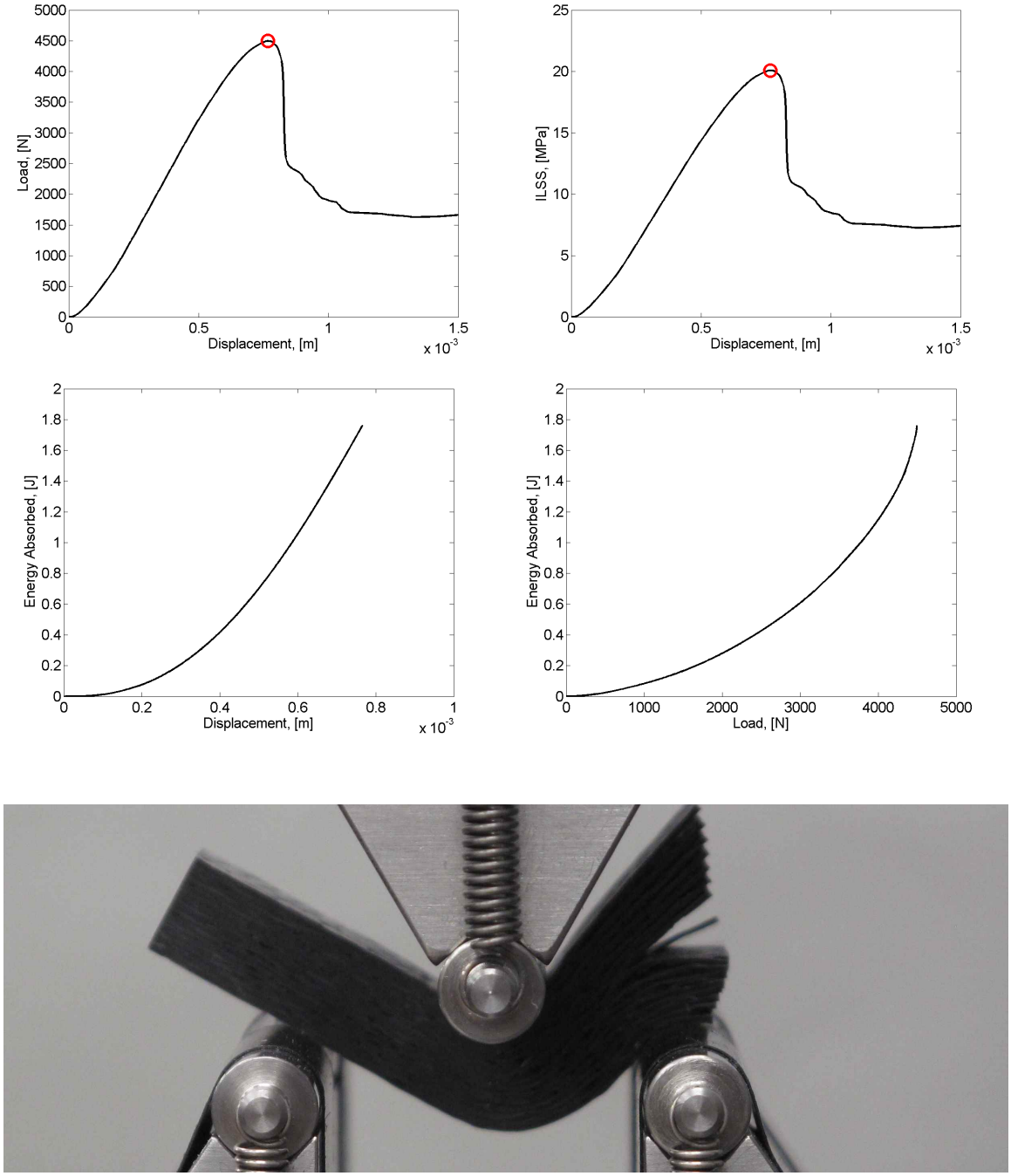

Figure 169: Measured and calculated response of Sample 208 subjected to short beam shear testing. Red circle indicates maximum load.

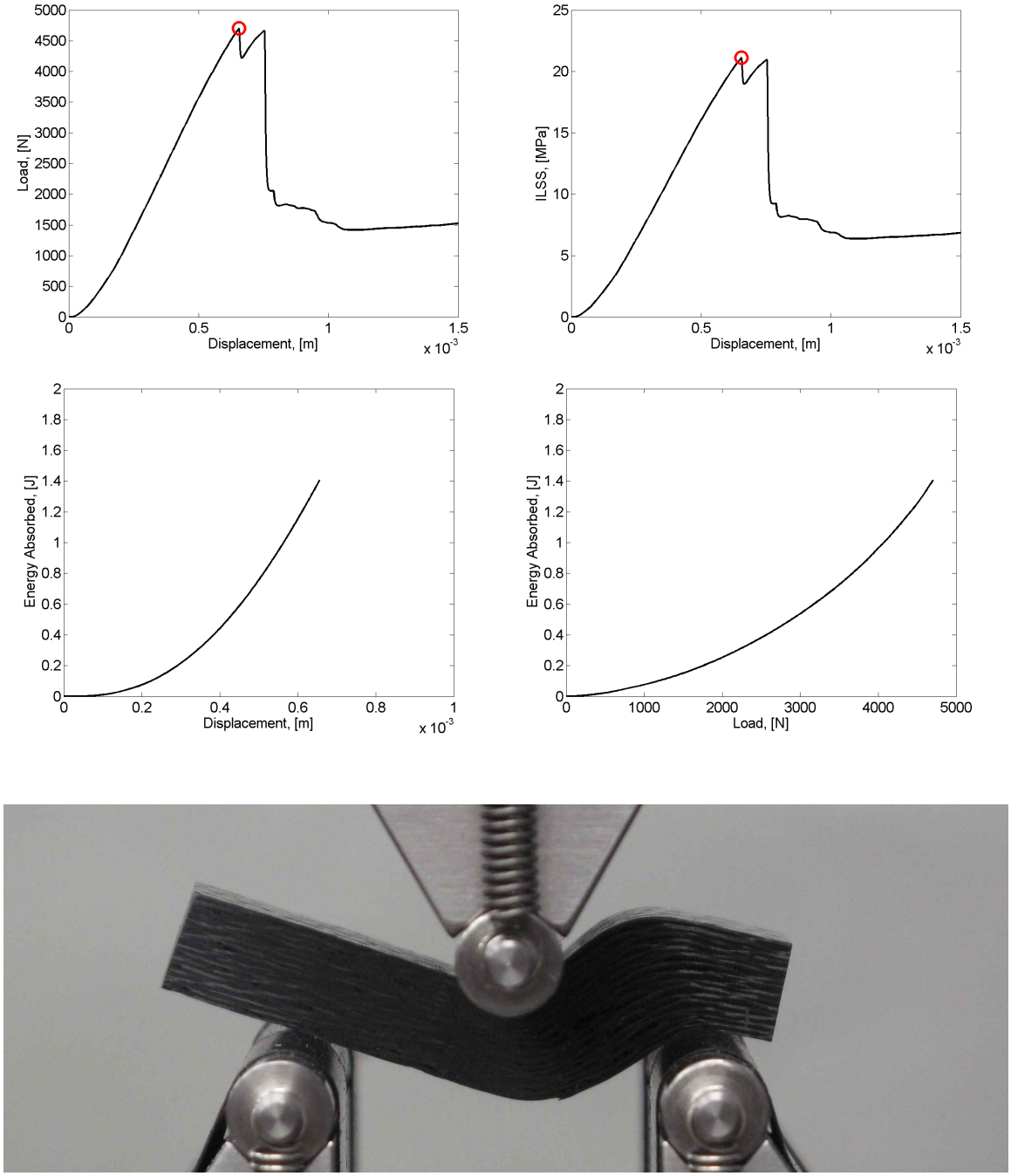

Figure 170: Measured and calculated response of Sample 209 subjected to short beam shear testing. Red circle indicates maximum load.

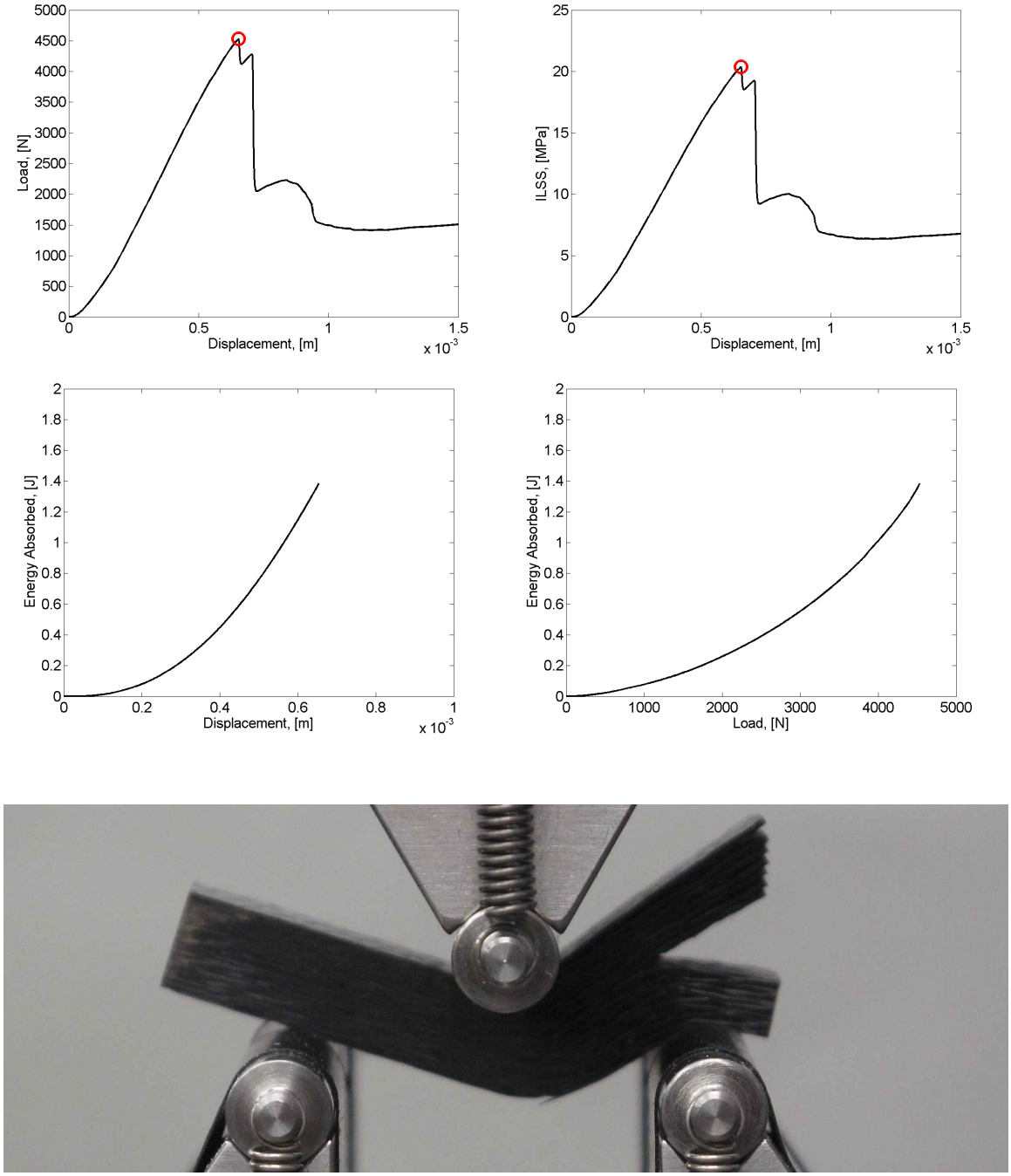

Figure 171: Measured and calculated response of Sample 210 subjected to short beam shear testing. Red circle indicates maximum load.

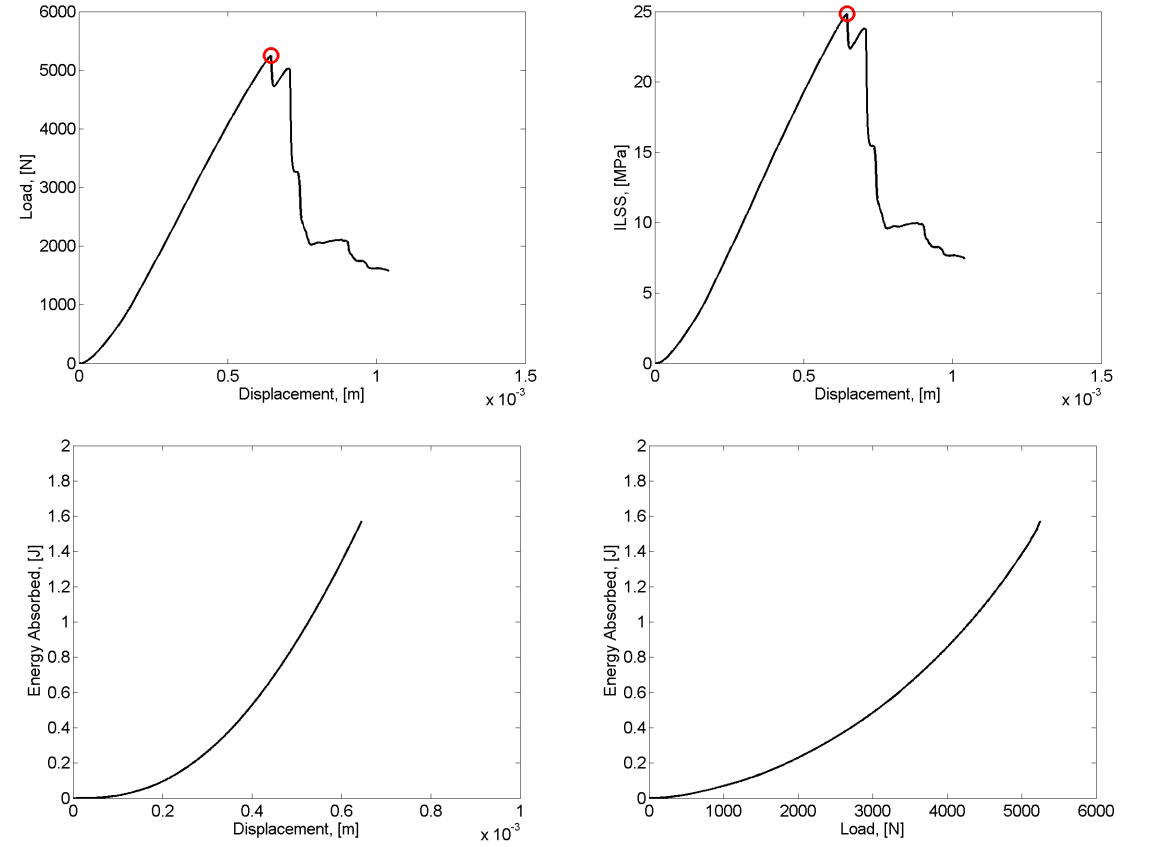

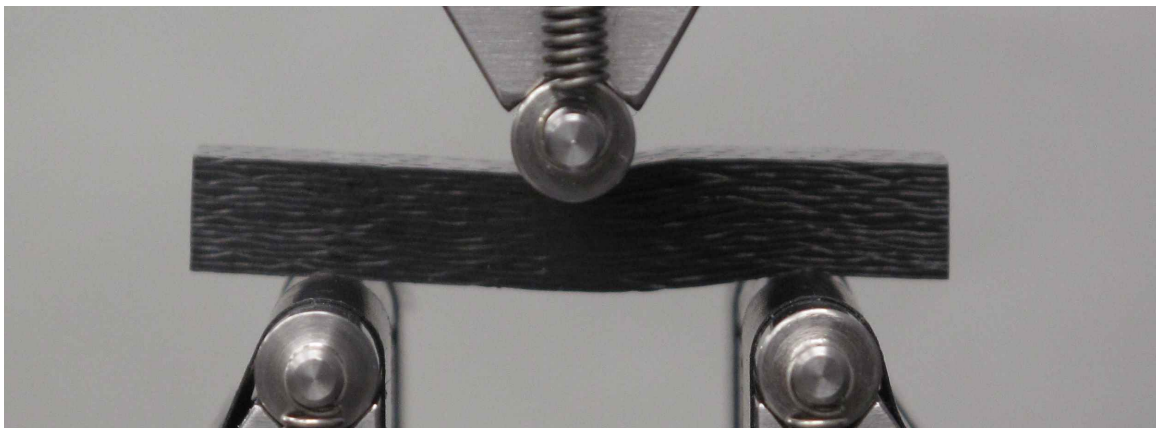

Figure 172: Measured and calculated response of Sample 301 subjected to short beam shear testing. Red circle indicates maximum load.

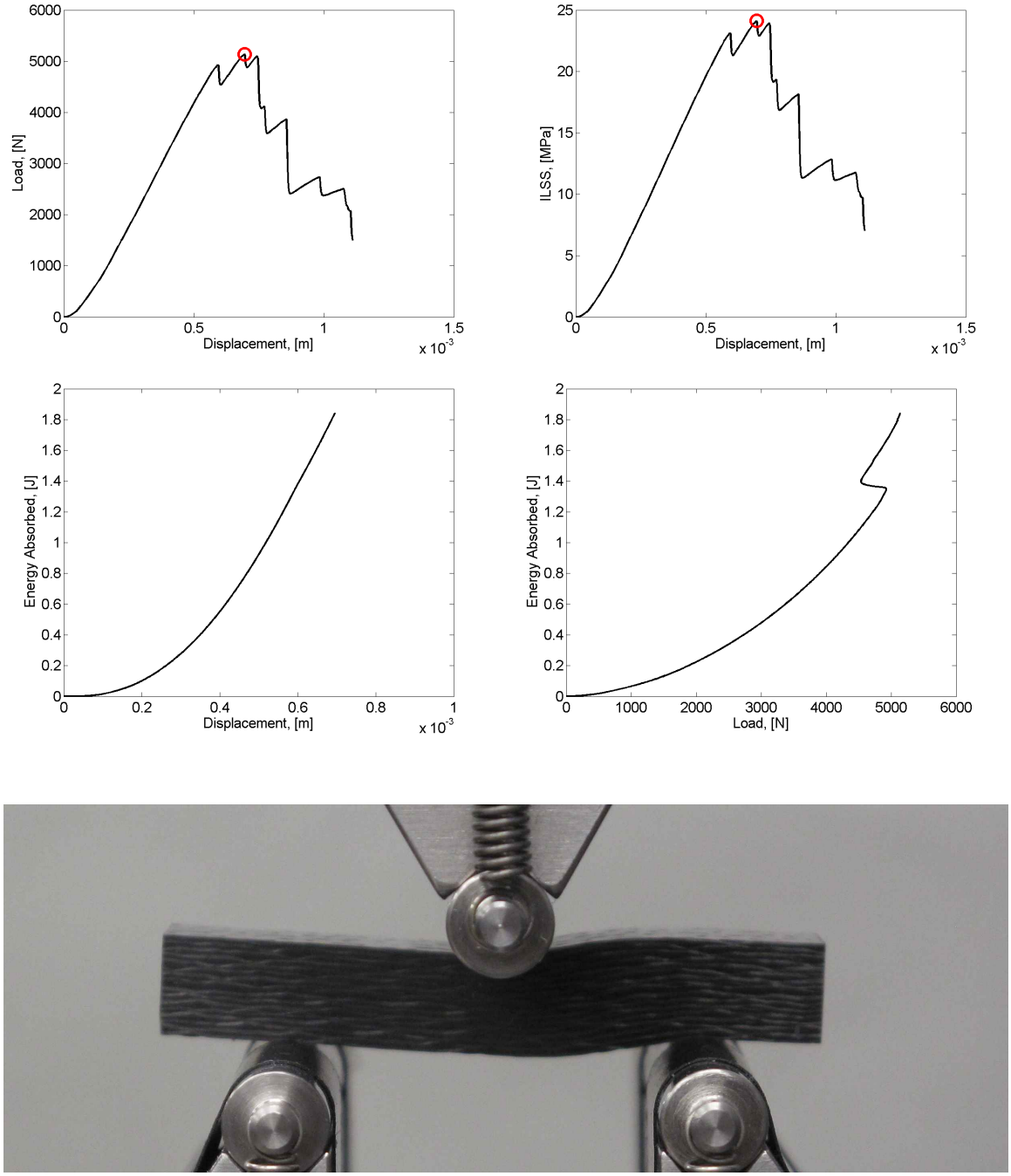

Figure 173: Measured and calculated response of Sample 302 subjected to short beam shear testing. Red circle indicates maximum load.

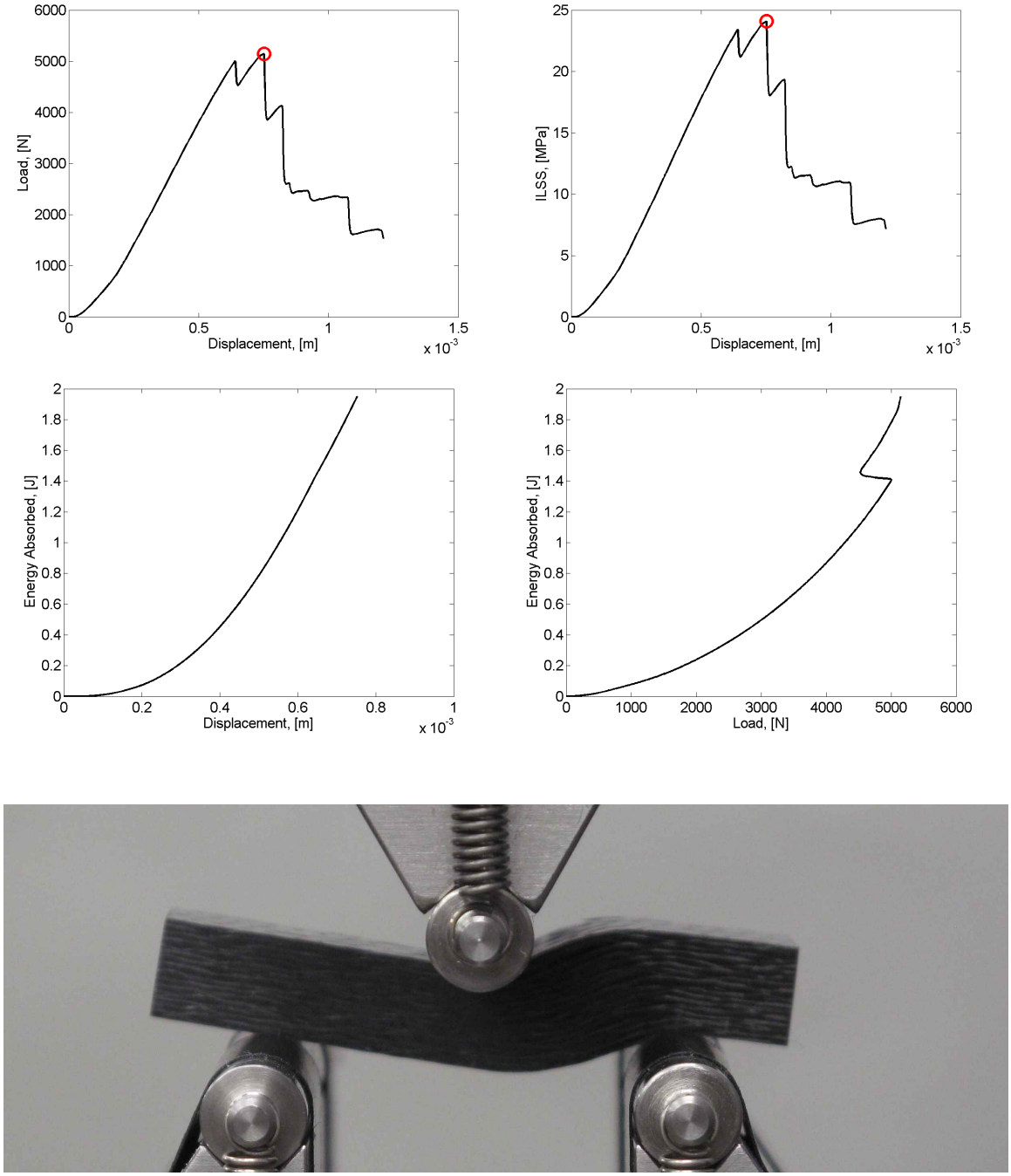

Figure 174: Measured and calculated response of Sample 303 subjected to short beam shear testing. Red circle indicates maximum load.

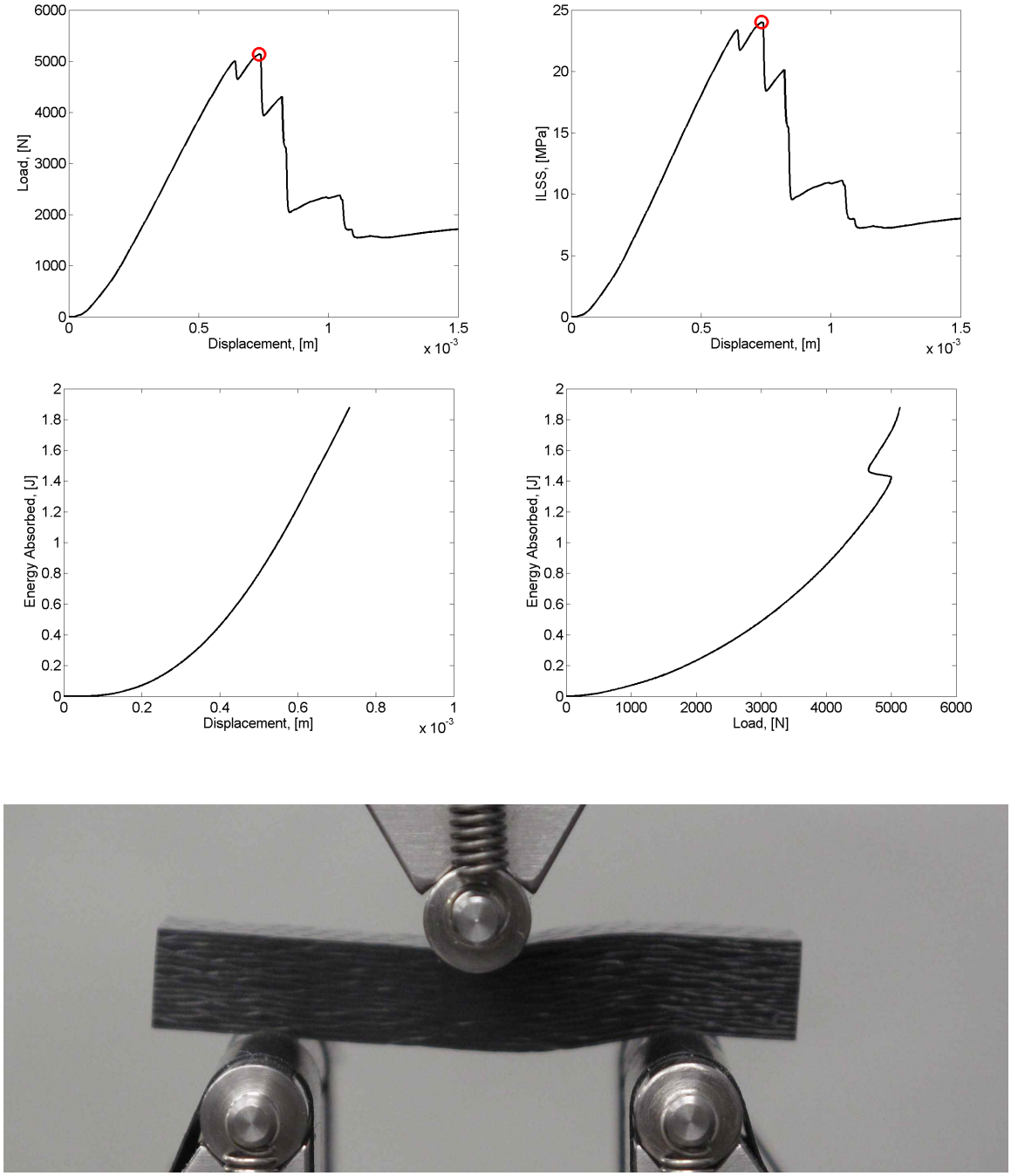

Figure 175: Measured and calculated response of Sample 304 subjected to short beam shear testing. Red circle indicates maximum load.

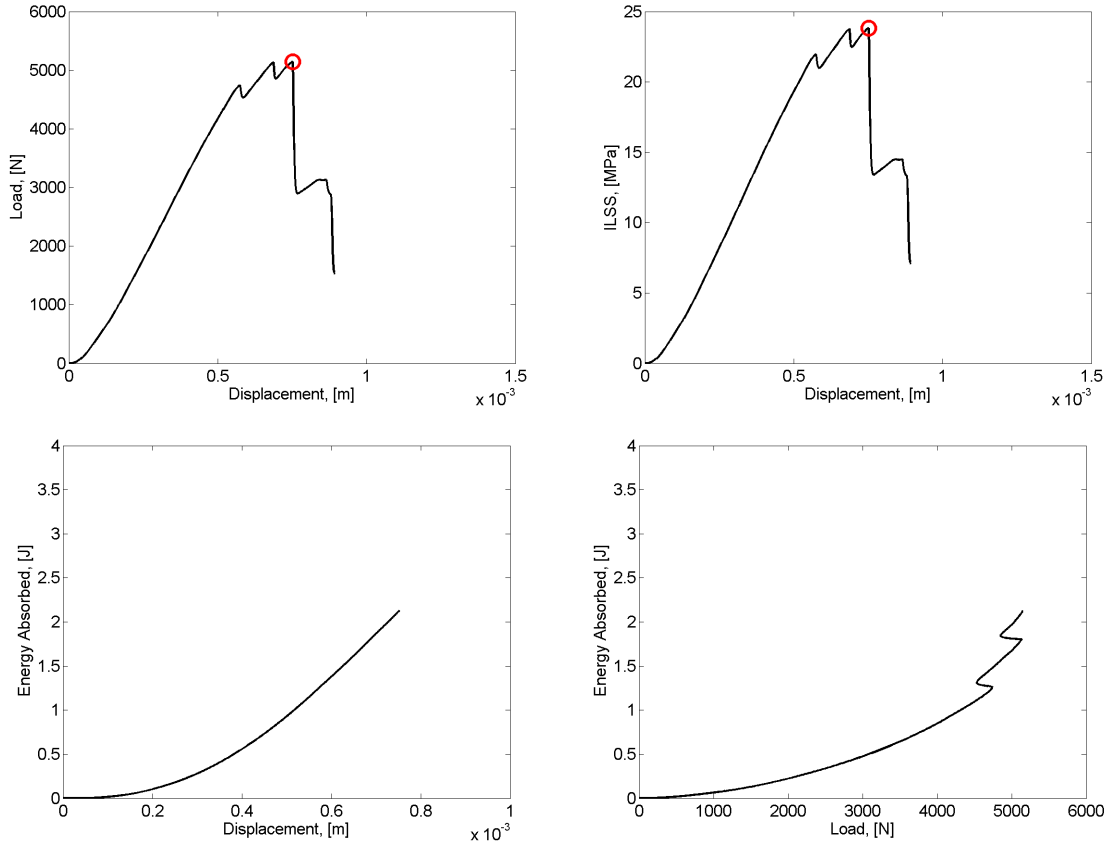

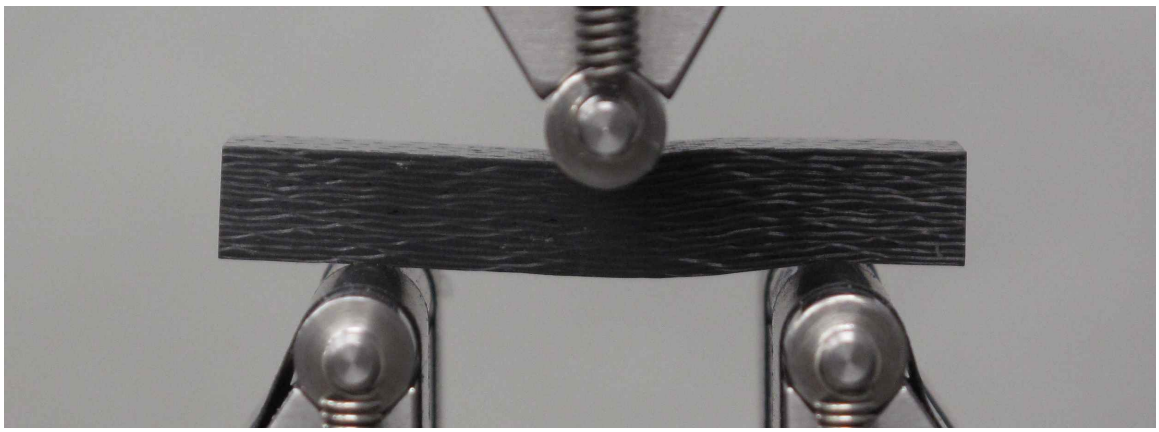

Figure 176: Measured and calculated response of Sample 307 subjected to short beam shear testing. Red circle indicates maximum load.

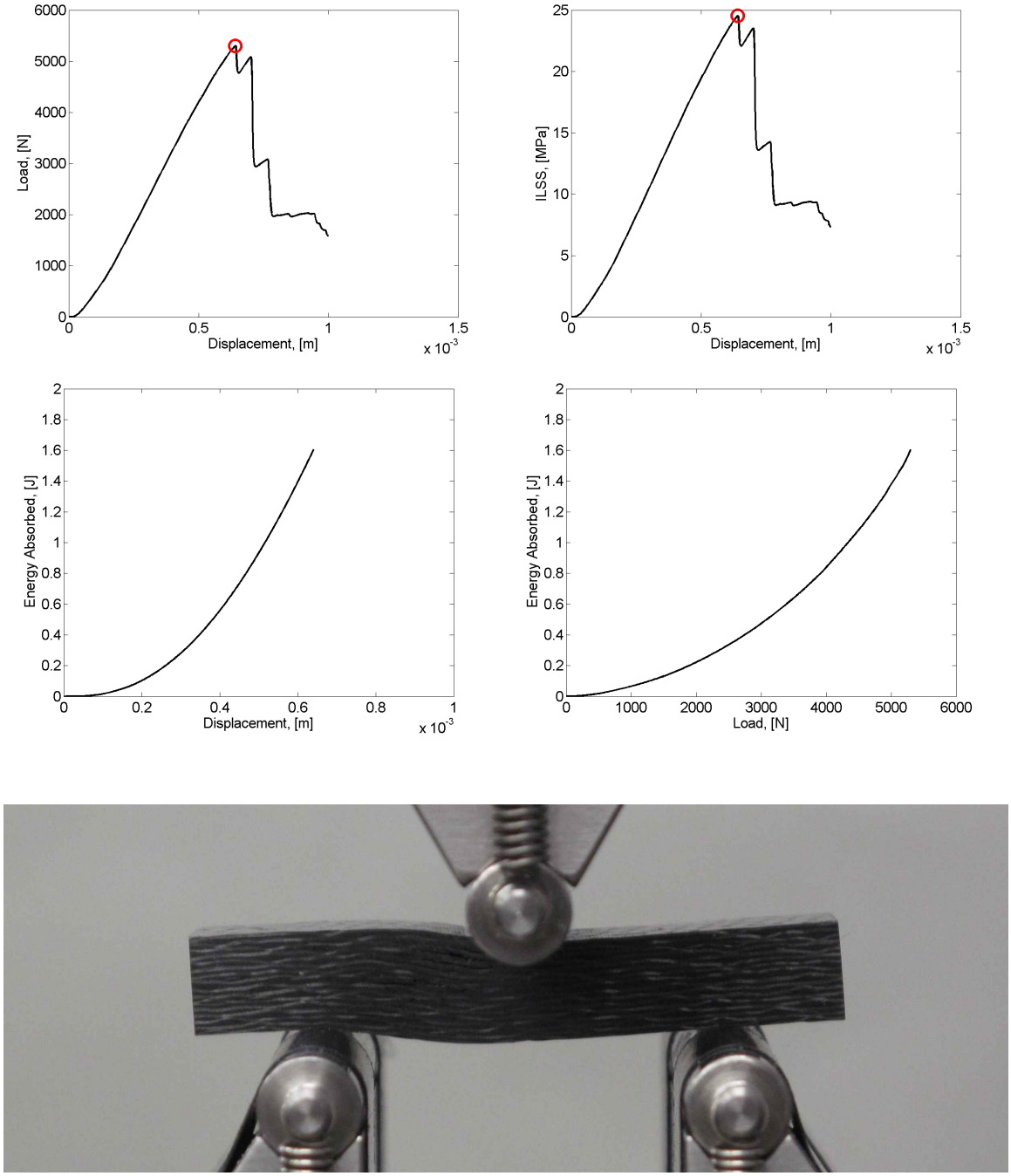

Figure 177: Measured and calculated response of Sample 308 subjected to short beam shear testing. Red circle indicates maximum load.

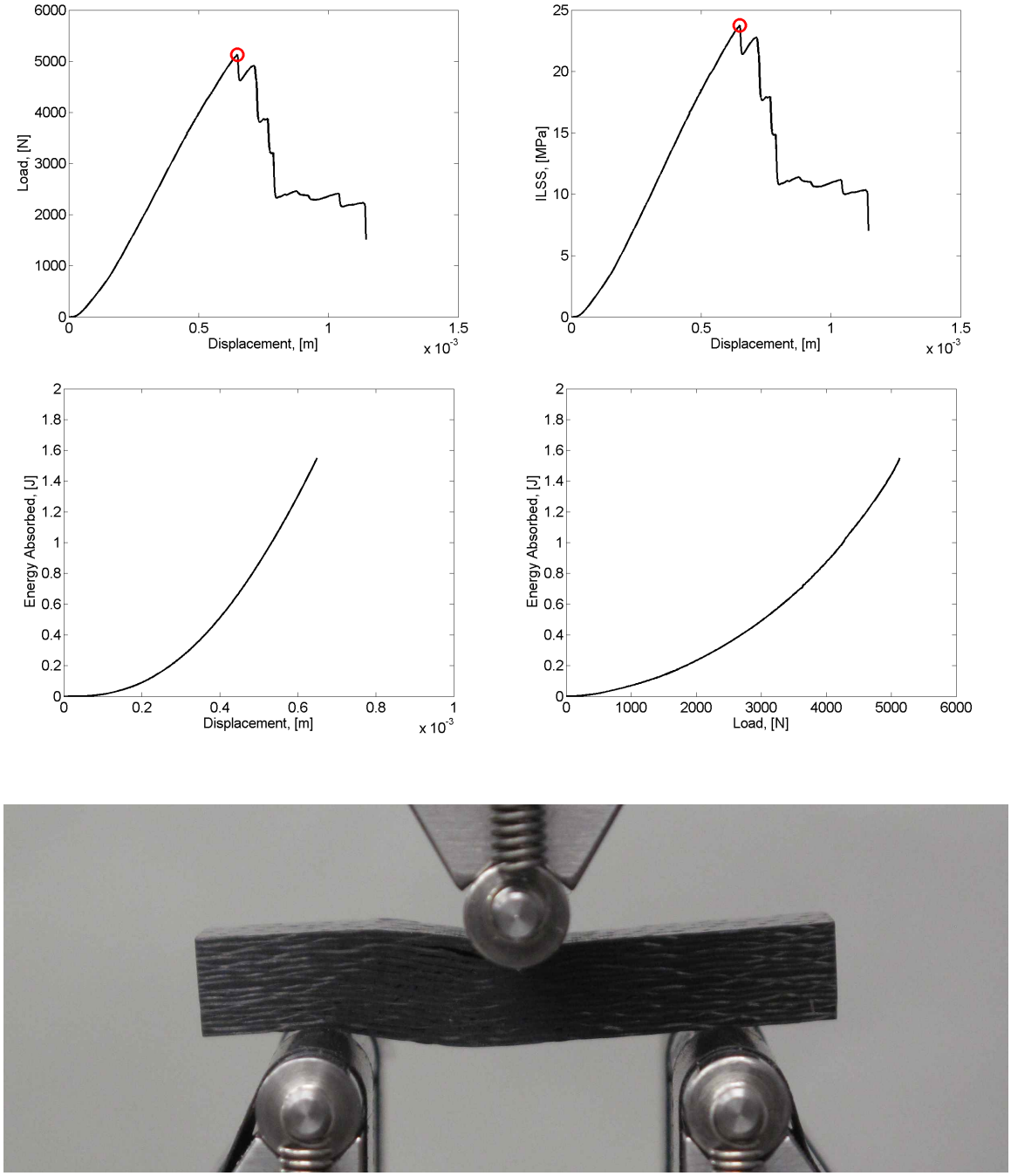

Figure 178: Measured and calculated response of Sample 309 subjected to short beam shear testing. Red circle indicates maximum load.

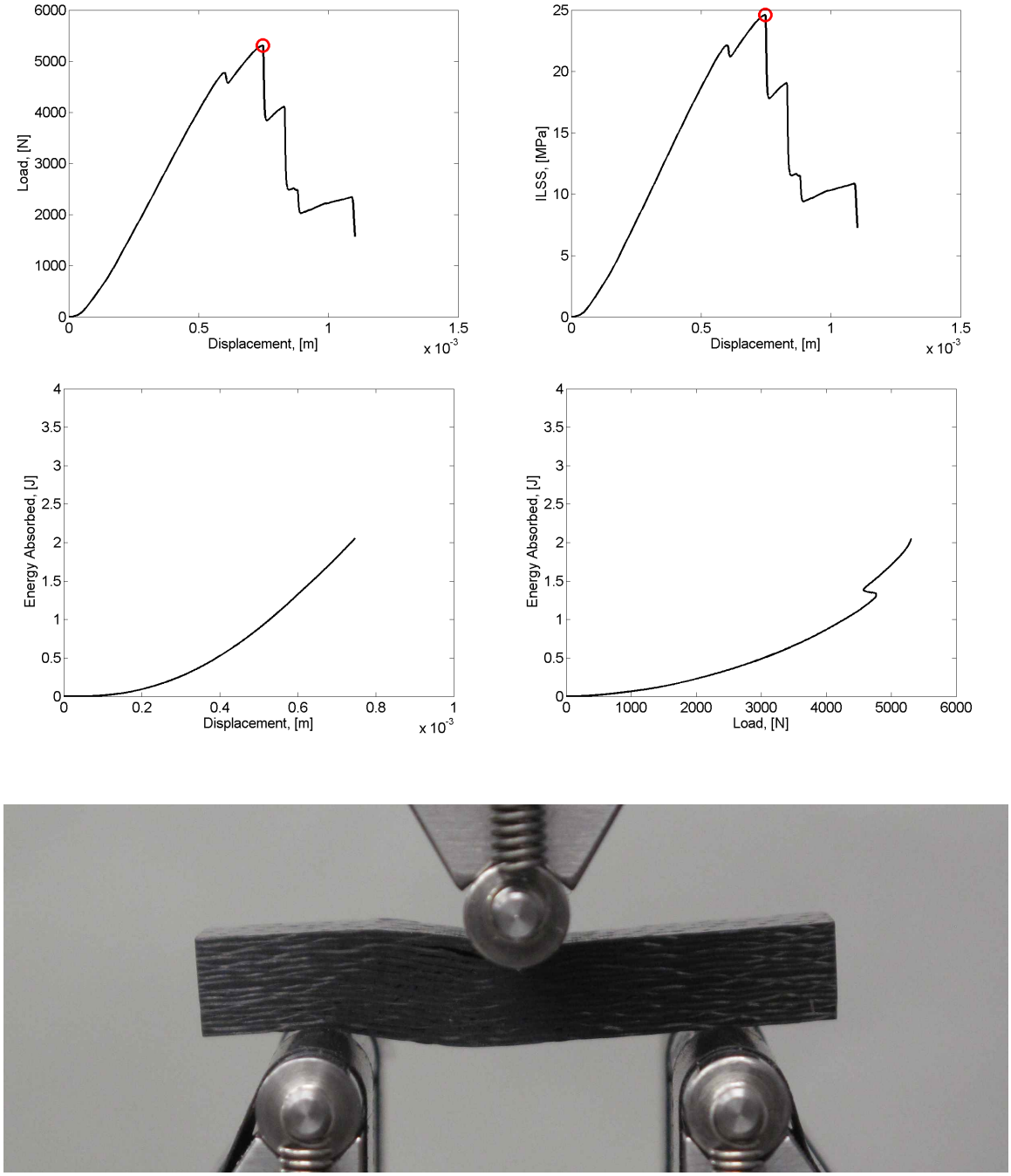

Figure 179: Measured and calculated response of Sample 310 subjected to short beam shear testing. Red circle indicates maximum load.

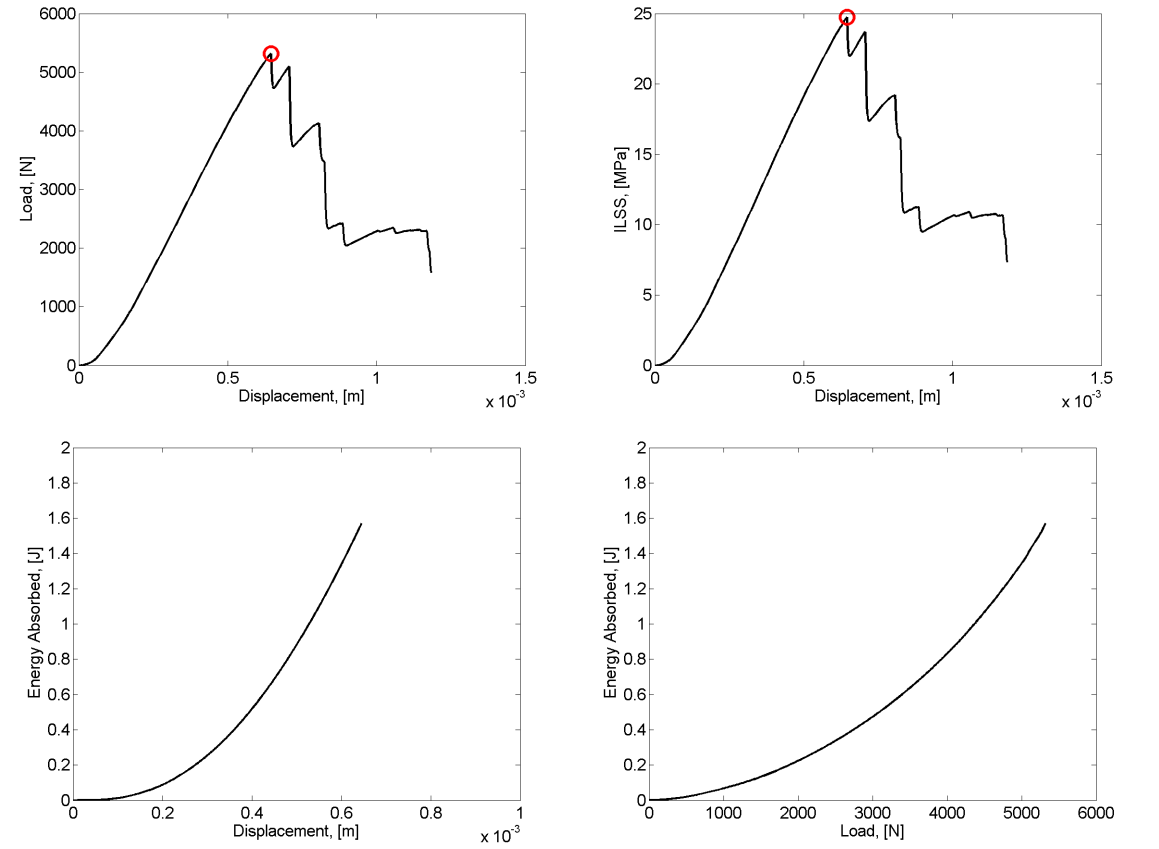

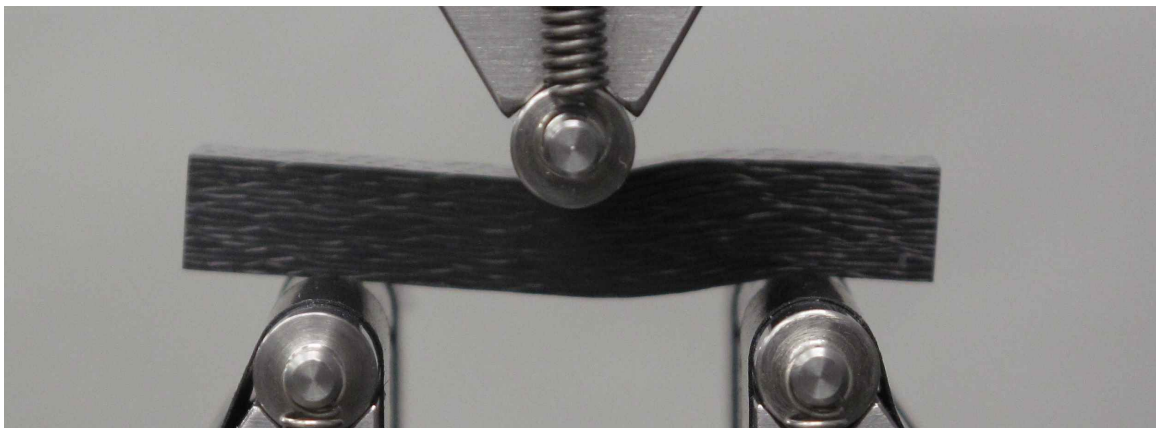

Figure 180: Measured and calculated response of Sample 401 subjected to short beam shear testing. Red circle indicates maximum load.

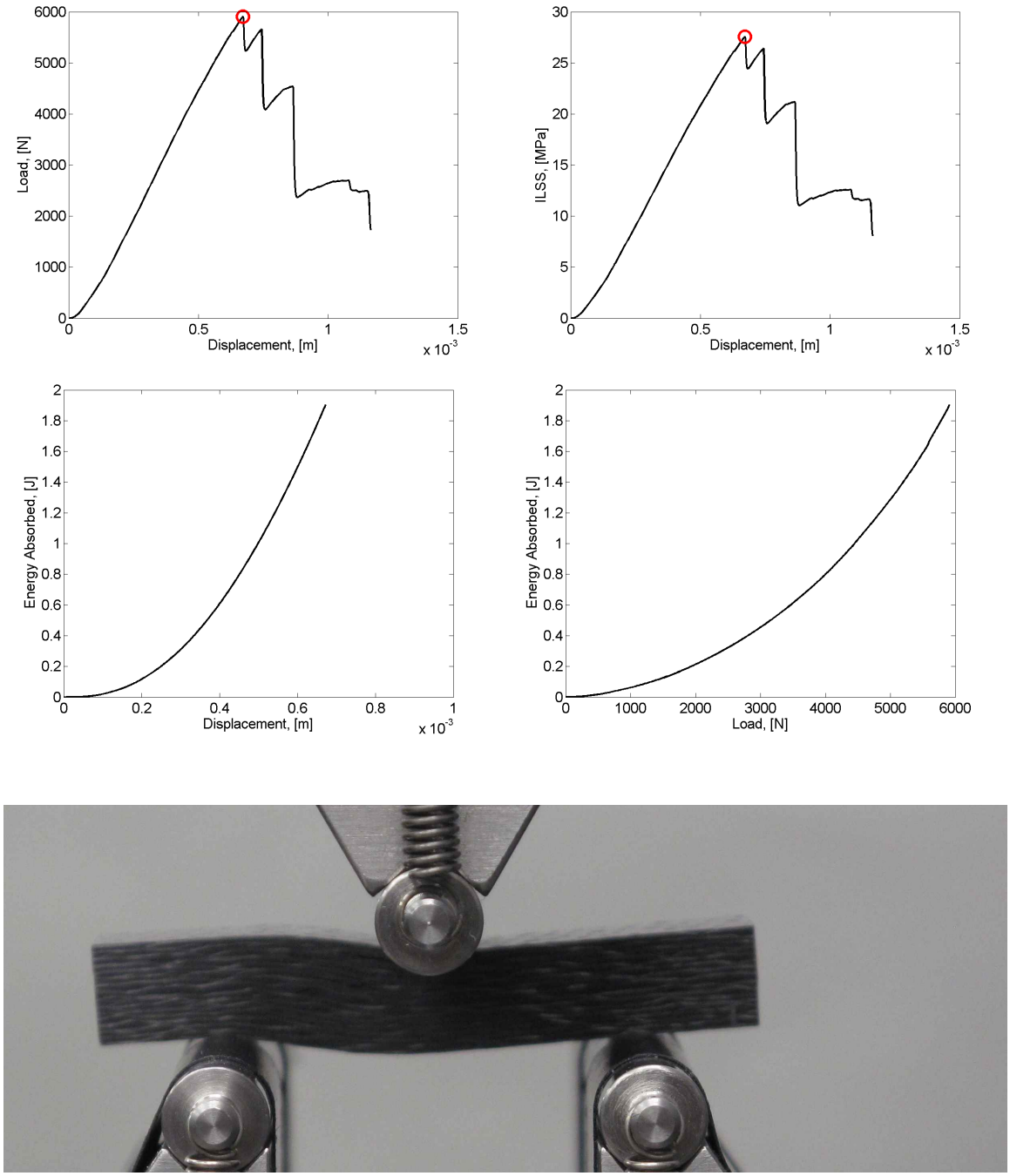

Figure 181: Measured and calculated response of Sample 402 subjected to short beam shear testing. Red circle indicates maximum load.

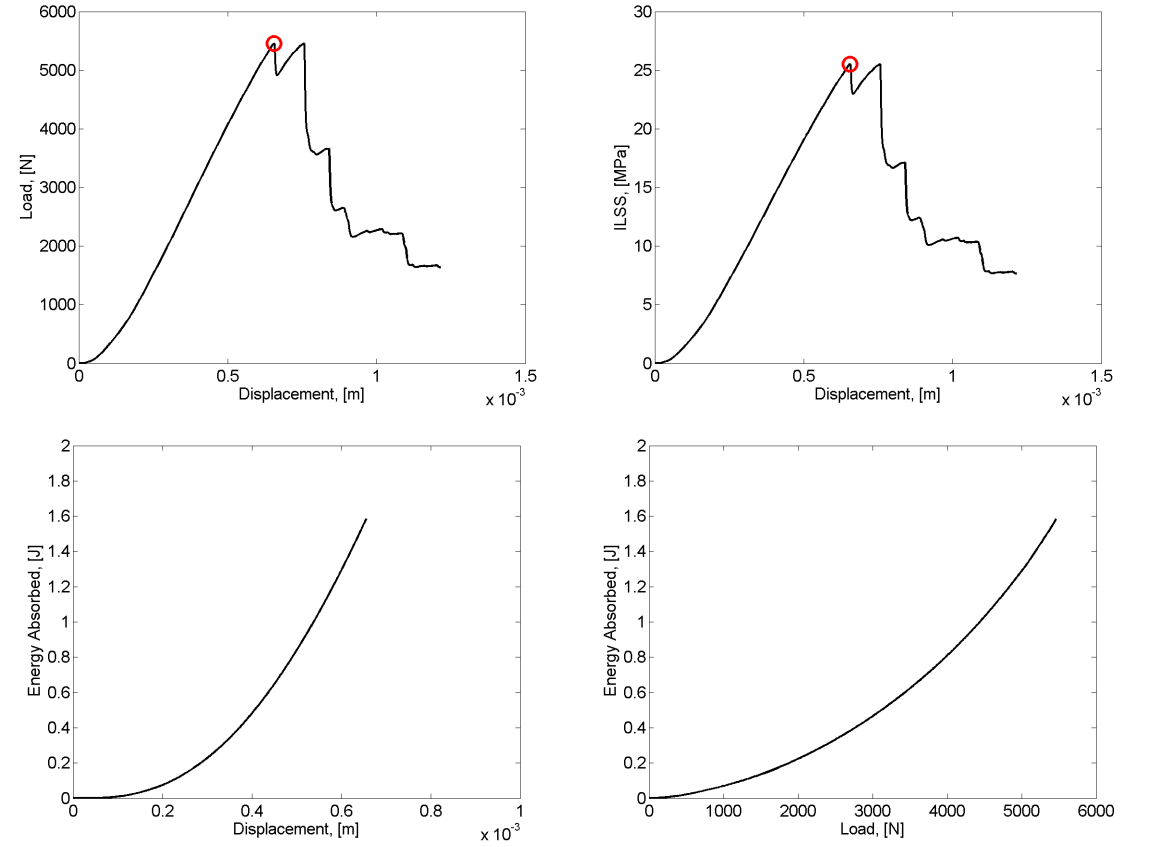

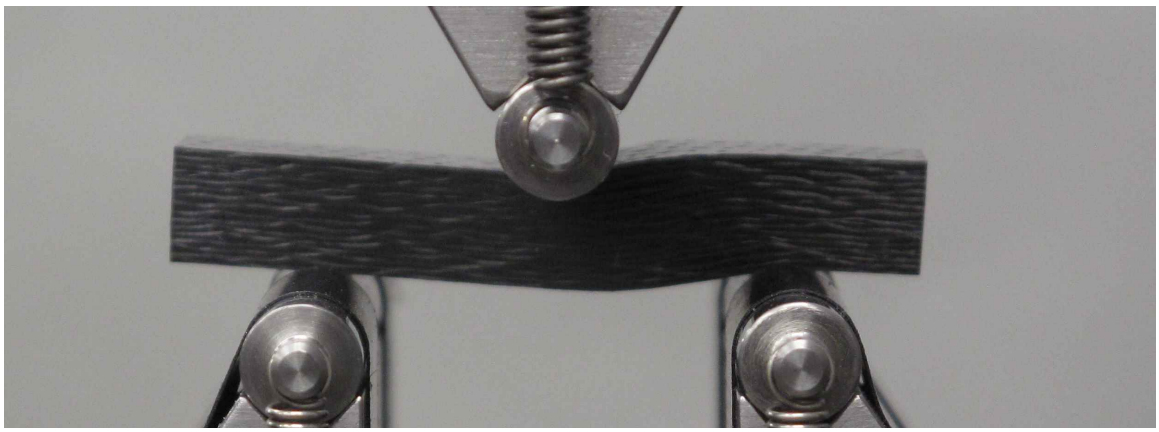

Figure 182: Measured and calculated response of Sample 403 subjected to short beam shear testing. Red circle indicates maximum load.

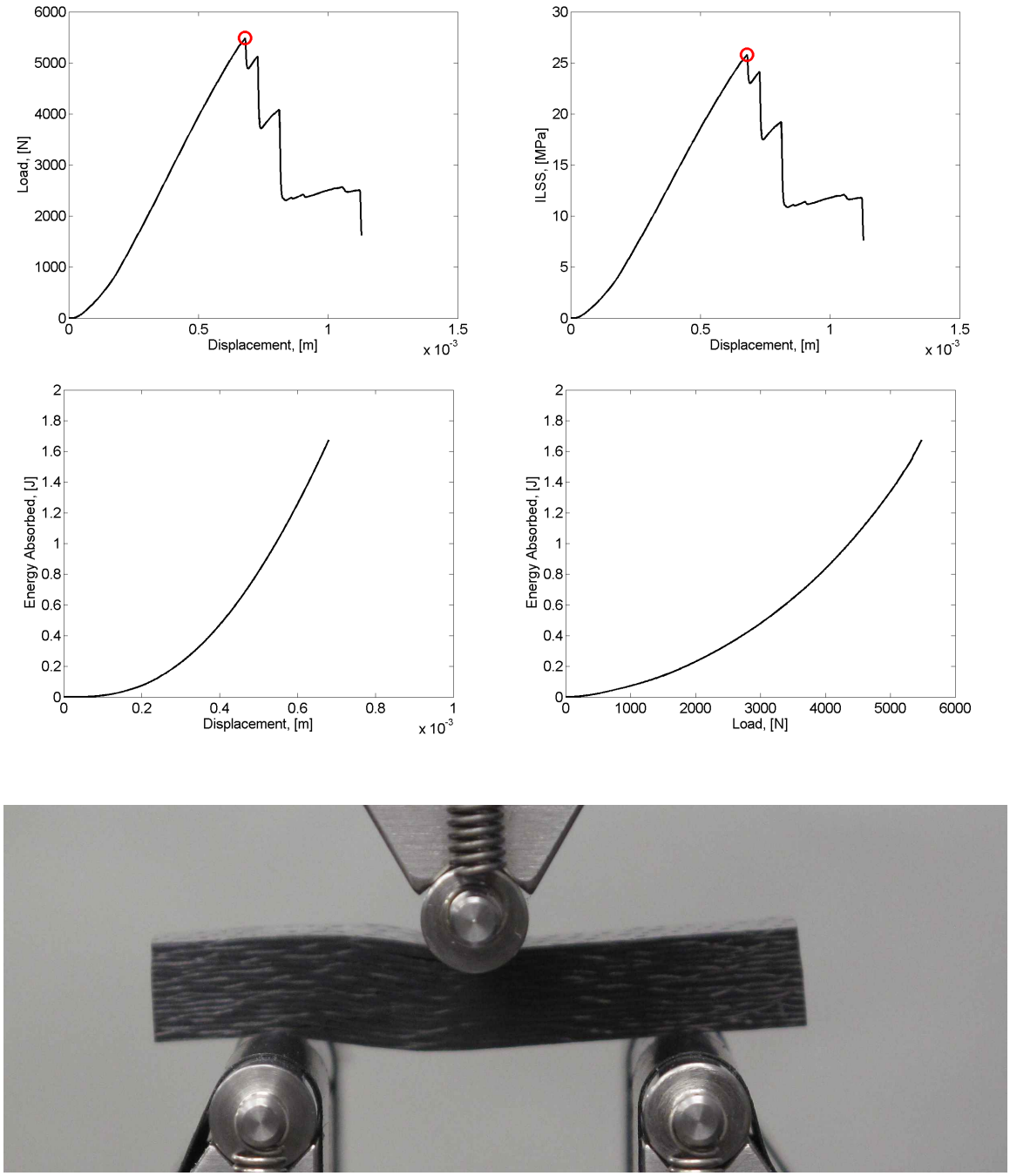

Figure 183: Measured and calculated response of Sample 404 subjected to short beam shear testing. Red circle indicates maximum load.

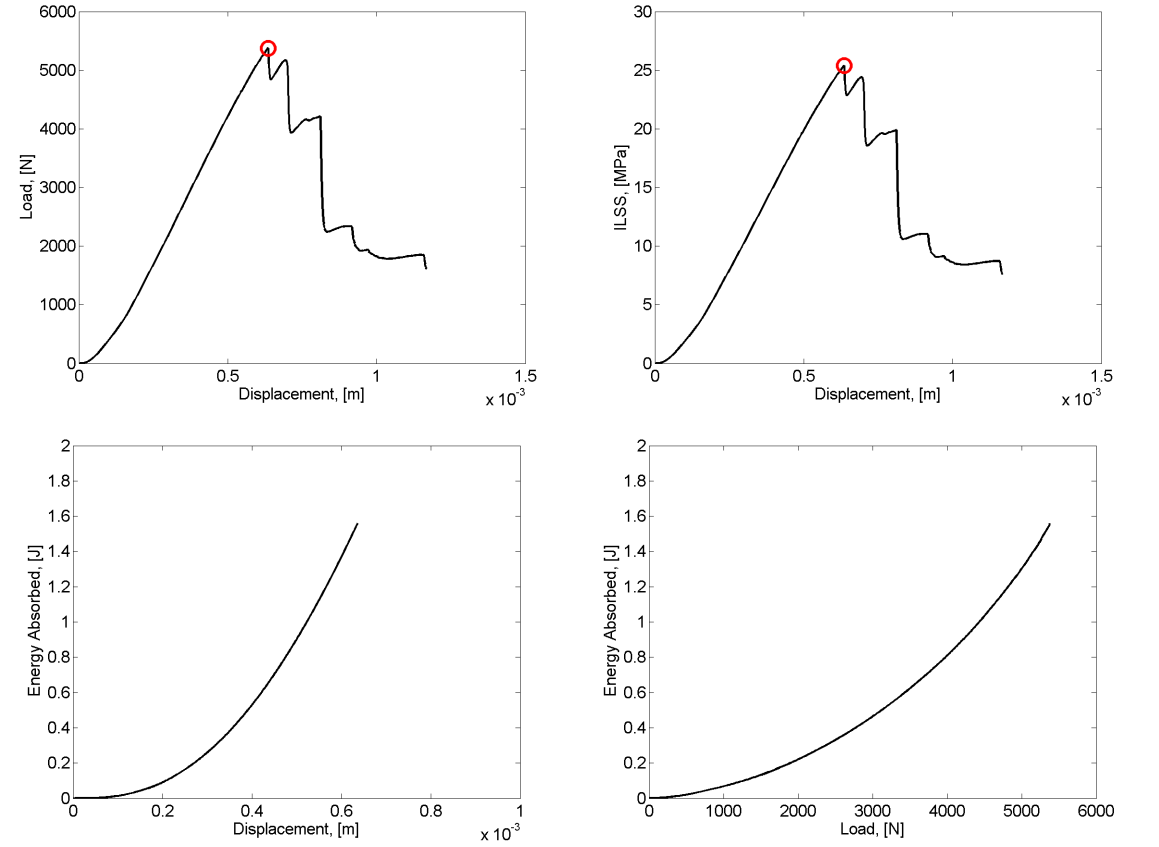

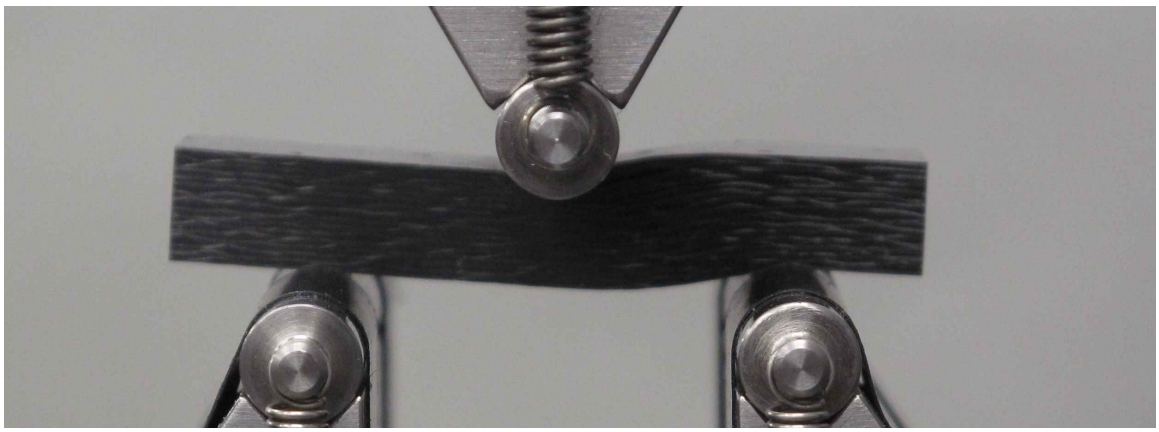

Figure 184: Measured and calculated response of Sample 407 subjected to short beam shear testing. Red circle indicates maximum load.

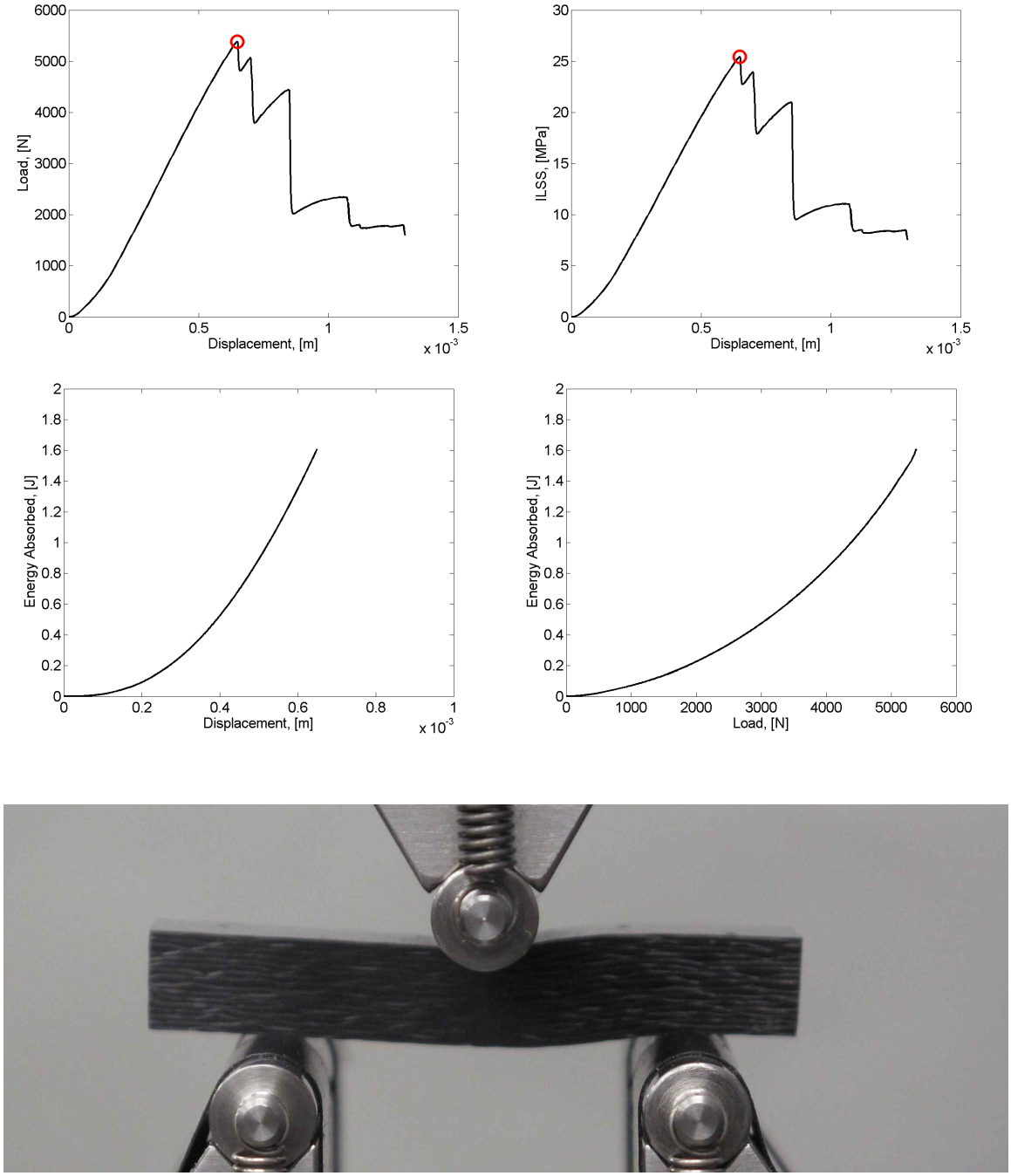

Figure 185: Measured and calculated response of Sample 408 subjected to short beam shear testing. Red circle indicates maximum load.

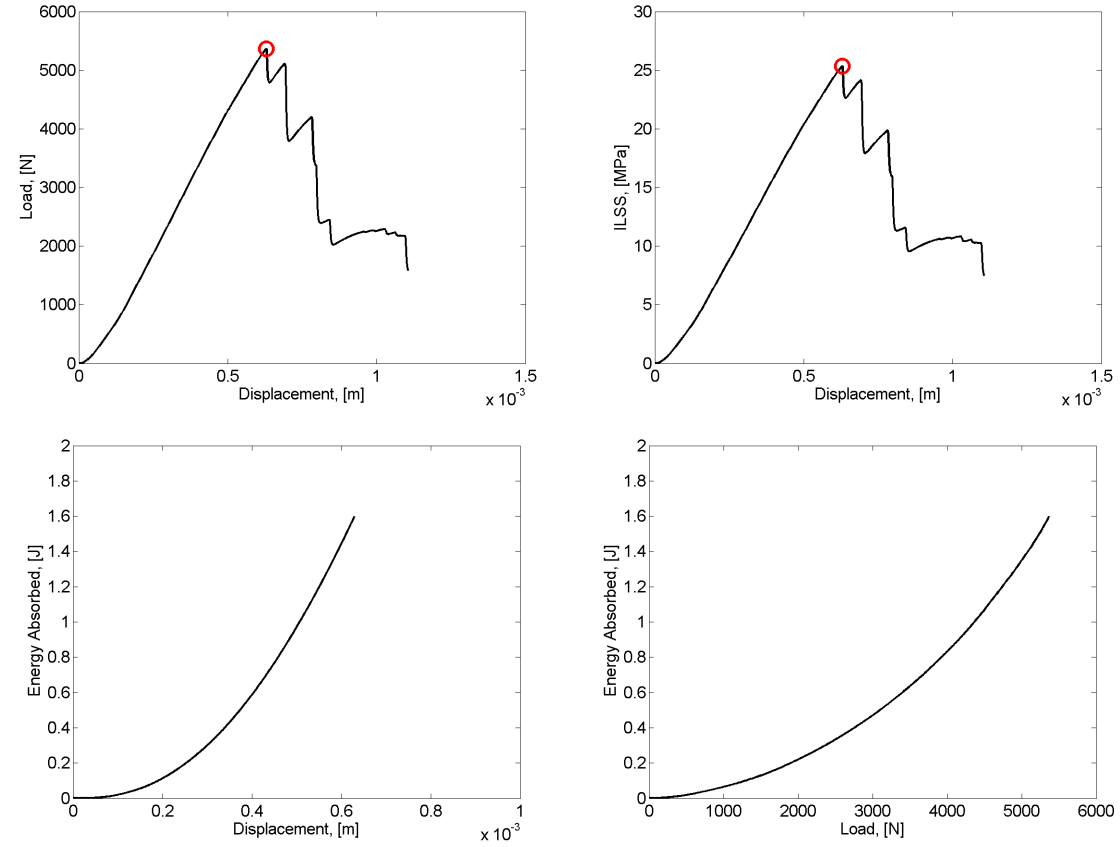

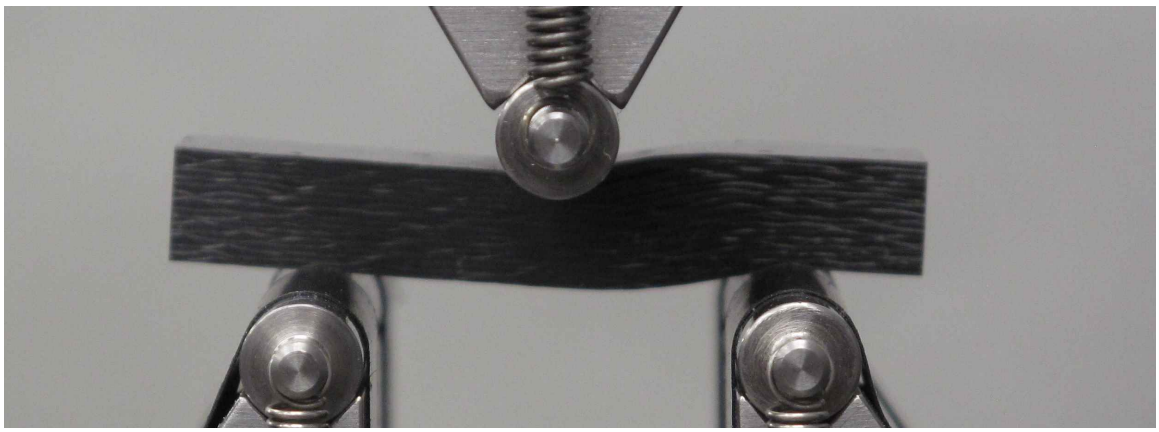

Figure 186: Measured and calculated response of Sample 409 subjected to short beam shear testing. Red circle indicates maximum load.

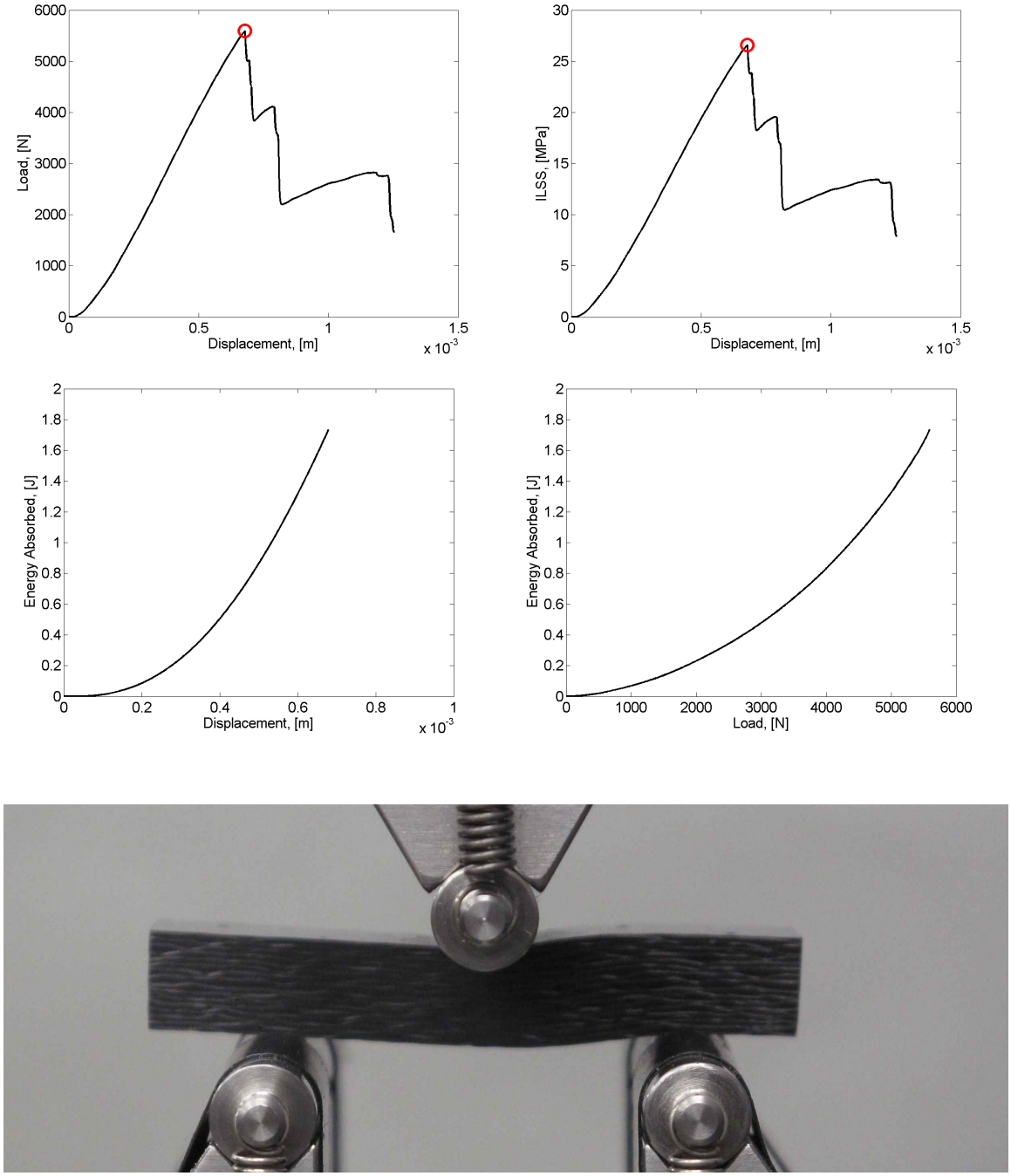

Figure 187: Measured and calculated response of Sample 410 subjected to short beam shear testing. Red circle indicates maximum load.

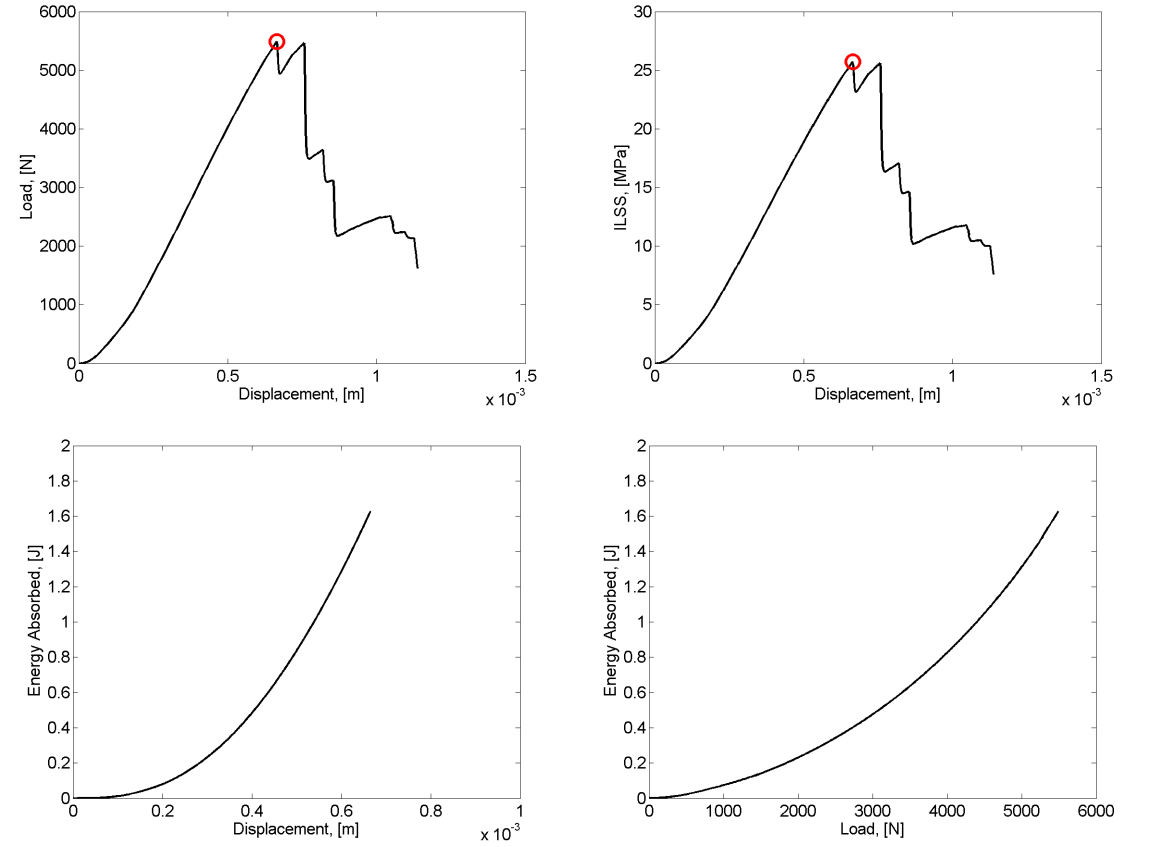

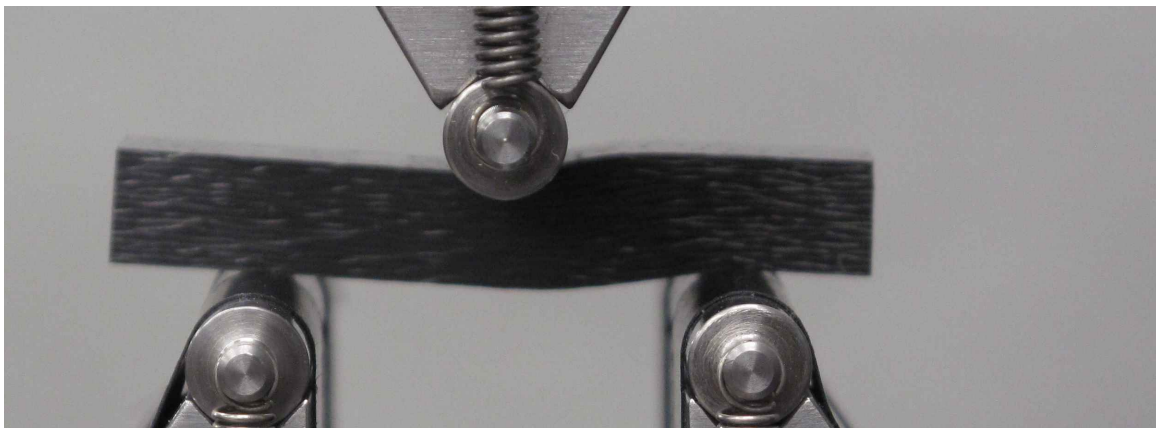

Figure 188: Measured and calculated response of Sample 501 subjected to short beam shear testing. Red circle indicates maximum load.

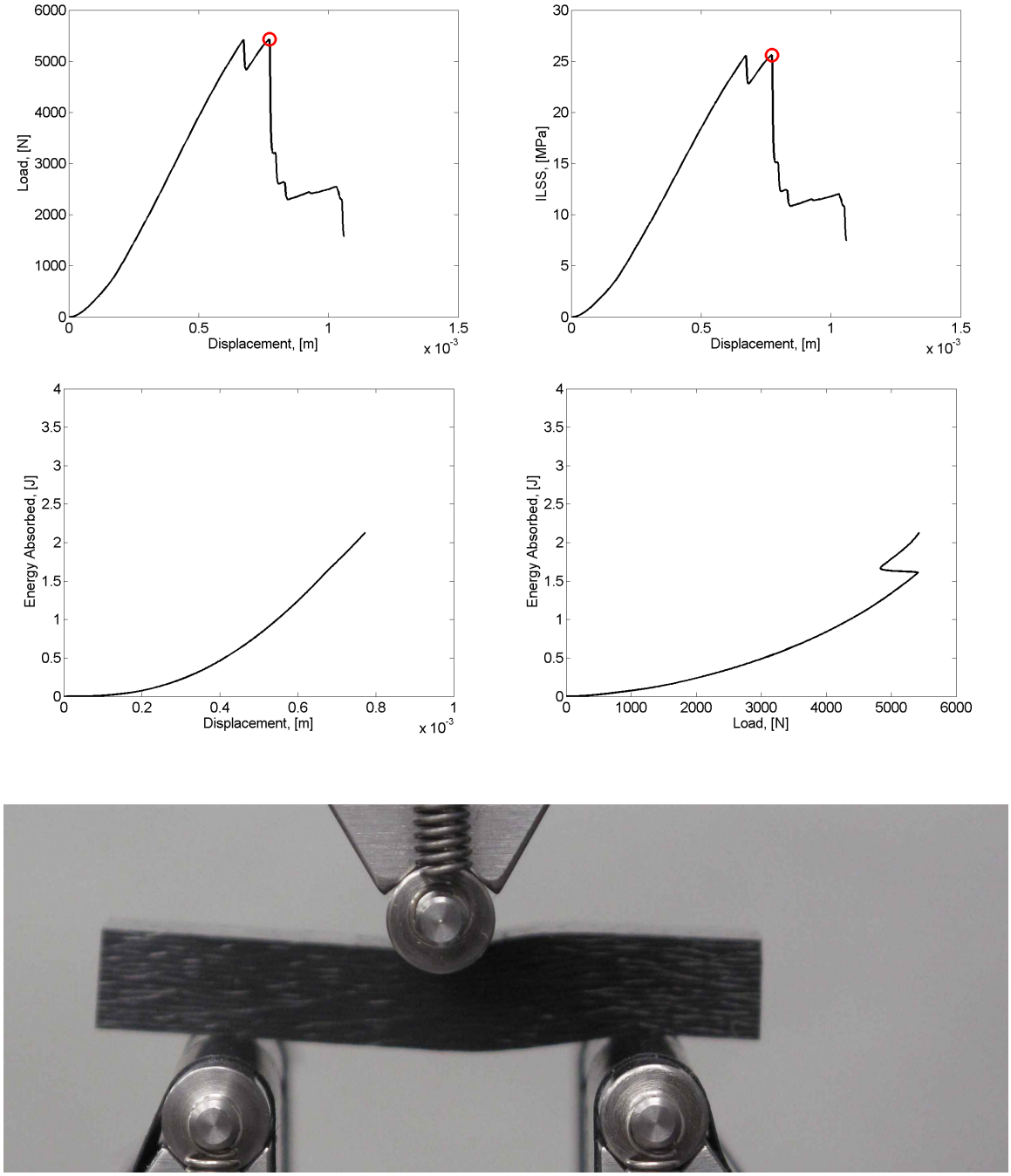

Figure 189: Measured and calculated response of Sample 502 subjected to short beam shear testing. Red circle indicates maximum load.

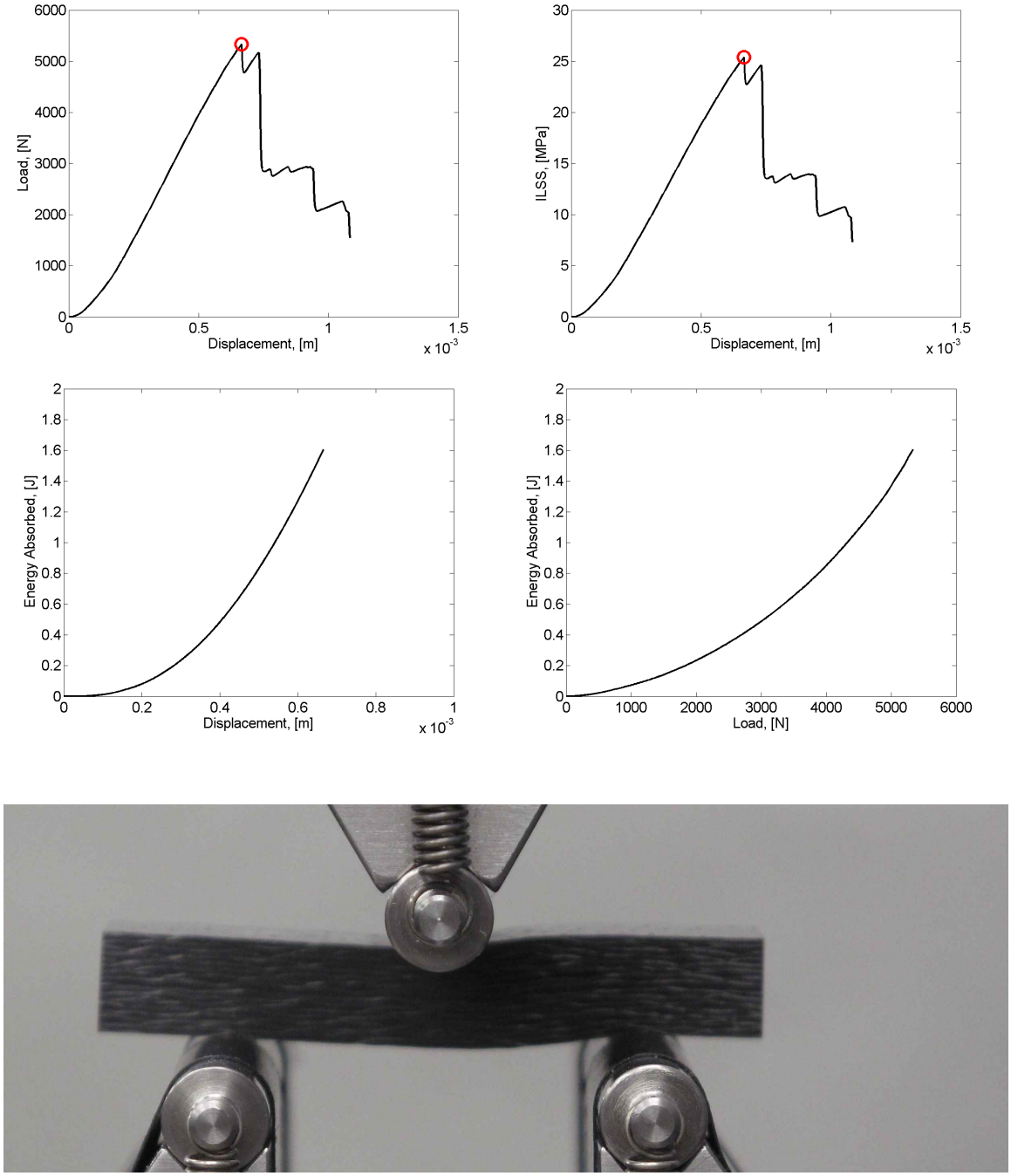

Figure 190: Measured and calculated response of Sample 503 subjected to short beam shear testing. Red circle indicates maximum load.

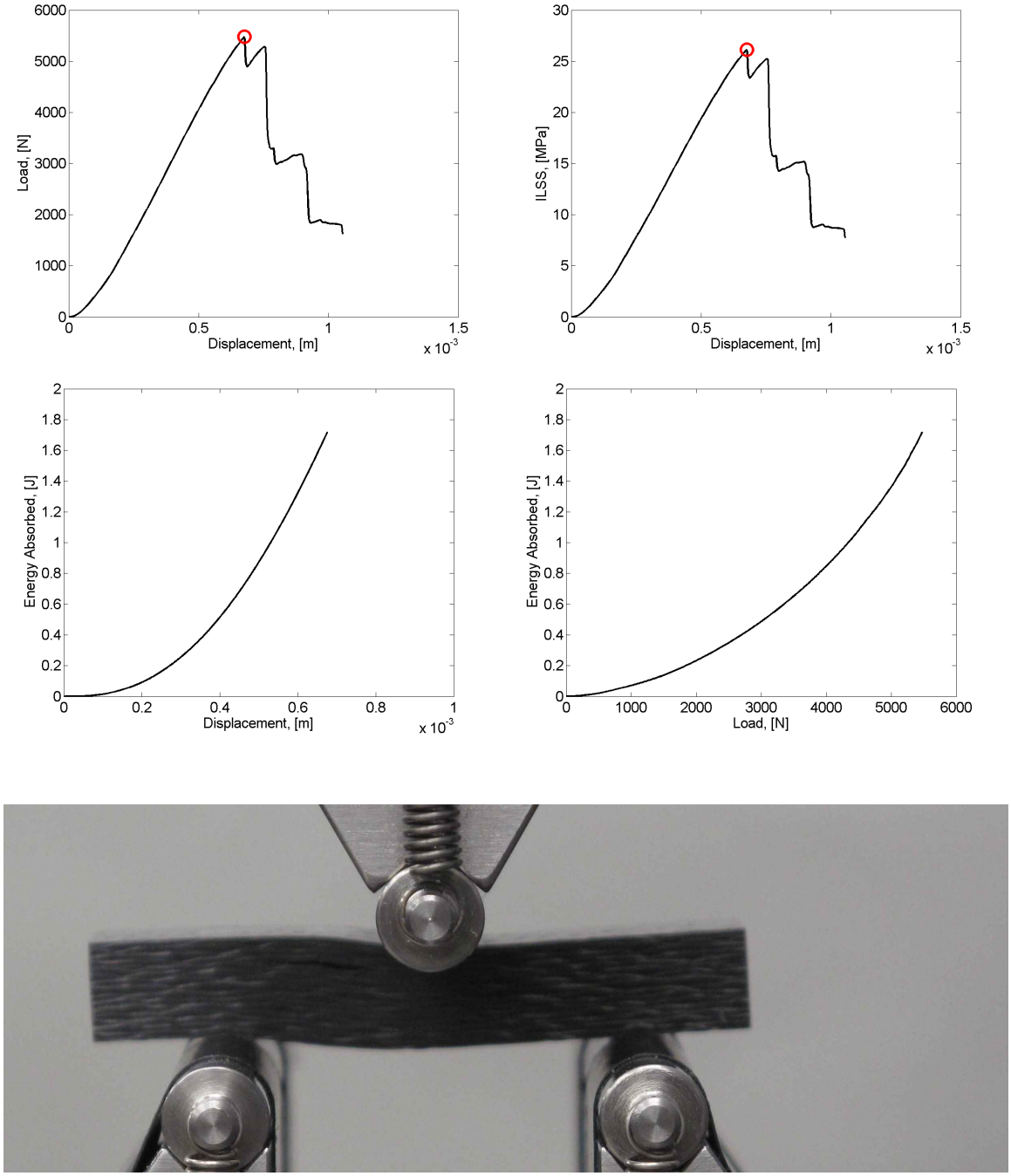

Figure 191: Measured and calculated response of Sample 504 subjected to short beam shear testing. Red circle indicates maximum load.

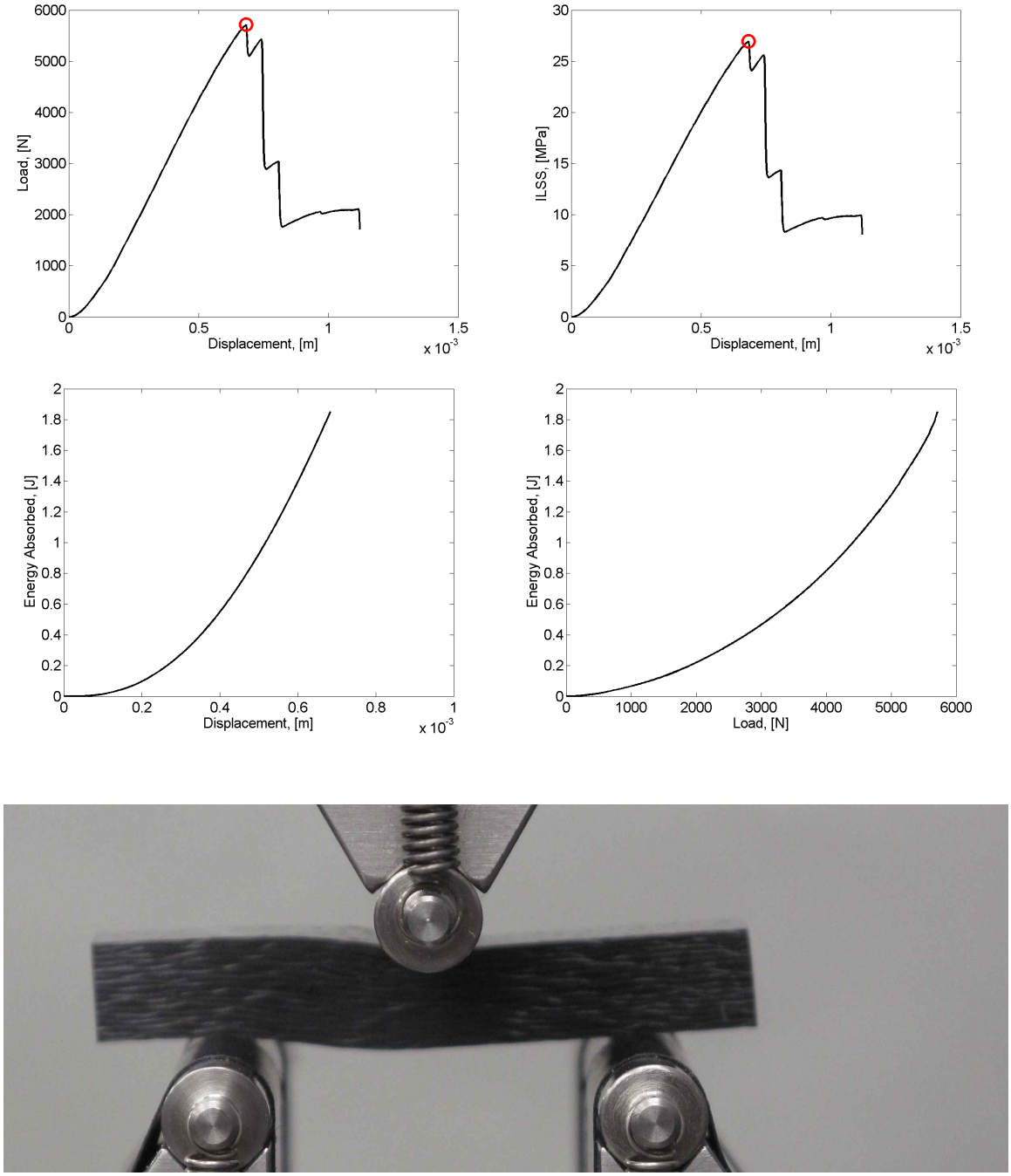

Figure 192: Measured and calculated response of Sample 507 subjected to short beam shear testing. Red circle indicates maximum load.

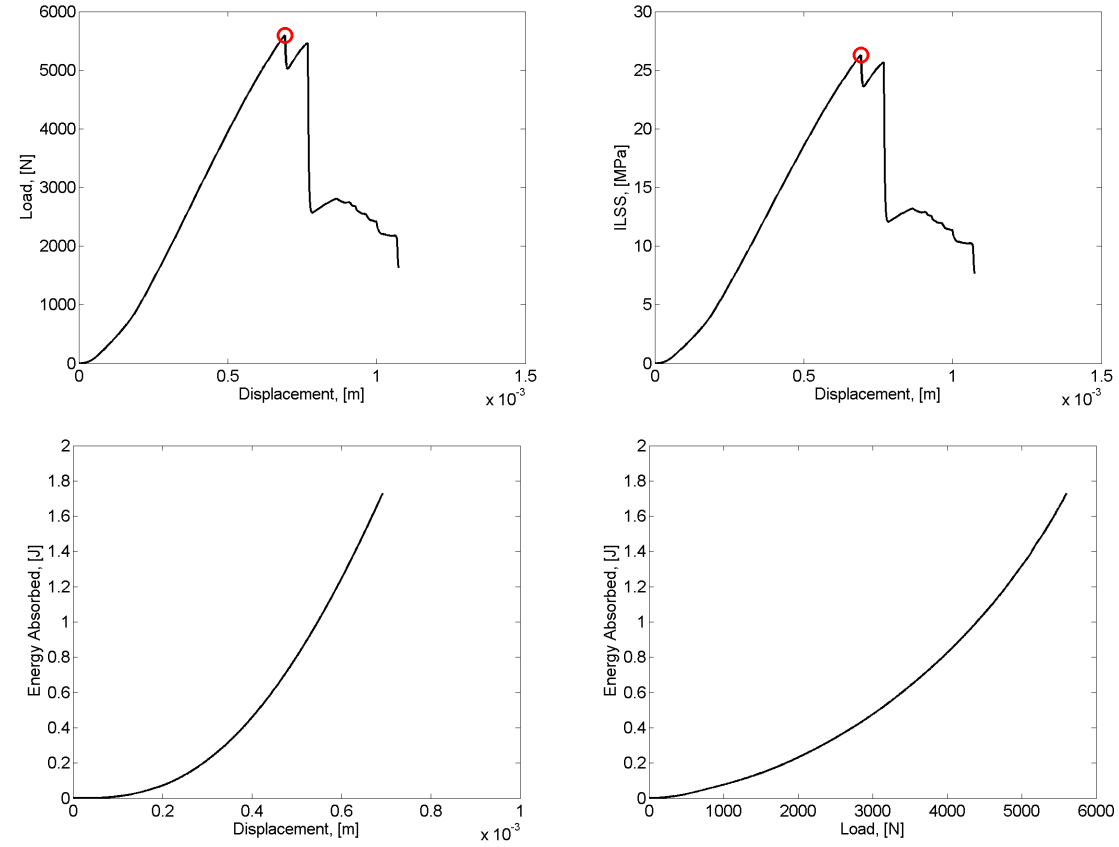

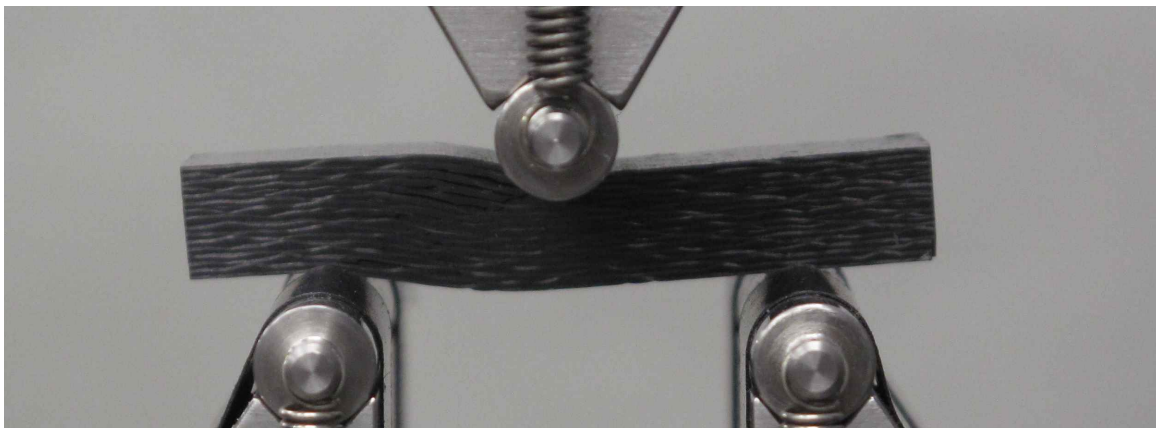

Figure 193: Measured and calculated response of Sample 508 subjected to short beam shear testing. Red circle indicates maximum load.

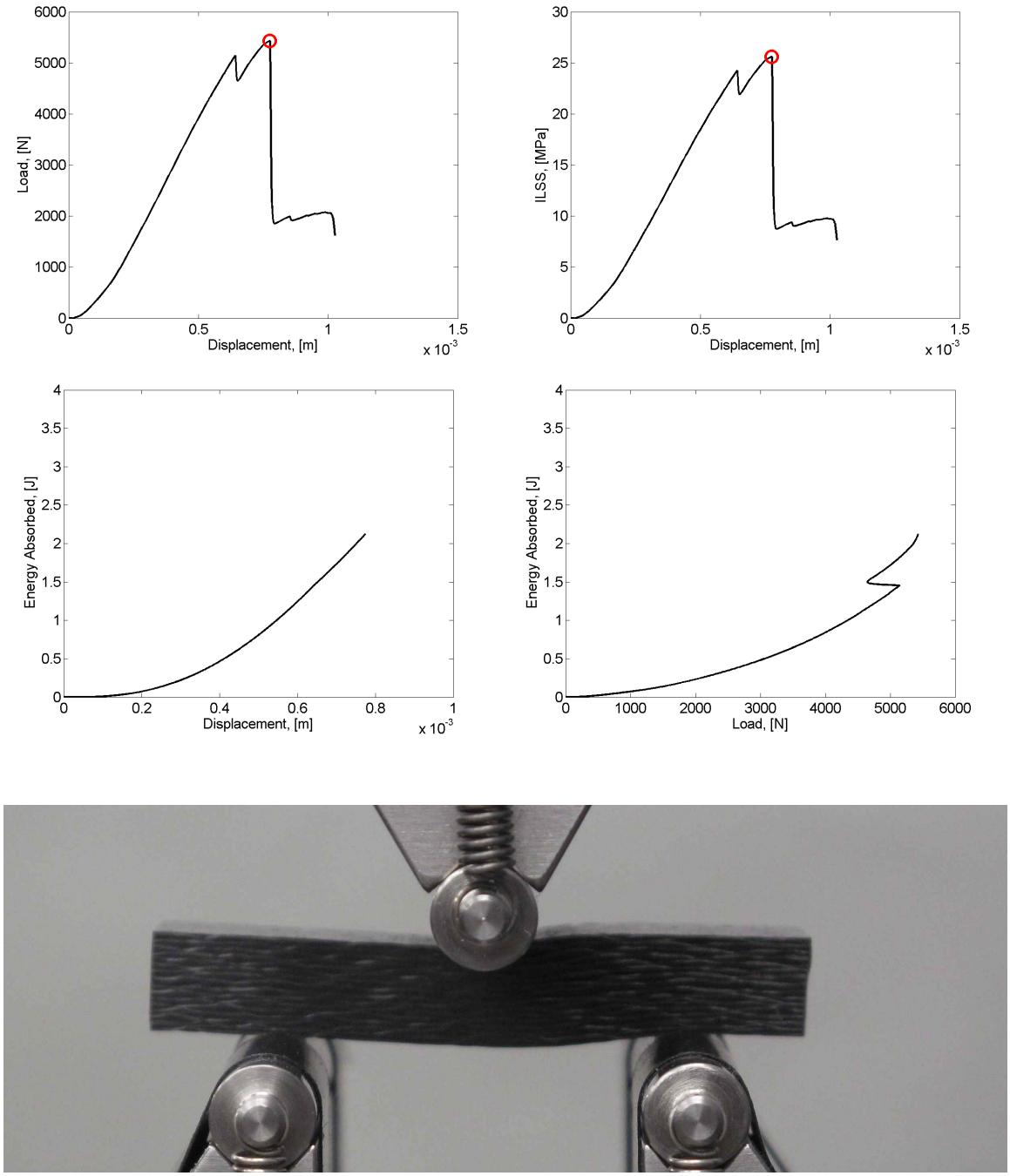

Figure 194: Measured and calculated response of Sample 509 subjected to short beam shear testing. Red circle indicates maximum load.

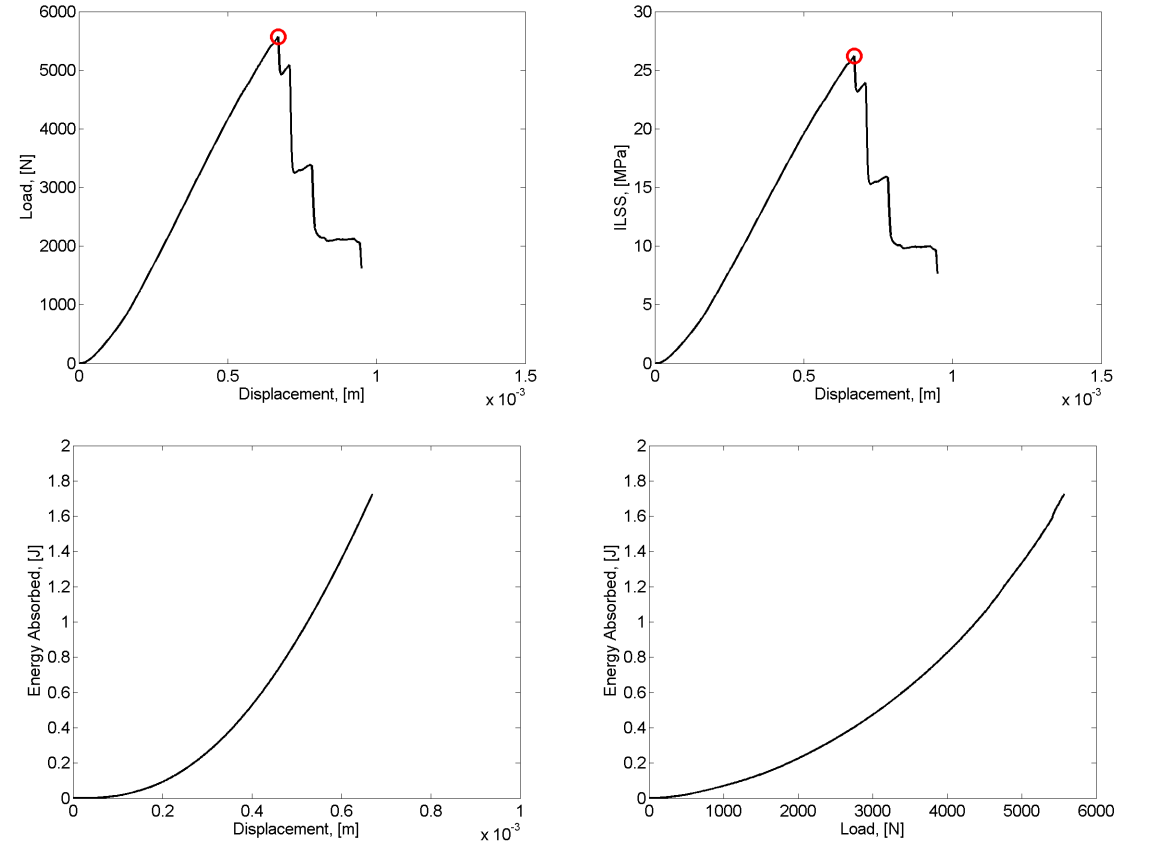

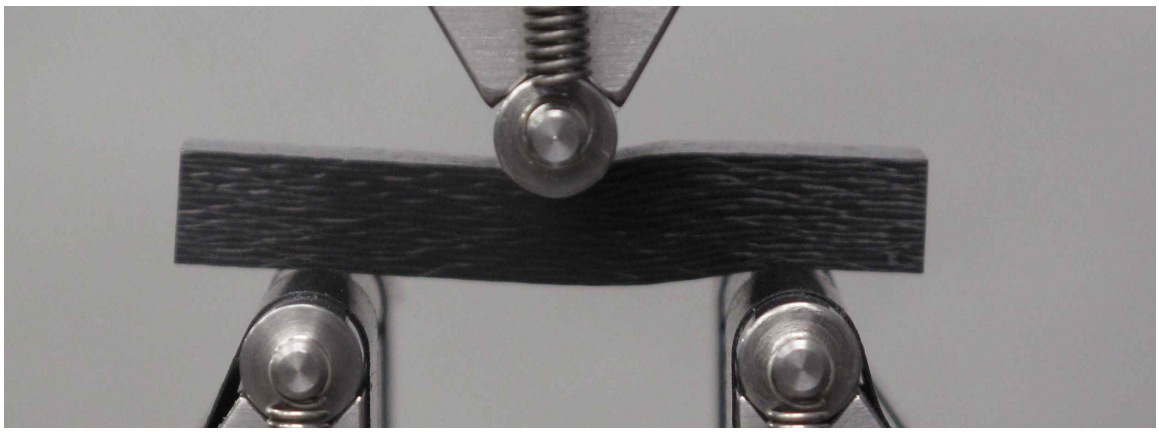

Figure 195: Measured and calculated response of Sample 510 subjected to short beam shear testing. Red circle indicates maximum load.

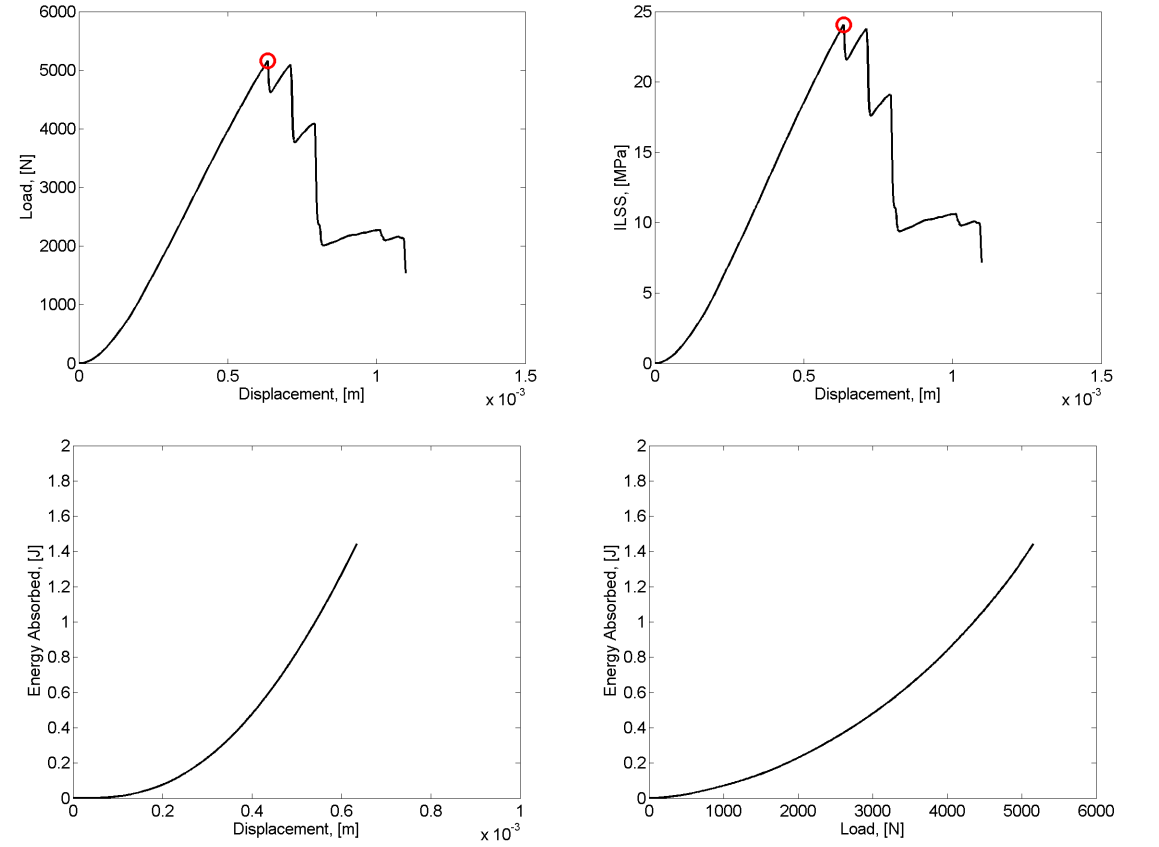

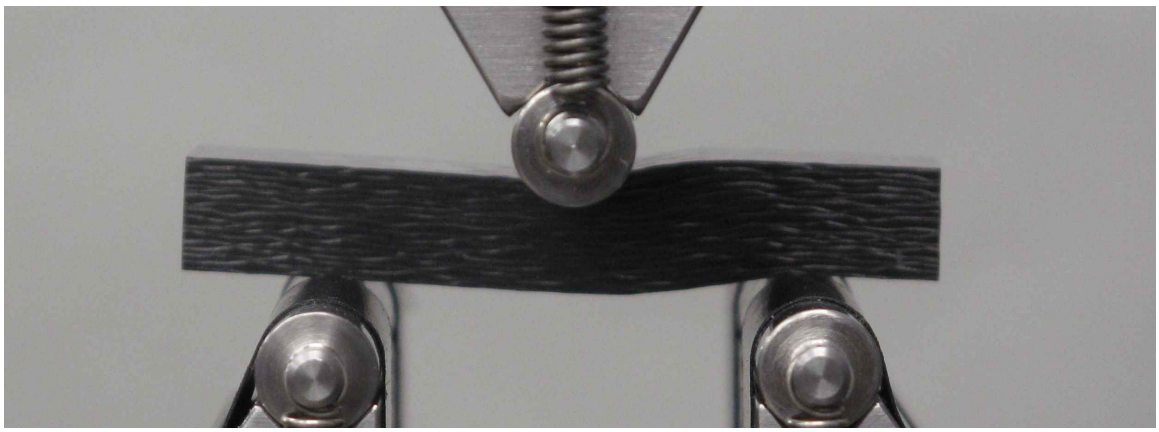

Figure 196: Measured and calculated response of Sample 601 subjected to short beam shear testing. Red circle indicates maximum load.

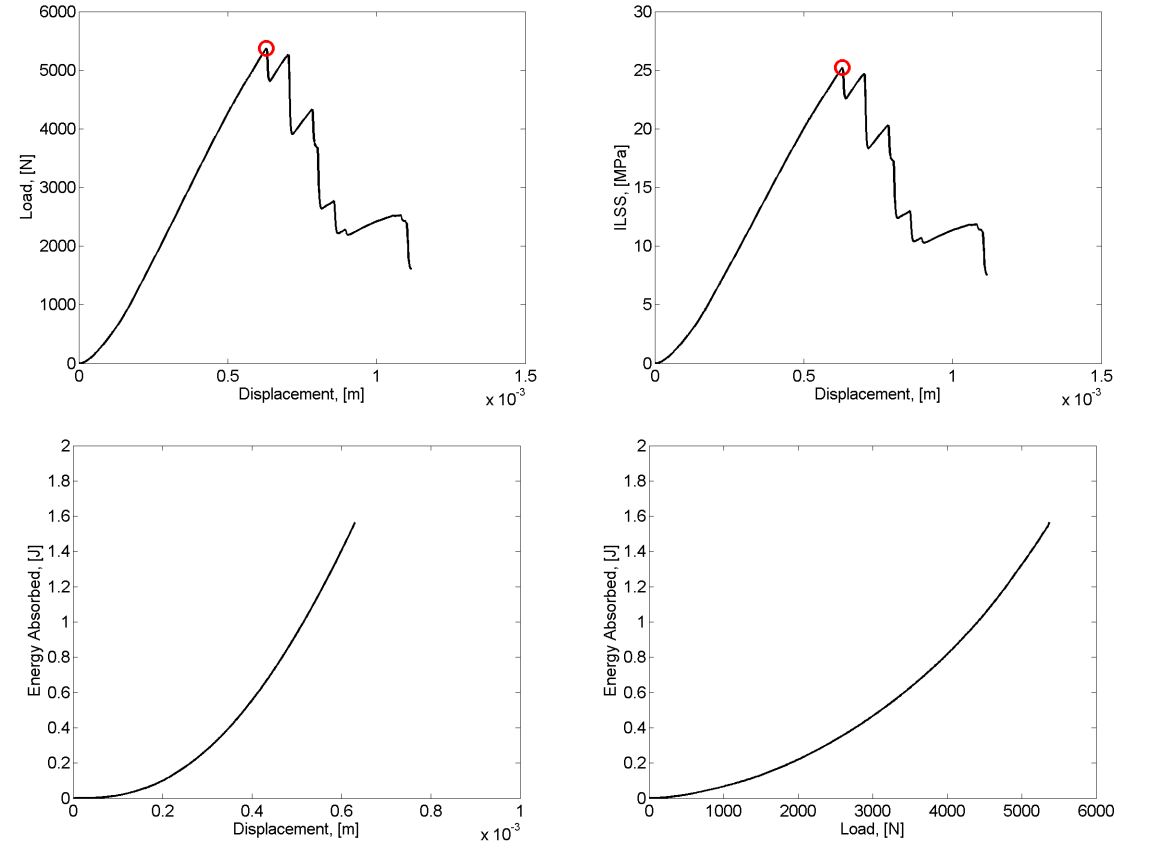

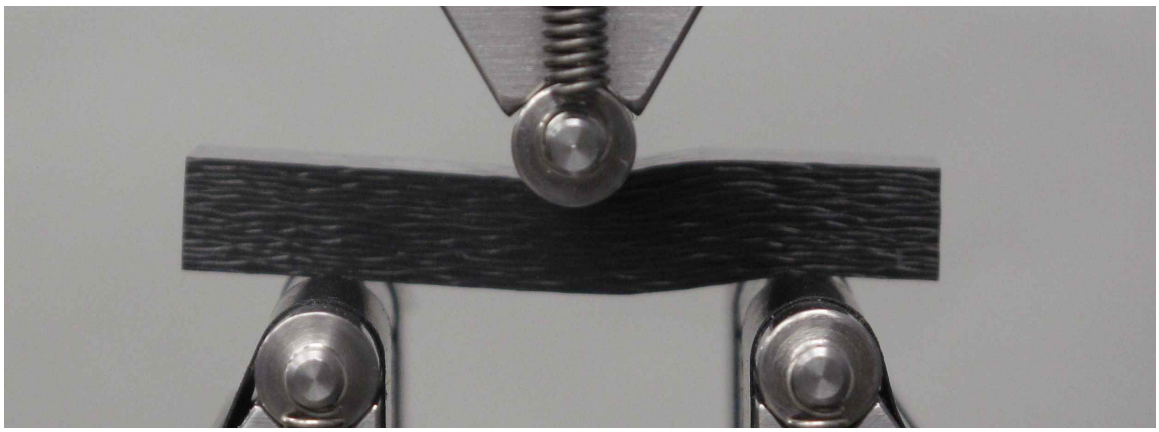

Figure 197: Measured and calculated response of Sample 602 subjected to short beam shear testing. Red circle indicates maximum load.

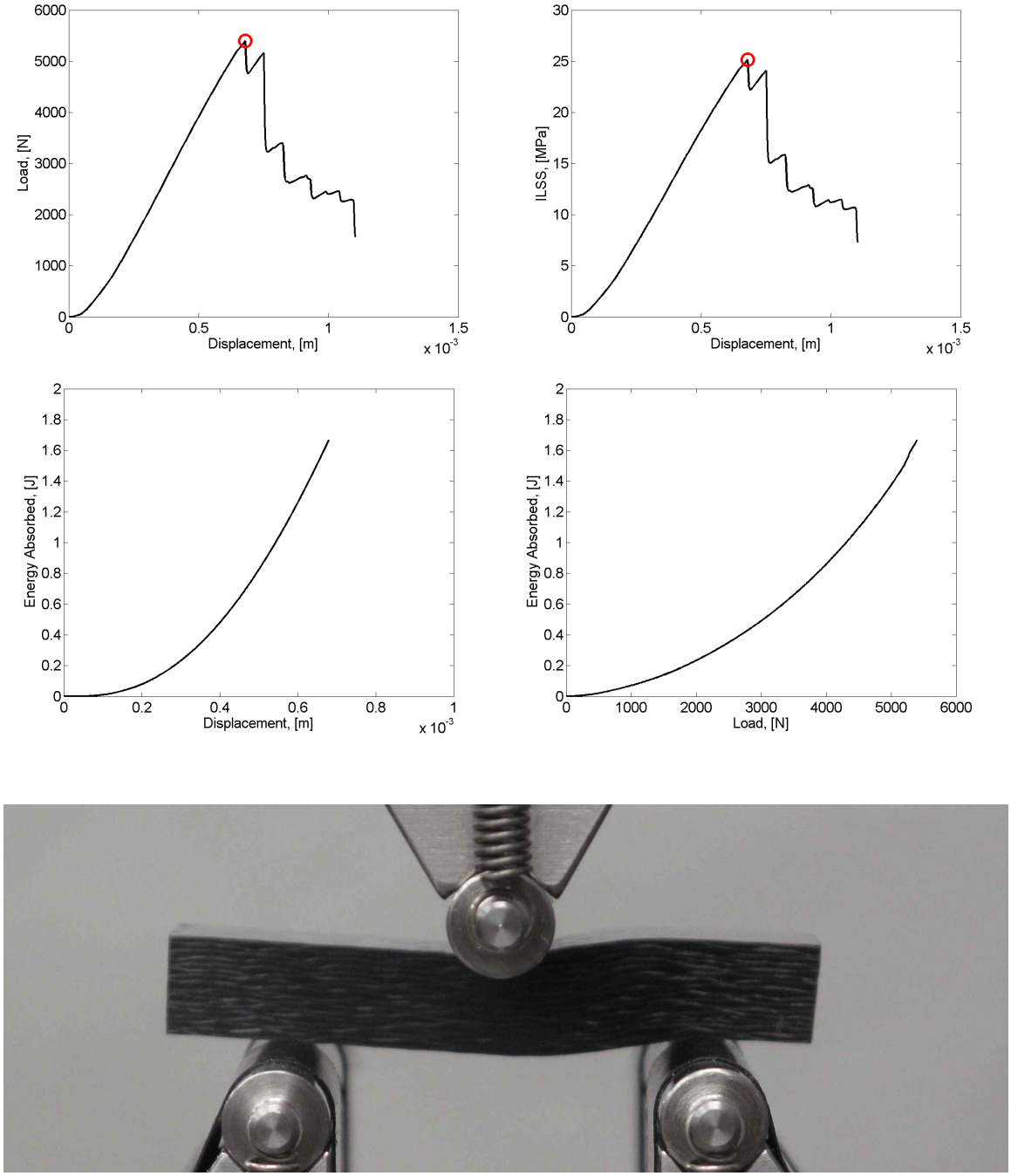

Figure 198: Measured and calculated response of Sample 603 subjected to short beam shear testing. Red circle indicates maximum load.

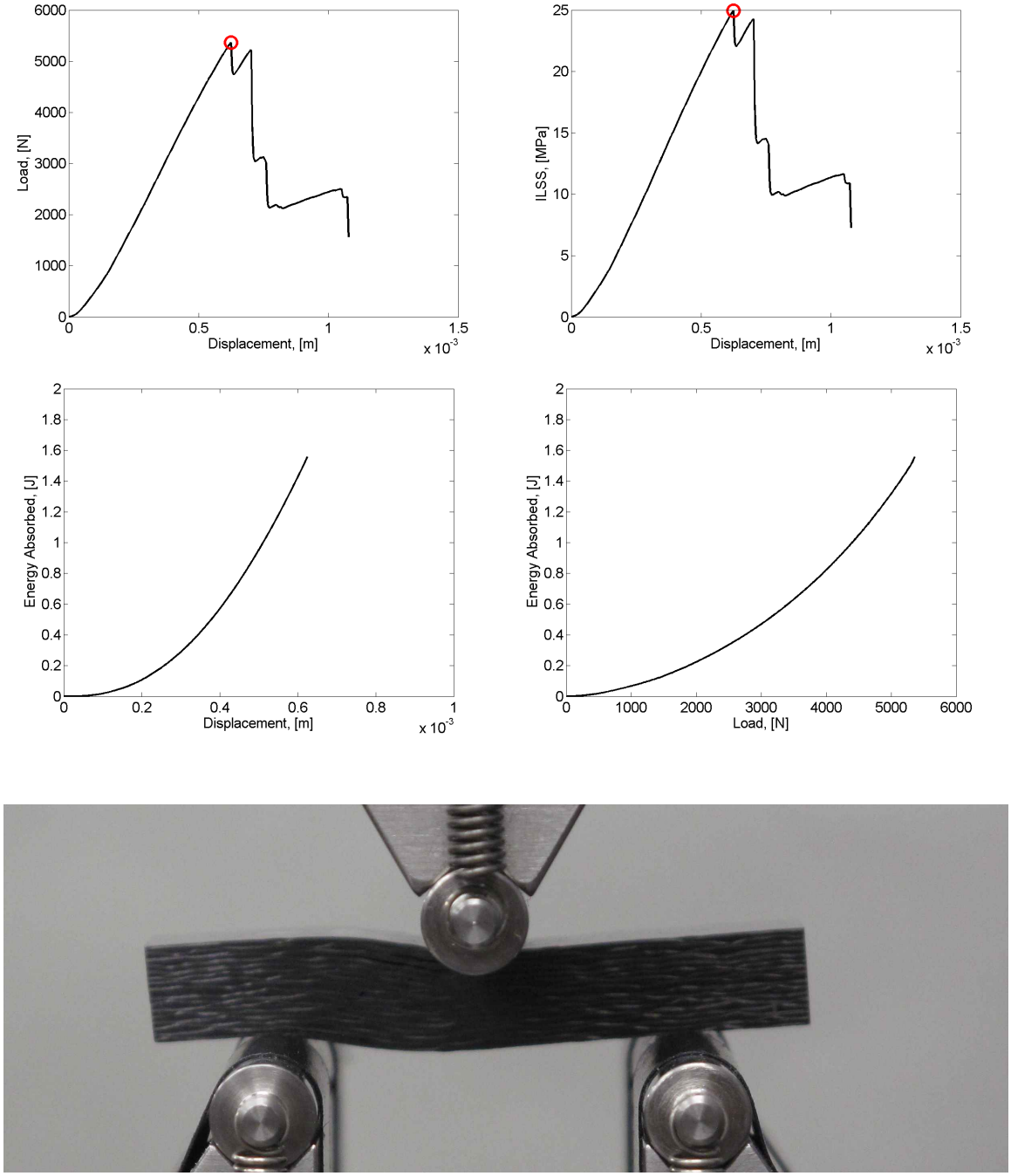

Figure 199: Measured and calculated response of Sample 604 subjected to short beam shear testing. Red circle indicates maximum load.

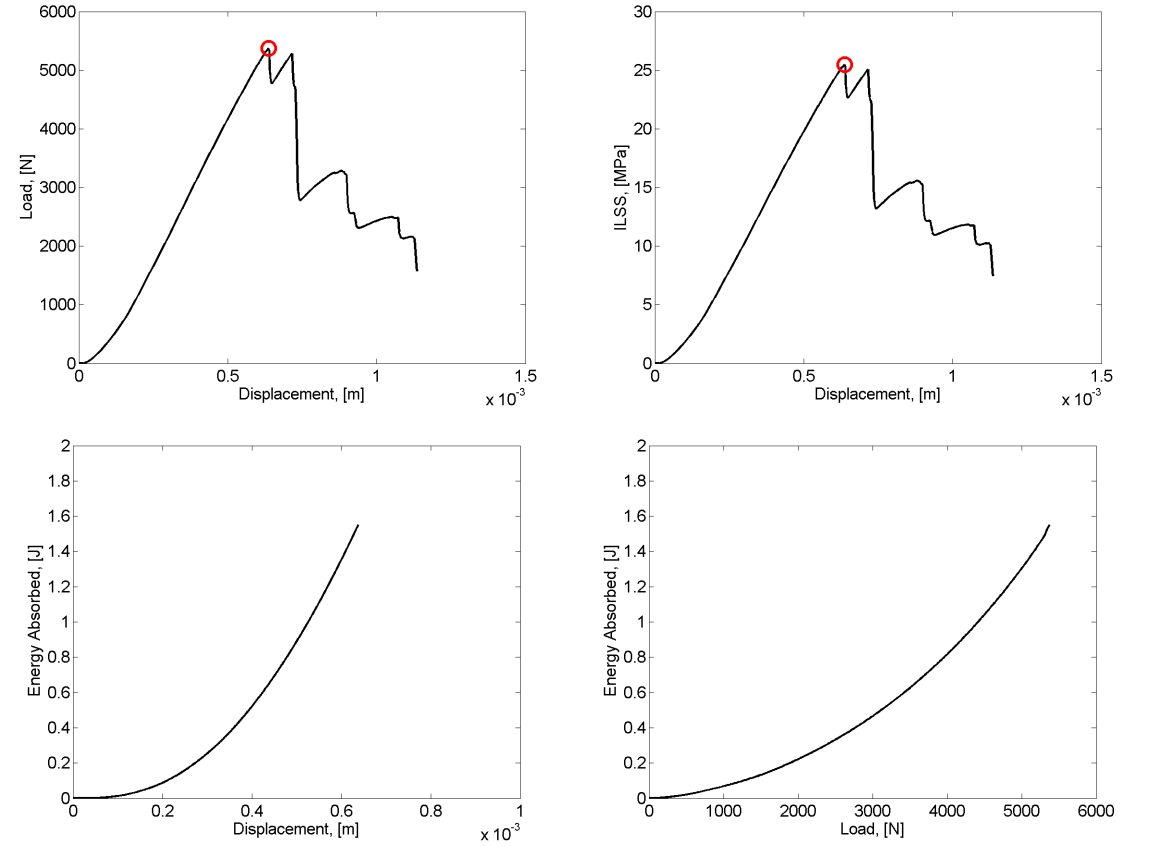

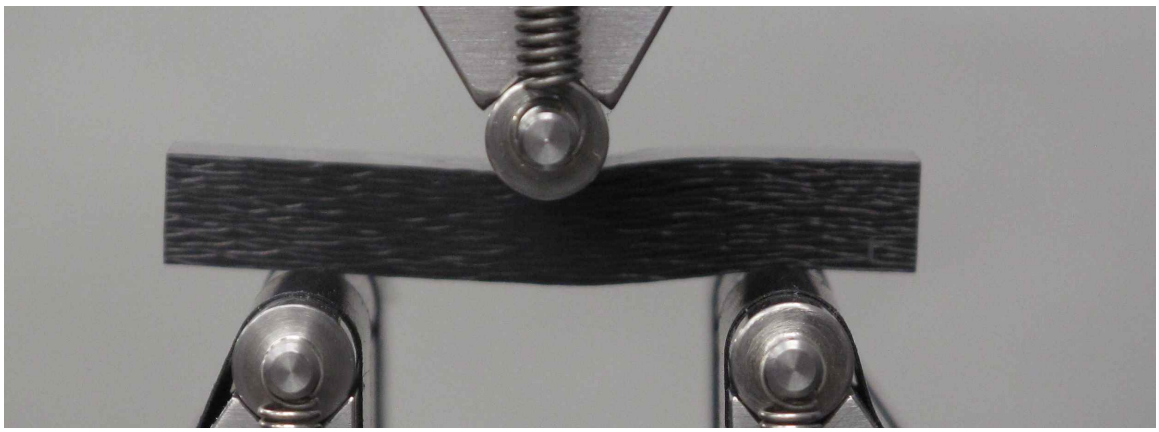

Figure 200: Measured and calculated response of Sample 607 subjected to short beam shear testing. Red circle indicates maximum load.

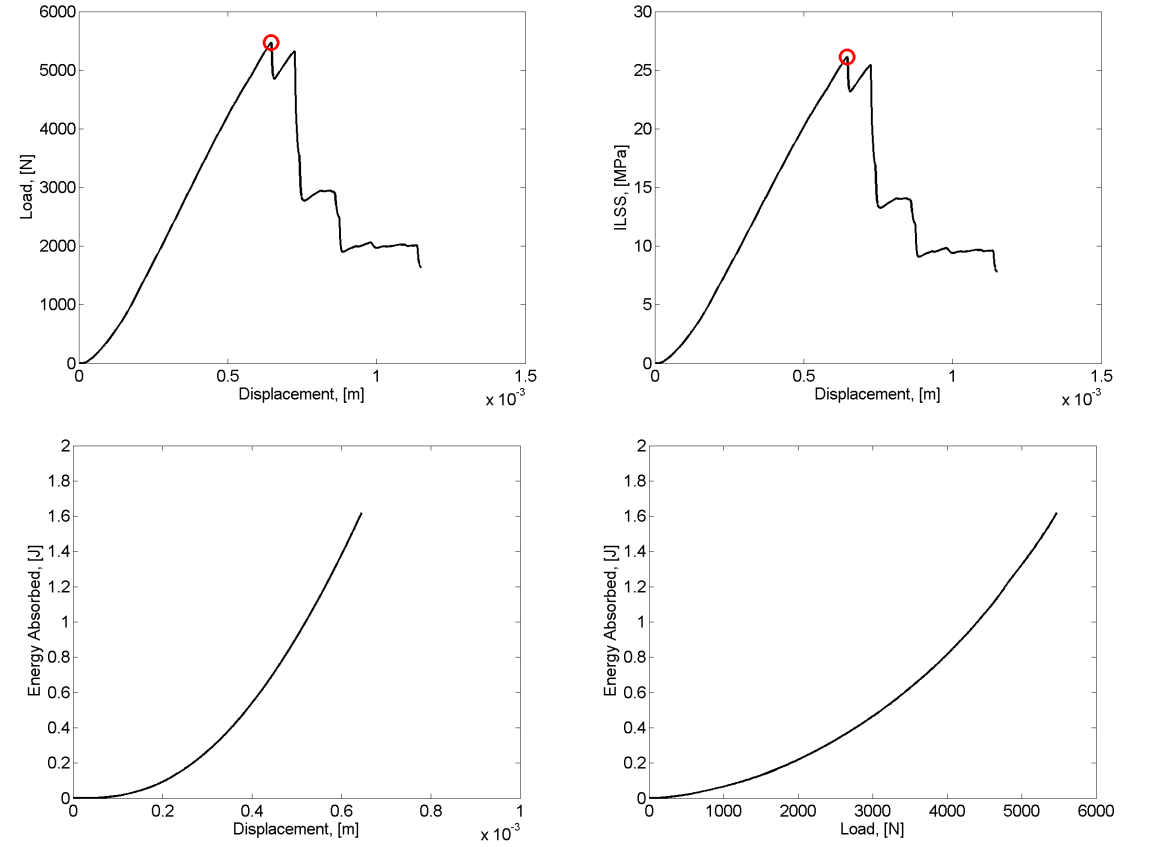

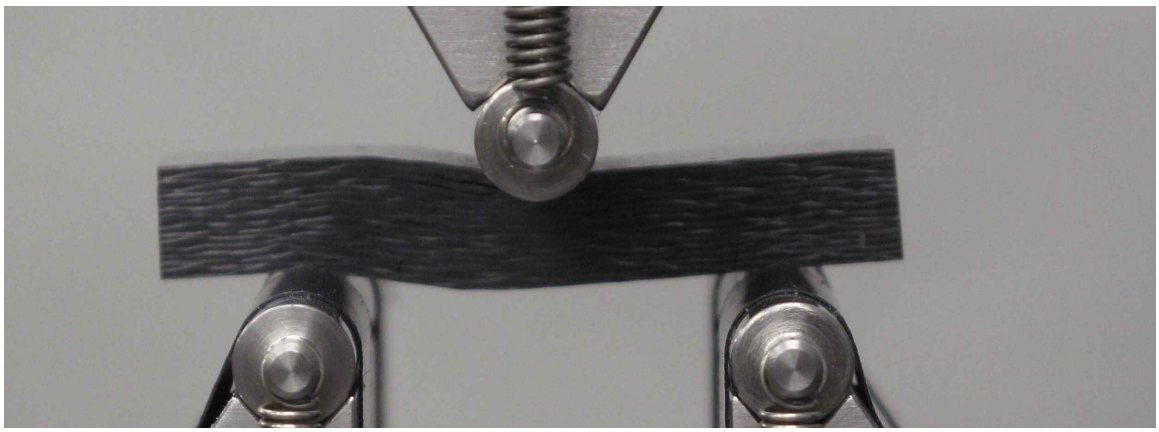

Figure 201: Measured and calculated response of Sample 608 subjected to short beam shear testing. Red circle indicates maximum load.

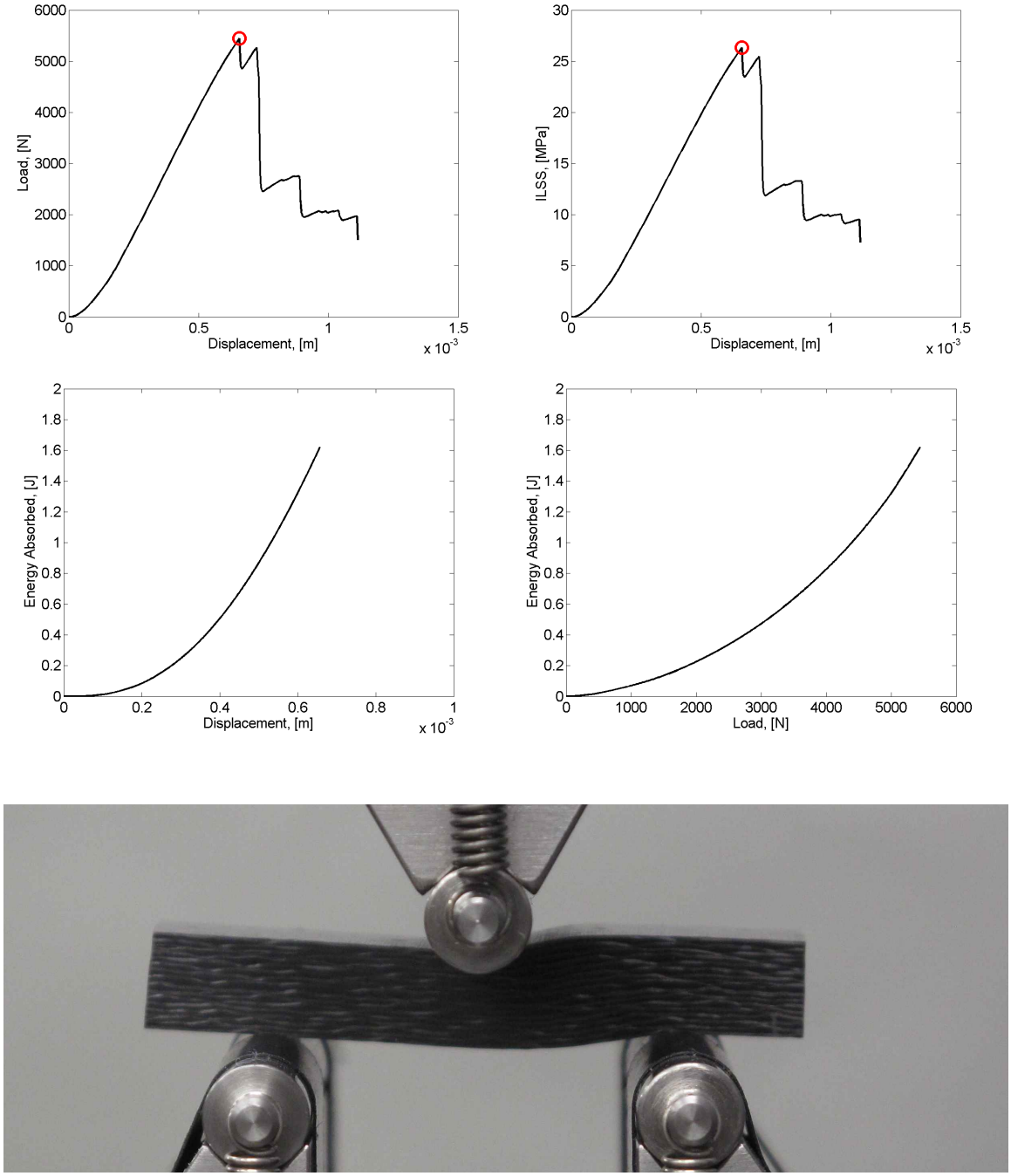

Figure 202: Measured and calculated response of Sample 609 subjected to short beam shear testing. Red circle indicates maximum load.

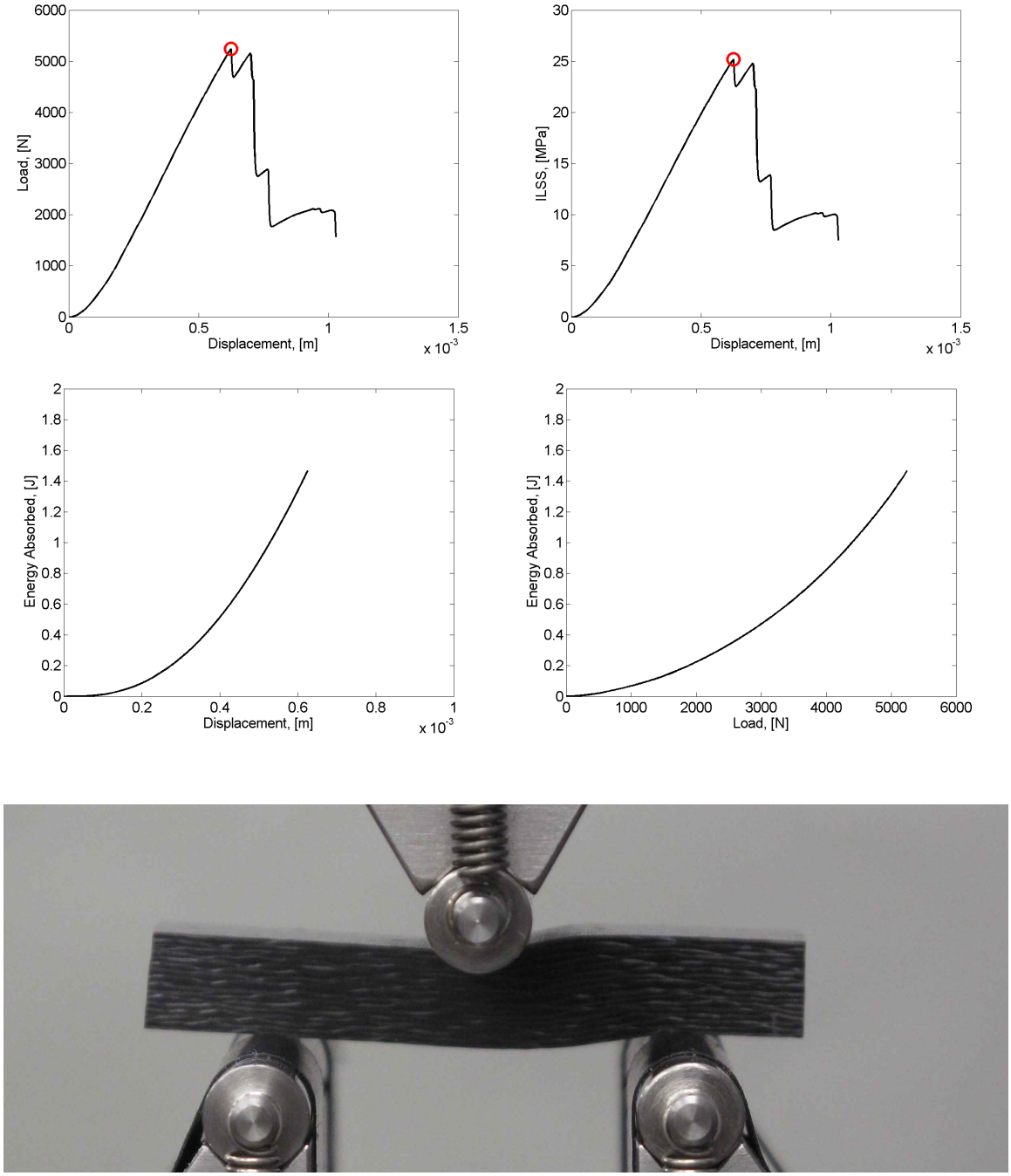

Figure 203: Measured and calculated response of Sample 610 subjected to short beam shear testing. Red circle indicates maximum load.

Appendix C: Impact–Hemispherical tup

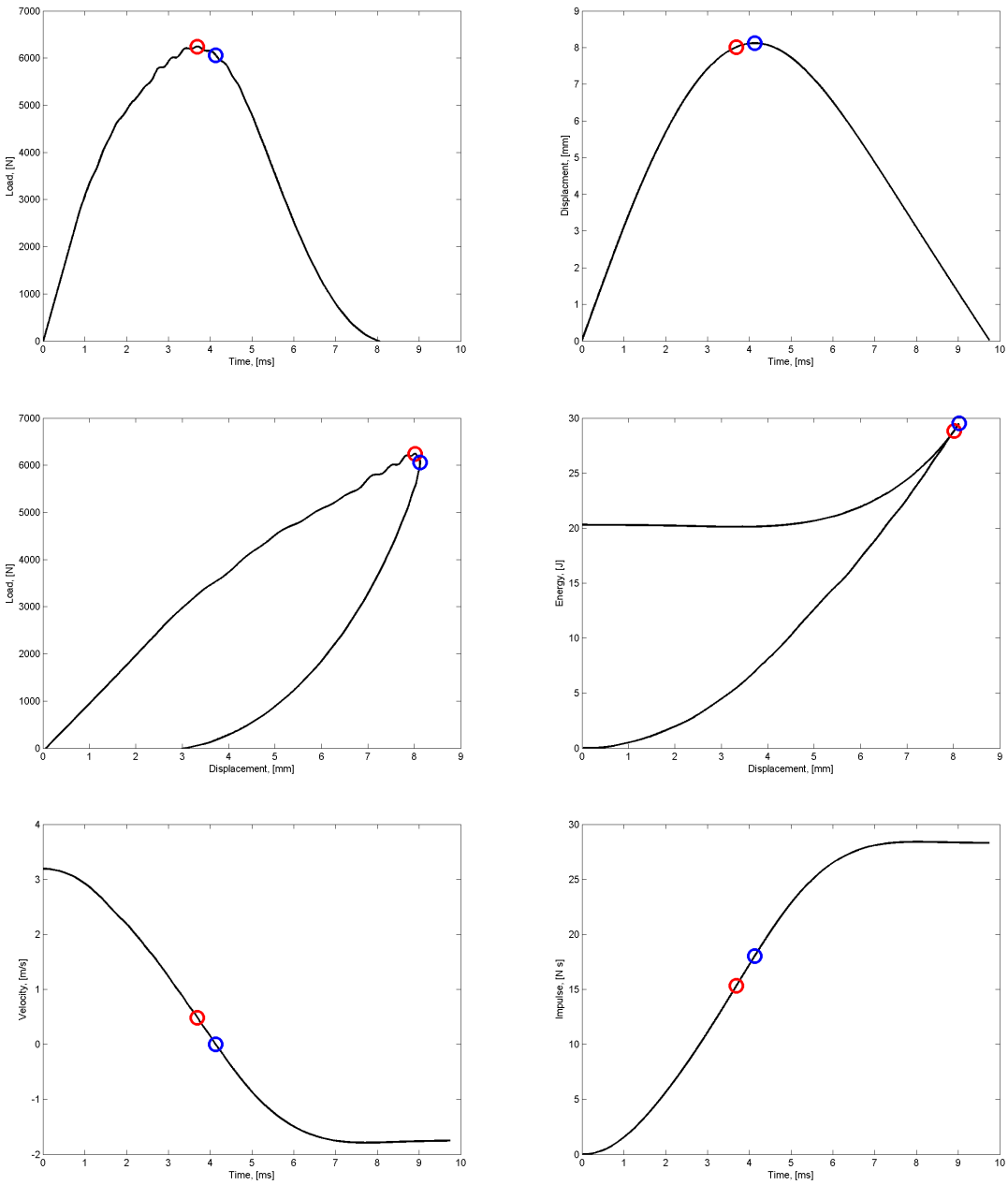

Figure 204: Measured and calculated response of Sample 107 subjected to hemispherical tup low-velocity drop weight testing. Red circle indicates maximum load, blue circle corresponds to maximum displacement.

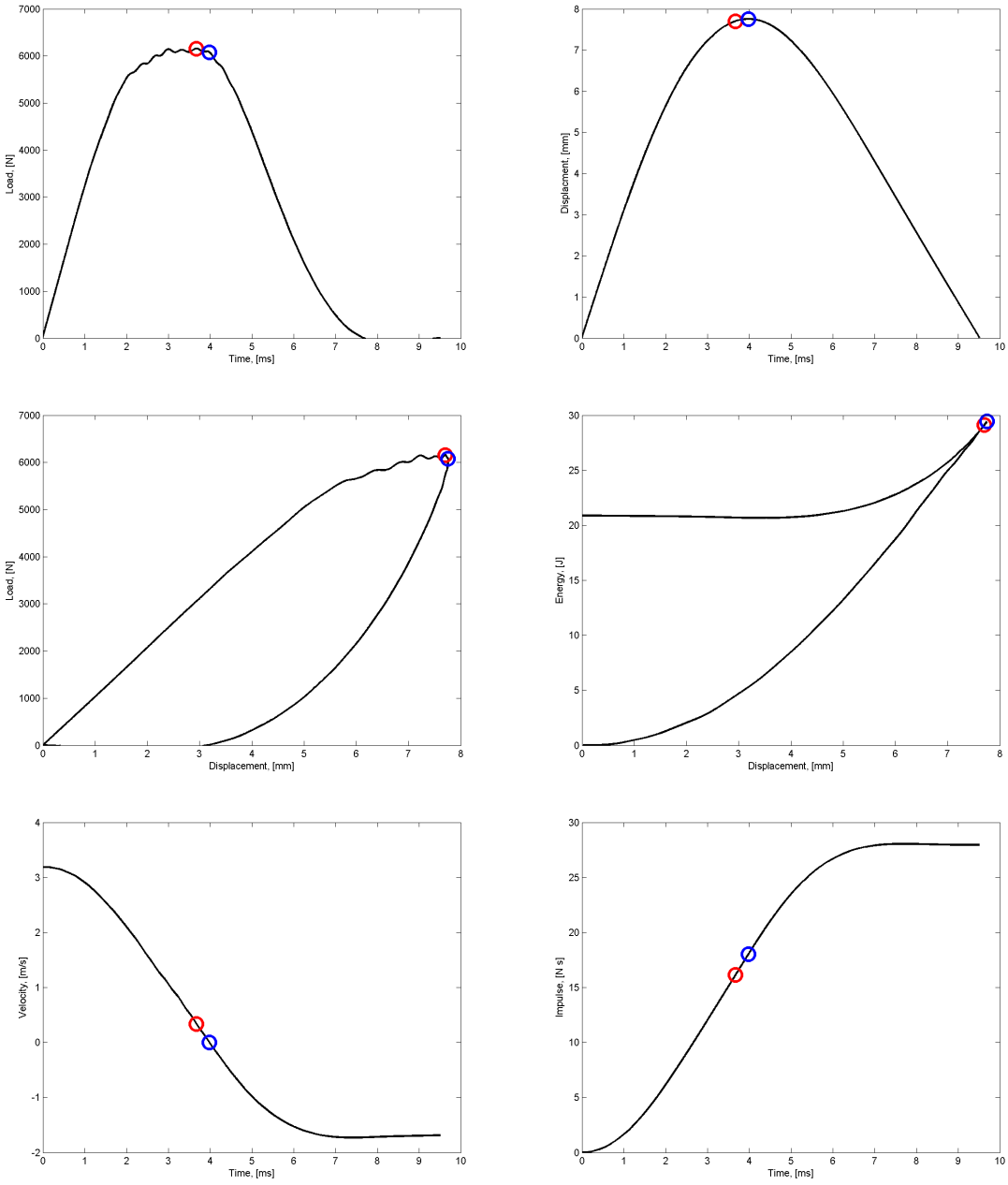

Figure 205: Measured and calculated response of Sample 108 subjected to hemispherical tup low-velocity drop weight testing. Red circle indicates maximum load, blue circle corresponds to maximum displacement.

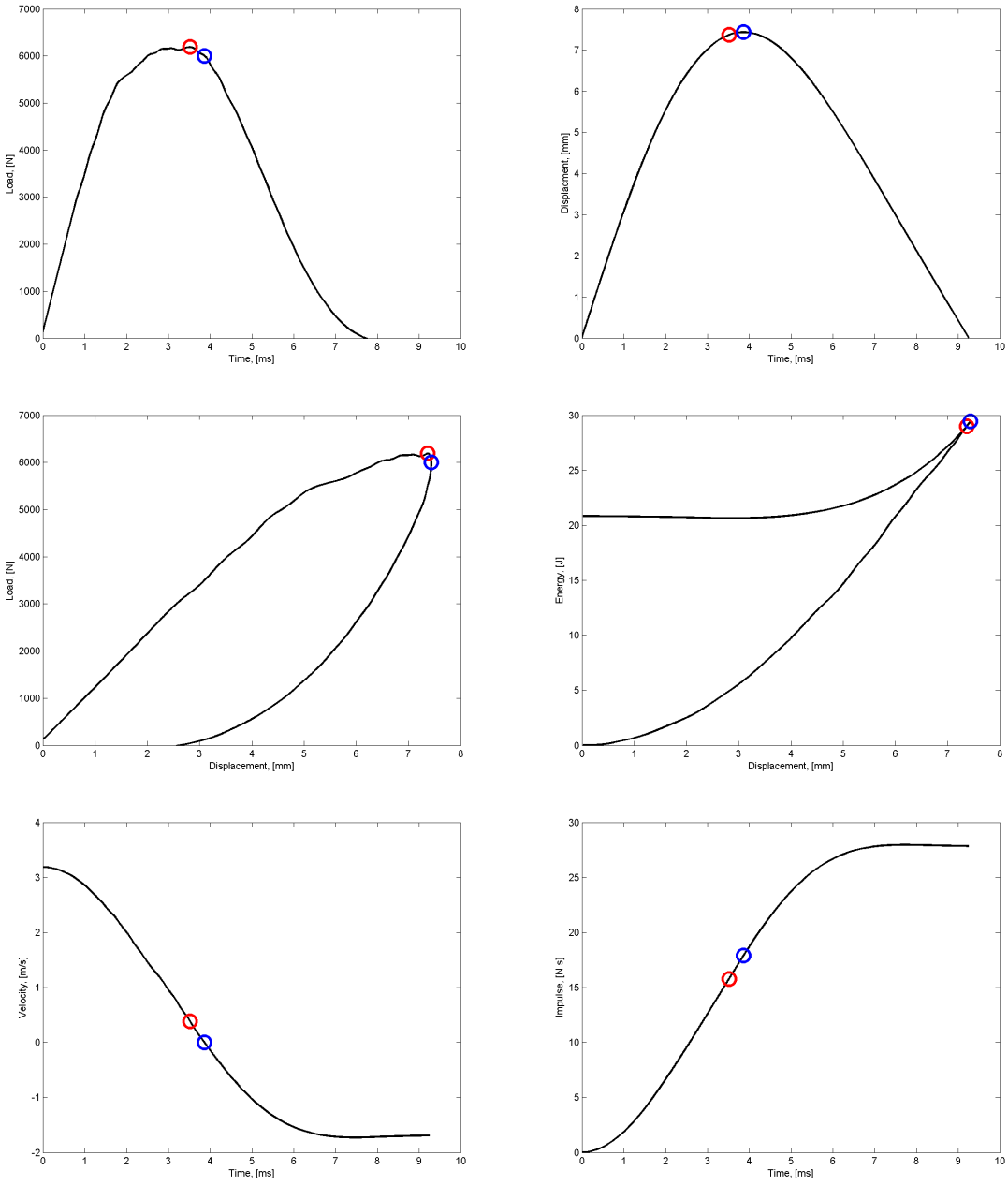

Figure 206: Measured and calculated response of Sample 109 subjected to hemispherical tup low-velocity drop weight testing. Red circle indicates maximum load, blue circle corresponds to maximum displacement.

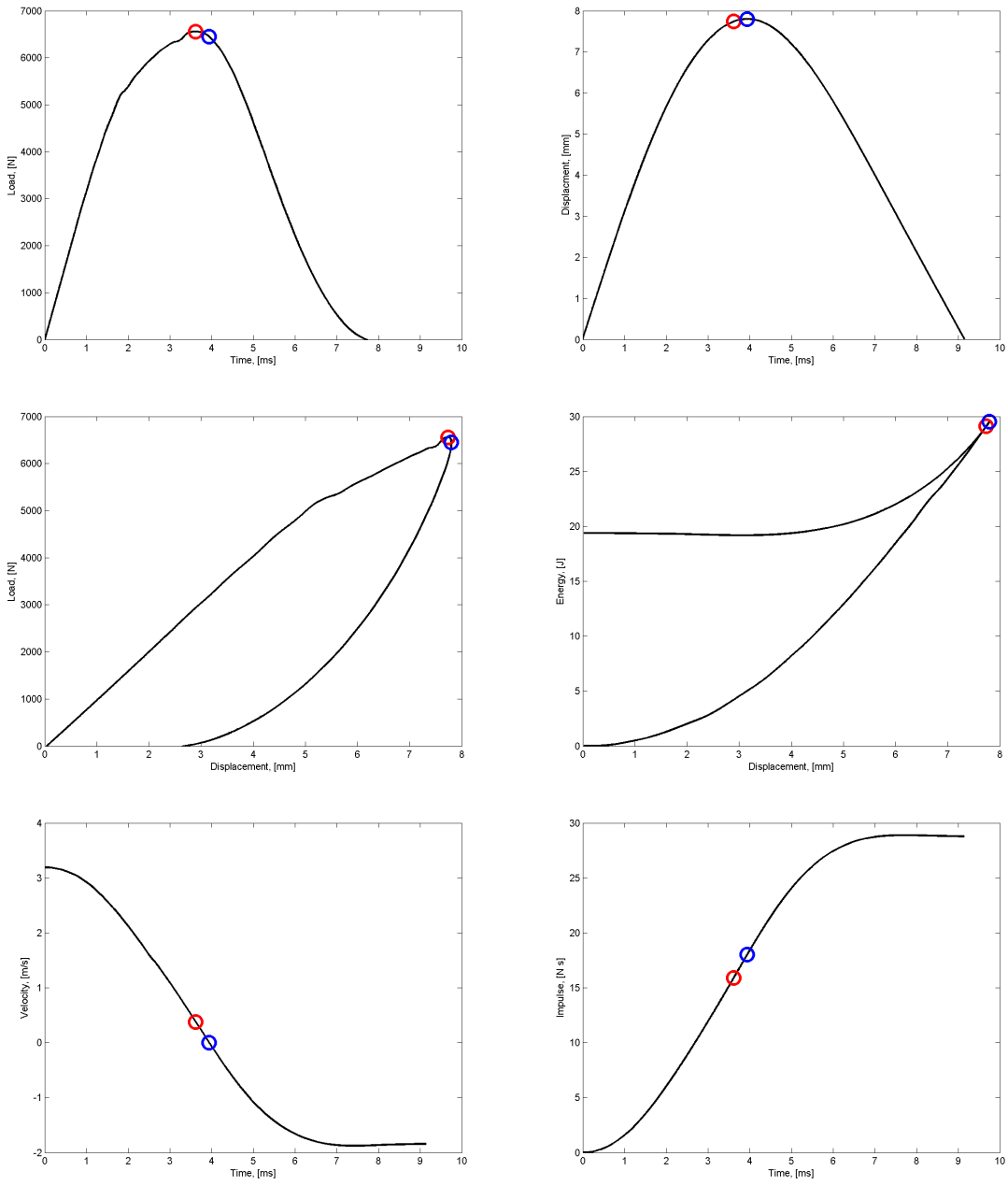

Figure 207: Measured and calculated response of Sample 110 subjected to hemispherical tup low-velocity drop weight testing. Red circle indicates maximum load, blue circle corresponds to maximum displacement.

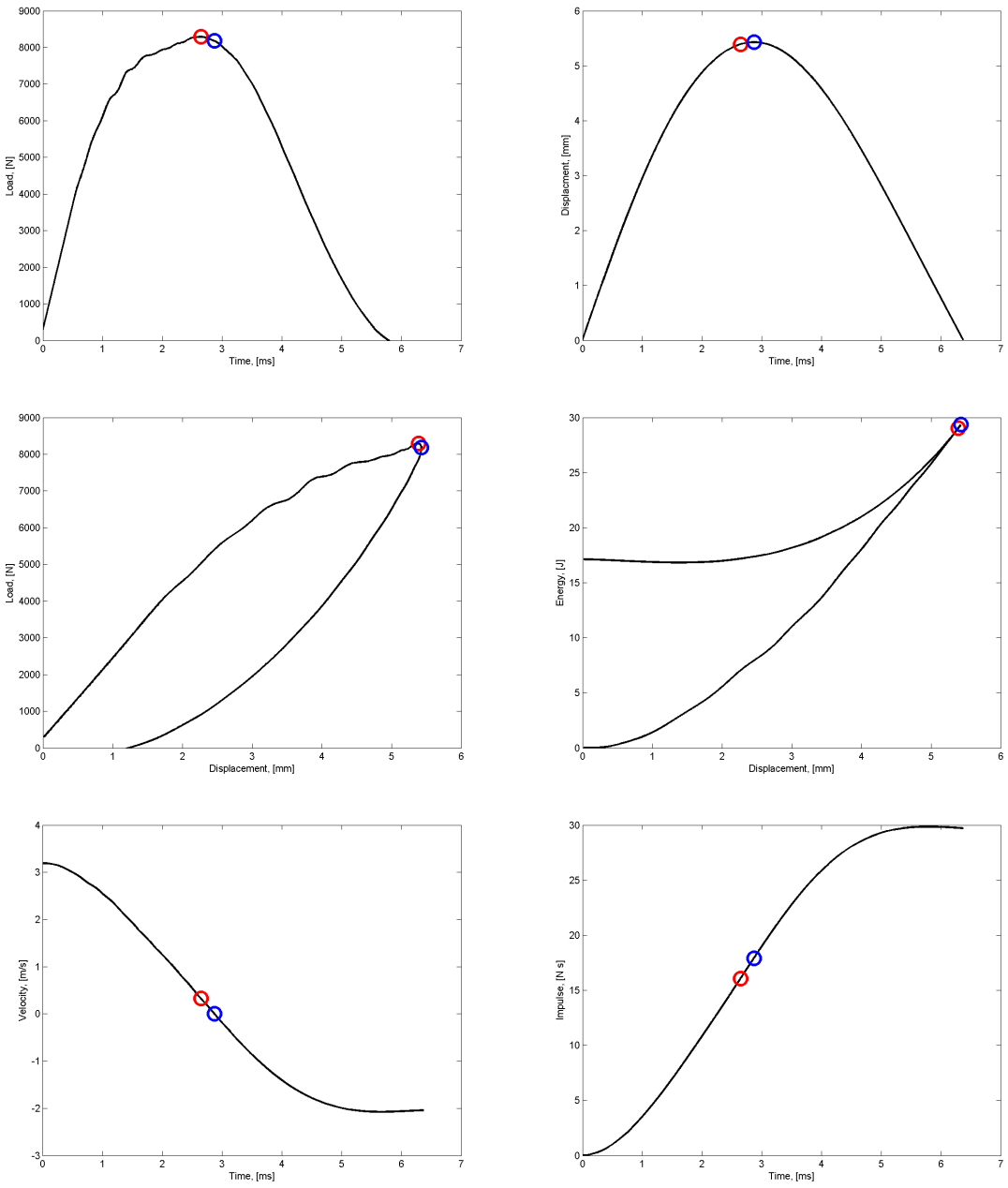

Figure 208: Measured and calculated response of Sample 208 subjected to hemispherical tup low-velocity drop weight testing. Red circle indicates maximum load, blue circle corresponds to maximum displacement.

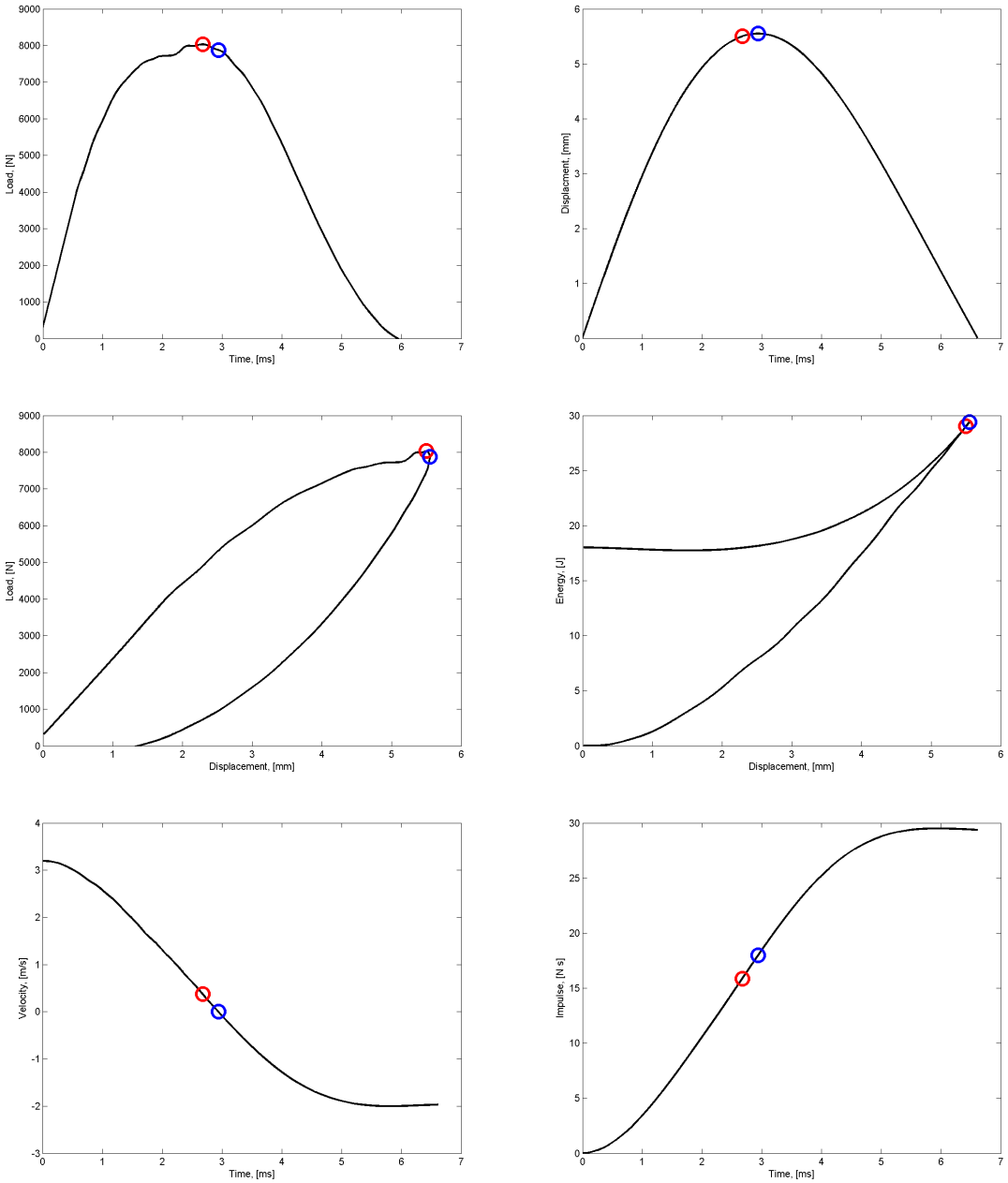

Figure 209: Measured and calculated response of Sample 209 subjected to hemispherical tup low-velocity drop weight testing. Red circle indicates maximum load, blue circle corresponds to maximum displacement.

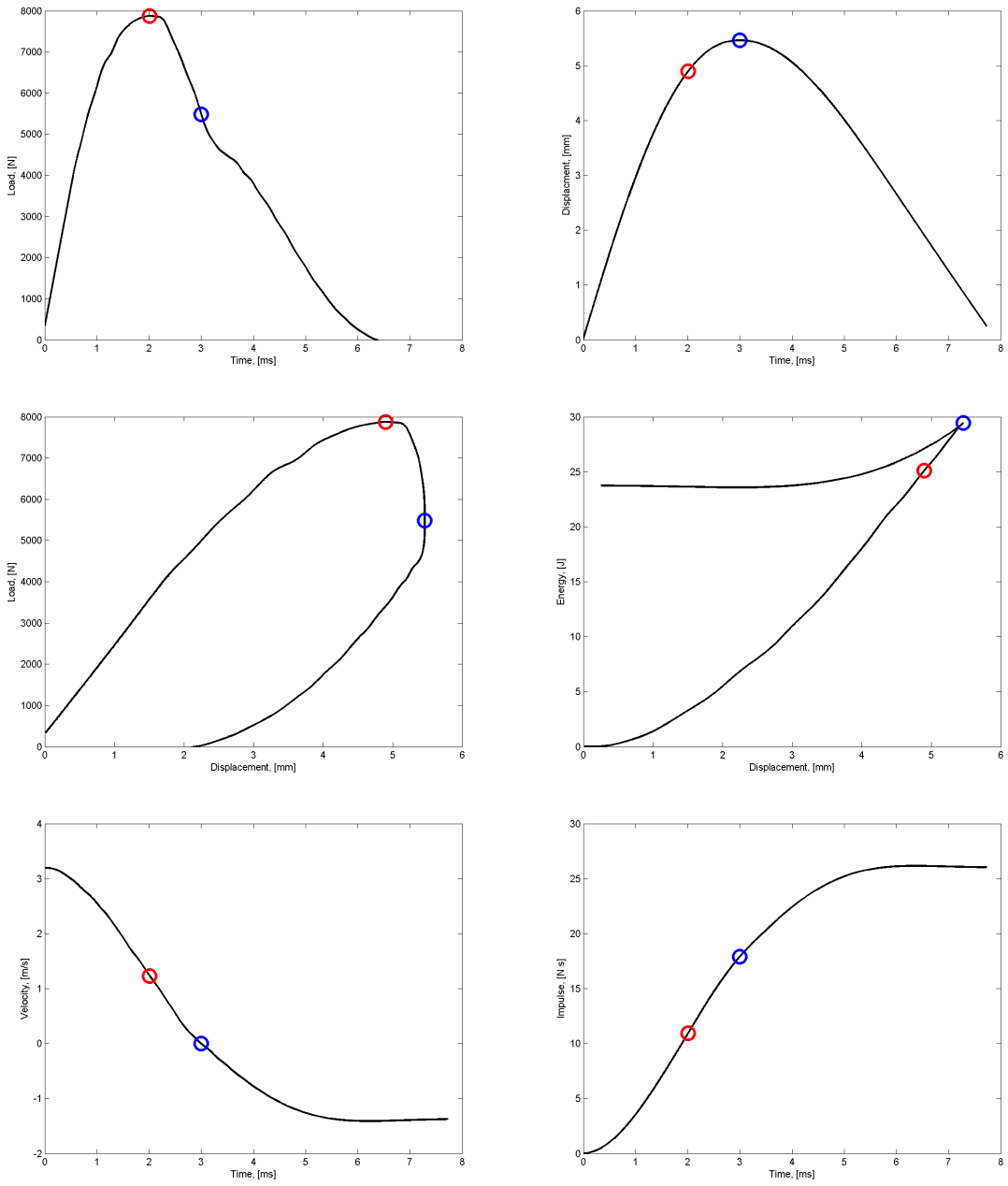

Figure 210: Measured and calculated response of Sample 210 subjected to hemispherical tup low-velocity drop weight testing. Red circle indicates maximum load, blue circle corresponds to maximum displacement.

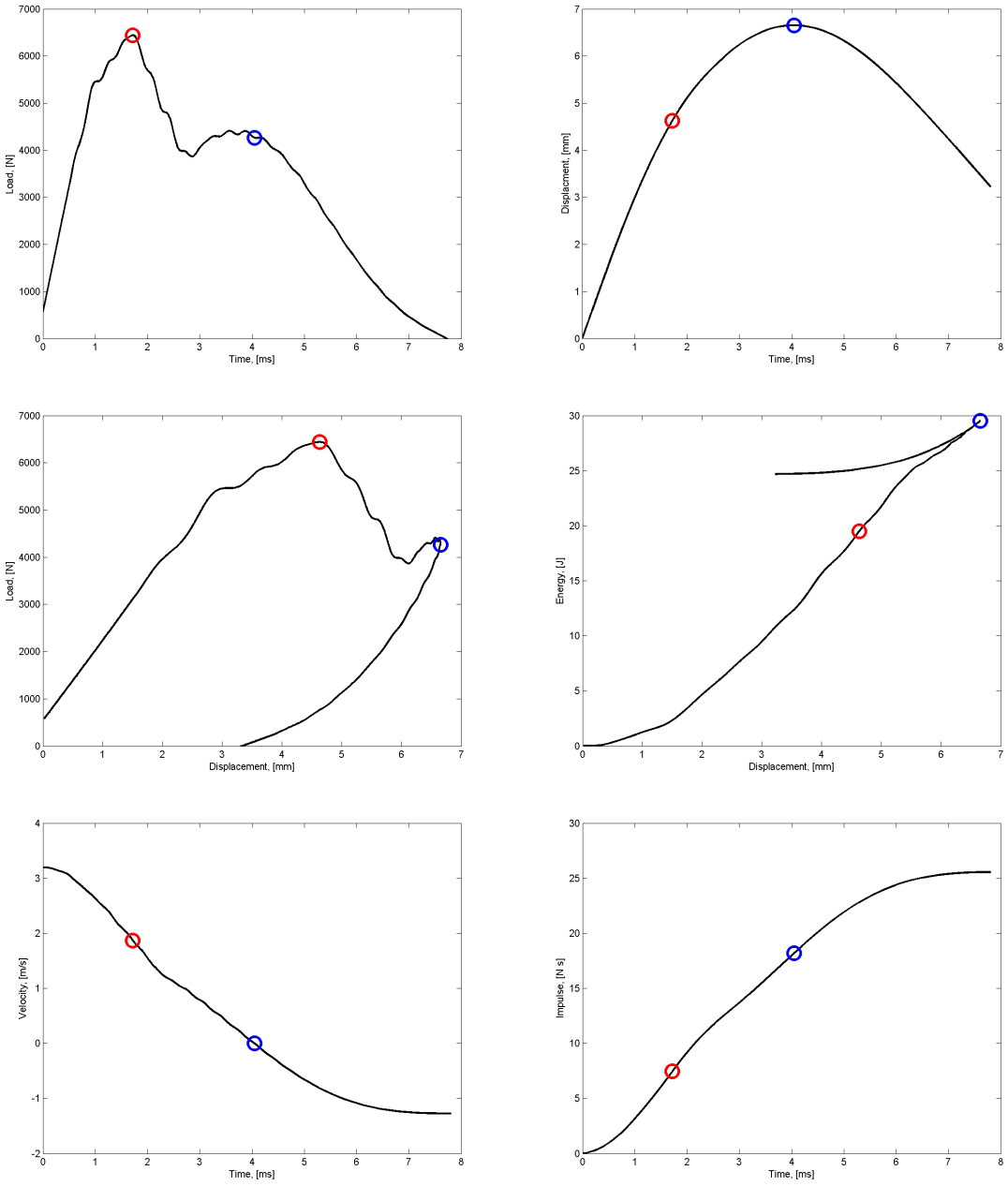

Figure 211: Measured and calculated response of Sample 307 subjected to hemispherical tup low-velocity drop weight testing. Red circle indicates maximum load, blue circle corresponds to maximum displacement.

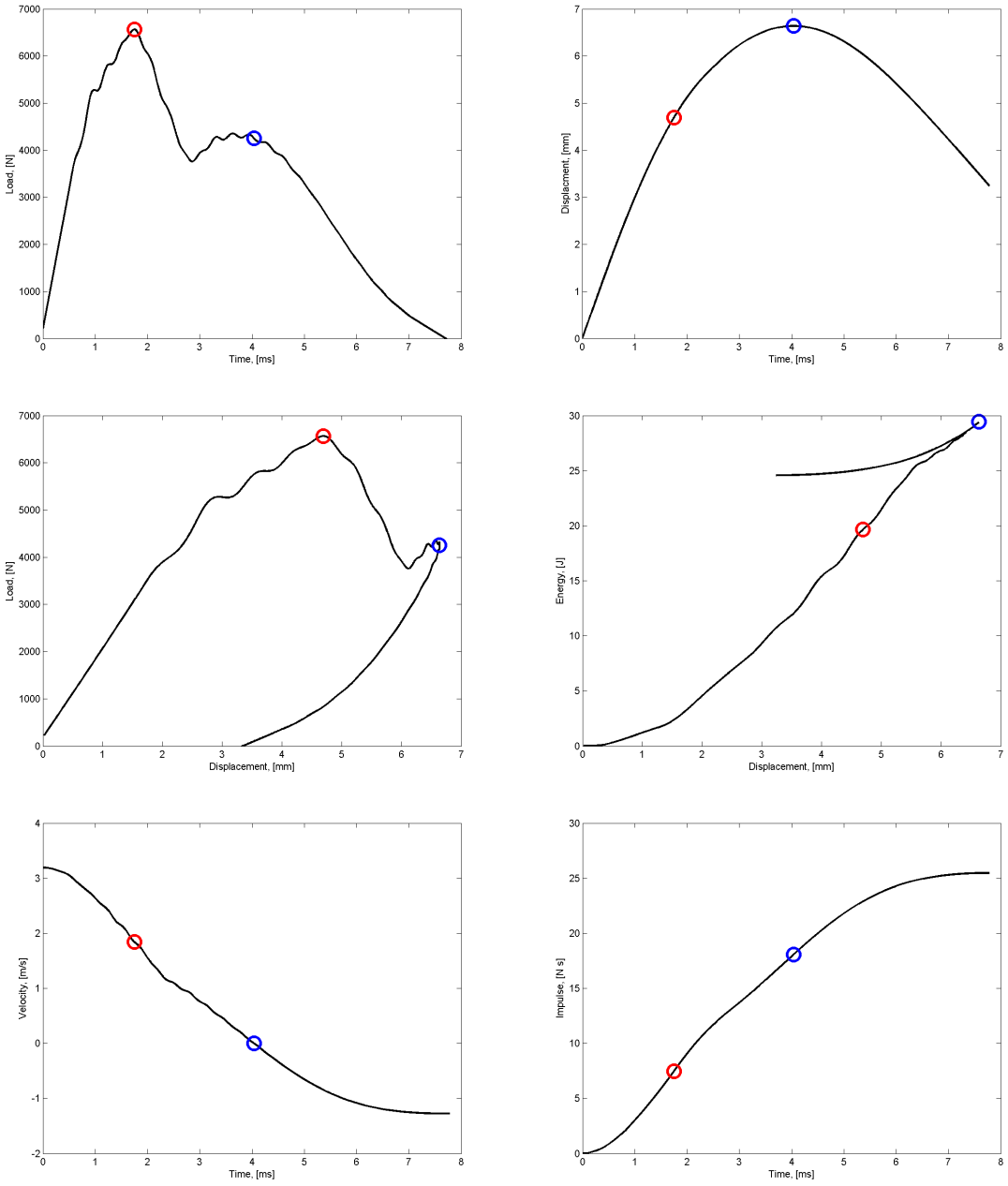

Figure 212: Measured and calculated response of Sample 308 subjected to hemispherical tup low-velocity drop weight testing. Red circle indicates maximum load, blue circle corresponds to maximum displacement.

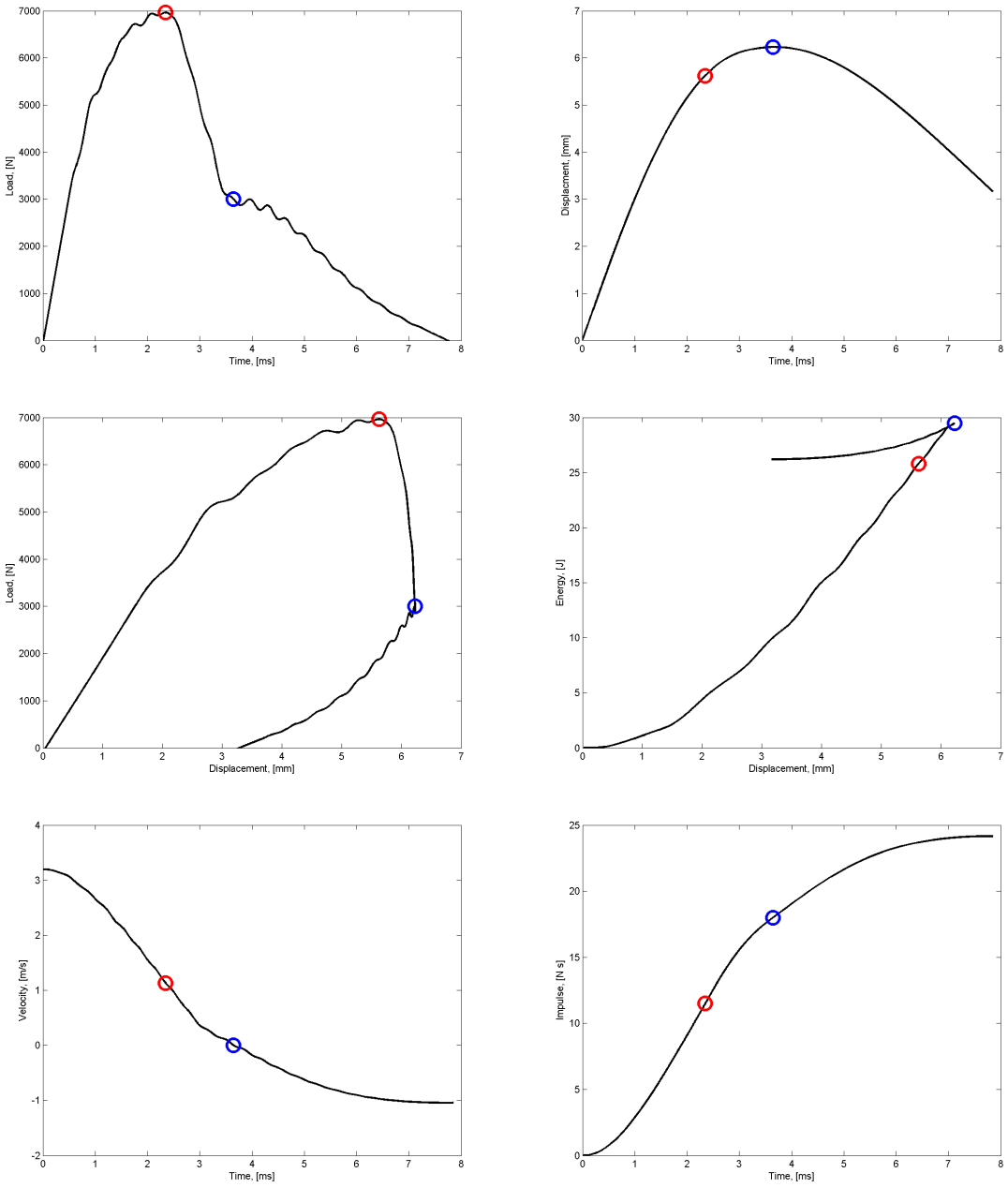

Figure 213: Measured and calculated response of Sample 309 subjected to hemispherical tup low-velocity drop weight testing. Red circle indicates maximum load, blue circle corresponds to maximum displacement.

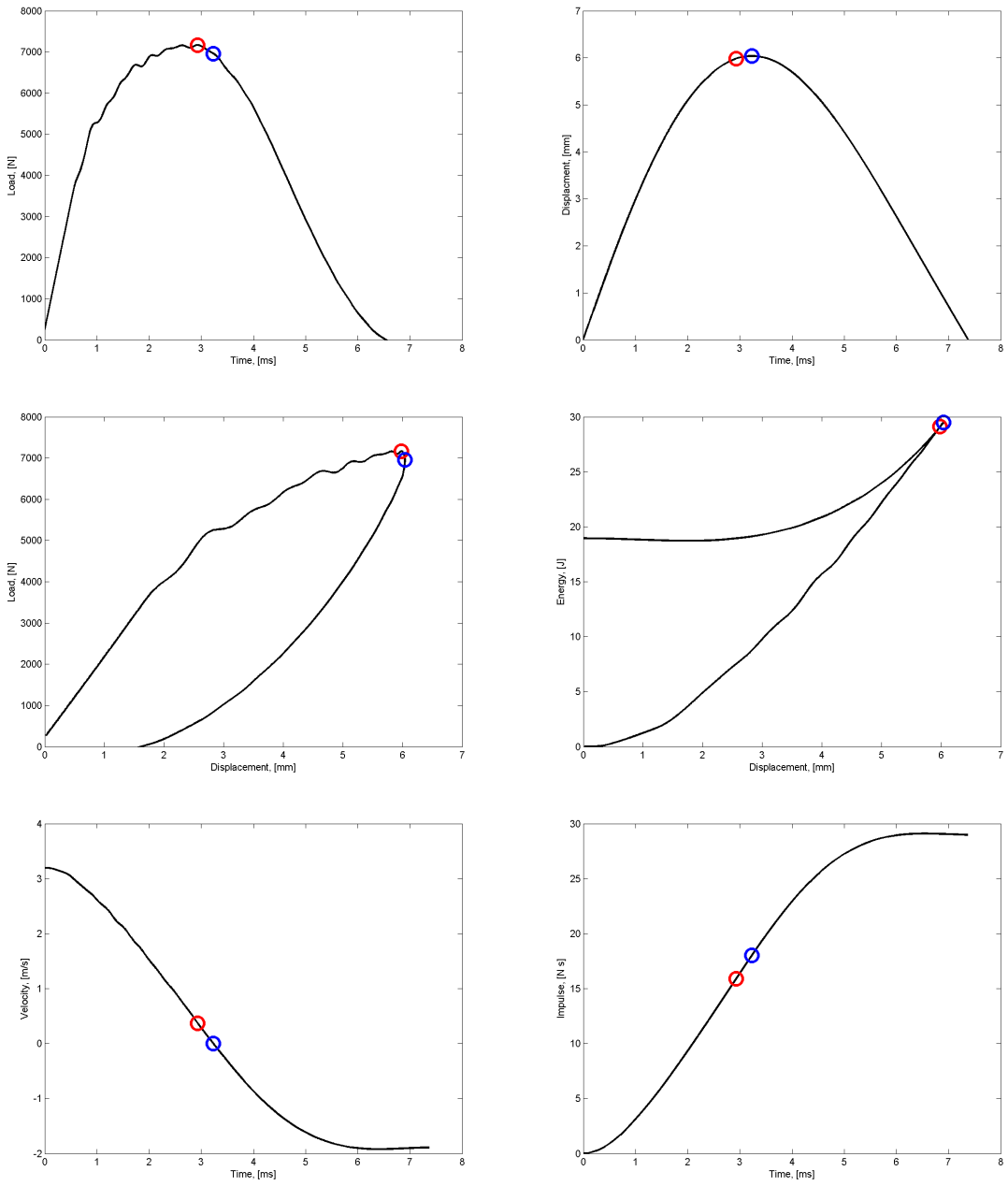

Figure 214: Measured and calculated response of Sample 310 subjected to hemispherical tup low-velocity drop weight testing. Red circle indicates maximum load, blue circle corresponds to maximum displacement.

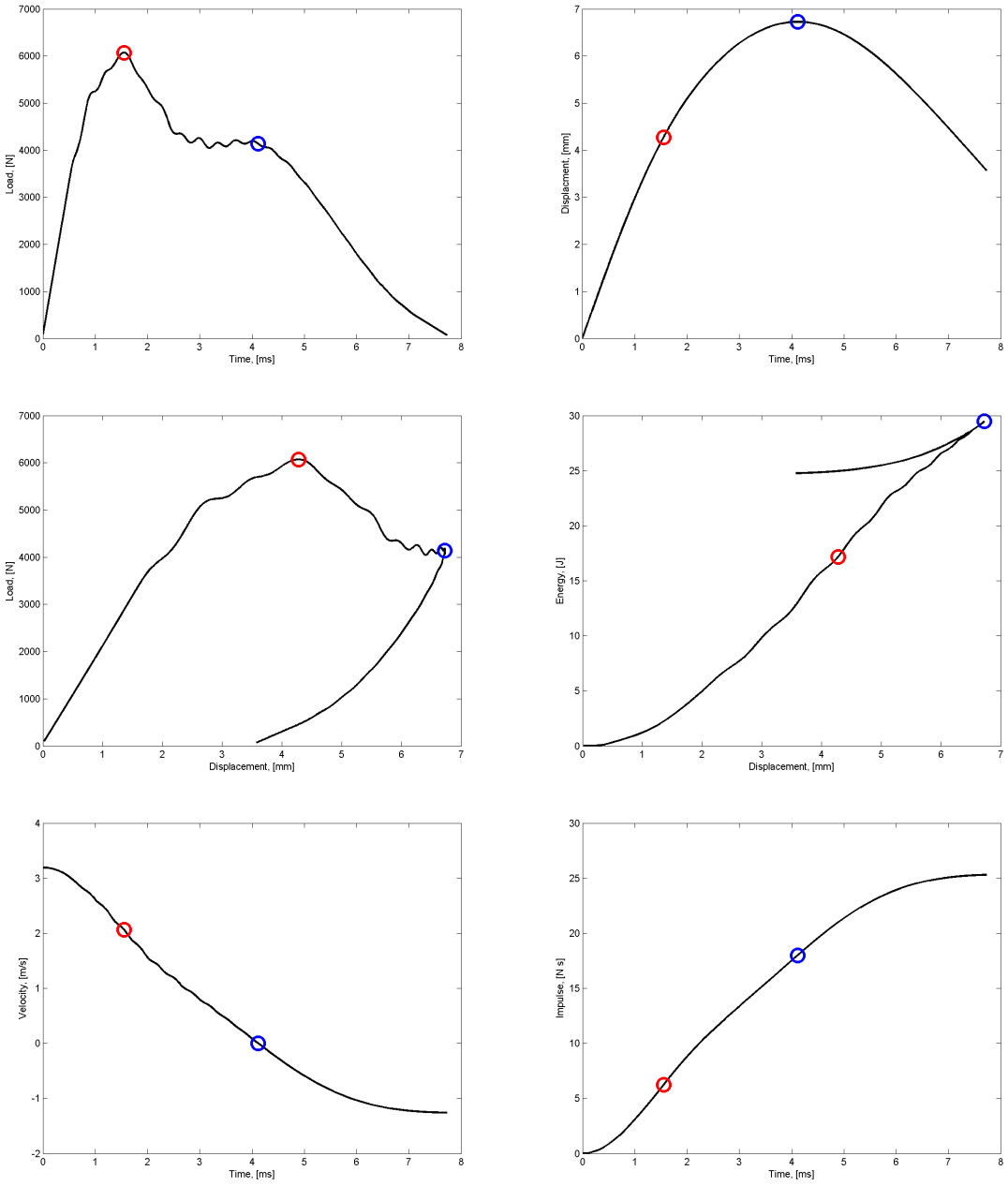

Figure 215: Measured and calculated response of Sample 407 subjected to hemispherical tup low-velocity drop weight testing. Red circle indicates maximum load, blue circle corresponds to maximum displacement.

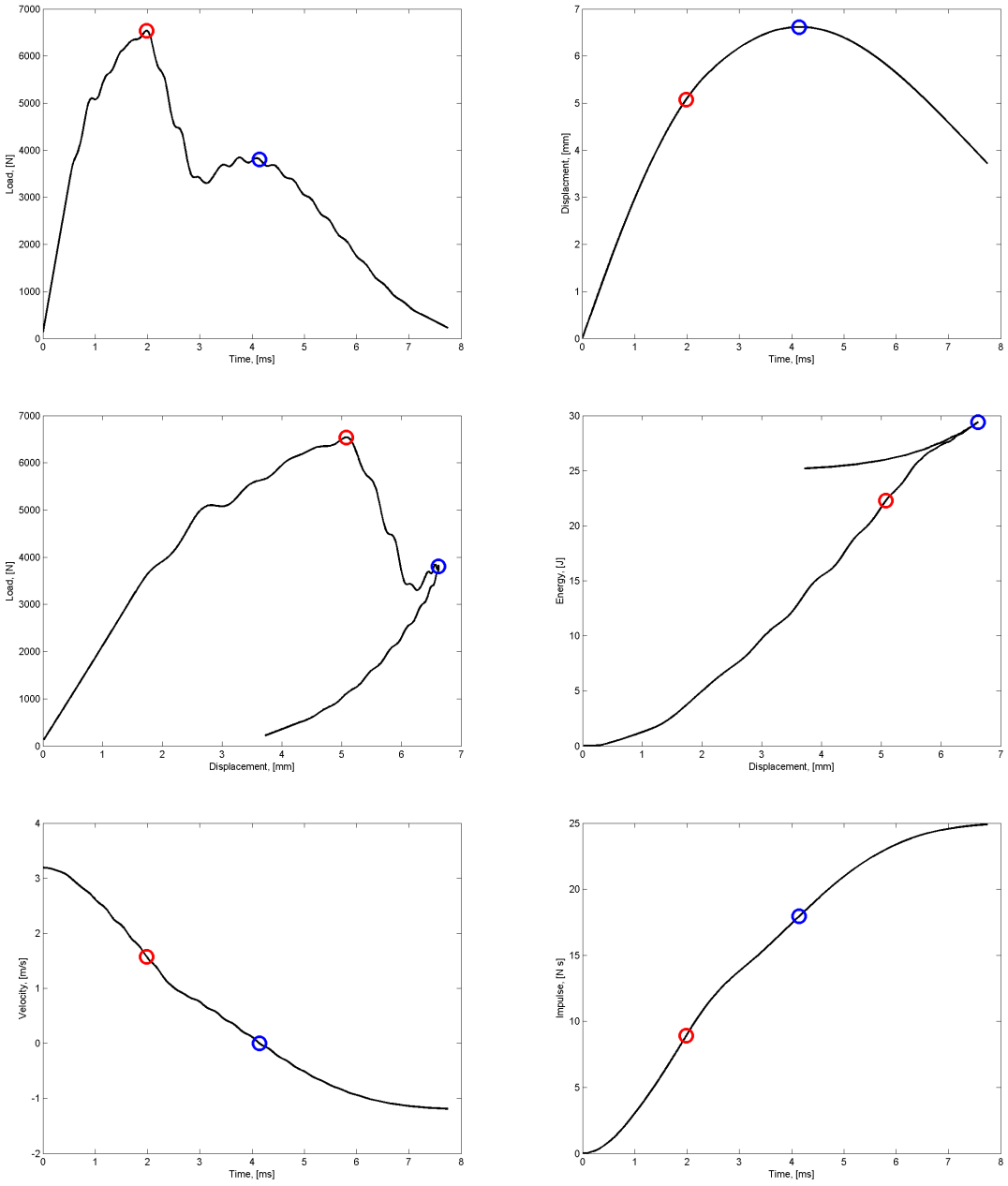

Figure 216: Measured and calculated response of Sample 408 subjected to hemispherical tup low-velocity drop weight testing. Red circle indicates maximum load, blue circle corresponds to maximum displacement.

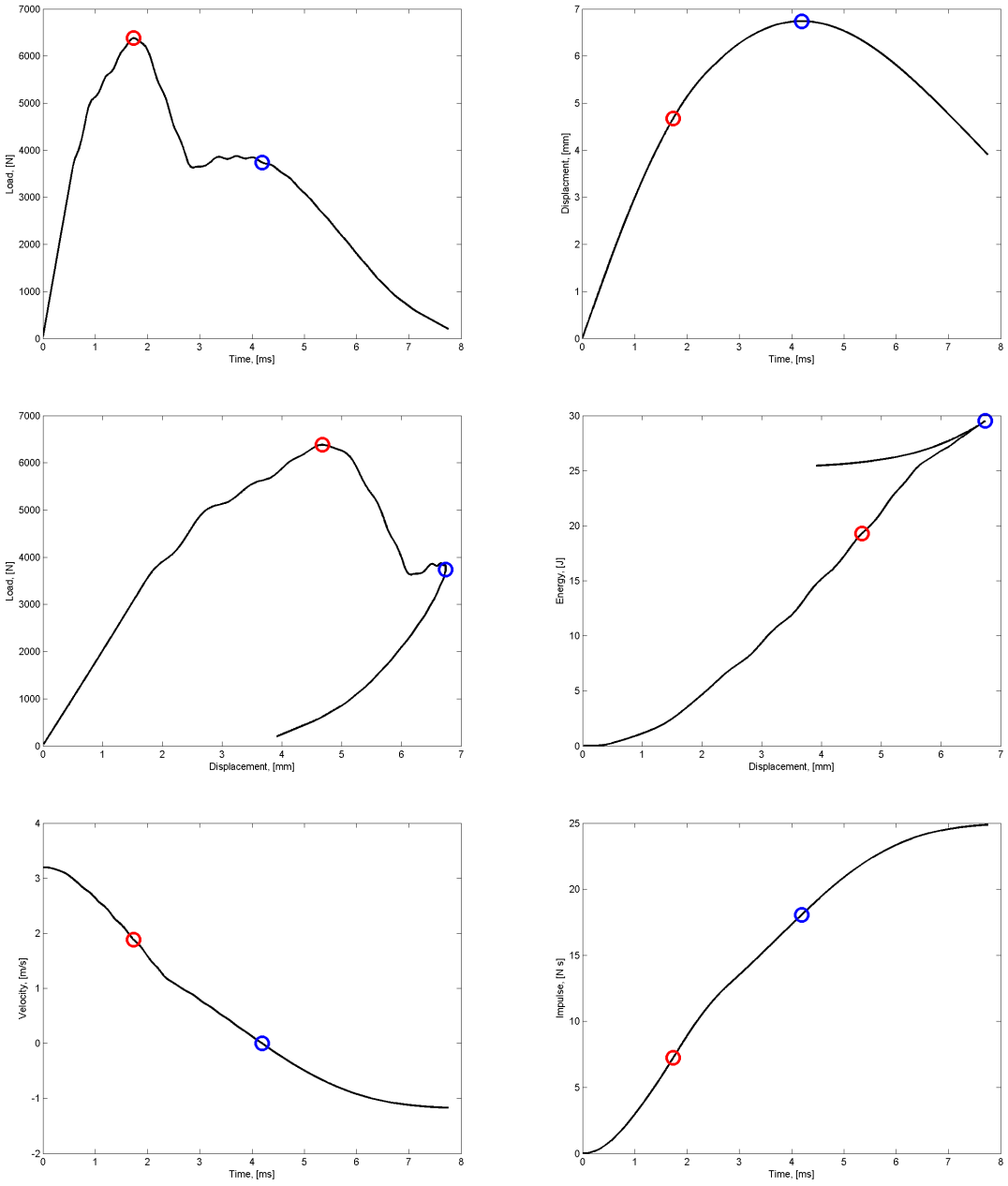

Figure 217: Measured and calculated response of Sample 409 subjected to hemispherical tup low-velocity drop weight testing. Red circle indicates maximum load, blue circle corresponds to maximum displacement.

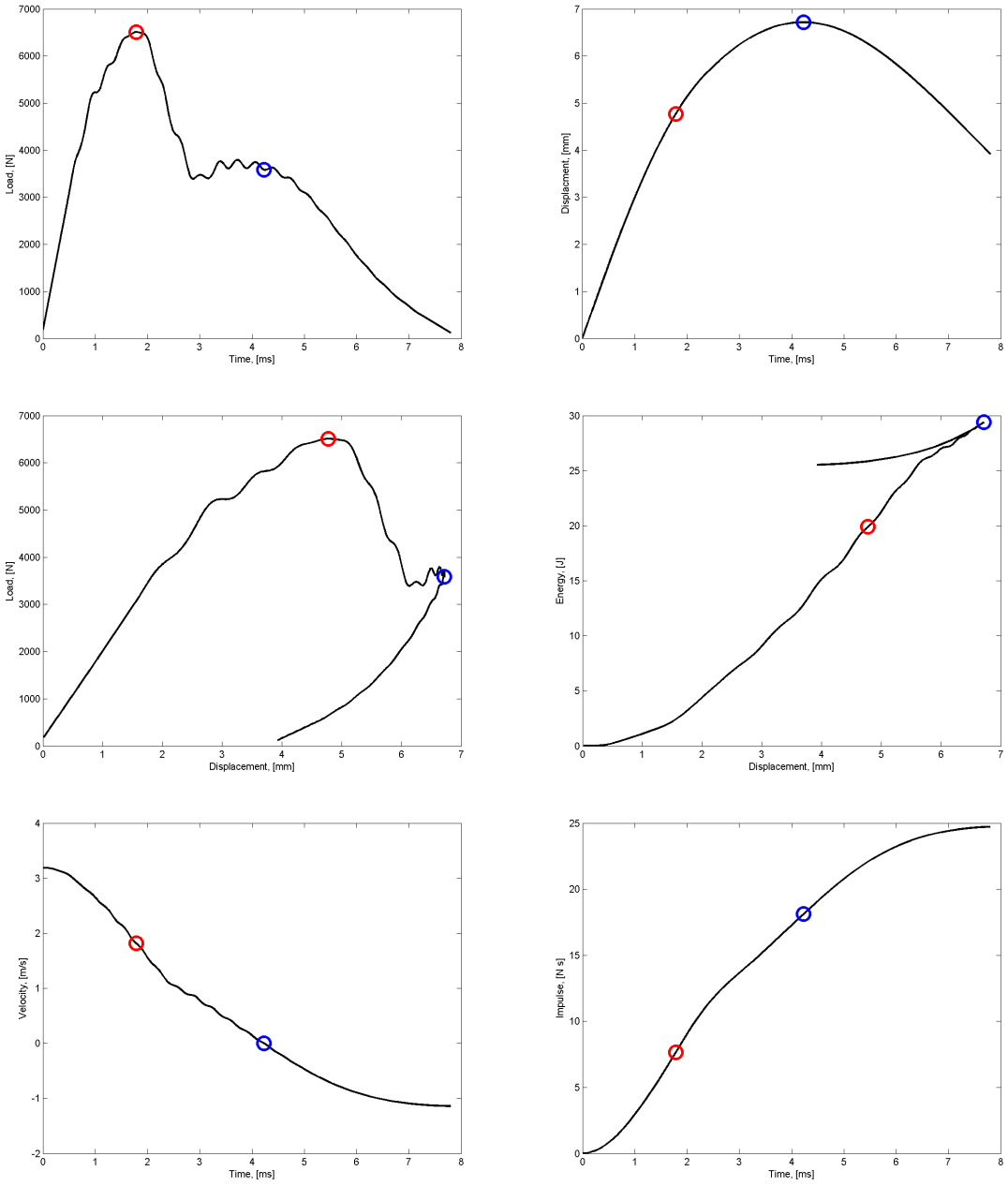

Figure 218: Measured and calculated response of Sample 410 subjected to hemispherical tup low-velocity drop weight testing. Red circle indicates maximum load, blue circle corresponds to maximum displacement.

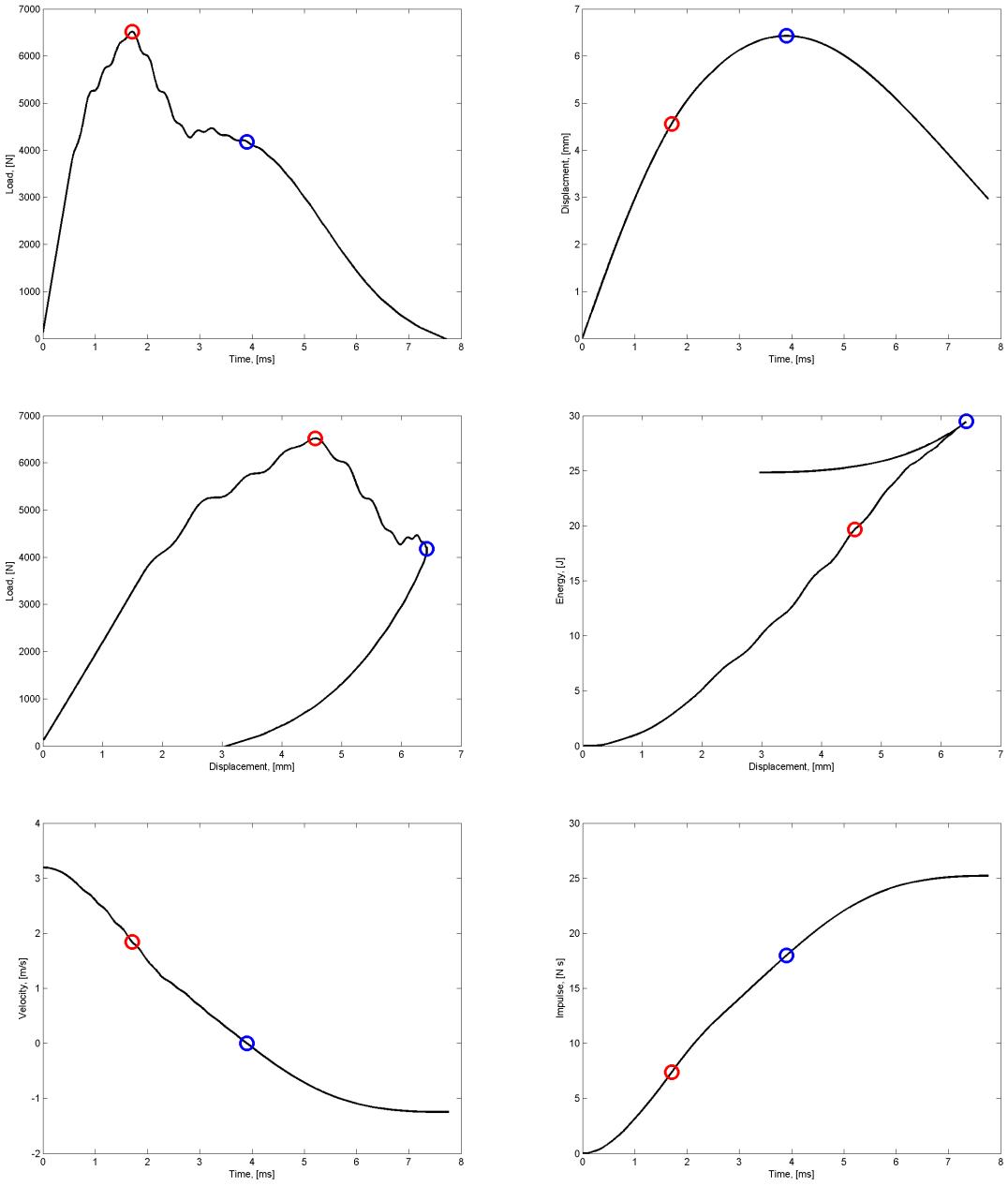

Figure 219: Measured and calculated response of Sample 507 subjected to hemispherical tup low-velocity drop weight testing. Red circle indicates maximum load, blue circle corresponds to maximum displacement.

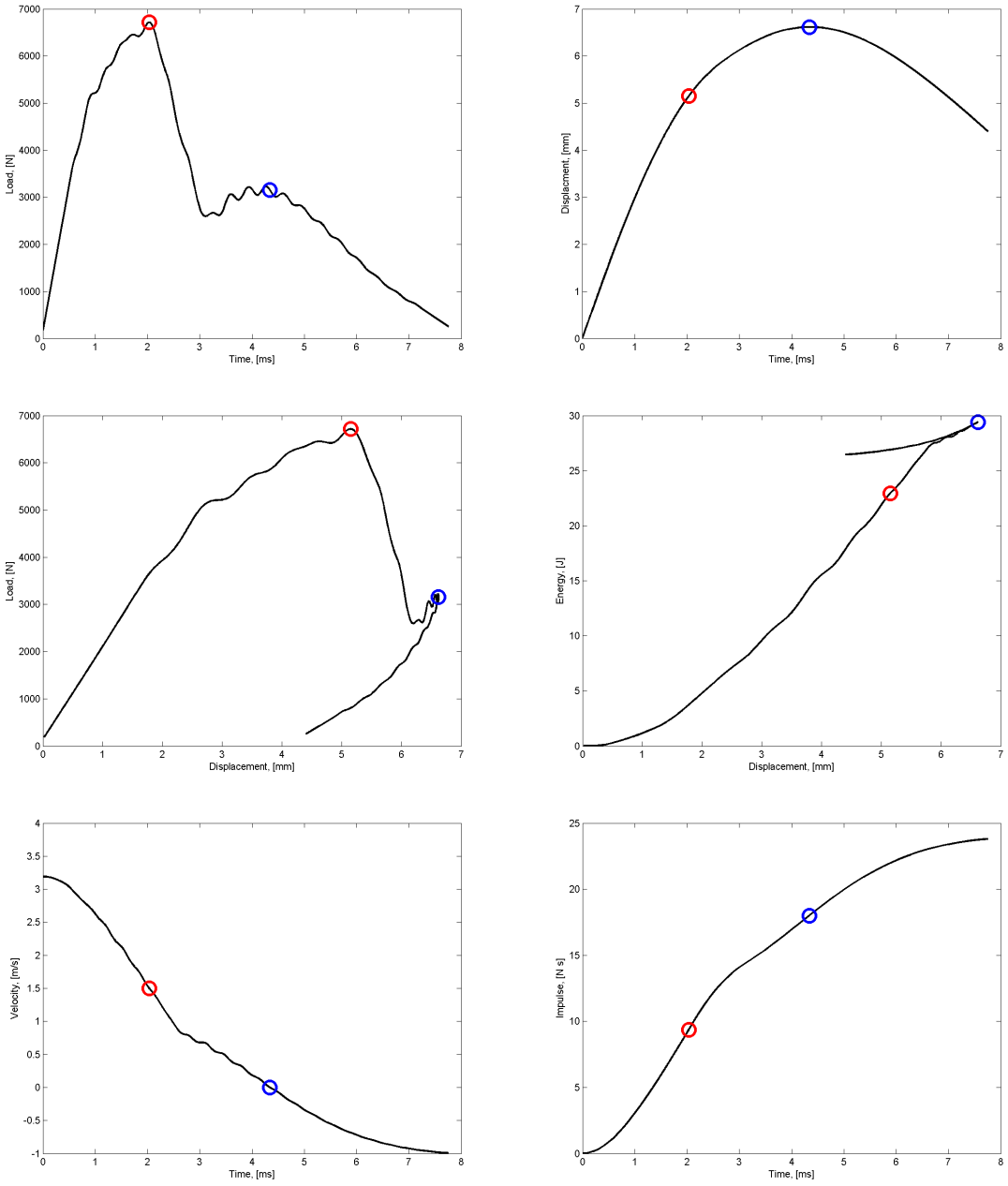

Figure 220: Measured and calculated response of Sample 508 subjected to hemispherical tup low-velocity drop weight testing. Red circle indicates maximum load, blue circle corresponds to maximum displacement.

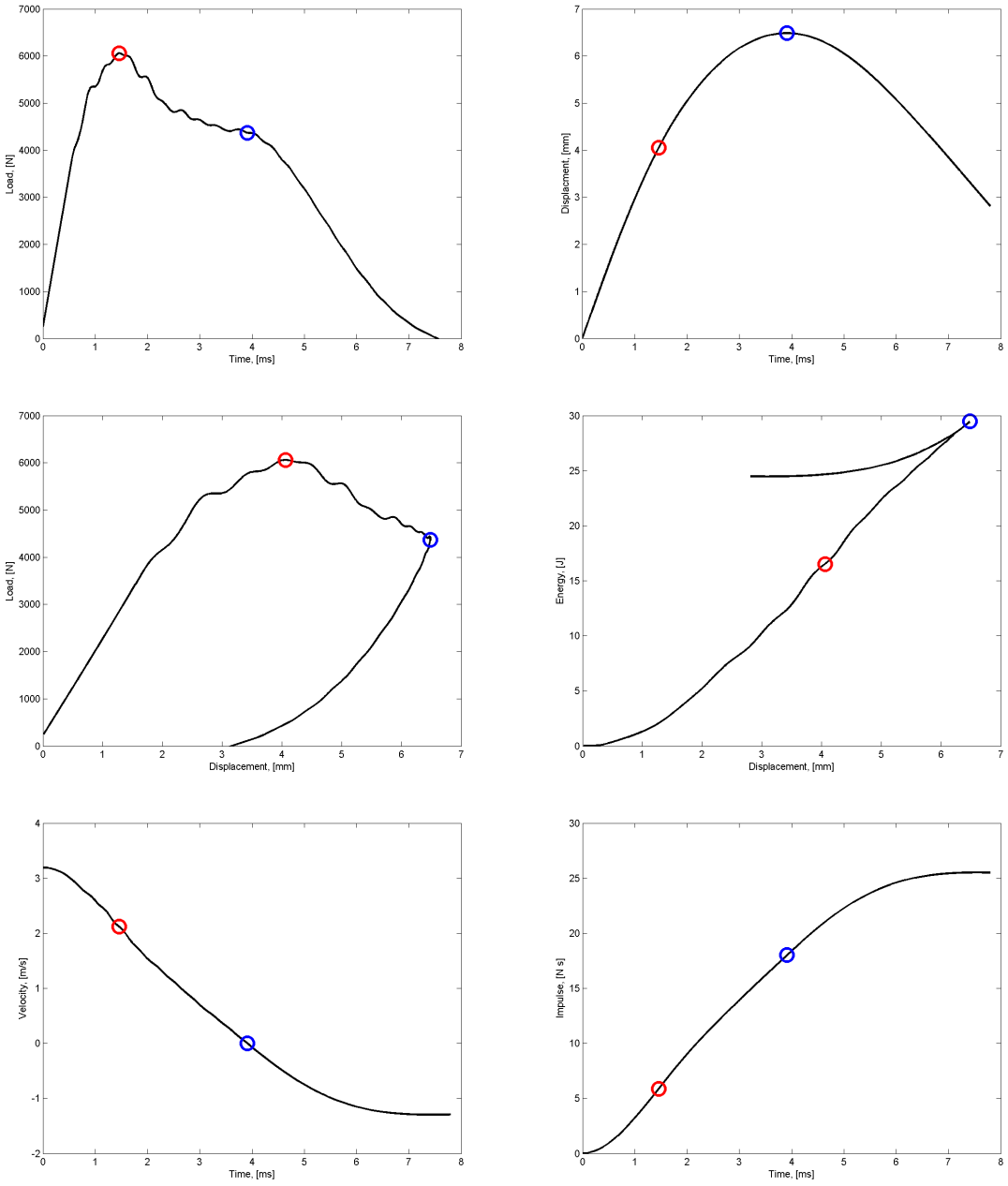

Figure 221: Measured and calculated response of Sample 509 subjected to hemispherical tup low-velocity drop weight testing. Red circle indicates maximum load, blue circle corresponds to maximum displacement.

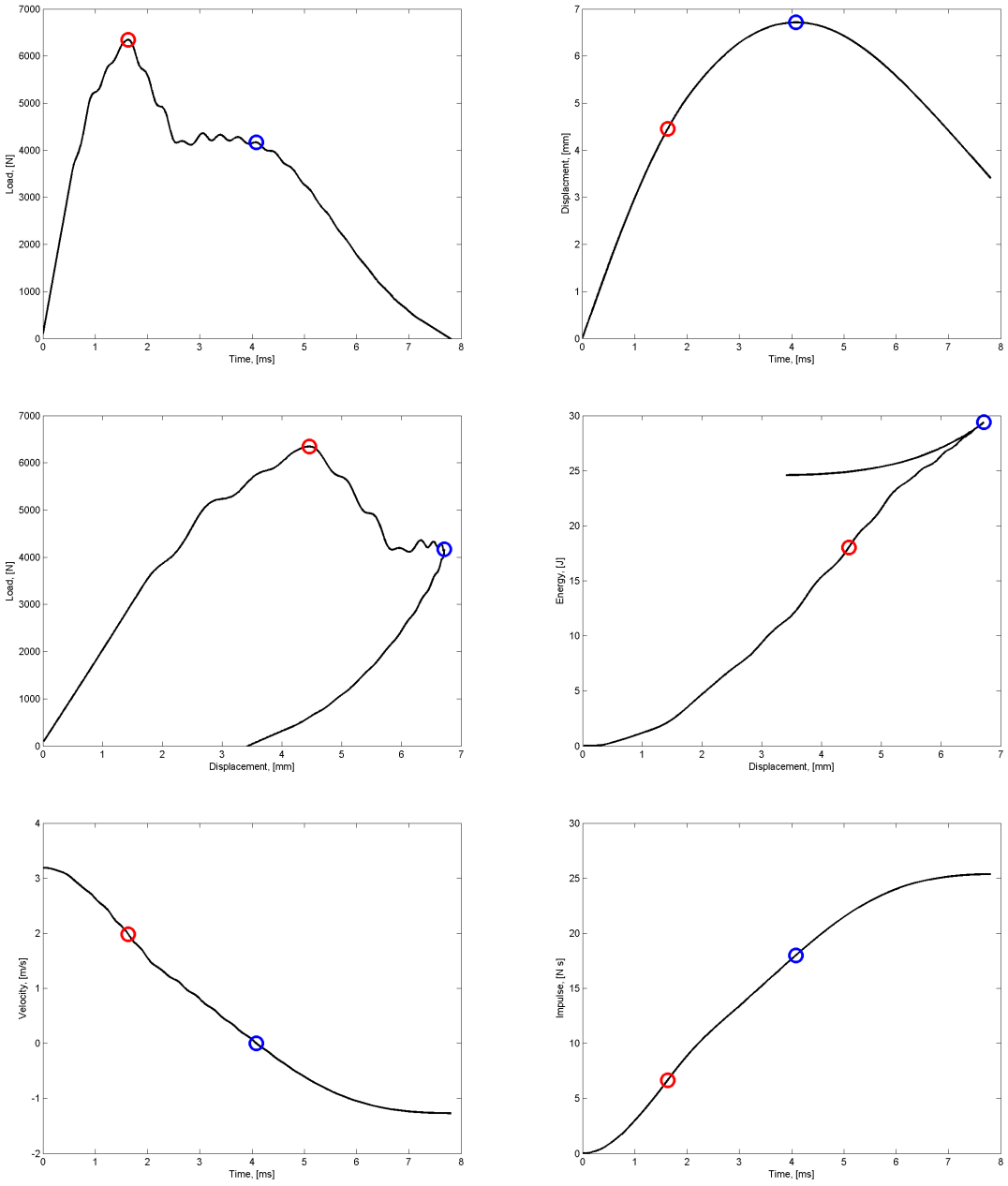

Figure 222: Measured and calculated response of Sample 510 subjected to hemispherical tup low-velocity drop weight testing. Red circle indicates maximum load, blue circle corresponds to maximum displacement.

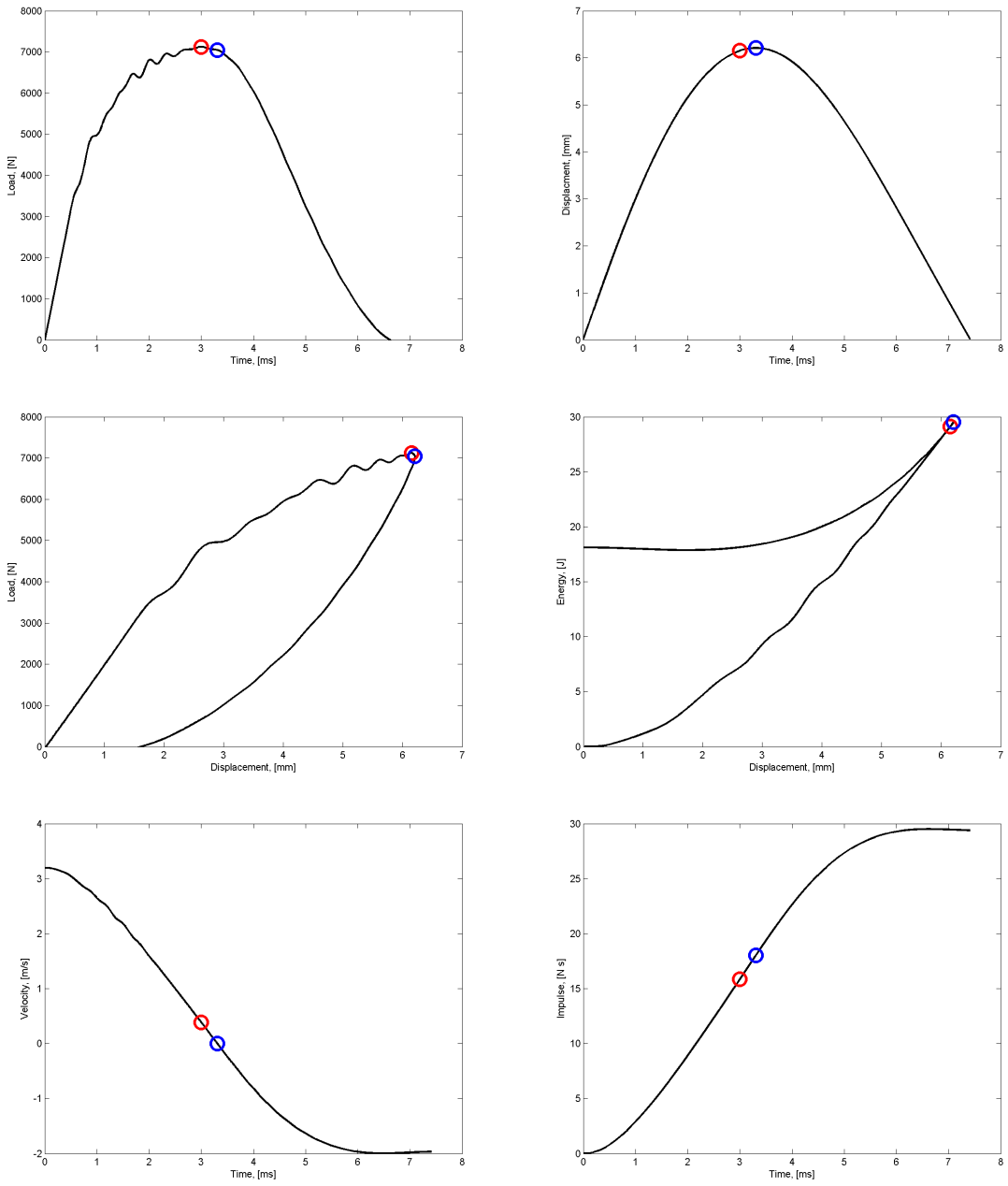

Figure 223: Measured and calculated response of Sample 607 subjected to hemispherical tup low-velocity drop weight testing. Red circle indicates maximum load, blue circle corresponds to maximum displacement.

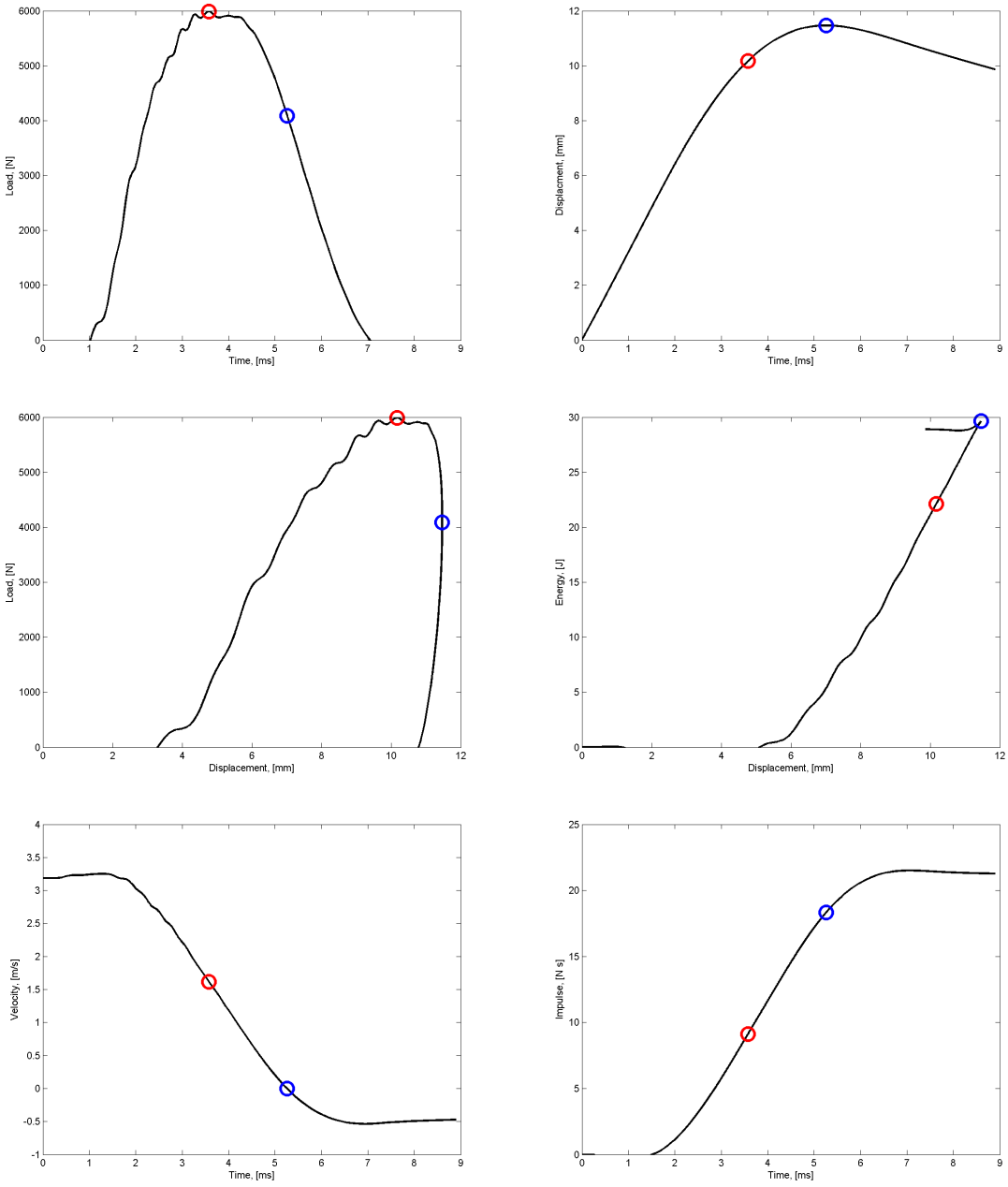

Figure 224: Measured and calculated response of Sample 608 subjected to hemispherical tup low-velocity drop weight testing. Red circle indicates maximum load, blue circle corresponds to maximum displacement.

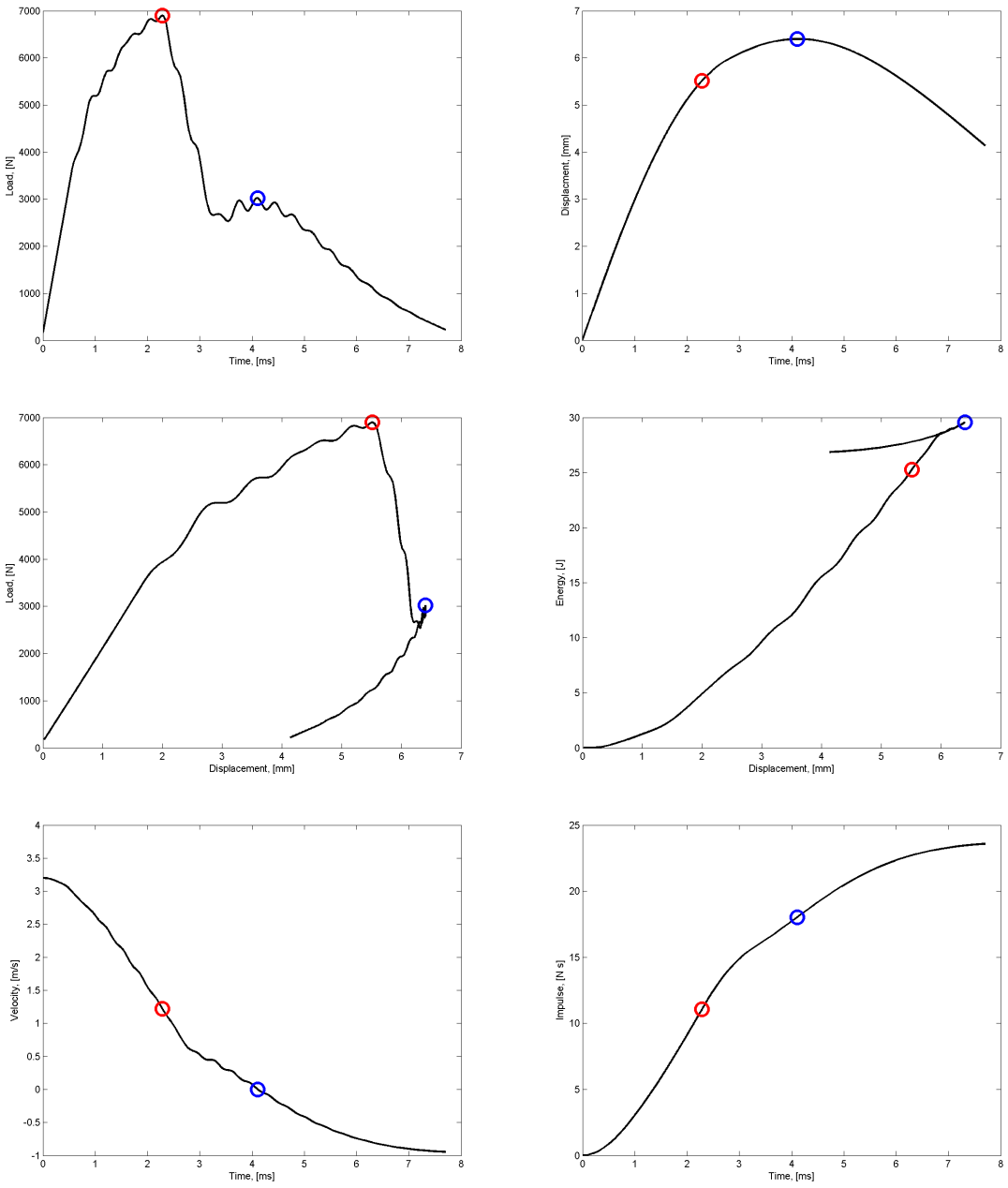

Figure 225: Measured and calculated response of Sample 609 subjected to hemispherical tup low-velocity drop weight testing. Red circle indicates maximum load, blue circle corresponds to maximum displacement.

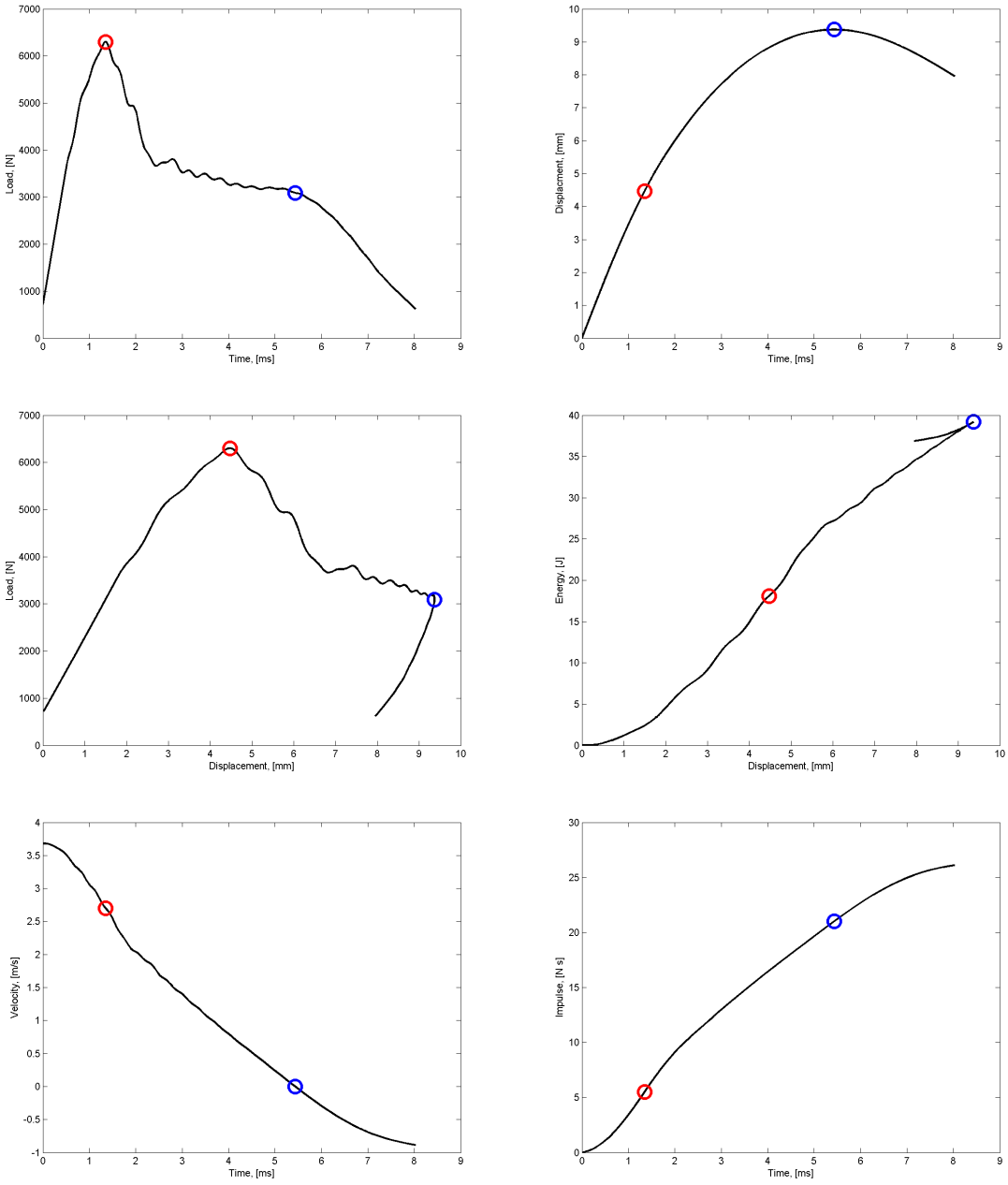

Figure 226: Measured and calculated response of Sample 610 subjected to hemispherical tup low-velocity drop weight testing. Red circle indicates maximum load, blue circle corresponds to maximum displacement.

Appendix E: Compression After Impact

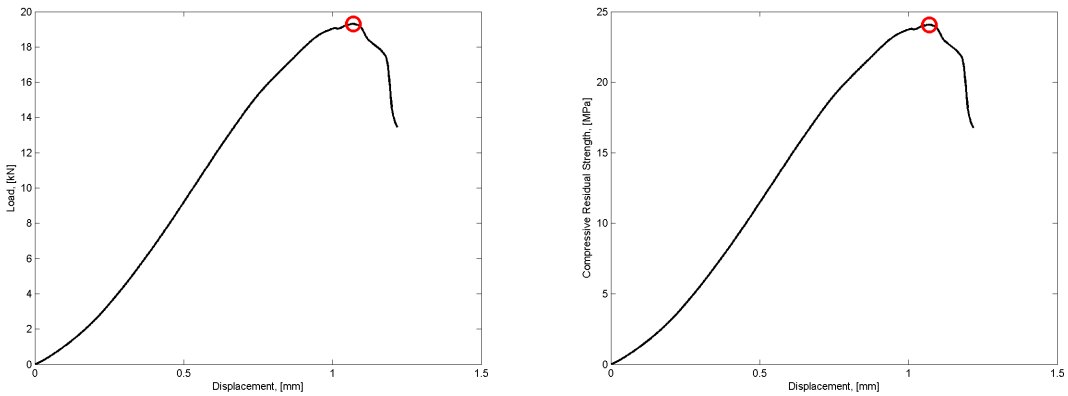

Figure 227: Measured and calculated response of Sample 102 subjected to compression after impact testing.

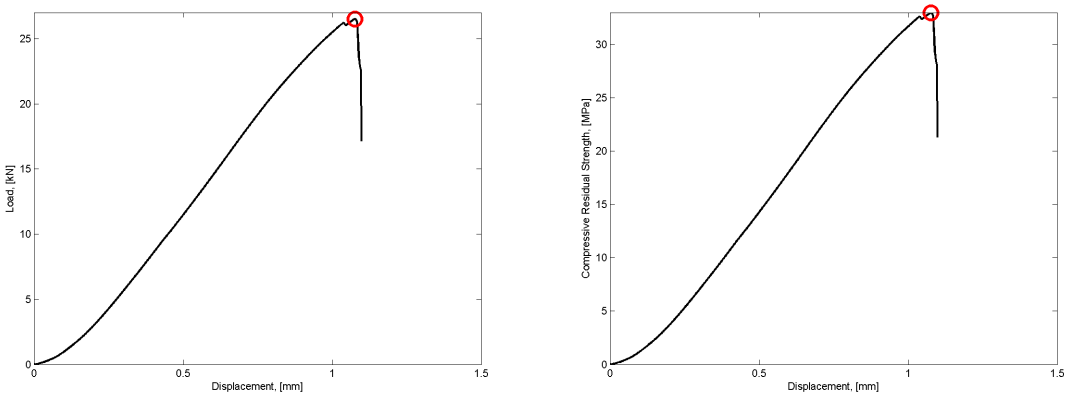

Figure 228: Measured and calculated response of Sample 103 subjected to compression after impact testing.

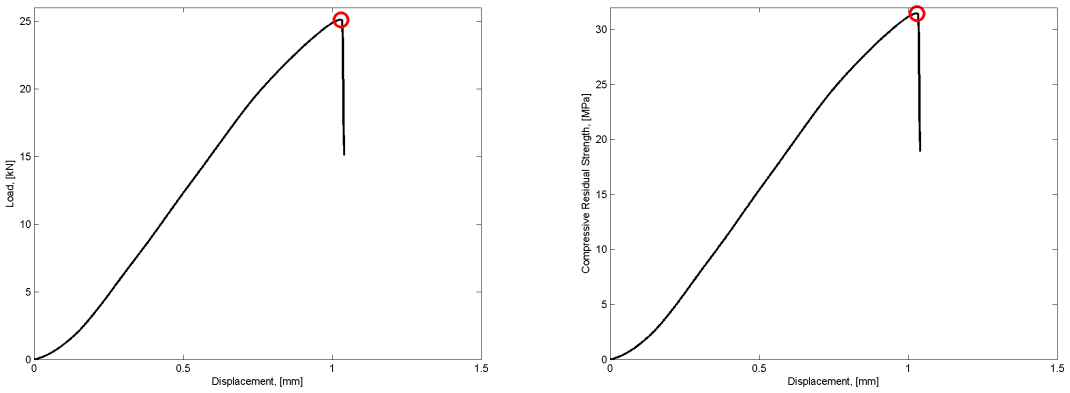

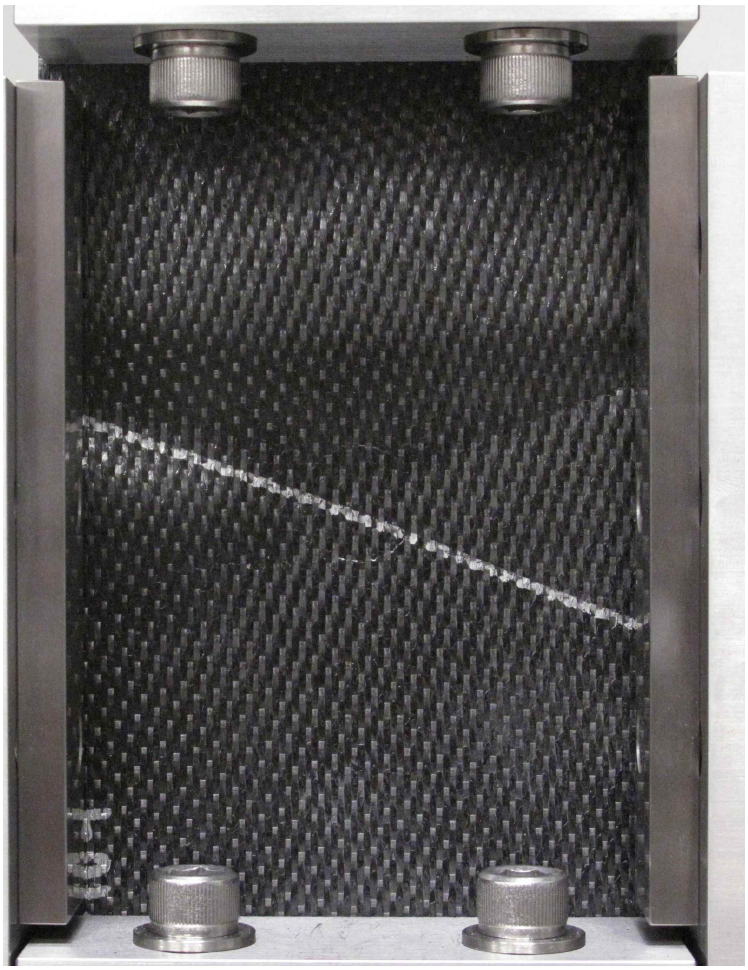

Figure 229: Measured and calculated response of Sample 104 subjected to compression after impact testing.

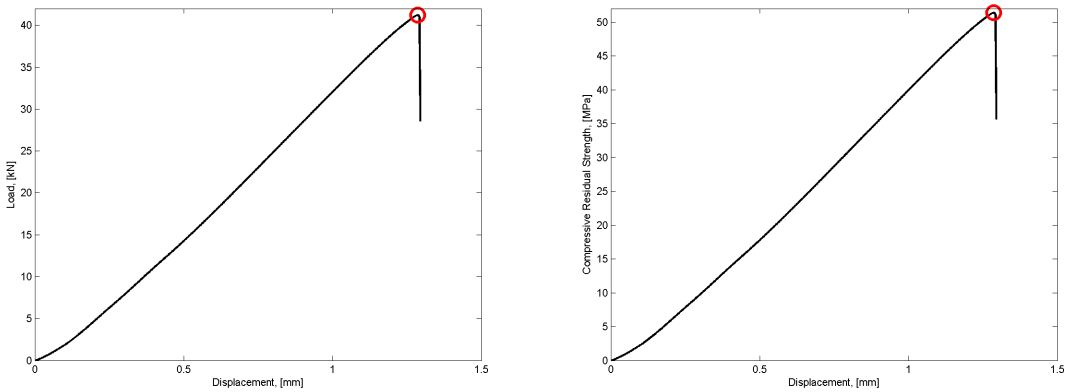

Figure 230: Measured and calculated response of Sample 107 subjected to compression after impact testing.

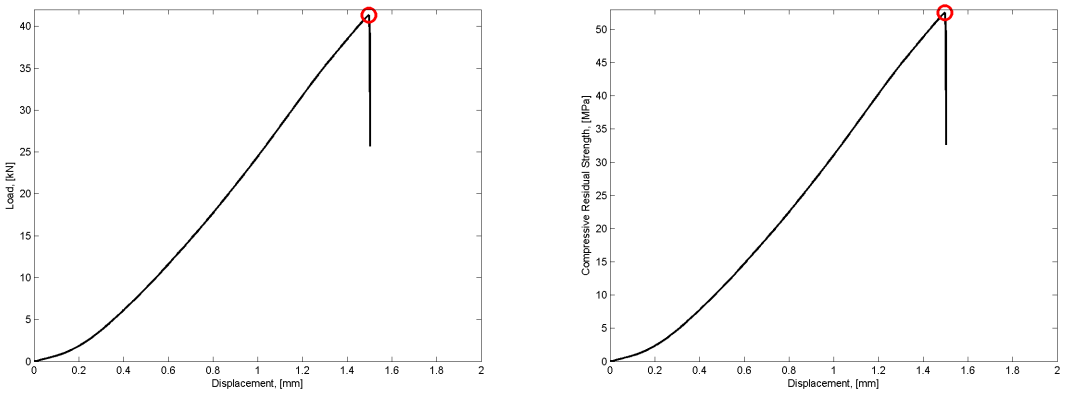

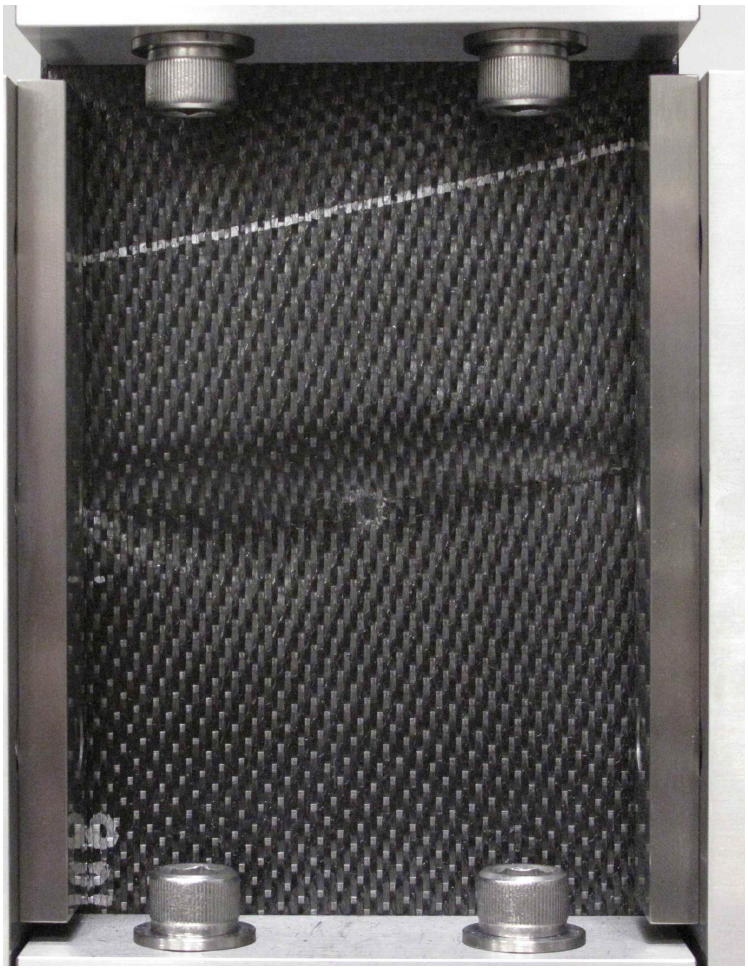

Figure 231: Measured and calculated response of Sample 108 subjected to compression after impact testing.

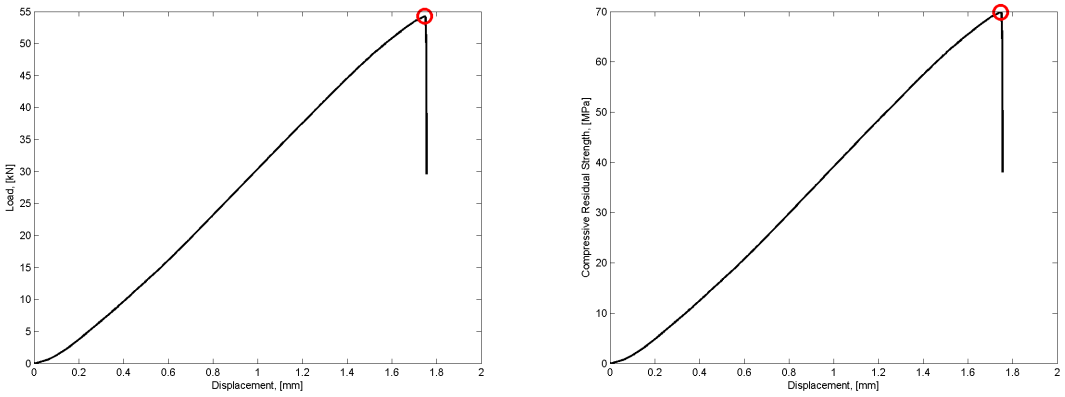

Figure 232: Measured and calculated response of Sample 109 subjected to compression after impact testing.

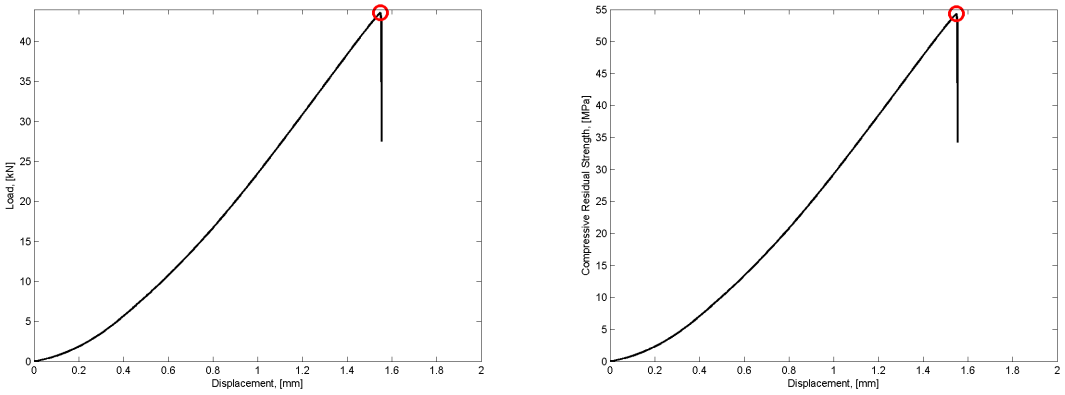

Figure 233: Measured and calculated response of Sample 110 subjected to compression after impact testing.

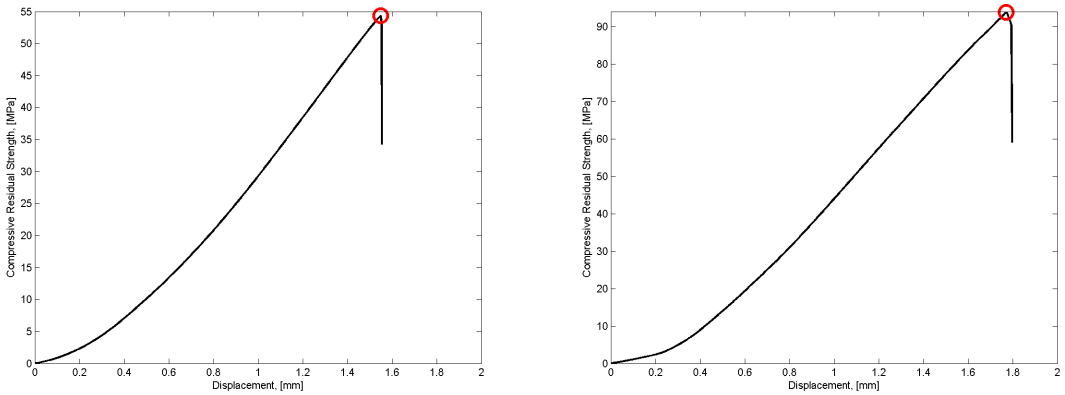

Figure 234: Measured and calculated response of Sample 202 subjected to compression after impact testing.

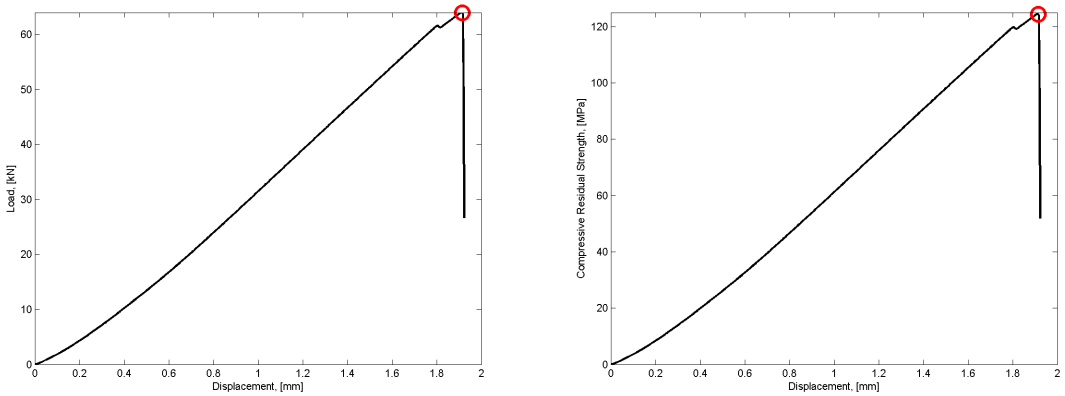

Figure 235: Measured and calculated response of Sample 203 subjected to compression after impact testing.

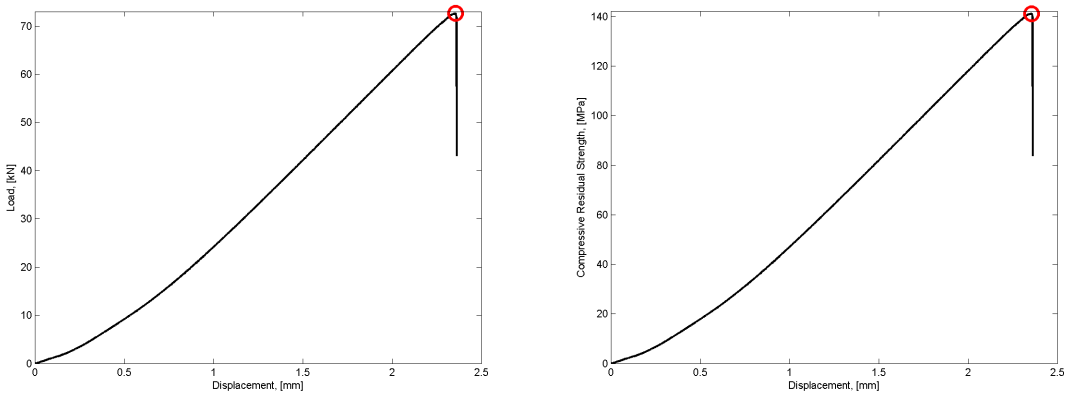

Figure 236: Measured and calculated response of Sample 204 subjected to compression after impact testing.

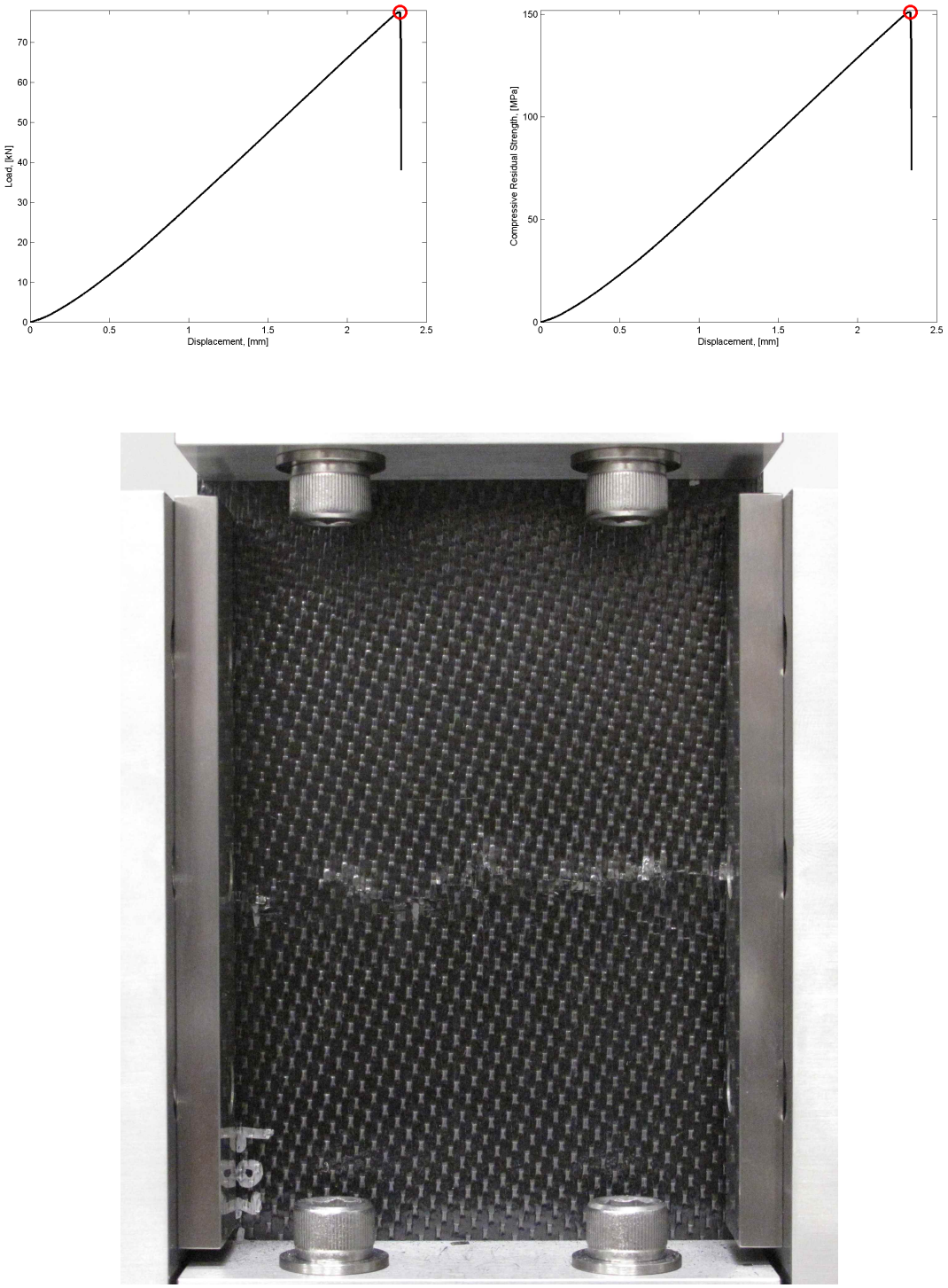

Figure 237: Measured and calculated response of Sample 207 subjected to compression after impact testing.

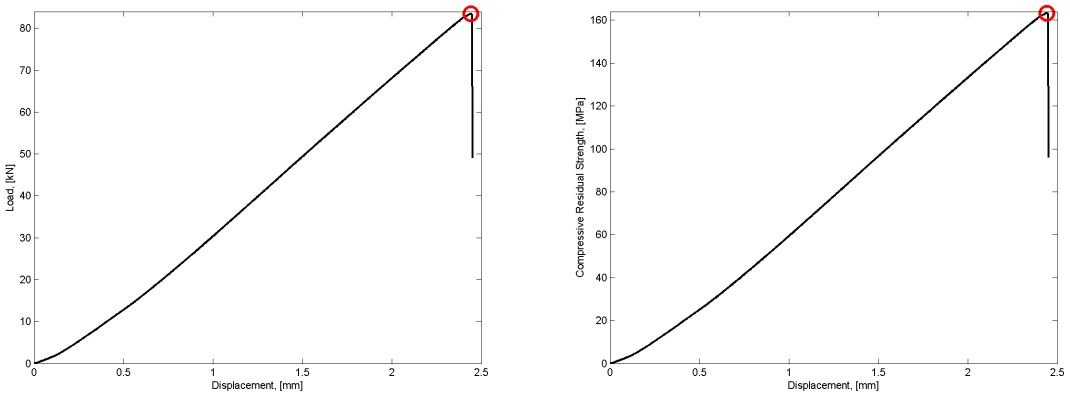

Figure 238: Measured and calculated response of Sample 208 subjected to compression after impact testing.

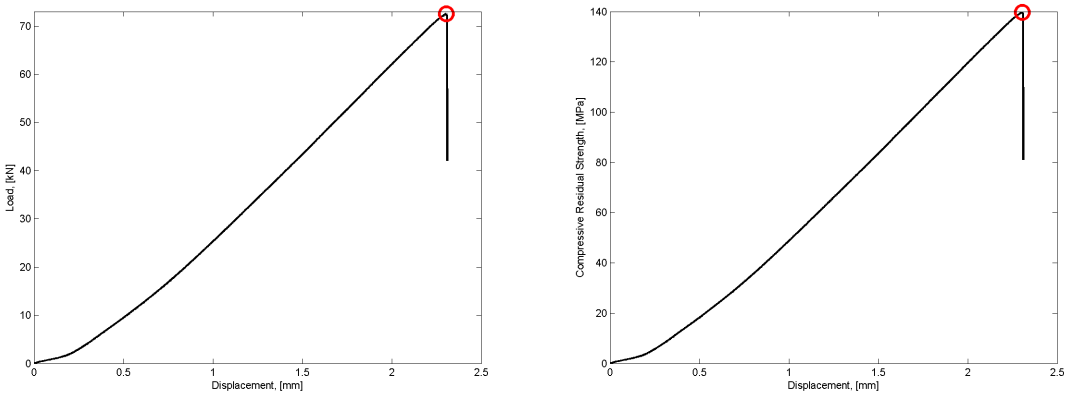

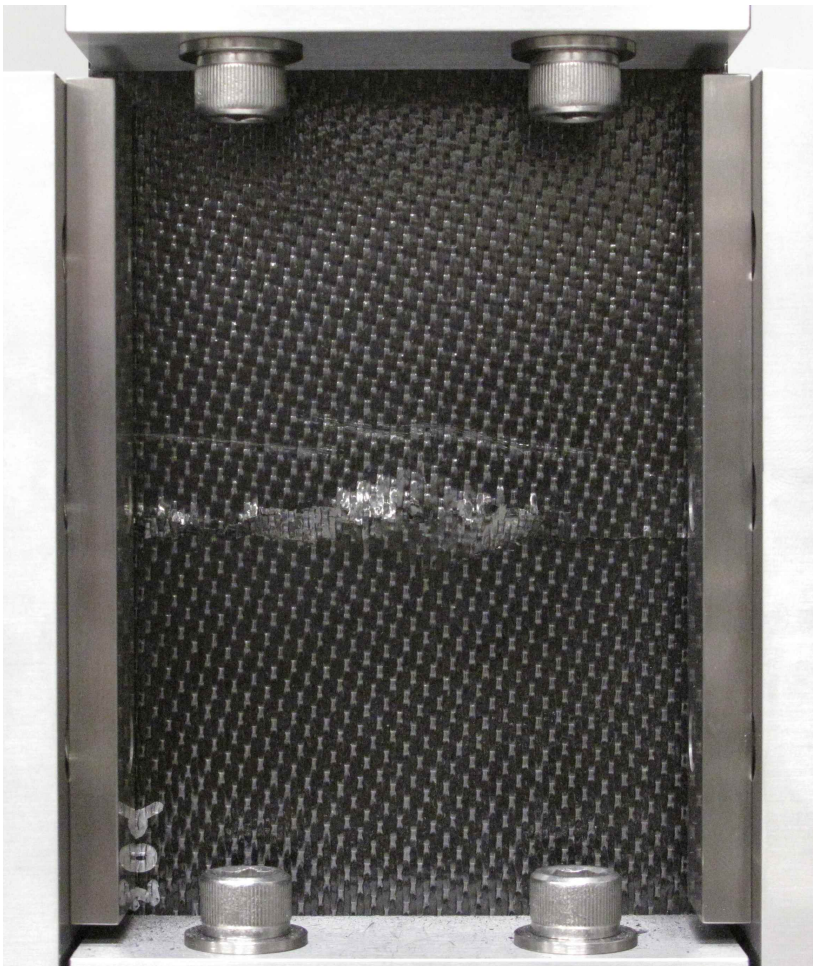

Figure 239: Measured and calculated response of Sample 209 subjected to compression after impact testing.

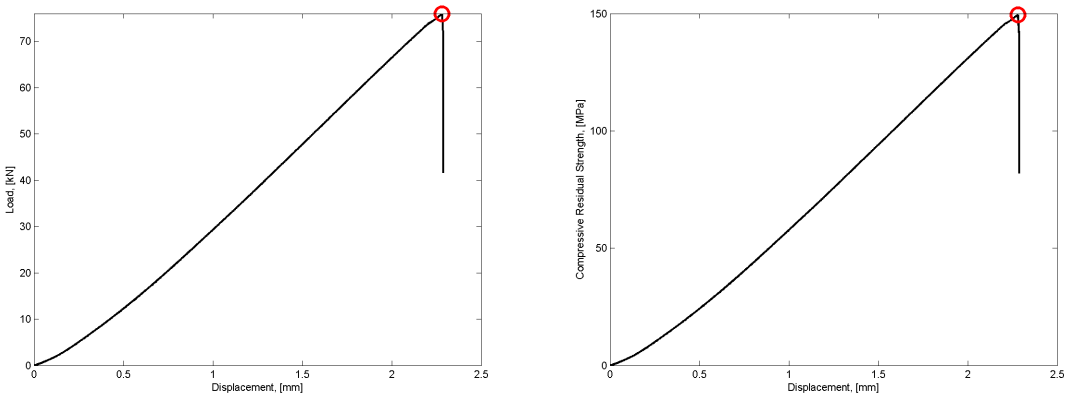

Figure 240: Measured and calculated response of Sample 210 subjected to compression after impact testing.

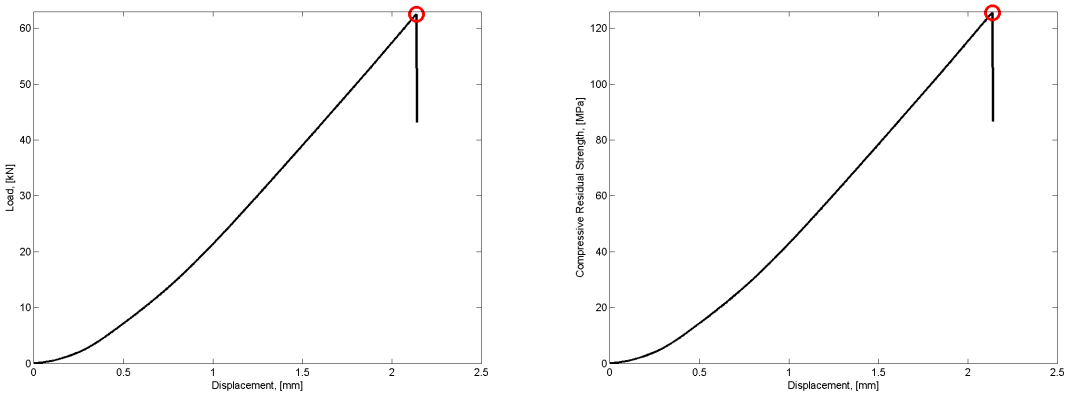

Figure 241: Measured and calculated response of Sample 302 subjected to compression after impact testing.

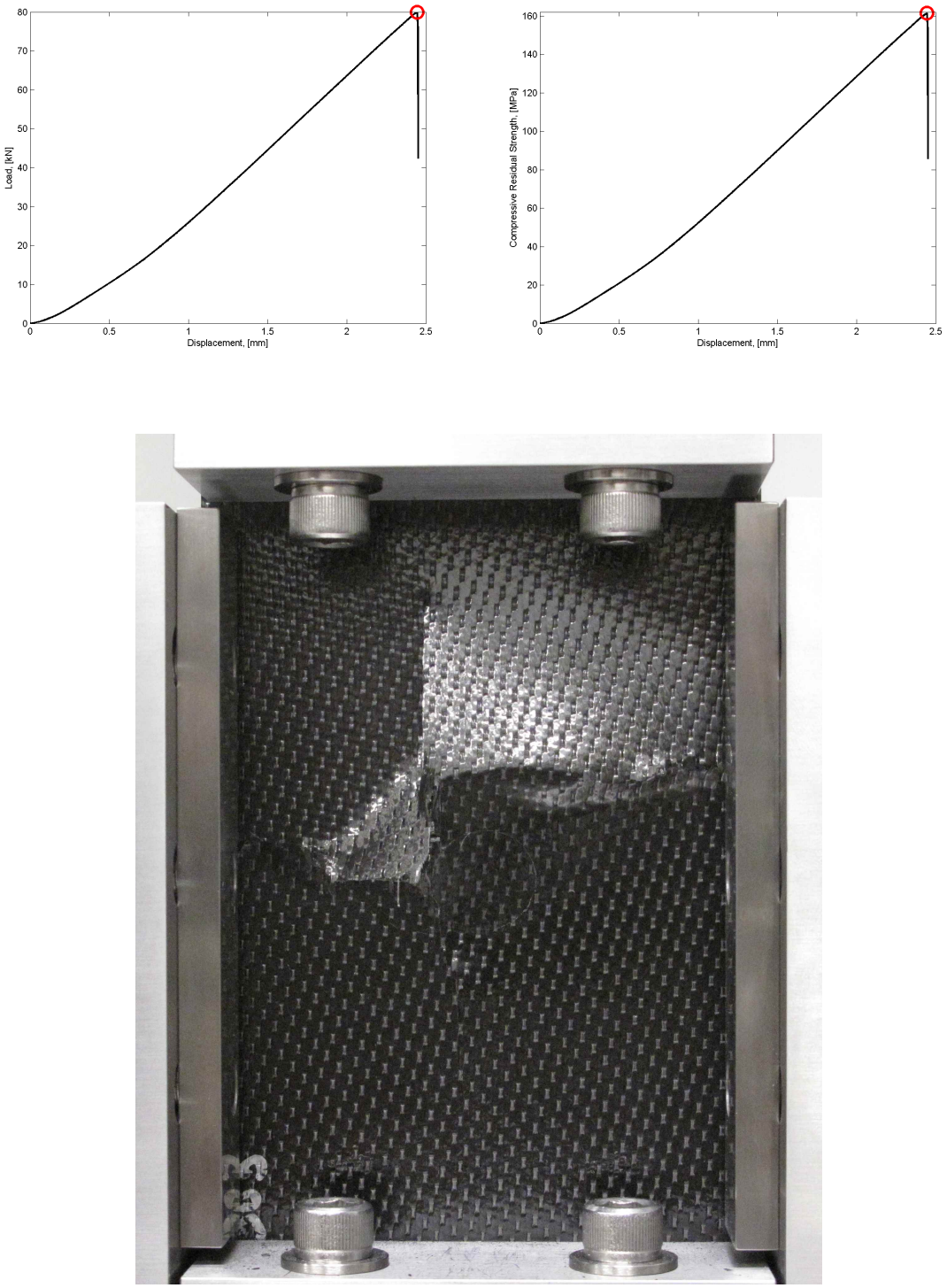

Figure 242: Measured and calculated response of Sample 303 subjected to compression after impact testing.

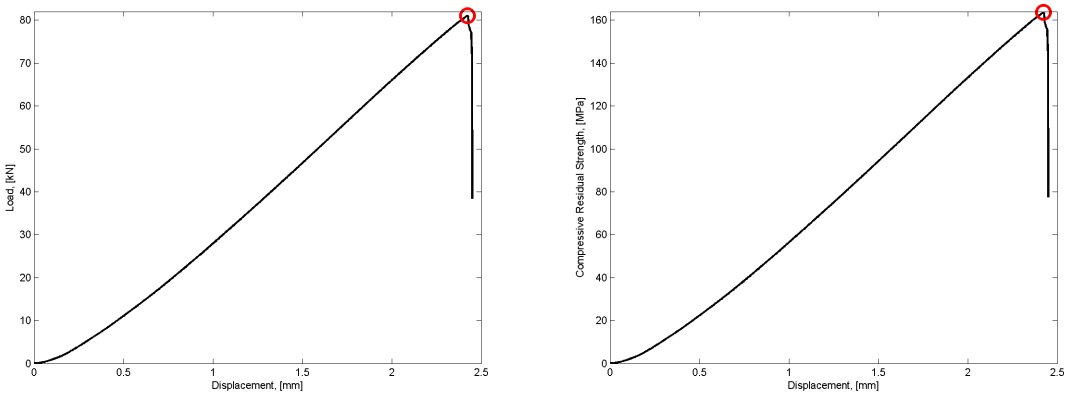

Figure 243: Measured and calculated response of Sample 304 subjected to compression after impact testing.

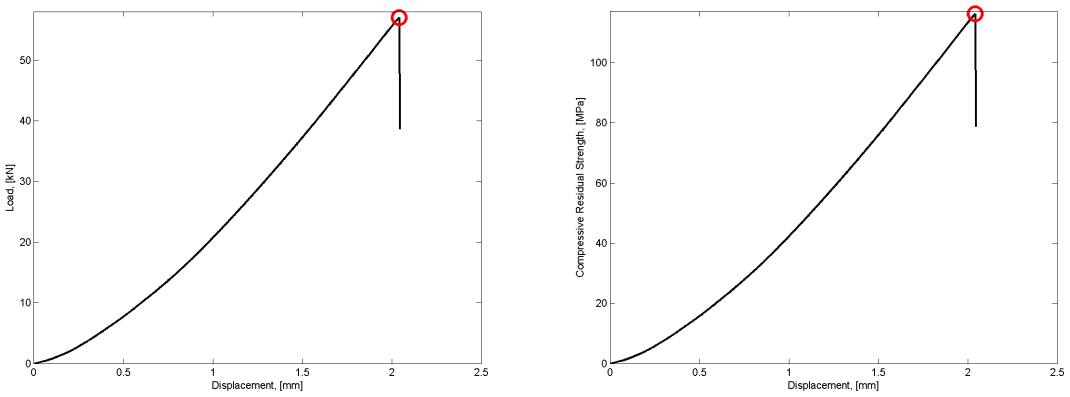

Figure 244: Measured and calculated response of Sample 307 subjected to compression after impact testing.

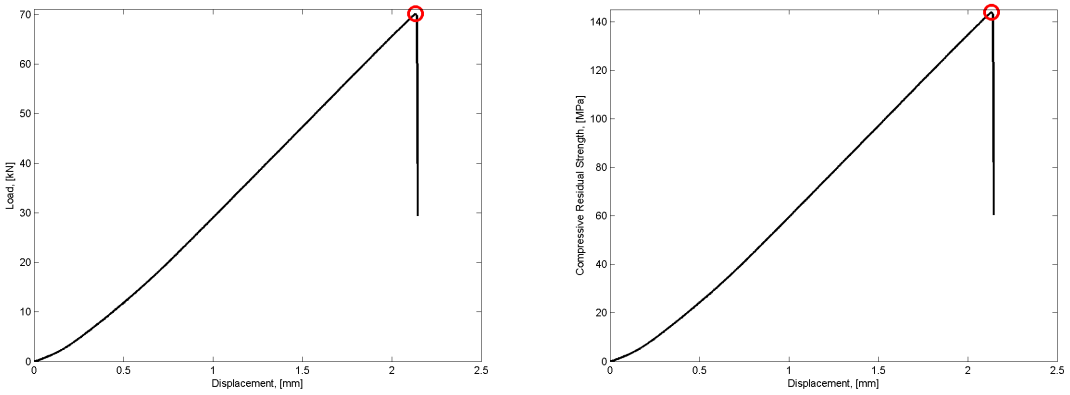

Figure 245: Measured and calculated response of Sample 308 subjected to compression after impact testing.

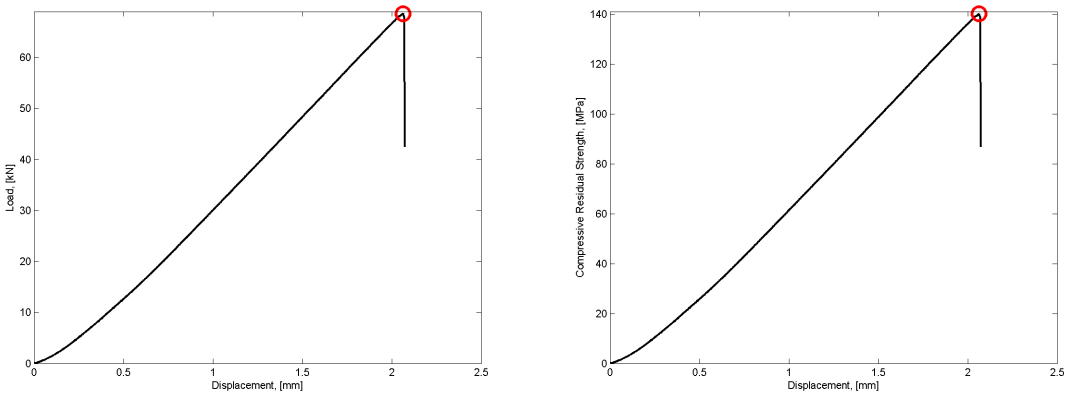

Figure 246: Measured and calculated response of Sample 309 subjected to compression after impact testing.

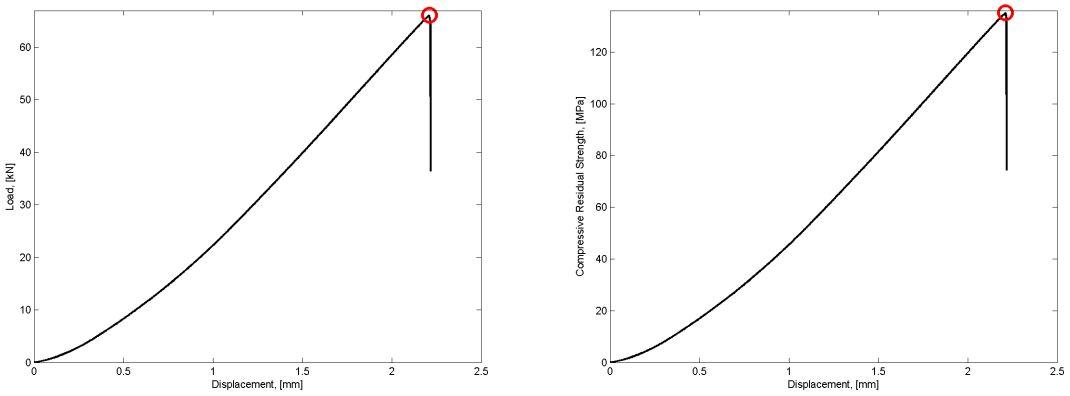

Figure 247: Measured and calculated response of Sample 310 subjected to compression after impact testing.

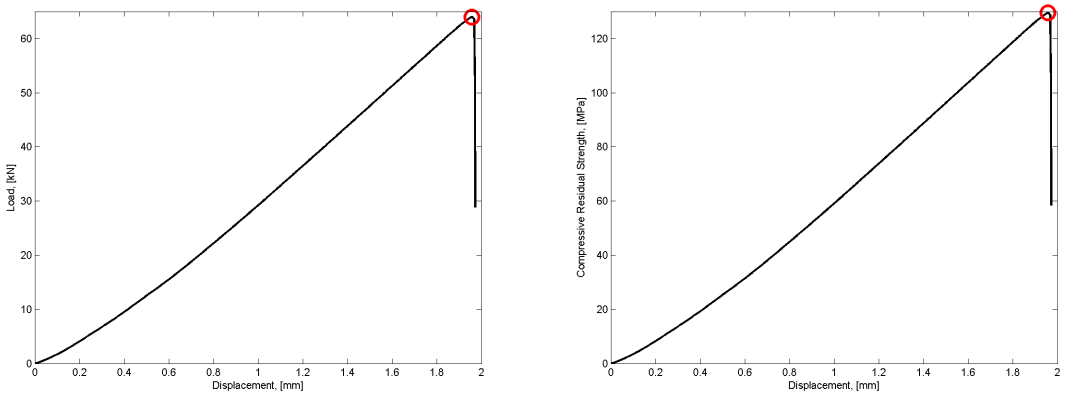

Figure 248: Measured and calculated response of Sample 402 subjected to compression after impact testing.

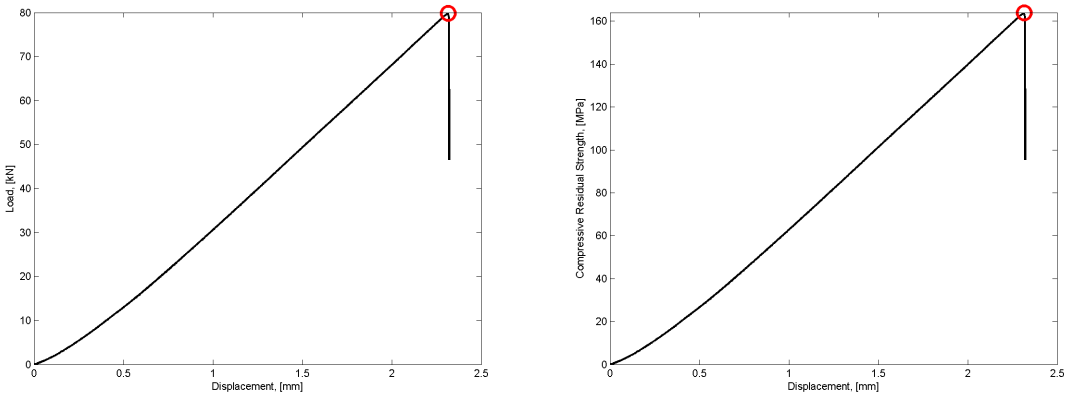

Figure 249: Measured and calculated response of Sample 403 subjected to compression after impact testing.

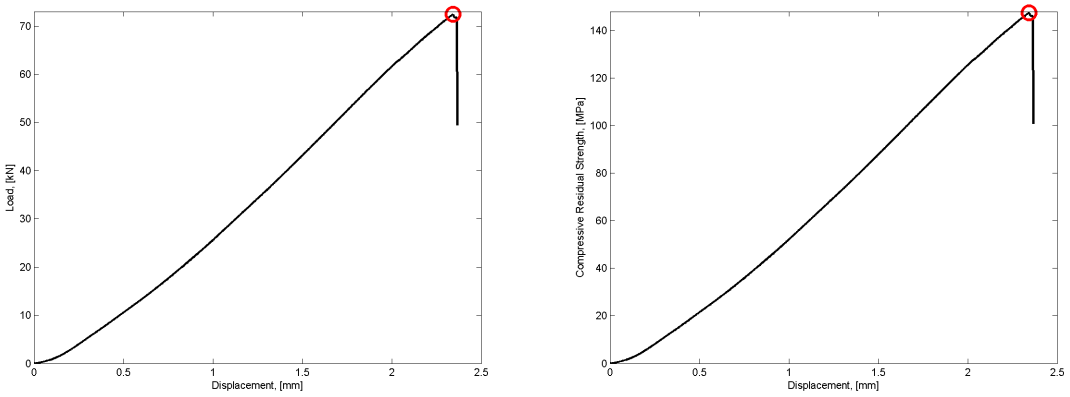

Figure 250: Measured and calculated response of Sample 404 subjected to compression after impact testing.

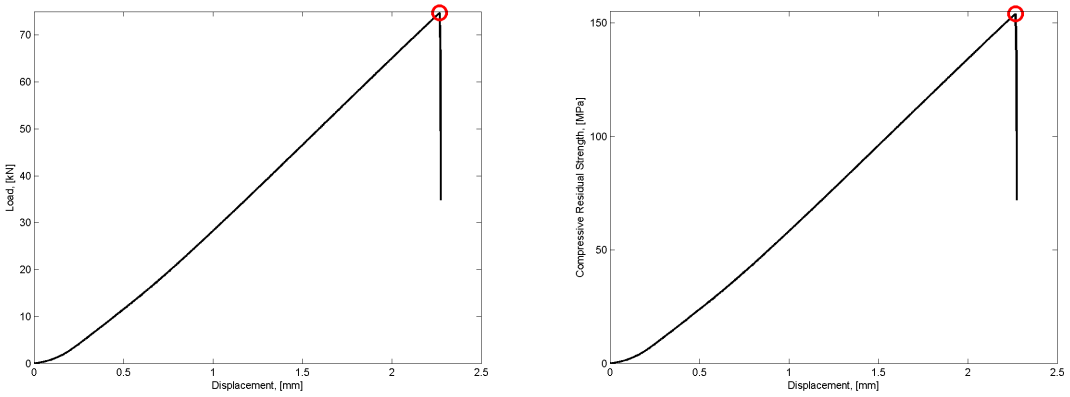

Figure 251: Measured and calculated response of Sample 407 subjected to compression after impact testing.

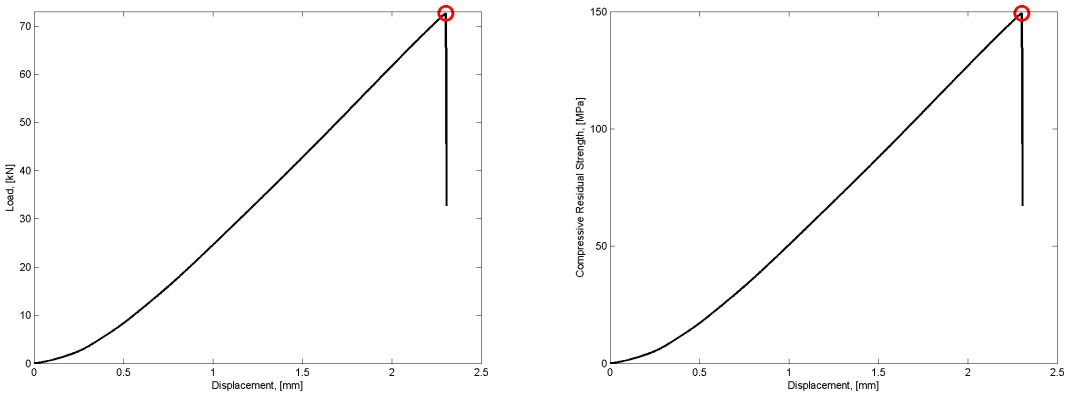

Figure 252: Measured and calculated response of Sample 408 subjected to compression after impact testing.

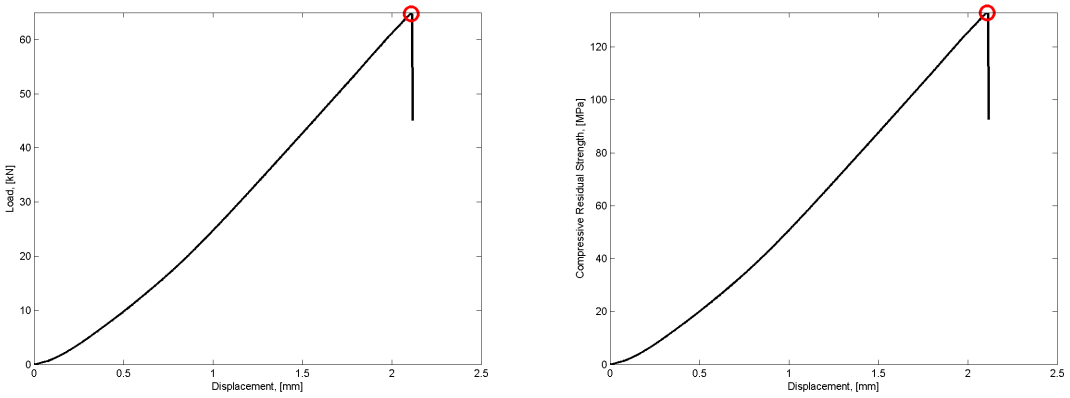

Figure 253: Measured and calculated response of Sample 409 subjected to compression after impact testing.

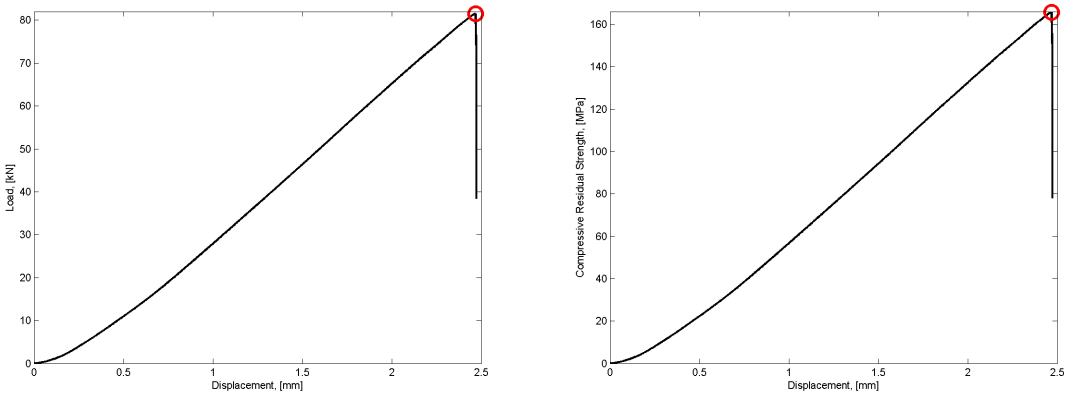

Figure 254: Measured and calculated response of Sample 410 subjected to compression after impact testing.

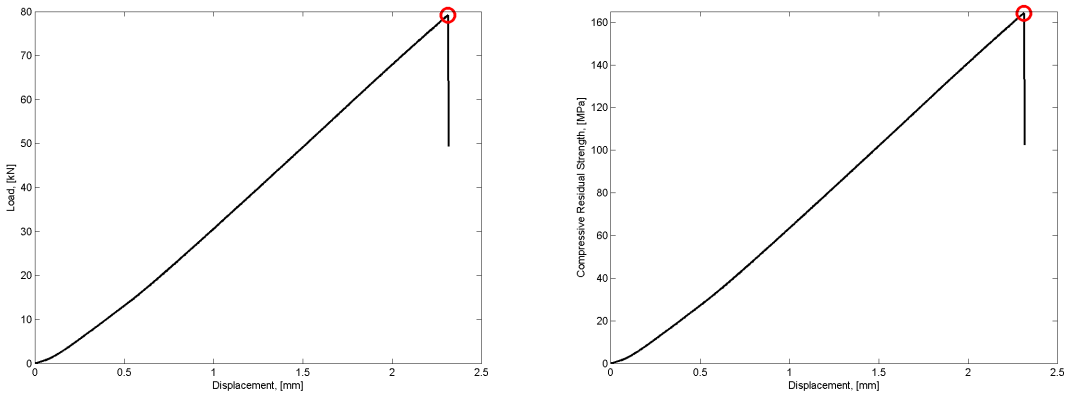

Figure 255: Measured and calculated response of Sample 502 subjected to compression after impact testing.

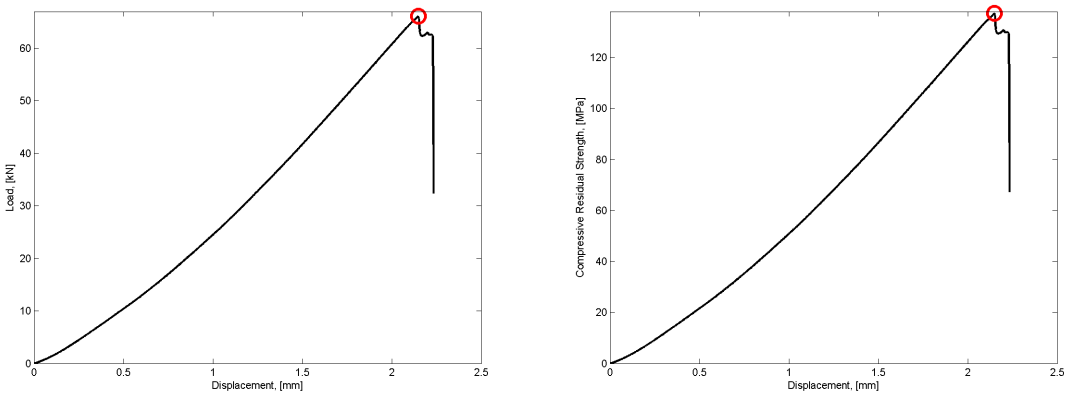

Figure 256: Measured and calculated response of Sample 503 subjected to compression after impact testing.

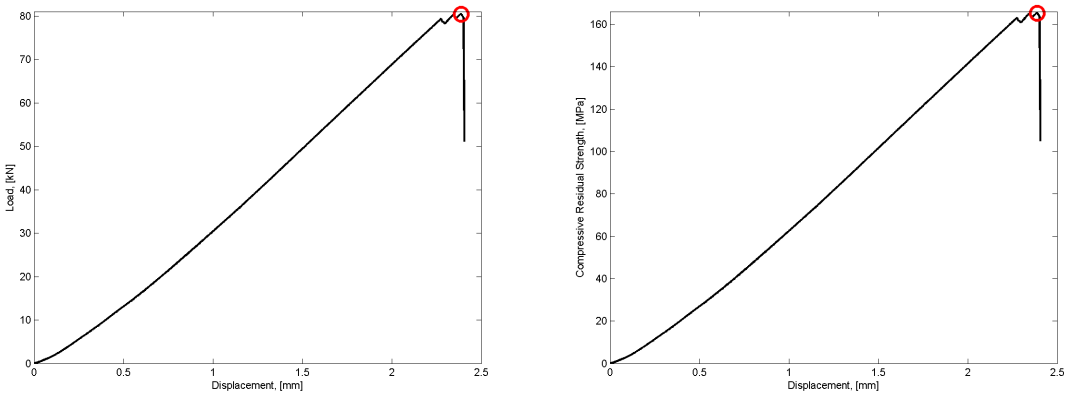

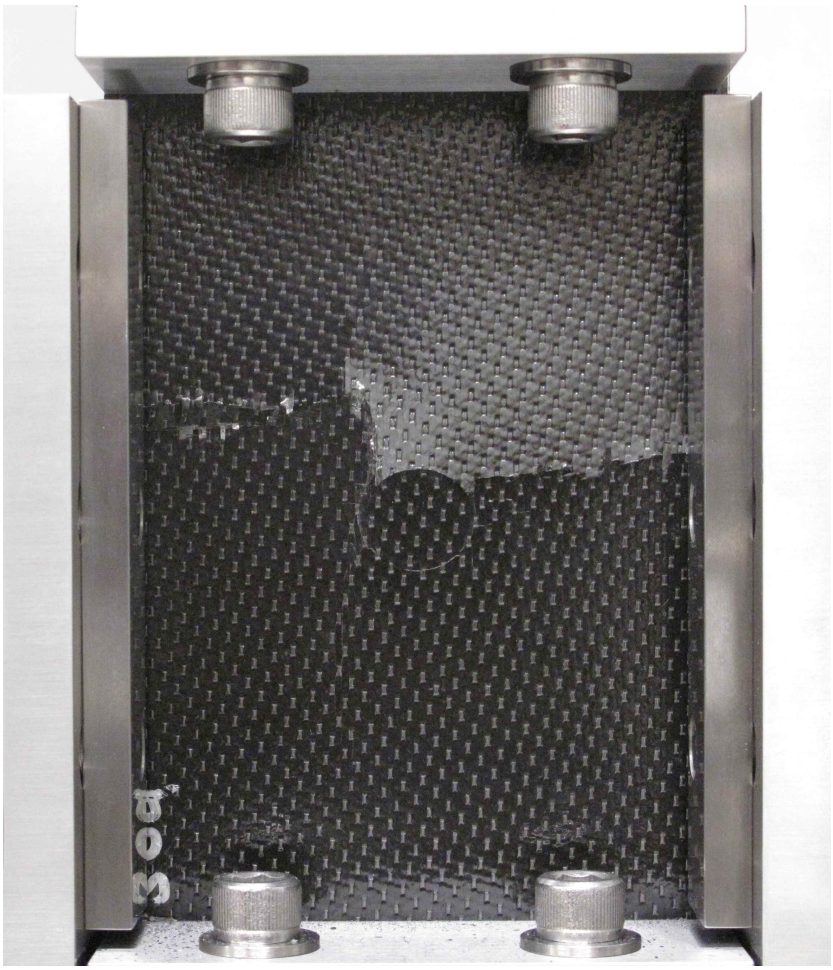

Figure 257: Measured and calculated response of Sample 504 subjected to compression after impact testing.

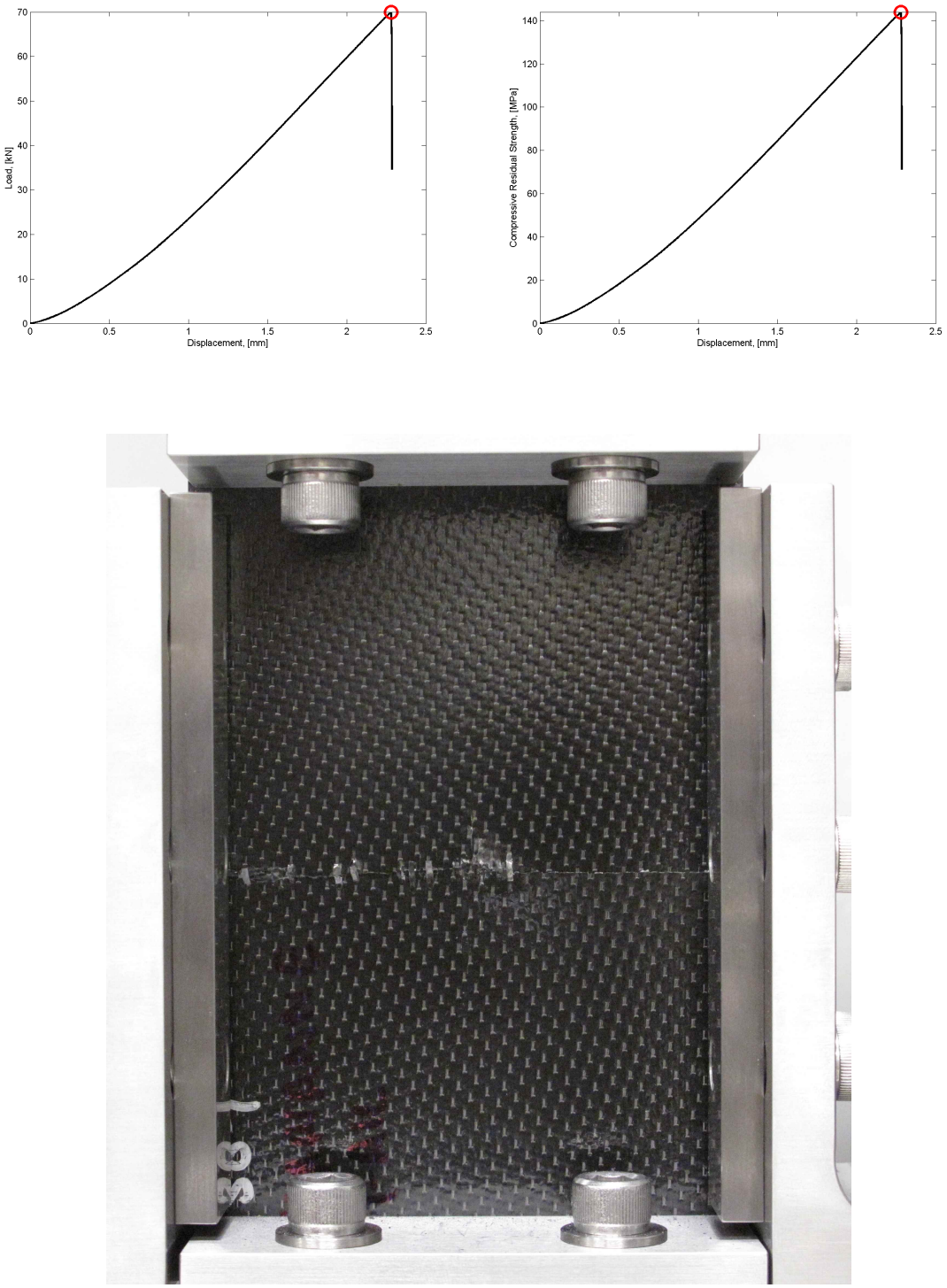

Figure 258: Measured and calculated response of Sample 507 subjected to compression after impact testing.

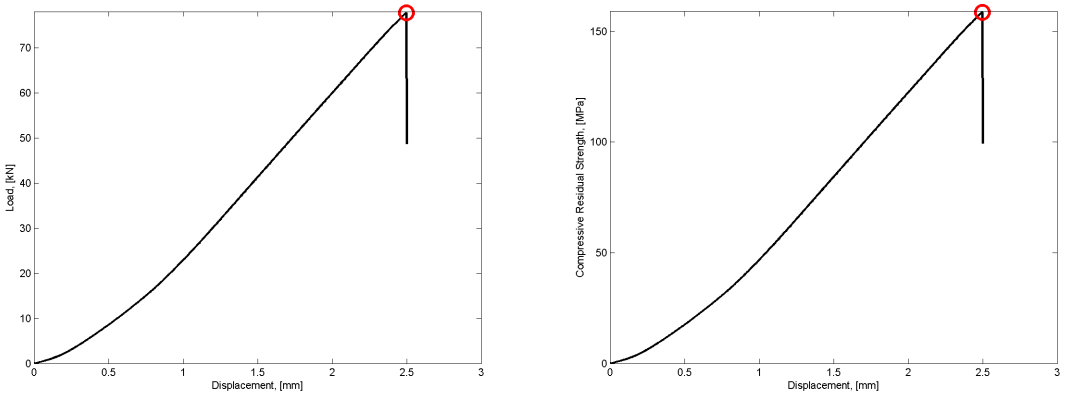

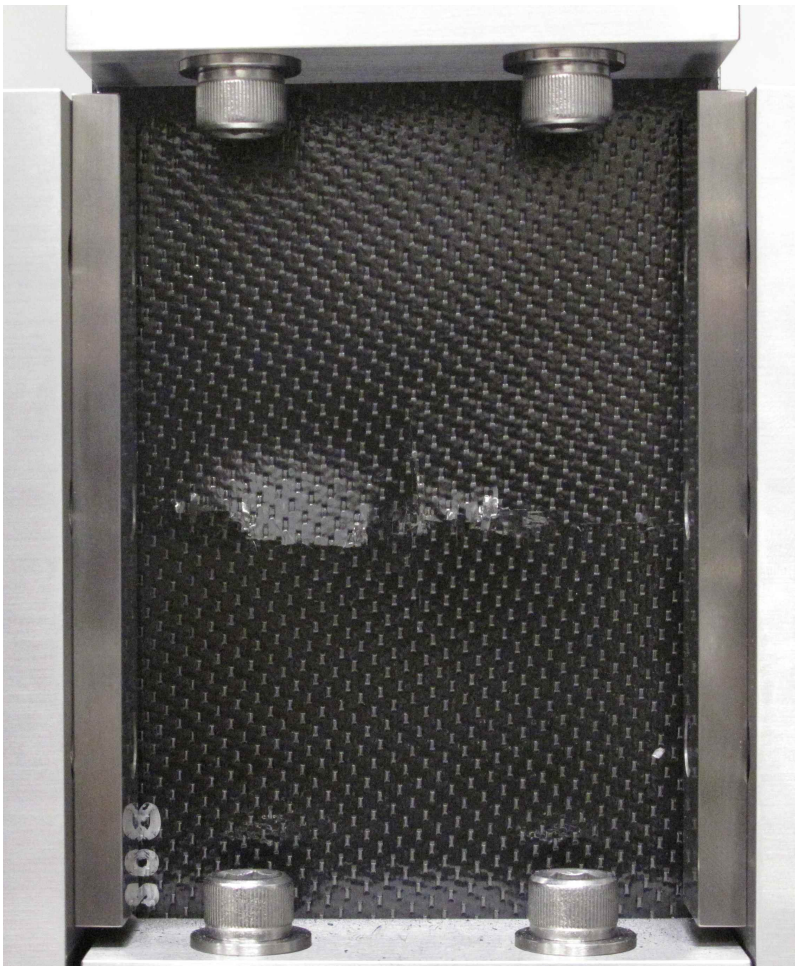

Figure 259: Measured and calculated response of Sample 508 subjected to compression after impact testing.

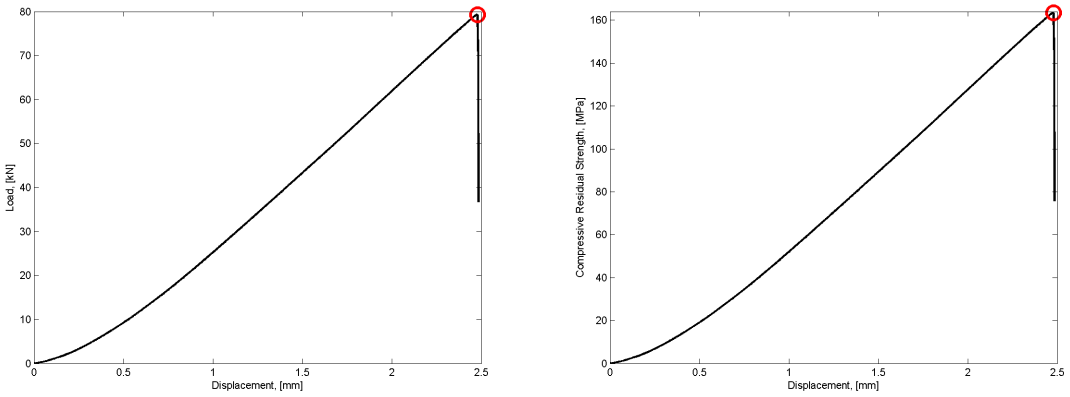

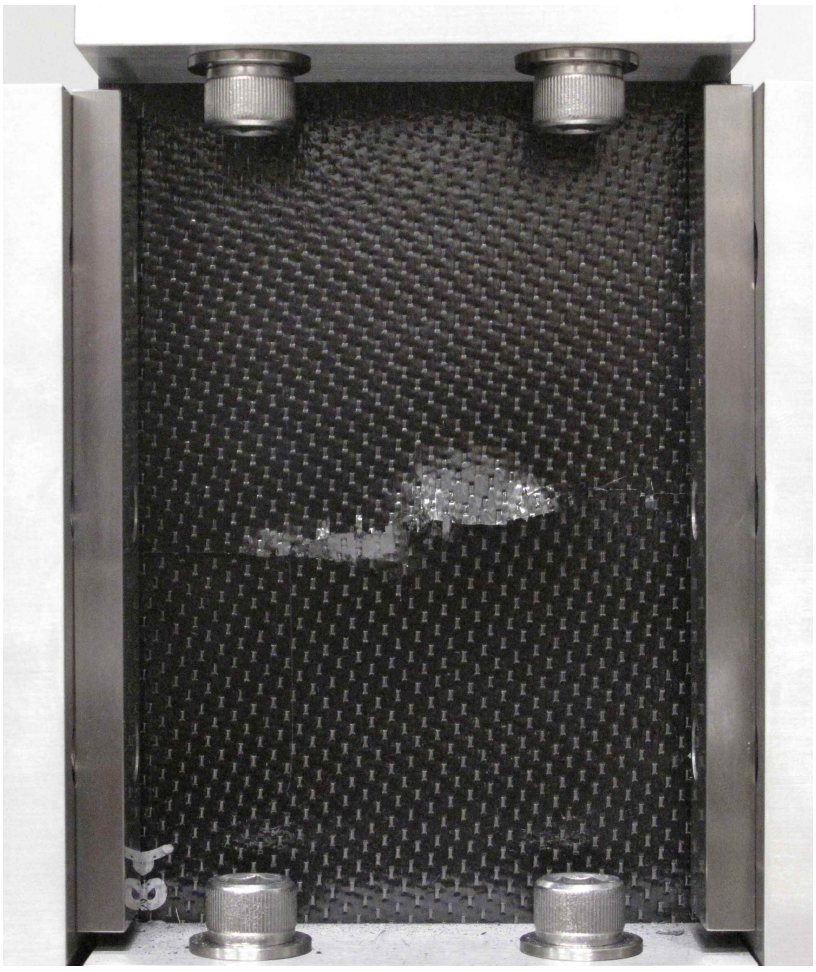

Figure 260: Measured and calculated response of Sample 509 subjected to compression after impact testing.

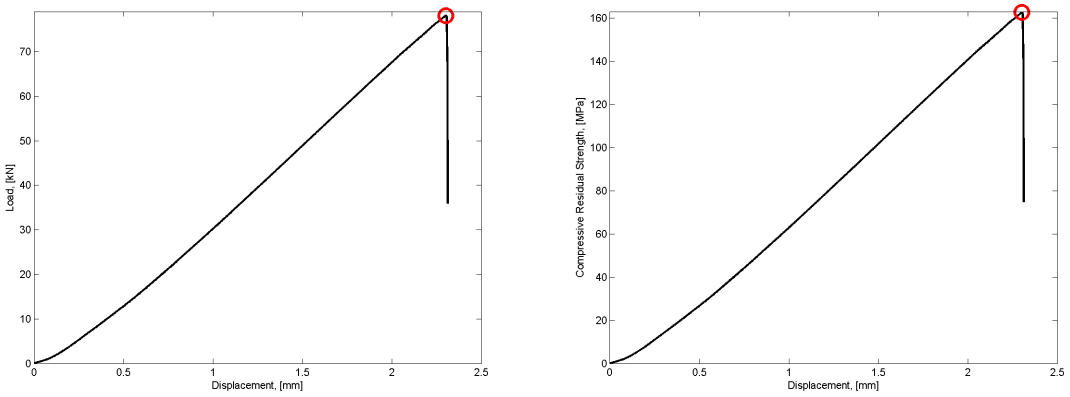

Figure 261: Measured and calculated response of Sample 510 subjected to compression after impact testing.

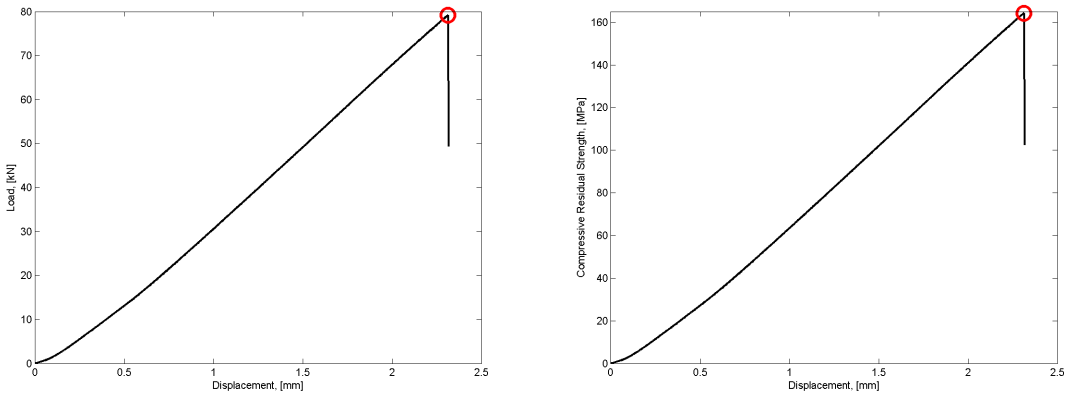

Figure 262: Measured and calculated response of Sample 602 subjected to compression after impact testing.

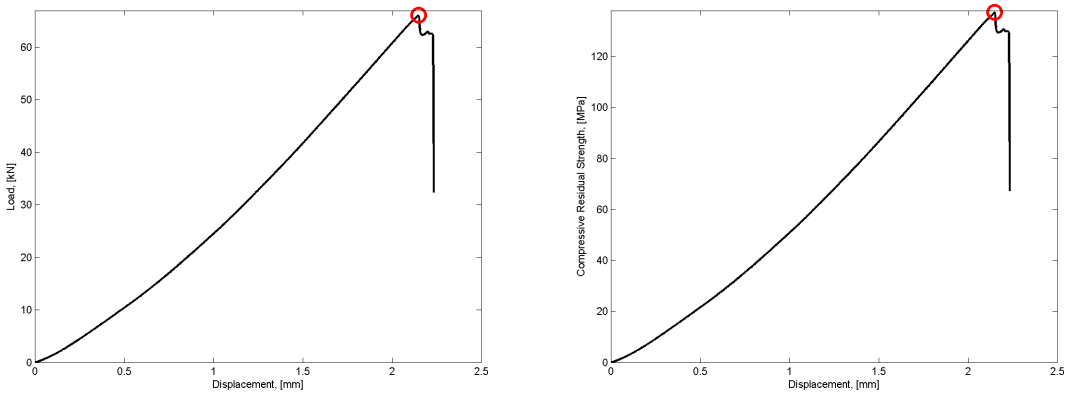

Figure 263: Measured and calculated response of Sample 603 subjected to compression after impact testing.

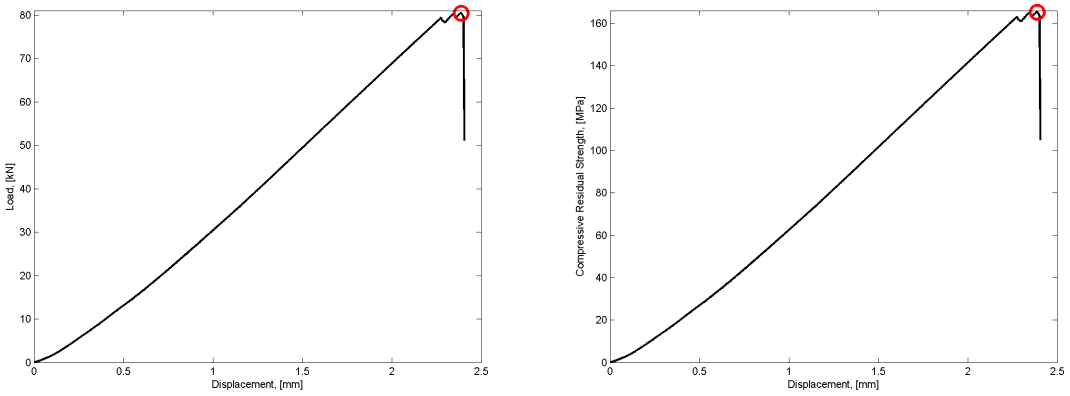

Figure 264: Measured and calculated response of Sample 604 subjected to compression after impact testing.

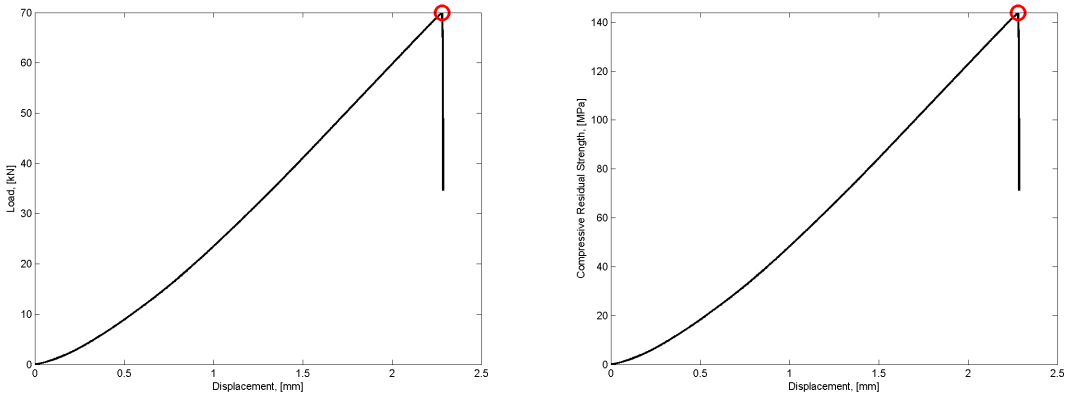

Figure 265: Measured and calculated response of Sample 607 subjected to compression after impact testing.

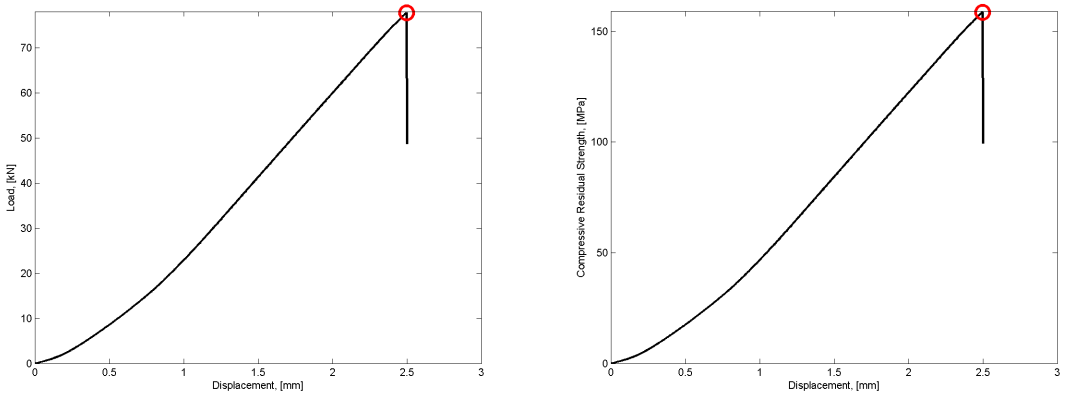

Figure 266: Measured and calculated response of Sample 608 subjected to compression after impact testing.

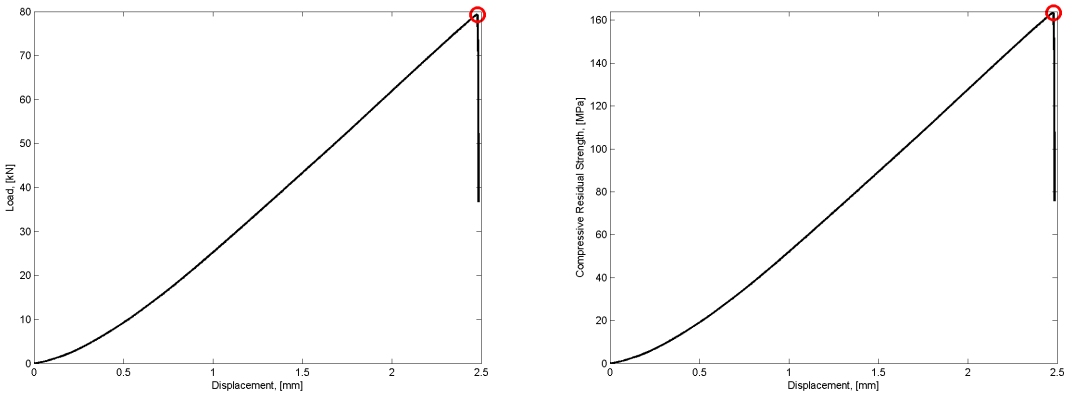

Figure 267: Measured and calculated response of Sample 609 subjected to compression after impact testing.

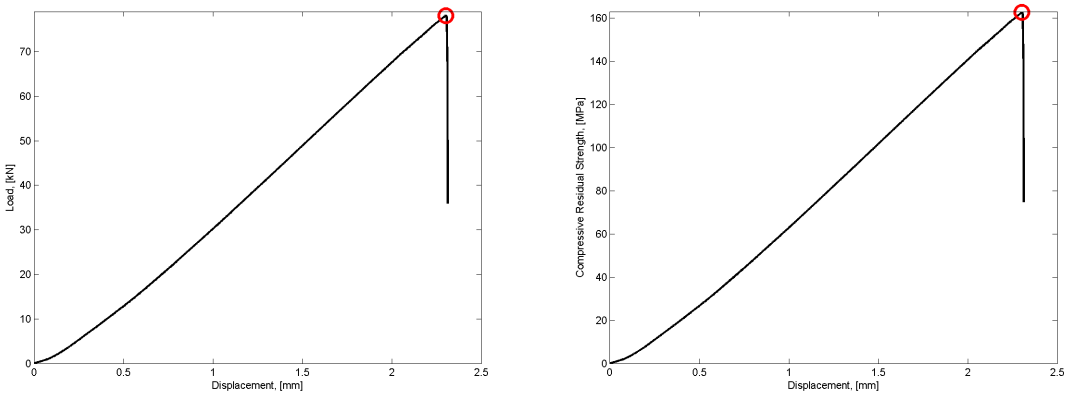

Figure 268: Measured and calculated response of Sample 610 subjected to compression after impact testing.

References

[1] Bhagwan Agarwal, Lawrence Broutman, and K. Chandrashekhara. *Analysis and Performance of Fiber Composites*. John Wiley and Son, Inc., 3 edition.

[2] David Cripps. Woven fabrics.

[3] John D. Buckley and Dan D. Edie. *Carbon-Carbon Materials and Composites*. William Andrew, December 1993.

[4] P. K. Mallick. *Fiber-Reinforced Composites: Materials, Manufacturing, and Design*. CRC Press, 2 edition, May 1993.

[5] Flake Campbell, Andrew Mallow, and C. Browning. Porosity in carbon fiber composites an overview of causes. *Journal of Advanced Materials*, 26(4):18–33, July 1995.

[6] P. Olivier, J. P. Cottu, and B. Ferret. Effects of cure cycle pressure and voids on some mechanical properties of carbon/epoxy laminates. *Composites*, 26(7):509515, 1995.

[7] J.-M. Tang, W. I. Lee, and G. S. Springer. Effects of cure pressure on resin flow, voids, and mechanical properties. *Journal of Composite Materials*, 21(5):421–440, January 1987.

[8] Ling Liu, Bo-Ming Zhang, Dian-Fu Wang, and Zhan-Jun Wu. Effects of cure cycles on void content and mechanical properties of composite laminates. *Composite Structures*, 73(3):303–309, June 2006.

[9] Hansong Huang and Ramesh Talreja. Effects of void geometry on elastic properties of unidirectional fiber reinforced composites. *Composites Science and Technology*, 65(13):1964–1981, October 2005.

[10] Srgio Frascino Mller de Almeida and Zabulon dos Santos Nogueira Neto. Effect of void content on the strength of composite laminates. *Composite structures*, 28(2):139148, 1994.

[11] Kenneth J. Bowles and Stephen Frimpong. Void effects on the interlaminar shear strength of unidirectional graphite-fiber-reinforced composites. *Journal of Composite Materials*, 26(10):1487–1509, October 1992.

[12] D. E. W. Stone and B. Clarke. Ultrasonic attenuation as a measure of void content in carbon-fibre reinforced plastics. *Non-destructive testing*, 8(3):137145, 1975.

[13] L.B. Greszuzuk. *Society of Plastic Engineers*, 20A:1–10, 1967.

[14] B.D. Harper and G.H. Staab. *Journal of Composite Materials*, 21, 1987.

[15] N.L. Hancox. Effects of flaws and voids on the shear properties of CFRP. *Journal of Materials Science and Technologies*, 10:234, 1975.

[16] N.L. Hancox. Effects of flaws and voids on the shear properties of CFRP. *Journal of Materials Science and Technologies*, 12:884–892, 1977.

[17] H.T. Yoshida and T. Ogasa. *Composites Science and Technology*, 25(3), 1986.

[18] A. Farouk and N.A. Langrana. *Polymer Composites*, 13(4), 1992.

[19] Ling Liu, Bo-Ming Zhang, Zhan-Jun Wu, and Dian-Fu Wang. Effects of cure pressure induced voids on the mechanical strength of Carbon/Epoxy laminates. *Journal of Materials Science and Technologies*, 21(1), 2005.

[20] F. Y. C. Boey and S. W. Lye. Effects of vacuum and pressure in an autoclave curing process for a thermosetting fibre-reinforced composite. *Journal of materials processing technology*, 23(2):121131, 1990.

[21] Seth R. Ghiorse. A comparison of void measurement methods for carbon/epoxy composites. 1991.

[22] Seth R. Ghiorse. Effect of void content on the mechanical properties of carbon epoxy laminates. *SAMPE Quarterly*, pages 54–59, January 1993.

[23] A. Subramanian, V. Dayal, and D. J. Barnard. Damage characterization of carbon/epoxy laminates using compression-after-impact (CAI) and ultrasonic NDE. pages 987–994, 2013.

[24] D30 Committee. Test method for compressive residual strength properties of damaged polymer matrix composite plates. Technical report, ASTM International, 2012.

[25] Serge Abrate. *Impact on composite structures*. Cambridge University Press, Cambridge, 1998.

[26] W. J. Cantwell. The influence of target geometry on the high velocity impact response of CFRP. *Composite structures*, 10(3):247265, 1988.

[27] R.C. Novak and M.A. DeCrescente. Impact behavior of unidirectional resin matrix composites tested in fiber direction. pages 311–323, Philadelphia, PA, 1972.

[28] P.W.R. Beaumont. A fracture mechanics approach to failure in fibrous composites. *Journal of Adhesives*, 6:107–137, 1974.

[29] D30 Committee. Test method for measuring the damage resistance of a fiber-reinforced polymer matrix composite to a drop-weight impact event. Technical report, ASTM International, 2012.

[30] D Lui and L.E. Malvern. Matrix cracking in impacted Glass/Epoxy plates. *Journal of Composite Materials*, 21(7):594–609, 1987.

[31] Himadri Samajder, Harsh Baid, Fabrizio Ricci, and Ajit Mal. Lamb waves in a honeycomb composite sandwich plate. In *SPIE Smart Structures and Materials+ Nondestructive Evaluation and Health Monitoring*, page 869505869505, 2013.

[32] I. M. Daniel, S. C. Wooh, and I. Komsky. Quantitative porosity characterization of composite materials by means of ultrasonic attenuation measurements. *Journal of nondestructive evaluation*, 11(1):18, 1992.

[33] W.N. Reynolds and S.J. Wilkinson. The analysis of fiber-reinforced porous composite materials by the measurement of ultrasonic wave velocities. *Ultrasonics*, pages 159–163, July 1978.

[34] James H. Williams Jr, Hamid Nayeb-Hashemi, and Samson S. Lee. Ultrasonic attenuation and velocity in AS/3501-6 graphite fiber composite. *Journal of Nondestructive Evaluation*, 1(2):137148, 1980.

[35] A. K. Mal, C.-C. Yin, and Y. Bar-Cohen. Ultrasonic nondestructive evaluation of cracked composite laminates. *Composites Engineering*, 1(2):85101, 1991.

[36] T.S. Jones and H. Berger. Application of nondestructive inspection methods to composites. *Materials Evaluation*, 47:390–400, 1989.

[37] P. Cawley. The rapid non-destructive inspection of large composite structures. *Composites*, 25:351–357, 1994.

[38] Rene Sicard. Inspection of complex aerospace structures using automated 3D ultrasonic scanning. Montreal, Quebec, November 2011.

[39] B.T. Astrom. Manufacturing of polymer compsoites. 2002.

[40] F.C. Campbell. Manufacturing process for advanced composites. 2004.

[41] D30 Committee. Test method for short-beam strength of polymer matrix composite materials and their laminates. Technical report, ASTM International, 2006.

[42] D20 Committee. Test methods for flexural properties of unreinforced and reinforced plastics and electrical insulating materials. Technical report, ASTM International, 2010.